# 2ND INTERNATIONAL WORKSHOP ON THE INTEGRITY OF NUCLEAR COMPONENTS

April 20;21, 1998

主 催　社団法人 日 本 溶 接 協 会
原 子 力 研 究 委 員 会
The Japan Welding Engineeing Society
Atomic Energy Reseach Committee

Safety and Structural Integrity Research Center,
Sung Kyun Kwan University

# Program of the Workshop

| | | |
|---|---|---|
| 4/20 | 9:30-10:00 | Registation |
| | 10:00-10:10 | Opening Address by G.Yagawa (University of Tokyo) |
| | 10:10-11:10 | Session I Design and Analysis |
| | | I-1 Concept of Advanced Design Standards for DFBR<br>Masahiro Ueta, JAPC, Japan |
| | | I-2 A Study of the Helical Effect on the Connection by Three Dimensional FEM Stress Analyses<br>Jien-Jong Chen &Yan-Shin Shih, Institute of Nuclear Energy Research Atomic Energy Council, Taiwan, Republic of China |
| | 11:10-11:40 | Break |
| | 11:40-13:10 | Session II Structural Integrity and Life Prediction |
| | | II-1 Probabilistic Fracture Mechanics of Nuclear Structural Components<br>Genki Yagawa, University of Tokyo, Japan |
| | | II-2 Remaining Life Prediction Method Using Operating Data and Knowledge on Mechanisms<br>Bom Soon Lee, Materials and Corrosion Research Laboratory, Korea Electric Power Research Institute, Korea Electric Power Corporation, Korea |
| | | II-3 Structural Integrity Assessment of the Reactor Pressure Vessel under the External Cooling Condition<br>Jong Sung Kim, Yoon Suk Chang, Tae Eun Jin, Korea Power Engineering Company, Inc., Korea |
| | 13:10-14:20 | Lunch |
| | 14:20-15:20 | Session III Plant Experiences |
| | | III-1 The Evaluation of IGSCC Problems of Stainless Steel Piping in Taiwan BWR-6 Nuclear Power Plant<br>Kuen Ting, Department of Nuclear Regulation Atomic Energy Council,Taiwan, Republic of China |
| | | III-2 ISI NDE in Korean Nuclear Power Plants<br>Yi-Hwan (Peter) Jeong, Korea Electric Power Research Institute, Korea |
| | 15:20-15:50 | Break |
| | 15:50-16:50 | Session III Plant Experiences (Continued) |
| | | III-3 Core Shroud Replacement of Fukushima-Daiichi Unit #3<br>Jun Matsumoto, Nuclear Power Plant Management Dept. Tokyo Electric Power Company, Japan |
| | | III-4 The Evaluation of Erosion-Corrosion Problems of PWR Carbon Steel Piping in Taiwan<br>Kuen Ting, Department of Nuclear Regulation Atomic Energy Council, Taiwan, Republic of China<br>Yin Pang Ma, Institute of Nuclear Energy Research Atomic Energy Council, Taiwan, Republic of China |

| | | |
|---|---|---|
| 4/21 | 10:00-12:00 | Session IV Piping and LBB |
| | | IV-1 Development of Modified Piping Evaluation Diagram for LBB Application<br>Y.J.Kim, Y.Z.Lee & N.S.Huh, Dept. of Mechanical Engineering, Sung Kyun Kwan Univ., Suwon, Korea<br>C.R.Pyo, Dept.of Mechanical Engineering, Induk college, Seoul, Korea<br>J.S.Yang, Korea Electric Power Research Institute, Daejon, Korea |
| | | IV-2 Fracture Mechanics Evaluation for The Cast Duplex Stainless Steel after Thermal Aging<br>Shigeru Urata, Manager of Nuclear Safety Engineering Section Kansai Electric Power Co. Inc., Japan |
| | | IV-3 Fracture Behavior of Carbon Steel Pipe with Local Wall Thinning Subjected to Bending Load<br>Katsumasa Miyazaki & Satoshi Kanno, Mechanical Engineering Research Laboratory, Hitachi Ltd., Japan<br>Masayuki Ishiwata & Kunio Hasegawa, Hitachi Works, Hitachi Ltd., Japan |
| | | IV-4 Leak-Before-Break Assessment of CANDU Pressure Tube Considering Leak Detection Capability<br>Youn-Won Park and Yeon-Ki Chung, Korea Institute of Nuclear Safety, Korea |
| | 12:00-13:30 | Lunch |
| | 13:30-14:30 | Session IV Piping and LBB (Continued) |
| | | IV-5 Approximate Evaluation Method for Ductile Fracture Analysis of Circumferentially Through-Wall-Cracked Pipe Subjected to Combined Bending and Tension<br>Naoki Miura (CRIEPI), Materials Science Department, Central Research Institute of Electric Power Industry, Japan |
| | | IV-6 Low Alloy Steel Piping Test for Fracture Criteria of LBB<br>Koji Koyama, Nuclear Plant Component Designing Section, Kobe Shipyard & Machinery Works, Mitsubishi Heavy Industries, Ltd., Japan |
| | 14:30-15:00 | Break |
| | 15:00-16:30 | Session V Material Characteristics |
| | | V-1 Effect of Reverse Cyclic Loading on Fracture Resistance Curves in CT Specimens<br>C. S. Seok, Sung Kyun Kwan University, Dept. of Mechanical Engineering, Korea<br>Y. J. Kim, Sung Kyun Kwan University, Dept. of Mechanical Design, Korea<br>J. I. Won, Sung Kyun Kwan University, Graduate School Dept. of Mechanical Design, Koera |
| | | V-2 The Frequency Effect on the Fatigue Crack Growth Rate of 304 Stainless Steel<br>J ien-Jong Chen & Yan-Shin Shih, Institute of Nuclear Energy Research Atomic Energy Council, Taiwan, Republic of China |
| | | V-3 Investigation on Fracture Toughness Evaluation Method for Reactor Pressure Vessel Surveillance<br>Kunio Onizawa, Tohru Tobitz & Masahide Suzuki, Reactor Component Reliability Laboratory, Japan Atomic Energy Research Institute, Japan |
| | 16:30-16:40 | Closing by M.Kikuchi (Science University of Tokyo) |

# Session I

# Design and Analysis

I-1 Concept of Advanced Design Standards for DFBR

Masahiro Ueta, JAPC, Japan

# CONCEPT OF ADVANCED DESIGN STANDARDS FOR DFBR

Masahiro UETA

THE JAPAN ATOMIC POWER COMPANY
1-6-1, Ohtemachi, Chiyoda-ku, Tokyo 100, JAPAN
Phone : 3-3201-6631 Fax : 3-3285-0542
E-mail : masahiro-ueta@japc.co.jp

Abstract

The Japan Atomic Power Company (JAPC) has been developing the demonstration fast breeder reactor (DFBR) under the sponsorship of nine Japanese electric companies and the Electric Power Development Co.Ltd since 1986. JAPC has drafted the structural design guide for the DFBR at elevated temperatures (DDS) based on that for the prototype FBR MONJU. However, in the last December the round-table committee, established in the Atomic Energy Commission, published the report that the construction of the DFBR should be projected based on experiences of operation and maintenance of MONJU and reflecting latest R&D achievement. As the result the DFBR project may be somewhat postponed. Meanwhile, the requirement to the DFBR are becoming more and more strict toward higher economy consistent with reliability. To cope with the requirement, JAPC has started drastic revision of the DDS. The main issues in the revision are rearrangement of code systems and improvement of estimation method of load conditions, accumulated strains by ratchetting and creep-fatigue damage. This paper describes the concept of the advanced DDS.

## 1. Introduction

Worldwide energy demand has been increasing with population increase and economic development especially in developing countries, although many countries are making efforts to save energy consumption. If the consumption of fossil energy increase with energy demand, energy resources, such as oil and natural gas, may be run out of in the middle of the

next century. And it is also forced to limit consumption of fossil energy from the view point of protecting global environment from greenhouse effect and acid rain caused by exhausted gas like carbon dioxide and other oxidant gases from fossil power plants. Nuclear power generation is the most promising and effective measures to cope with both energy demand and environment protection. Nuclear people convince that nuclear power generation will play the essential role in energy supply in the next century.

Fast breeder reactors (FBRs) have the potential to utilize uranium resources much more effectively than light water reactors (LWRs) by more than 50 times, and so it is expected that FBRs can secure worldwide energy supply for more than thousands of years. FBRs also have fascinating potential to be able to incinerate minor actinides which are radioactive wastes of ultra-long half-lives originated from nuclear power plants. Therefore, Japanese government and utilities have been promoting the development of FBR since the initial stage of nuclear energy development.

The Japan Atomic Power Company (JAPC) has been developing the demonstration fast breeder reactor (DFBR) following the prototype FBR MONJU under the auspices of nine Japanese electric power companies and the Electric Power Development Co.Ltd. since 1986. Main specifications of the DFBR were settled in January 1994. In December 1995, the sodium leak incident occurred in MONJU. It showed that it is essentially important for FBRs to prevent sodium fire which may result in long-term plant outage and lower plant availability of FBRs. And deregulation in electric power industries forces nuclear industries to reduce power generation cost as fossil power generation of which cost is drastically reduced recently. Therefore, JAPC has been conducting the conceptual design study of the DFBR aiming at eliminating anxiety of sodium fire and reducing construction cost of the DFBR far below 1.5 times that of LWRs on the 1000MWe basis. In this study the DFBR would be provided with comprehensive countermeasures against sodium leak and fire to eliminate instrumentation well through sodium boundaries, to enclose whole sodium piping by guard pipes, and to install auxiliary sodium systems as purification systems into vessels.

The MONJU incident induced nationwide discussion on FBR development in Japan, and the round-table committee was established in the Atomic Energy Commission. This committee reported in December 1997 that FBR is one of the promising options of future energy resources, that MONJU

should be restarted for research and development (R&D) of FBR, and that the DFBR should be projected reflecting experience obtained in operation and maintenance of MONJU and incorporating latest R&D achievements. Therefore, sufficient time is kept until construction of the DFBR enough to achieve innovative R&Ds for improving economy of the DFBR drastically.

The current structural design guide for the DFBR at elevated temperatures (DDS) was drafted based on that for MONJU and incorporating R&D achievements after MONJU. It has been applied as the design standard to design studies of the DFBR. However, it is required to improve accuracy of design evaluation for realizing economical design consistent with reliability. Therefore, JAPC has started the long-range study for the advanced DDS as a typical embodiment of innovative R&Ds.

This paper describes the policy to revise the DDS.

## 2. Policy to Improve DFBR Design

### 2.1 Reducing Uncertainty in Design

The nuclear steam supply system (NSSS) of the DFBR should have reliability prior to others, because sufficient experiences have not been accumulated in FBR operation and maintenance. Economy improvement compatible with reliability can be realized by reducing uncertainty in whole design process as shown in Fig. 1. The policies to reduce uncertainty are as follows.

(1) Material

To reduce scattering of material strength, chemical compositions and heat treatment conditions should be specified rigorously as far as material cost does not increase significantly.

To reduce inaccuracy in extrapolation of material strength, data of long-term creep rupture, ultra-high cycle fatigue and creep-fatigue in low strain range should be acquired.

To improve prediction of time-dependent effects, data of long-term aging effect at elevated temperatures, neutron irradiation effect and sodium environment effect on material strength should be acquired.

(2) Structure

To reduce deviation of strength from normal value and to eliminate unforeseen trouble, requirements on quality assurance should be imposed on design, fabrication, construction, installation and inspection considering cost impact.

To reduce uncertainty of structural strength caused by worker's skill and discontinuities in material or geometry, simple and robust design should be aimed at.

(3) Loading condition

Thermal transient load is critical in assuring structural integrity of FBR components since it is much more difficult to predict thermal transient load than pressure load. Improvement of thermal load prediction will contribute to economical design consistent with reliability. Thermal hydraulic model tests are useful to understand thermal hydraulic behaviors, to improve accuracy of thermal load prediction and to verify computer codes for design analysis.

Usually thermal stresses are classified into the secondary stress, but they may act as the primary stress in case elastic follow-up is significant at elevated temperatures. Therefore, strain intensification due to elastic follow-up should be evaluated carefully in elevated temperature design. The current method employed in the DDS has shown to be too conservative in many cases, To realize economical design consistent with reliability, new concept considering the mechanism of elastic follow-up should be introduced into the advanced DDS.

(4) Design criteria of failure

Design criteria of failure should be well correlating with actual failure modes and should conservatively envelope actual failure limits as close as possible. Creep damage evaluation is the key toward well-correlated design criteria. The current method applies time fraction concept for creep damage evaluation. To realize economical design consistent with reliability, creep damage evaluation method should be improved through discussions taking sufficient time to reach consensus among the related specialists and engineers. New methods as ductility exhaustion concept will be investigated in addition to modifying the current time fraction concept.

2.2 Safety Margin

Design margins should be kept sufficiently in design criteria in DDS, for example, 20 of number of cycles and 2 of strain range in fatigue design. Different margins should be defined dependent upon frequencies and significance of failure events.

Evaluation methods applied in design should envelope failure limits on a conservative side, but as close to the limits as possible. In other word, design margin should not be shared to inaccuracy of evaluation method, while additional margin is not expected in evaluation methods.

2.3 Inelastic analysis

Computer analysis is making great advance in recent years. Inelastic analysis will be employed widely to DFBR design to realize economical design consistent with reliability. JAPC will employ inelastic analysis to estimate ratchetting strain in design, to find optimized design by numerical experiments in place of model tests, to define appropriate elastic follow-up parameters, and to confirm that sufficient design margin is kept.

The guideline of inelastic analysis should be prepared to assure conservatism and to attain licensability of designs employing inelastic analysis.

3. Policies for Advanced DDS

3.1 General

The advanced DDS will adopt the graded code system as shown in Fig.2. The discussion has started to introduce the graded code system into the design of plants in non-nuclear fields with future prospect of introducing that system also into nuclear fields.

The first grade is a performance-based code, such as MITI ordinance No. 62, which specifies only requirements from the view point of safety and reliability. The second grade is a general structural design code which provides the limits of load, stress, strain, damage and other parameters from the viewpoint of assuring structural integrity. The third grade is a supplemental code which would provide local rules, for instance, seismic design guideline under a site-dependent earthquake condition. Non-

mandatory rules for special configurations such as tube plates are also included in the third grade. The guideline of inelastic analysis may be classified into the third grade. The fourth grade is the document to explain the basis and background of codes and standards. The document would include data of tests, experiments and analyses to validate the code.

The advanced DDS will aim at the code which has merit to do detailed design analysis. For this purpose the advanced DDS will be composed of screening rules using simplified analysis, standard rules using detailed elastic analysis, and general rules in which it would be permitted to validate the design by experiment and detailed inelastic analysis.

3.2 Main items to be revised

(1) Accumulated inelastic strain

While current codes provide constant values of accumulated inelastic strain limit independent of material, the advanced DDS would define the limit values material by material to take advantage of improved ductility.

Several modes of ratchetting may occur under the combination of primary loads and secondary thermal loads as shown in Fig.3. It is not easy to estimate inelastic strain due to all ratchetting modes using elastic analysis. On the contrary, inelastic analysis can conservatively estimate whole ratchetting behaviors by one calculation using appropriate model and considering all loading conditions. Therefore, the advanced DDS would adopt design using inelastic analysis to ratchetting as a standard method. The guideline of inelastic analysis should be prepared to provide the procedure to ensure conservatism of analysis results.

(2) Fatigue

High cycle fatigue is a important cause of cracking and failure of structures in FBR, because sodium flow with high velocity at different temperatures may occur flow-induced vibration and thermal fluctuation. The key issue is to establish the method to estimate loading conditions as forces, stresses and frequencies. The guideline should be prepared for high cycle fatigue design to enhance reliability.

Since ultra-high cycle fatigue data are very limited at elevated temperatures, current elevated temperature fatigue curves are drawn by linear extrapolation to ultra-high cycles without fatigue limit, although it

may be too conservative. High cycle fatigue data should be acquired to define design fatigue curves with balanced safety margin.

(3) Creep-fatigue

It is thought that structures in FBRs may have huge margin in creep-fatigue because creep damage evaluation methods have over-conservatism. JAPC is studying to improve evaluation methods of creep-fatigue damage based on the following policies.

a. The objective of improvement is to realize economical design consistent with reliability.
b. The damage evaluation method should well correlate with actual failure behavior in service conditions.
c. The damage evaluation method should not have so many material constants. Material constants should be defined without any special sophisticated tests.
d. It is recommended that damage can be evaluated using easily available material data
e. The same concept should be applied to both base metal and weldment of any type of austenitic stainless steels,

(4) Strength of weldment

It is well known that weldment has much higher probability of cracking and failure than base metal region has because of geometrical and material discontinuities. Residual stress and aging deterioration may affect the integrity of weldment. It is difficult to predict the effects of those factors on weldment strength by computer analysis. It may be feasible as an evaluation method for weldment to modify the method for base metal by introducing coefficients which would consider reduction in strength due to factors as above mentioned. Since the coefficients are critical to realize economical structural design consistent with reliability, it should be defined carefully based on results of material tests, structure model tests and computer analyses.

(5) Buckling

The DFBR will adopt horizontal seismic isolation design to the reactor building with the prospect of commercial FBRs applying three dimensional

seismic isolation to standardize plant design. Horizontal seismic isolation building may intensify vertical floor response compared with aseismic buildings. Therefore, the advanced DDS will cover buckling of shells under vertical seismic loads considering interaction with horizontal seismic loads.

## 4. Future Program

JAPC has started the DDS committee by entrusting to The Japan Welding Engineering Society (JWES). The DDS committee has 3 working groups, code system WG, creep-fatigue WG and ratchetting WG. In near future material WG will join in.

Since globalization of code systems is progressing, it is important for the DDS to be in line with overseas codes such as ASME in U.S.A, RCC-MR in France, R5 in UK and so on. JAPC would welcome specialists and engineers in the world to join discussion of the advanced DDS, and JAPC have the plan to do collaborative work in benchmark analysis and data acquisition.

We have the perspective to establish the advanced DDS as follows.

~2005 : First draft of the advanced DDS

~2010 : Discussion and approval of the advanced DDS in the code committee

## 5. Concluding Remarks

Japanese government and utilities have been promoting the development of FBR which will play the important role in energy supply in the 21st century. The Japan Atomic Power Company (JAPC) has been conducting the development of the demonstration fast breeder reactor (DFBR) since 1986. The conceptual design study of the DFBR are ongoing aiming at eliminating anxiety of sodium fire and reducing plant construction cost below 1.5 times that of LWRs on 1000 MWe output basis. However, construction of the DFBR may be postponed through discussion triggered by sodium leak incident in MONJU. We have somewhat long time until construction of the DFBR. Therefore, JAPC is challenging to the advanced DDS which will contribute to enhance economy of the DFBR consistent with reliability.

The key issues in the advanced DDS are to reduce uncertainty in strength of materials and structures, to correlate design criteria well with actual failure behaviors, and to improve accuracy of evaluation methods especially of ratchetting, high cycle fatigue and creep-fatigue.

JAPC has started the DDS committee to draft the advanced DDS by entrusting to The Japan Welding Engineering Society (JWES). The advanced DDS will be embodied around 2010.

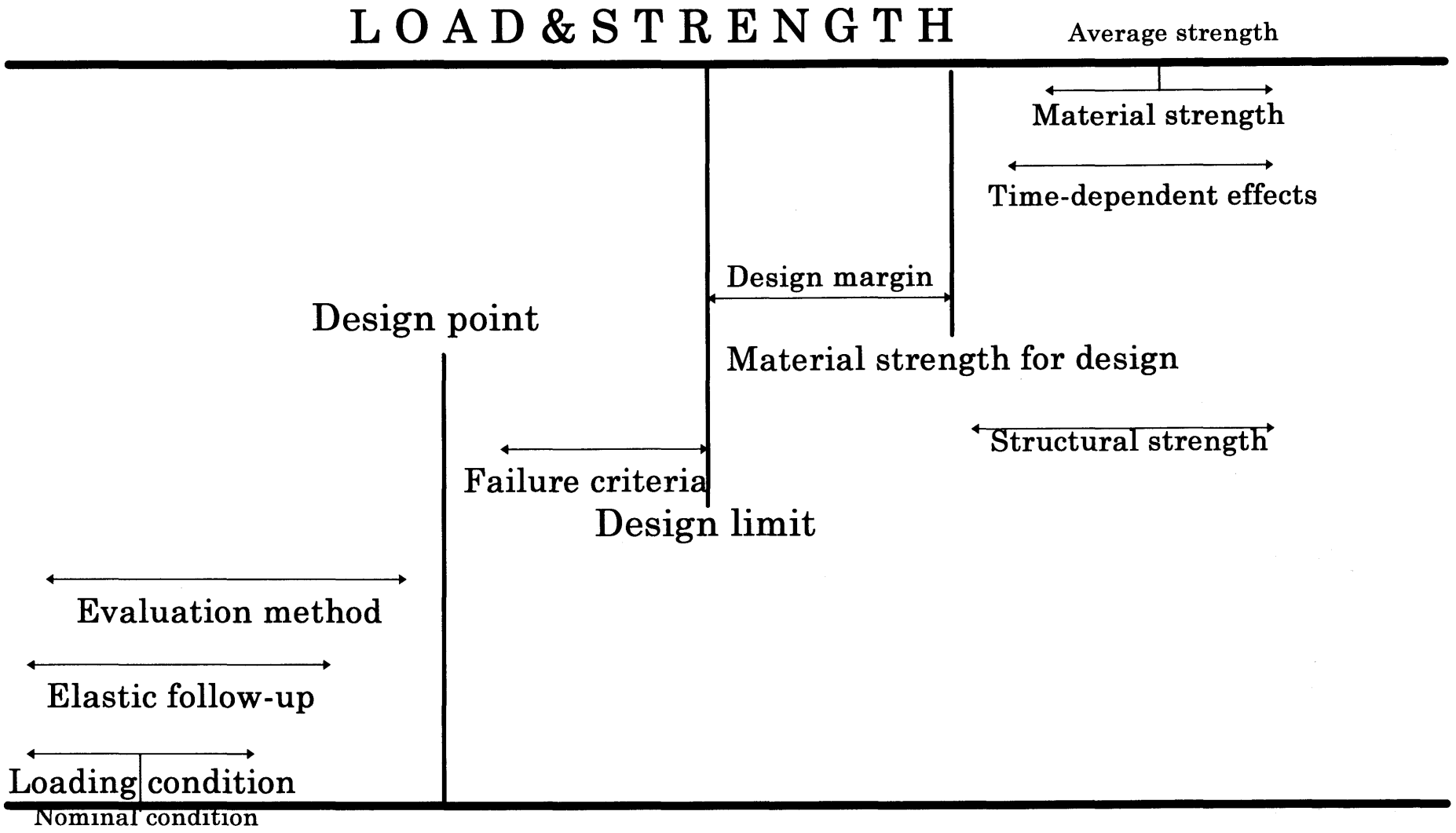


Figure 1 Uncertainty in Design

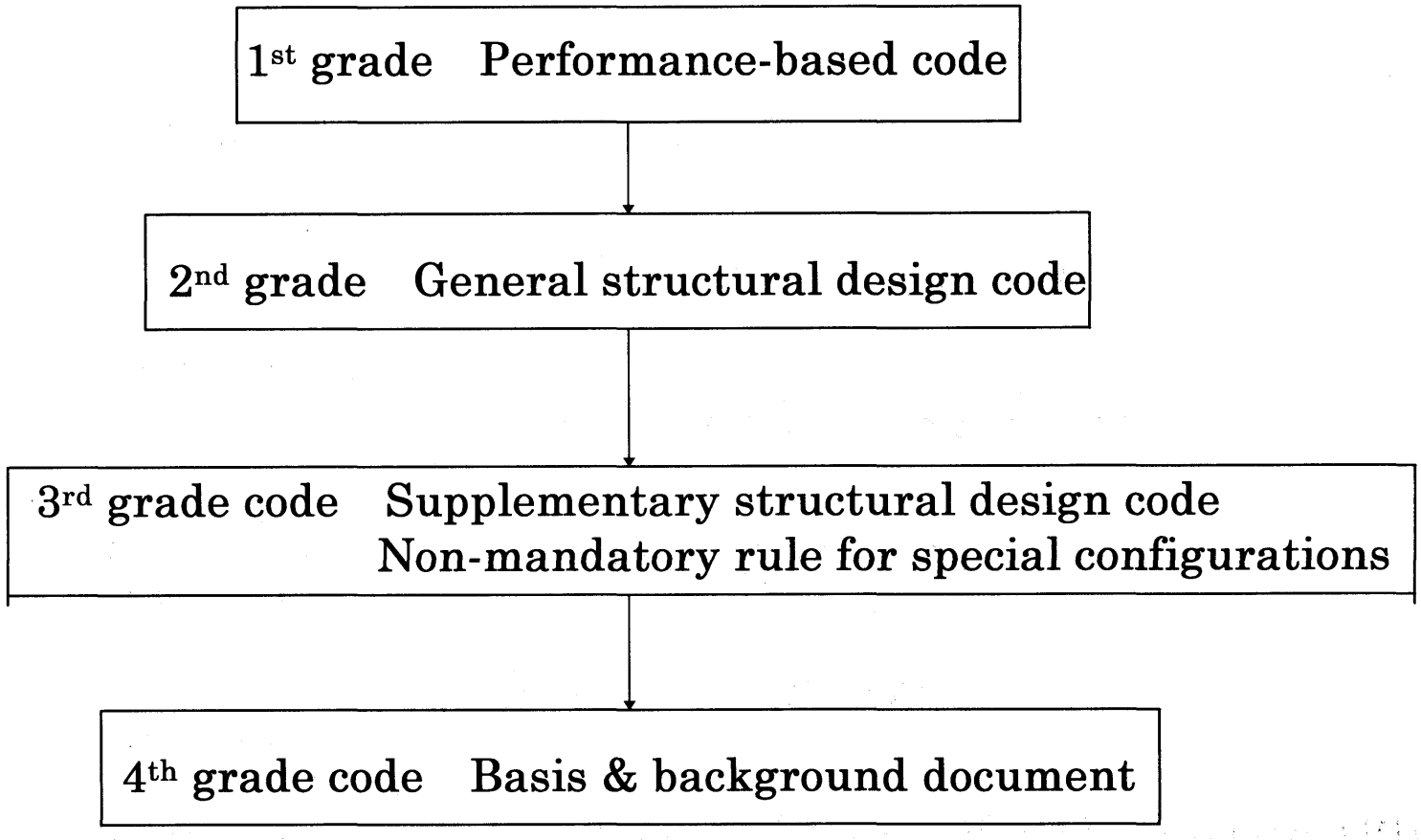


Figure 2 DDS code system to be aimed

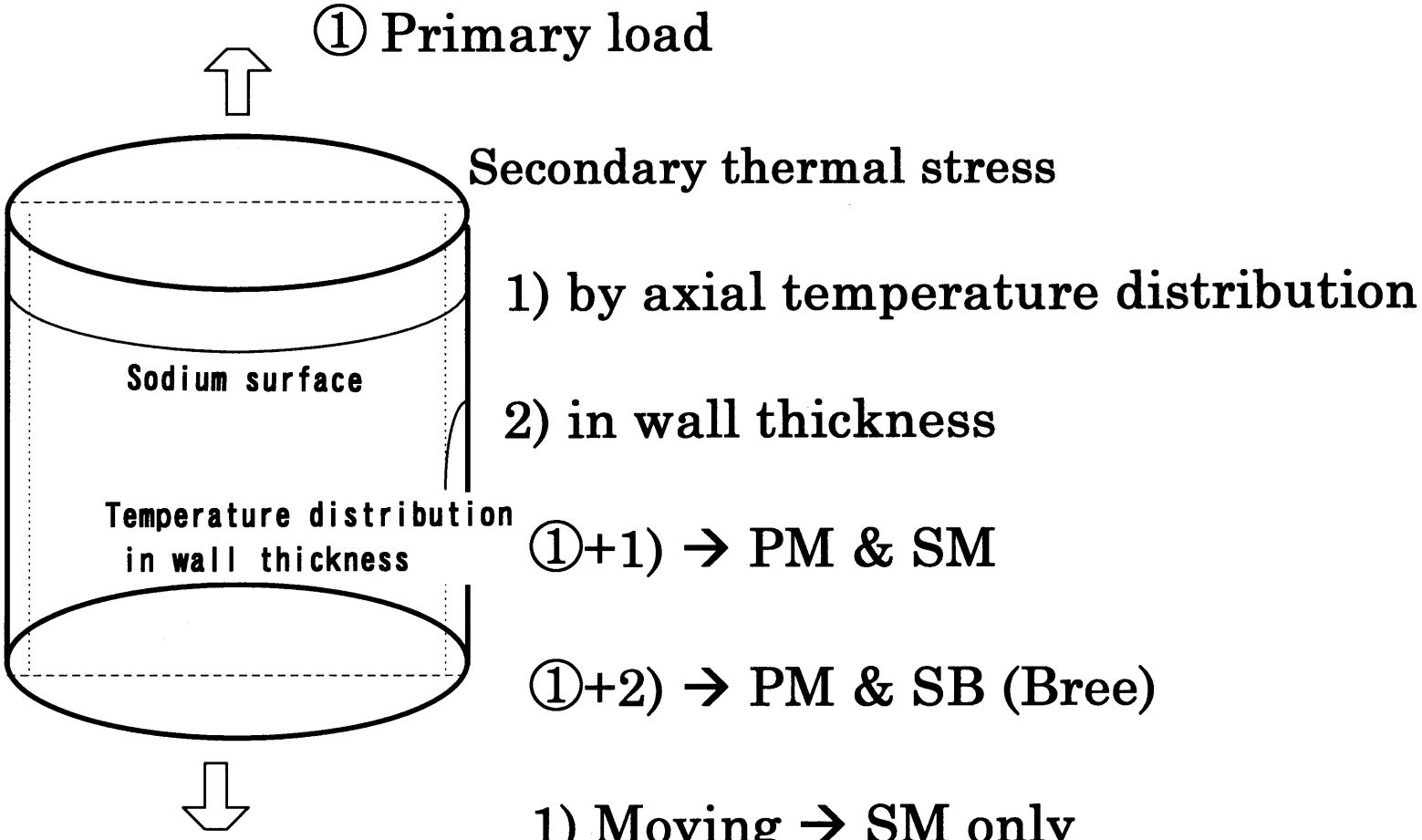


Figure 3 Ratchetting modes

I-2 A Study of the Helical Effect on the Connection by Three Dimensional FEM Stress Analyses

Jien-Jong Chen &Yan-Shin Shih, Institute of Nuclear Energy Research Atomic Energy Council, Taiwan, Republic of China

# A study of the helical effect on the thread connection by three dimensional finite element analysis

Jien-Jong Chen[a,b] and Yan-Shin Shih[b]

[a]Nuclear Division, Institute of Nuclear Energy Research, P. O. Box 3-3,

Lung-Tan, Taoyuan, Taiwan, ROC

[b]Department of Mechanical Engineering, Chung-Yuan Christian University,

Chung-Li,32023 Taiwan, ROC

**Abstract**

The three dimensional finite element analysis of the bolted joints with finite sliding deformable contact has been studied, and the helical and friction effect on the load distribution of each thread is analyzed. It shows the analytical analysis by Yamamoto's method reaches a lower value of load ratio than the finite element analysis at the first thread. The load distribution on each thread between axisymmetrical model and three dimensional model are provided. Hence, although increasing the coefficient of friction and decreasing of the lead angle may improve the load distribution slightly, for 1"-16UNF bolt joints, the error of load ratio at the first thread in axisymmetrical finite element model is 12% with respect to three dimensional analysis.

## I. Introduction

The bolted joint is a typical connection that is widely used for the construction of structural components. Owing to the easy replacement and installation, the bolted joint has been applied to many components of nuclear power plants. However, two problems of bolted joints connection should be concerned. The first one is the

functionality of the joints which threaded end closure is still kept, and the second is the load bearing fraction on each thread of the bolt and nut. In the recent year, many authors (Chaaban et. al. 1992, Grosse et. al. 1990, Wileman et. al 1991, Lehnhoff et. al 1996) have focused on the study of threaded end closure of the bolted joint. But the load distribution analysis has been seldom mentioned during last few decades. The investigation of the load distribution in the threaded connection has been studied since 1940's. The Sopwith theory (Sopwith 1948) for predicting the load distribution of the threaded fasteners is a well known analytical model. The action of a number of strains is formuated by the axial extension of the bolt and compression of the nut in Sopwith theory. These strains include the bending deflection of the thread, an axial recession due to radial compression of the threads, and an axial recession due to axial contraction of the bolt and expansion of the nut caused by radial pressure of the joints. Alternatively, Yamamoto (Yamamoto 1980) proposed a procedure for calculating the deflection due to bending moment, shear loading and radial contraction and expansion on the bolt and nut. The assumption of plane strain has also been made by Yamamoto for dealing with thread region. Hence, the three dimensional bolt-nut assembly can be simply analyzed by axisymmetrical model to calculate the load distribution along the axial direction of bolt. The analytical and axisymmetrical finite element analysis have been studied in the literature (Chaaban et. al. 1992, Grosse et. al. 1990, Wileman et. al 1991, Lehnhoff et. al 1996). However, the lead angle due to helical effect can not be modeled by axisymmetrical model, such that, the helical effect to the load distribution is still lacking on the literature. Due to the progress of the modern finite element method, modeling of the finite sliding, and deformable to deformable contact problem becomes possible by using ABAQUS code( Hibbitt et.al 1998). The curiosity is risen for

exploring the difference among theoretical, axisymmetrical and three dimensional finite element models, and that is the purpose of the present study.

## II. Modeling and Assumption.

A standard one inch bolt (8UNC) and two fine threaded bolt (12UNF and 16UNF) are used to study the helical effect of the bolts. Four axisymmetrical finite element models with the different mesh on the threads are shown in Figure 1. In the axisymmetrical model, the radial symmetric is assumed on the center line of bolt. The three dimensional model of the standard bolt assembly is shown in Figure 2, and the model of the fine thread bolt is shown in Figure 3. Due to the difficulty of the three dimensional modeling, a small hole is assumed at the center of the bolt, this will slightly reduces the area of the applied load. The elastic material is used through out this work, where the Young's modulus($E$) is assumed as 30E+6 psi, Poisson ratio($\nu$) as 0.3, and the coefficient of friction($\mu$) as 0.1 in this analysis. The uniform pressure loading ($p$= 10000 psi) is applied on the top root surface of the bolt in this study.

## III. Analytical Analysis

The load distribution analysis has been calculated by means of Yamamoto's method. The total deflection of the bolt($\delta_b$)and nut($\delta_n$) can be expressed as

$$\delta_b = \frac{K_b}{E_b} w \cos\alpha \quad \text{and} \quad \delta_n = \frac{K_n}{E_n} w \cos\alpha . \tag{1}$$

where $K$ is the stiffness of the bolt or nut, $w$ is the unit applied load, the sub index $b$ and $n$ represents the bolt and nut. From the geometrical parameters of this analysis model, the stiffness of bolt and nut can be obtained as follows,

$$K_b = 3.57 \quad \text{and} \quad K_n = 4.70. \tag{2}$$

The load distribution equation can be expressed as,

$$F = F_b \frac{\sinh(\lambda x)}{\sinh(\lambda L)}. \tag{3}$$

where $F_b$ is the load on the first thread of the bolt, $L$ is the engaged length of the bolted joints, and $\lambda$ is a characteristic length and expressed as

$$\lambda = \sqrt{\frac{\frac{1}{A_b E_b} + \frac{1}{A_n E_n}}{\left(\frac{K_b}{E_b} + \frac{K_n}{E_n}\right)\tan\beta}} \approx 0.0847 \tag{4}$$

where $A$ is the crosssection area, $\beta$ is the lead angle. Hence, the result of the load distribution on each thread can be shown on Table 1.

## I. Finite element analysis.

From the literature(Chaaban et. al. 1992, Grosse et. al. 1990, Wileman et. al 1991), the extremely high density of finite element mesh of the bolted joint is used for studying the bolt. However, these high dense mesh not only expends a lot of computer resource on calculating but also increases the difficulty of three dimensional finite element analysis. Hence, the mesh density verification is studied for axisymmetrical model. firstly. Four models of the axisymmetrical finite element analysis with different meshing density are shown in Figure 1. The load distribution analysis for these models of finite element meshing are shown as Table 2. For the 1"-8UNC bolt, the total force ($F_b$) due to applied pressure is 5160 lbf.

$$\begin{aligned} F_b &= P\frac{\pi \cdot d_i^2}{4} \\ &= 10000 * \frac{\pi(0.810557)^2}{4} = 5160\,(lbf) \end{aligned} \tag{5}$$

where $d_i$ is the root diameter of the bolt. The maximum error of total contact force with respect to total applied loads on Table 2 is 1.55E-4, that is shown a good

agreement with four types of axisymmetrical meshed model. From the Figure 4, the maximum deviation is happened at first thread of the bolted joints, and the maximum differential is 6% between coarse mesh model and fine mesh model. Therefore, the coarse meshed model used in this study can be proposed for studying helical and friction effects on the three dimensional finite element analysis. Figure 5 shows the load distribution of analytical, coarse meshed axisymmetrical and three dimensional finite element analysis results. The load distribution with analytical prediction has shown somewhat lower than the result of finite element analysis.

## II. Result and Discussion

### *A. Helical effect on the load distribution.*

The simplified axisymmetrical model and three dimensional model of 1 inch 8UNC, 12UNF and 16UNF of threaded connections are analyzed in the present work. The load distribution on each thread of the axisymmetrical model and three dimensional model are shown on Table 3 and Table 4. Through the comparison of load ratio of axisymmetrical model with three dimensional model from Figure 5-7, The results show the loading ratio quite similar on each thread between axisymmetrical and three dimensional models except 16UNF threaded joints with a little difference. Hence, it can be concluded that the helical effect does not influence the load distribution, and the axisymmetrical model can give a well estimating on load distributions of 8UNC and 12UNF joints. For 16UNF, load ratio of the first thread has 12% error of axisymmetrical model with respect to three dimensional model. Besides, the other two contact forces orthogonal to axial direction can be calculated in the three dimensional load distribution analysis. It shows that these two contact forces are only the small fraction of the total applied load, and these can not be obtained from axisymmetrical

finite element analysis, because of the orthogonal contact force is the response of opposite reaction force on the axisymmetrical model. Comparison of the load distribution among 8UNC, 12UNF and 16UNF threads, shown in Figure 8, one can obtains that the load distribution at the first thread is improved significantly with a finer thread configuration.

*B. Effect on the coefficient of friction to the load distribution*

There are four friction coefficient have been used in this section, which is 0, 0.1, 0.3 and 0.5. The results of load distribution with different coefficient of friction have been shown on Table 5. It is shown that increasing the coefficient of friction improves the load distribution very slightly, but increasing the coefficient of friction reduces slightly the load bearing on the first thread.

Owing to the lead angles of the one inch 8UNC, 12UNF and 16UNF are the values of 2.66, 2.02 and 1.39 degree, these angle are such small and may not alter the normal contact force significantly. However, the results of load ratio on the first thread in the three dimensional finite element analysis exist somewhat lower than the axisymmetrical analysis. Hence, the load distribution of the bolted joints assembly can be modeled with axisymmetrical models for 1" 8UNC and 12UNF bolted joints.

## I. Conclusion

The three dimensional load distribution on the finite sliding contact analysis between two deformable elastic bolted joint assembly with 8 active threads have been studied. The results can be concluded as follows.

1. The analytical calculation of load distribution by Yamamoto's method on the first thread is lower than the results from axisymmetrical and three dimensional finite element analysis of one inch 8UNC standard thread bolted joints.

2. The load distribution of the first thread is improved more significantly by using 16UNF instead of 8UNC bolted joints for axisymmetrical and three dimensional contact analysis.
3. The effect of coefficient of friction on the load distribution of bolted joint assembly is not evident, although increasing of friction will improve the load distribution slightly.
4. The deviation of load ratio at the first thread are small for 1" 8UNC and 12UNF, but the error approaches to 12% for 16UNF bolted joint.

**Acknowledgments**

This work is supported by Institute of Nuclear Energy Research. The authors wish to acknowledge the help from our colleagues at INER. The authors also wish to express our appreciation to Dr. Kuen Ting encouragement .

**Reference**

Chaaban A., Jutras M., 1992. Static analysis of buttress threads using the finite element method", Journal of Pressure Vessel Technology, Vol. 114, pp. 209-212.

Grosse I. R., Mitchell L. D., 1990. Nonlinear axial stiffness characteristic of axisymmetric bolted joint. Transaction of the ASME, Journal of Mechanical Design, Vol. 112, pp. 442-449.

Hibbitt , Karlsson, Sorenson 1998. ABAQUS Finite Element Code version 5.7.

Lehnhoff T. F., Wistehuff W. E., 1996. Nonlinear effects on the stress and deformations of bolted joints. Transaction of the ASME, Journal of Mechanical Design, Vol. 118, pp. 54-58.

Sopwith D. G., 1948. The distribution of load in screw threads. Institute of Mechanical Engineering, Applied Mechanics Proceedings 159, pp. 373-383.

Wileman J., Choudhury M., Green I., 1991. Computation of member stiffness in bolted connections. Transaction of the ASME, Journal of Mechanical Design, Vol. 113, pp. 432-437.

Yamamoto A., 1980. The Theory and Computation of Thread Connection. Pressed Youkendo, Tokyo pp. 39-54.(in Japanese)

Table 1. The load distribution of each thread by Yamamoto method.

| thread no. | $F/F_b$ | F/Total (%) |
|---|---|---|
| 1 | 1 | 28.89 |
| 2 | 0.7566 | 21.86 |
| 3 | 0.5684 | 16.42 |
| 4 | 0.4216 | 12.18 |
| 5 | 0.3055 | 8.83 |
| 6 | 0.2115 | 6.11 |
| 7 | 0.133 | 3.84 |
| 8 | 0.0641 | 1.85 |

Table 2. The contact force on each threads of the different mesh density of axisymmetrical finite element model.

| Meshing density thread no. | Coarse meshed | Middle meshed | Fine meshed | Extremely fine meshed |
|---|---|---|---|---|
| 1 | 1777 | 1734 | 1665 | 1699 |
| 2 | 1049 | 1043 | 1046 | 1039 |
| 3 | 710.4 | 717.3 | 729.5 | 721.9 |
| 4 | 513.2 | 523.1 | 536.4 | 530.1 |
| 5 | 388.0 | 398.2 | 410.9 | 405.4 |
| 6 | 305.8 | 315.5 | 327.2 | 322.9 |
| 7 | 246.4 | 254.6 | 264.9 | 261.8 |
| 8 | 169.4 | 174.6 | 180.5 | 180.1 |
| Total | 5159.2 | 5160.4 | 5160.4 | 5160.2 |

Table 3. The load distribution of axisymmetrical model with three types of bolt joints.

| Thread no. | 8-UNC | 12-UNF | 16-UNF |
|---|---|---|---|
| 1 | 1777 | 1739 | 1767 |
| 2 | 1049 | 1113 | 1167 |
| 3 | 710.4 | 829.8 | 899.7 |
| 4 | 513.2 | 665.6 | 746.9 |
| 5 | 388.0 | 555.2 | 636.7 |
| 6 | 305.8 | 467.1 | 537.6 |
| 7 | 246.9 | 379.5 | 425.4 |
| 8 | 169.4 | 247.4 | 256.3 |
| Total (lbf) | 5159.2 | 5996.6 | 6364.6 |

Table 4. The load distribution of three dimensional model with three types of bolt joints.

| Thread no. | 8-UNC | 12-UNF | 16-UNF |
|---|---|---|---|
| 1 | 1730 | 1695 | 1557 |
| 2 | 1035 | 1086 | 1120 |
| 3 | 703.7 | 810.6 | 898.4 |
| 4 | 506.9 | 653.4 | 766.6 |
| 5 | 379.8 | 546.6 | 668.2 |
| 6 | 297.1 | 463.8 | 576.9 |
| 7 | 242.3 | 385.3 | 468.9 |
| 8 | 190.0 | 275.1 | 299.7 |
| Total (lbf) | 5084.8 | 5915.6 | 6355.7 |

Table 5. The load distribution with effect of friction coefficients.

| Thread no. | 0 | 0.1 | 0.3 | 0.5 |
|---|---|---|---|---|
| 1 | 1783 | 1777 | 1770 | 1762 |
| 2 | 1049 | 1049 | 1050 | 1049 |
| 3 | 709 | 710.4 | 713 | 714.7 |
| 4 | 512. | 513.2 | 515.6 | 517.4 |
| 5 | 387 | 388.0 | 389.8 | 391.3 |
| 6 | 305.1 | 305.8 | 307.1 | 308.3 |
| 7 | 246.0 | 246.4 | 247.1 | 247.8 |
| 8 | 169.5 | 169.4 | 169.4 | 169.4 |
| Total (lbf) | 5160.6 | 5159.2 | 5162 | 5160 |

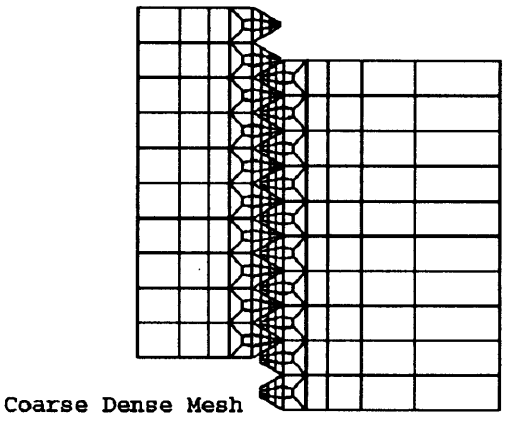


Fig 1(a) :Coarse meshed model

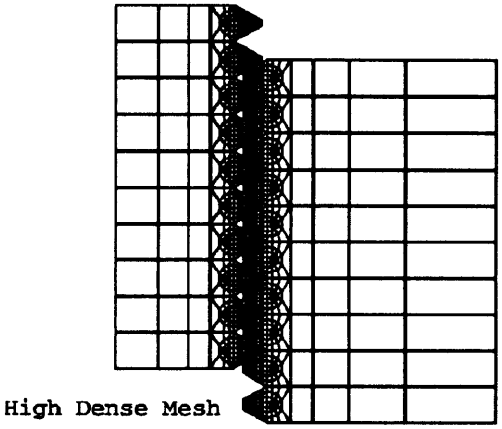


Fig 1(C) :Fine meshed model

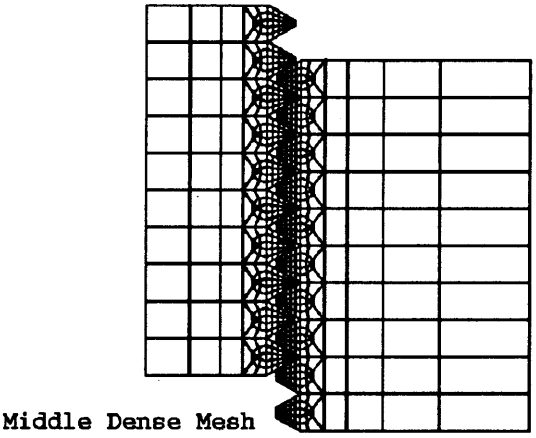


Fig 1(b) :Middle meshed model

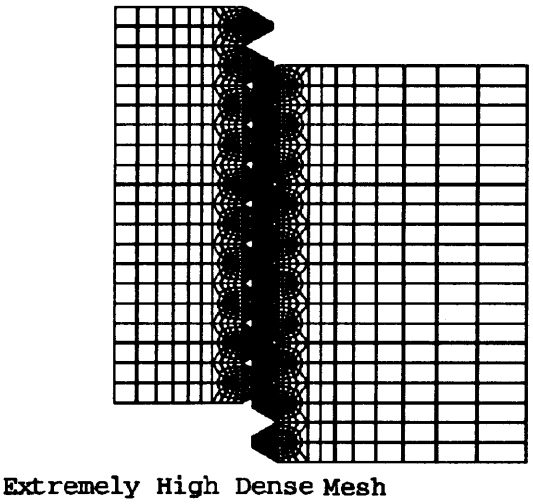


Fig 1(a) :Extremely high meshed model

Fig 1: Four types of the finite element axisymmetrical models.

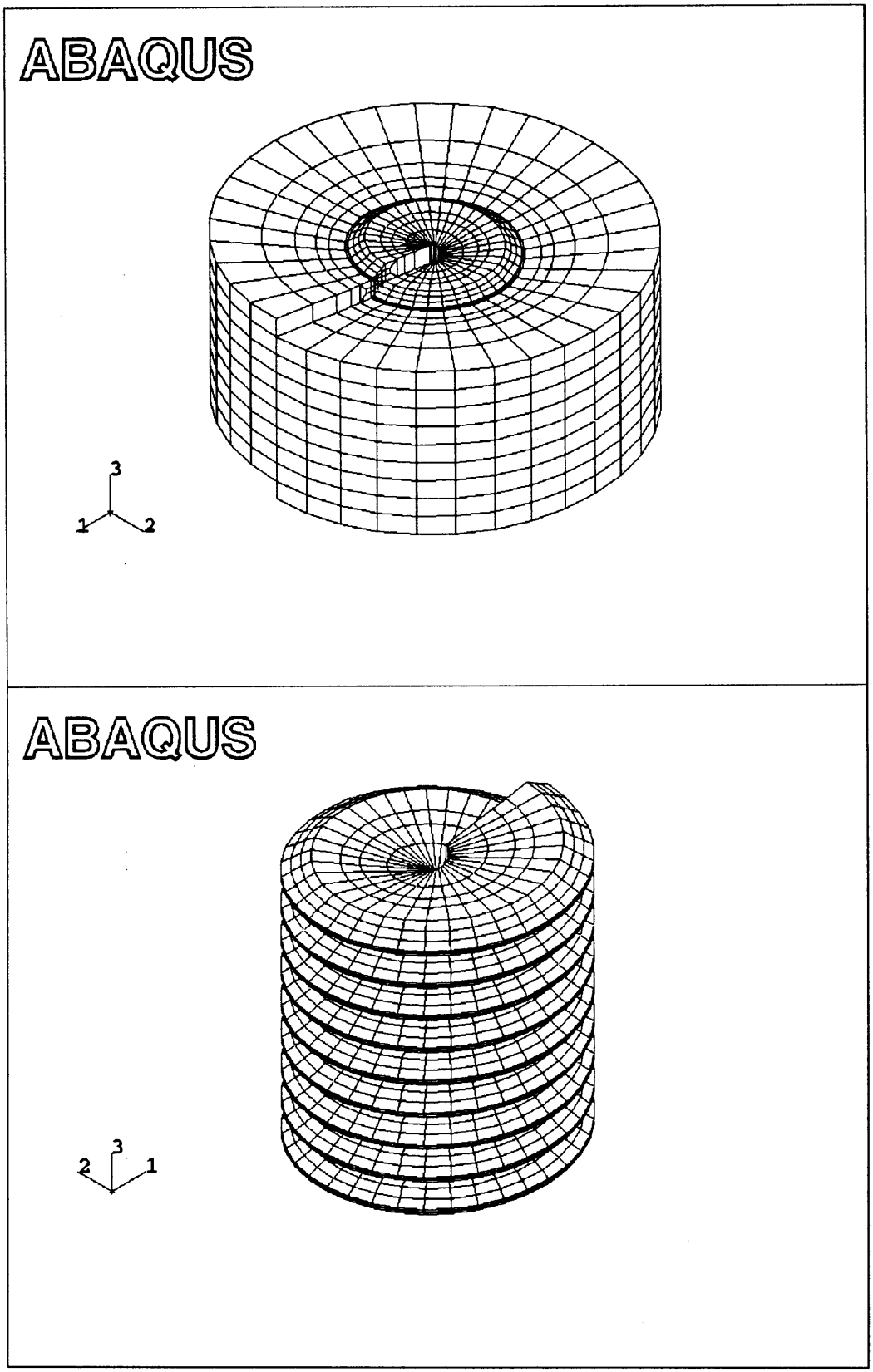


Fig 2 : The three dimensional model mesh of standard bolted joints assembly(upper) and bolt itself (lower)

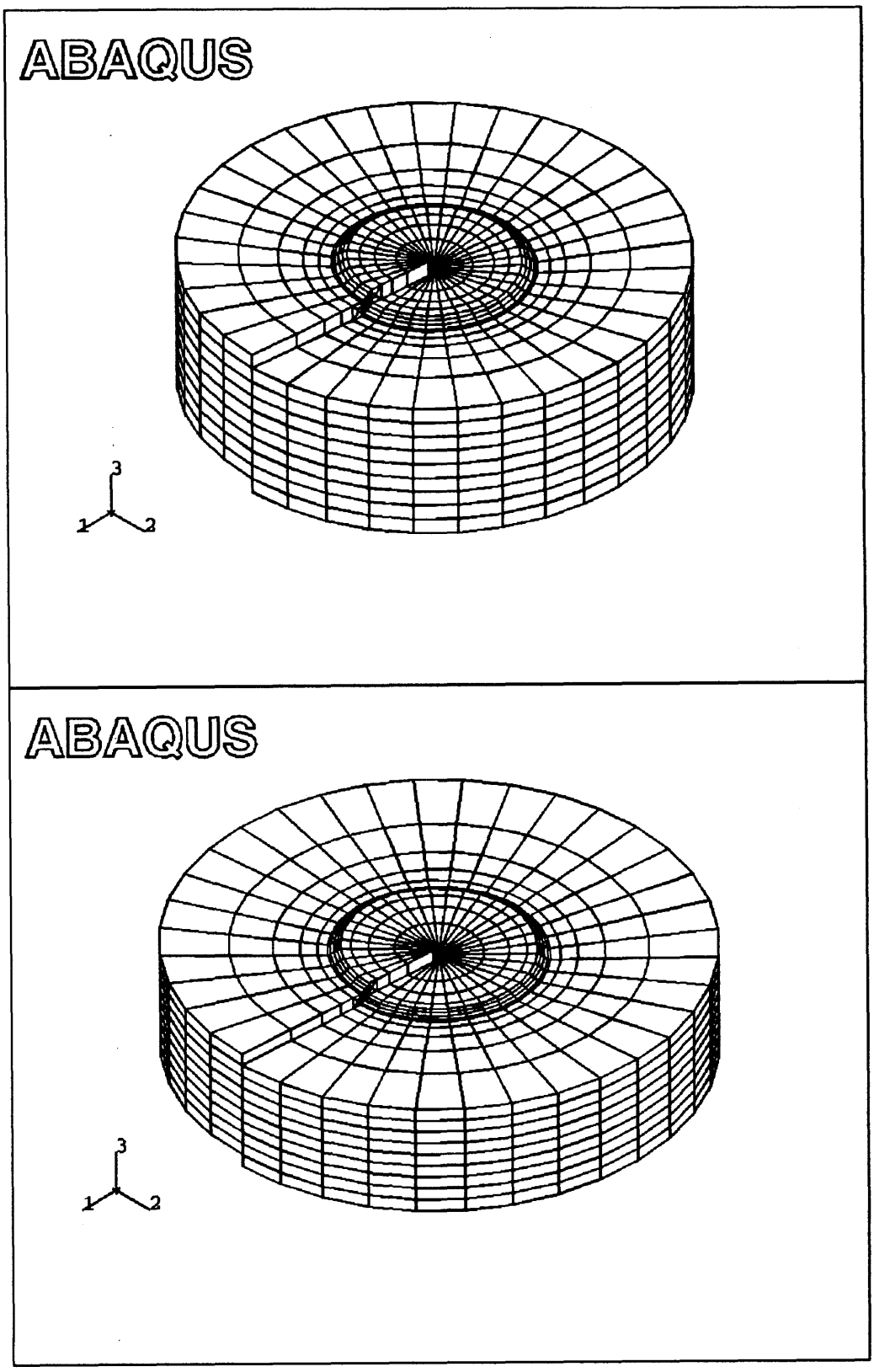


Fig 3 : The three dimensional models of the 1 inch 12UNF and 16UNF bolted joint assembly

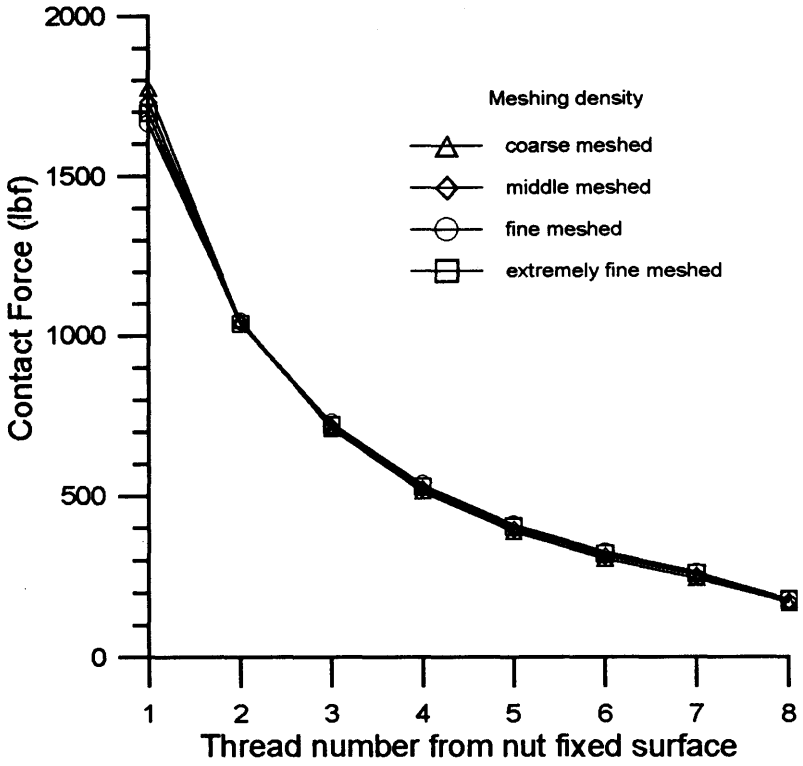


Fig. 4 : The contact force on each thread for different axisymmetrical finite element model

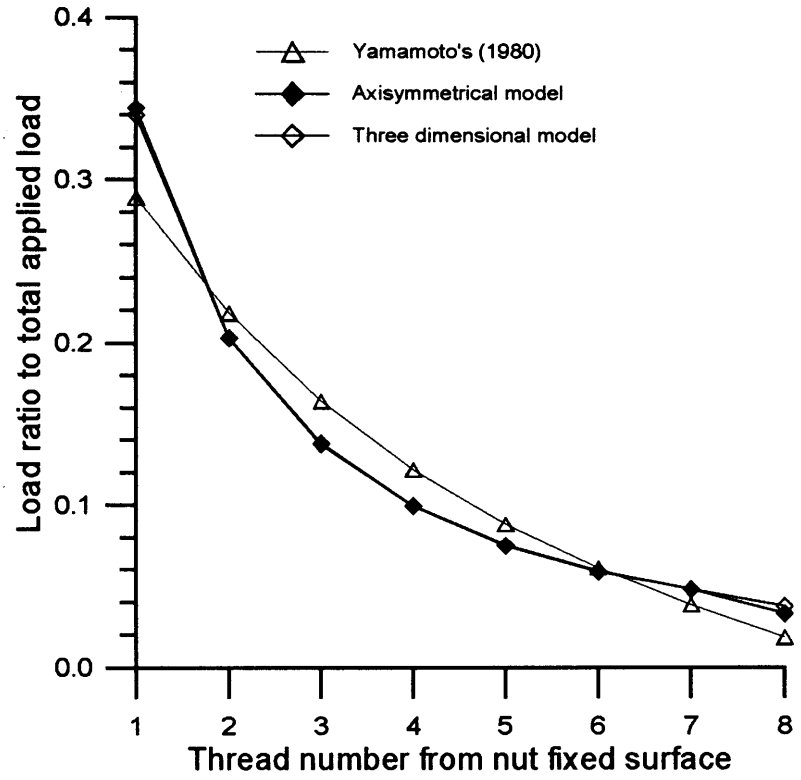


Fig. 5 : The load ratio on each thread for 1" 8UNC bolted joints

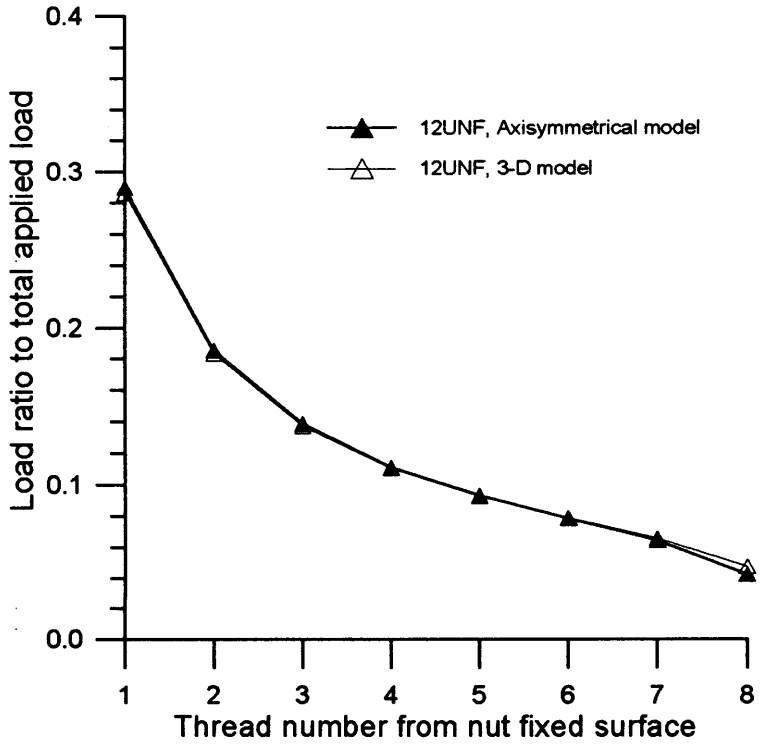


Fig 6 : The load ratio on each thread of 1"-12UNF bolt.

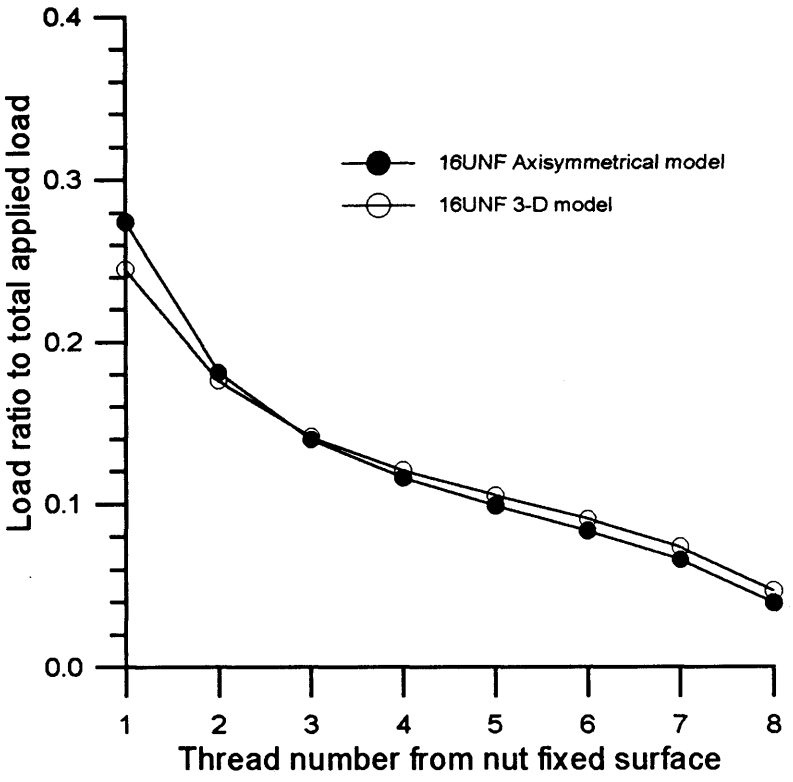


Fig. 7 : The load ratio oon each thread of 1" -16UNF bolt.

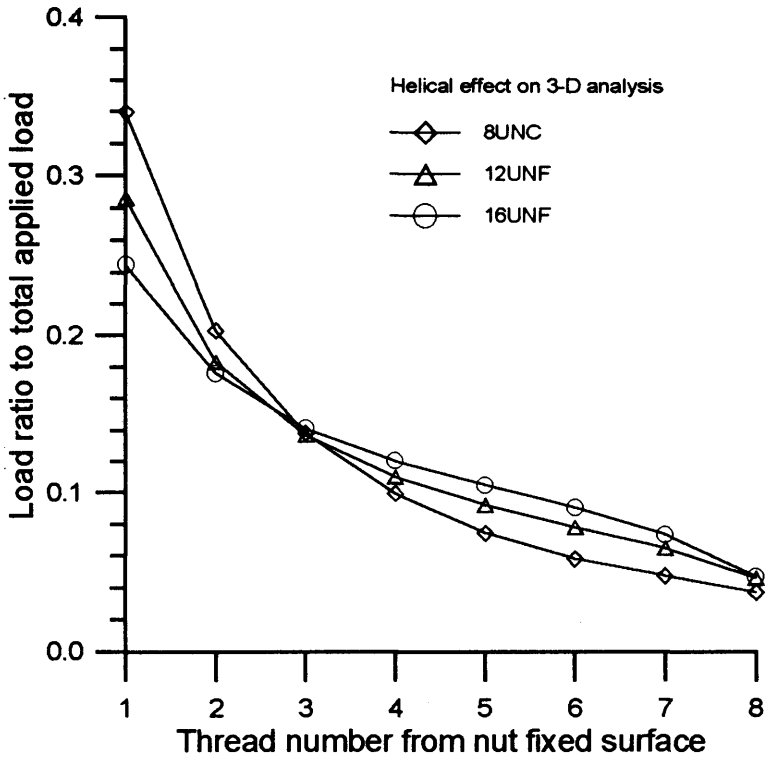


Fig. 8 : The contact force ratio on each thread of three typical bolt model with three dimensional analysis

# Session II

# Structural Integrity and Life Prediction

# II-1 Probabilistic Fracture Mechanics of Nuclear Structural Components

Genki Yagawa, University of Tokyo, Japan

# PROBABILISTIC FRACTURE MECHANICS OF NUCLEAR STRUCTURAL COMPONENTS : CONSIDERATION OF TRANSITION FROM EMBEDDED CRACK TO SURFACE CRACK

Genki Yagawa[1)], Yasuhiro Kanto[2)] and Shinobu Yoshimura[1)]

1) School of Engineering, University of Tokyo,
7-3-1 Hongo, Bunkyo, Tokyo 113-0033, Japan

2) Department of Mechanical Engineering,
Toyohashi University of Science and Technology,
Tempaku, Toyohashi 441-8122, Japan

## ABSTRACT

This paper describes a probabilistic fracture mechanics (PFM) analysis of aged nuclear reactor pressure vessel (RPV) material. New interpolation formulas are first derived for both embedded elliptical surface cracks and semi-elliptical surface cracks. To investigate effects of transition from embedded crack to surface crack in PFM analyses, one of PFM round-robin problems set by JSME-RC111 committee, i.e. "aged RPV under normal and upset operating conditions" is solved, employing the interpolation formulas.

## 1. INTRODUCTION

In design and integrity evaluation processes for nuclear structural components, deterministic approaches have mainly been employed. All kinds of uncertainty related to operating history, material property change and damage mechanisms are taken into account in so-called safety factors. It is easily expected that the results obtained are too conservative to perform a rational evaluation of plant safety and to make judgement of life extension because of the accumulation of conservatisms of all related factors.

Probabilistic Fracture Mechanics (PFM) has become an important tool [1, 2]. The PFM approach is regarded as an appropriate method in rationally evaluating plant life and in risk-based decision making such as risk-informed inspection [3] since it can consider various uncertainties such as sizes and distributions of cracks, degradation of material strength due to aging effects, fluctuating loading histories, accuracy and frequency of pre- and in-service inspections. Thus, various PFM

computer programs have been developed and applied in practical situations in the last two decades.

In Japan, one research activity on PFM approaches to the integrity studies of nuclear pressure vessels and piping (PV&P) was initiated in 1987 by the LE-PFM subcommittee organized within the Japan Welding Engineering Society (JWES) under a subcontract of the Japan Atomic Energy Research Institute (JAERI), and continued for three years [4]. The activity was followed by the RC111 research committee organized in the Japan Society of Mechanical Engineers (JSME) in 1991, and finished in March, 1995 [5]. Succeeding it, a new PFM subcommittee organized in JWES started again in May, 1996 [6], and is scheduled to continue until March, 1999. The purpose of the continuous activity is to establish standard procedures for evaluating failure probabilities of Japanese nuclear structural components such as PV&P and steam generator tube, combining the state-of-the art knowledge on structural integrity of nuclear structural components and modern computer technology such as parallel processing. Within the LE-PFM and JSME-RC111 activities, we have set up the following three kinds of PFM roud-robin problems on

(a) primary piping under normal operating conditions,
(b) aged reactor pressure vessel (RPV) under normal & upset operating conditions, and
(c) aged RPV under pressurized thermal shock (PTS) events.

The basic part of the last PTS problems is taken from some of US benchmark problems [7, 8]. For these round-robin problems, various sensitivity analyses were performed to quantify effects of uncertainty of data on failure probabilities. Some of the detailed analysis results can be found in elsewhere [9-15].

In those analyses, we always assumed semi-elliptical surface cracks as initial cracks for the purpose of convenience. However, as well known, embedded cracks seem more practical and probable as initial cracks. Thus as one of main tasks in the JWES-PFM subcommittee, we are developing a new PFM model considering transition from embedded to surface cracks during crack growth. This paper describes its latest results. Here new interpolation formulas are first derived for both embedded elliptical cracks and semi-elliptical surface cracks. To investigate effects of transition from embedded to surface cracks in PFM analyses, one of PFM round-robin problems set by JSME-RC111 committee, i.e. "aged RPV under normal and upset operating conditions" is solved employing the interpolation formulas.

## 2. OUTLINE OF PFM ANALYSIS

Figure 1 illustrates the flow of a typical PFM analysis. Firstly, some random variables are selected according to an analysis model employed. Random variables to be considered include initial crack sizes (crack depth and crack aspect ratio) and location, accuracy and frequency of nondestructive tests, i.e. PSI and ISI, material properties, cycles and amplitudes of applied loads. Next, crack growth simulations are performed. Fracture mechanics models employed are based on the linear elastic fracture mechanics, i.e. Newman-Raju solutions [16], influence functions [17-20] and others [21], and the nonlinear fracture mechanics, i.e. fully plastic solutions [22, 23] or their combination [24, 25]. Besides, creep crack growth can be simulated based on the nonlinear fracture mechanics [26, 27]. During the crack growth simulation, PSI and ISI are considered, and failure judgements of leakage and break are performed. Cumulative failure probabilities are calculated as functions of operation time in round-robin problems (a) and (b), while failure probabilities for one PTS event are calculated in round-robin problem (c). To effectively calculate accurate failure probabilities, the Stratified sampling Monte Carlo (SMC) algorithm is offen employed. Its parallel version is also very efficient [11].

## 3. INTERPOLATION FORMULAS OF STRESS INTENSITY FACTORS FOR EMBEDDED ELLIPTICAL CRACK & SEMI-ELLIPTICAL SURFACE CRACK

### 3.1 Stress Intensity Factors for Embedded Elliptical Cracks

Soneda and Fujioka calculated stress intensity factors (SIFs) of various elliptical cracks embedded in thick-wall cylinder subjected to arbitrarily distributed loadings, and constructed an influence function database [28]. They employed the finite element alternating method developed by Nishioka and Atluri [29]. The analysis process is schematically illustrated in Figure 2 and summarized as follows :

1) Solve the uncracked finite body under the given external loads by using the finite element method. The uncracked body has the same geometry with the given problem except the crack.
2) Compute the stresses $\sigma_{crack}$ at the location of the original crack, using the finite element solution.
3) Compare the residual stresses $\sigma_{crack}$ calculated in 2) with a permissible stress magnitude. In the present study, 0.1 % of the initial $\sigma_{crack}$ value was used for the permissible stress magnitude.
4) Calculate theoretically the SIF, $K_I^{(i)}{}_{\text{-infinite}}$ of the crack in infinite body,

applying the stresses $\sigma_{crack}$ onto the crack surface.

5) Solve the cracked infinite body, applying the reversed stresses - $\sigma_{crack}$ onto the crack surface.
6) Compute the stresses $\sigma_{surface}$ at the boundary of the original finite body, using the finite element solution.
7) Solve the uncracked body under the $\sigma_{surface}$ onto its boundary by using the finite element method.

Repeat 2)-7) steps in the iteration process until the residual stresses $\sigma_{crack}$ on the crack surface become negligible (Step 3). To obtain the final SIF solution $K_I$, add the stress intensity factors of all iterations as :

$$K_I = \sum_{i=0}^{n} K_{I-infinite}^{(i)} \tag{1}$$

where *n* is the number of iterations.

Here we consider only the axial elliptical crack embedded in cylinder as in Figure 3. Following a typical influence function method, a stress distribution in the thikness direction of the cylinder is first approximated by 4th-order polynomial in a normalized coordinate. Then the SIF values are expressed with the coefficients $A_i$ of the polynomial as follows :

$$K_I(\theta) = \sqrt{\frac{\pi a_2}{Q a_1}} \left(a_1^2 \sin^2\theta + a_2^2 \cos^2\theta\right)^{1/4} \sum_{i=0}^{4} A_i G_i \tag{2}$$

where $G_i$ is the influence function for the *i*-th order stress distribution, Q is the square of elliptic integral of second kind and is approximated by the following equation :

$$Q = 1 + 1.464\ (a_2 / a_1)^{1.65} \tag{3}$$

where $a_1$ and $a_2$ are half lengths of the crack in the axial and thickness directions, respectively. $G_i$ values are tabulated in Ref. [28]. In the present study, $G_i$ values are evaluated at the three points of elliptic angle $\theta=\pi/2$, 0 and $-\pi/2$. In the three cases, $(*)^{1/4}$ term in Eq. (2) reduces to $(a_1)^{1/4}$, $(a_2)^{1/4}$ and $(a_1)^{1/4}$, respectively.

When only tensile stress $\sigma_T$ and bending stress $\sigma_B$ are considered, the coefficients $A_i$ in Eq. (2) are simplified as follows :

$$\begin{aligned} A_0 &= \sigma_T - \sigma_B \\ A_1 &= 2\sigma_B \\ A_k &= 0, \text{ for } k \geq 2 \end{aligned} \tag{4}$$

Table 1 shows parameter ranges for which influence functions $G_i$ are given in Ref. [28]. We then interpolate those influence function solutions in the following.

$$G_i = \sum_{p=0}^{3} \sum_{q=0}^{2} \sum_{r=0}^{2} \phi_{i;pqr} \xi^p \eta^q \zeta^r \tag{5}$$

where

$$\xi = \frac{e/t - \left\{(e/t)_{max} + (e/t)_{min}\right\}/2}{(e/t)_{max} - (e/t)_{min}} = \frac{e/t - 1/2}{0.90 - 2a_2/t} \tag{6a}$$

$$\eta = \frac{a_2/a_1 - \left\{(a_2/a_1)_{max} + (a_2/a_1)_{min}\right\}/2}{(a_2/a_1)_{max} - (a_2/a_1)_{min}} = \frac{a_2/a_1 - 2/3}{2/3} \tag{6b}$$

$$\zeta = \frac{2a_2/t - \left\{(2a_2/t)_{max} + (2a_2/t)_{min}\right\}/2}{(2a_2/t)_{max} - (2a_2/t)_{min}} = \frac{2a_2/t - 0.4}{0.6} \tag{6c}$$

In the present study, only $G_i$ values of axial elliptical cracks for linear components of stress distributions are interpolated, although more other solutions are given in Ref. [28]. The coefficients $\phi_{i;pqr}$ in Eq. (5) are tabulated in Table 2.

Figures 4(a) and 4(b) show some comparison of original and interpolated $G_i$ values. These figures confirm that Eq. (5) provides accurate interpolation for all the solutions. It should be also noted here that, as shown in Figure 4(b), Eq. (5) exrapolates in the range of $a_2/a_1$=0-1/3. Its validity in the range is not proven yet.

3.2 Stress Intensity Factors for Semi-elliptical Surface Cracks

In PFM analyses considering the embedded elliptical cracks as described in 3.1, one can take into account uncracked ligament as small as 0.05t, where t is cylinder thickness. On the other hand, original finite element K solutions of Newman-Raju [16], which have been employed in the PFM round-robin problems (a) and (b) are obtained till crack depth a =0.8t, i.e. uncracked ligament of 0.2t. Miyoshi et al. performed precise finite element analyses for much deeper cracks than a=0.9t [30]. To make K solutions for surface cracks consistant with those for embedded cracks, a new interpolation formula is also derived in this study using both Newman-Raju's finite element solutions [16] and Miyoshi's [30].

Fundamental policy for this task is as follows :

1) Since K solutions increase rapidly over a/t > 0.95, the present interpolation certifies its validity until a/t=0.95.

2) When a/c < 0.2 or a/t is smaller, Newman-Raju's equation is adopted.
3) The interpolation is performed only for K solutions at elliptic angle of $\phi$=0 and $\pi$/2.

The interpolation formula obtained is expressed as follows :

$$K_I = (\sigma_t + \sigma_b)\sqrt{\pi a/Q}F_1 \tag{7}$$

where

$$Q = 1.0 + 1.464(a/c)^{1.65} \tag{8a}$$

$$F_1 = \sum_{i=0}^{2}\sum_{j=0}^{2} G_{ij}\xi^i\left(\frac{a}{c}\right)^j \tag{8b}$$

$$\xi = 1 - \sqrt{1 - a/t} \tag{8c}$$

where $G_{ij}$ are given in Table 3. The validity range of this interpolation is summarized in Table 4. Beyond the validity range in Table 4, Newman-Raju's equation is adopted except a/t > 0.95. Figures 4(a) and 4(b) show the comparison between finite element solutions and the interpolation of Eq. (7) for the purpose of convenience.

## 4. ANALYSIS PROBLEM : AGED RPV UNDER NORMAL AND UPSET OPERATING CONDITION

A PFM model analyzed here is basically the same as the PFM round-robin problem for an aged RPV under normal and upset operating condition, which was given by JSME-RC111 committee [5] except consideration of embedded cracks.

### 4.1 Analysis Models

Two kinds of cracked models are assumed here. The one is a plate with a semi-elliptical surface crack, while the other is a plate with an axial embedded elliptical crack. These are illustrated in Figures 6(a) and 6(b). The embedded elliptical crack may be converted to the semi-elliptical surface crack, according to a certain conversion criterion as described later. In both models, plate thickness and width are taken to be t = 0.2m and 2b = 12.6m, considering the beltline portion of PWR pressure vessels. The plates are assumed to be subjected to various magnitudes of remote uniform tensile and bending stresses. For the purpose of simplicity, we ignore curvature effects of actual pressure vessels in evaluating 3-dimensional SIFs. Cumulative failure probabilities of one existing crack, whose unit is 1/crack, are calculated as functions of operation years.

4.2 Probabilistic Density Distributions for Ssemi-elliptical Surface Crack

As for the semi-elliptical surface crack, an initial crack depth (a) and a crack aspect ratio ($\beta$=c/a) are assumed to be random variables. As probabilistic density functions, we employ the Marshall distribution for (a) [31], and a log-normal distribution for ($\beta$) [32] as follows :

$$p(a) = \frac{\exp\left(-\frac{a}{\mu}\right)}{\mu\left(1-\exp\left(-\frac{t}{\mu}\right)\right)} \tag{9a}$$

$$p(\beta) = \frac{\alpha}{\beta\gamma\sqrt{2\pi}}\exp\left(-\frac{\left\{\ln\left(\beta/\beta_m\right)\right\}^2}{2\gamma^2}\right), \quad \beta = \frac{c}{a} \tag{9b}$$

where $\alpha$ = 1.035, $\beta_m$= 1.336, $\gamma$ = 0.5382, $\mu$ = 6.248 x $10^{-3}$ m and t = 0.2 m.

4.3 Probabilistic Density Distributions for Embedded elliptical crack

As for embedded elliptical cracks, half length of longer axis ($a_1$), that of shorter axis ($a_2$) and depth (e) are assumed to be random variables. The probabilistic density distributions of $a_1$ and $\beta = a_1/a_2$ are simply taken to be the same as Eqs. (9a) and (9b), respectively. (e) is assumed to be a uniform random variable. It should be noted here that this assumption might lead larger average crack sizes for embedded cracks.

4.4 Conversion Criterion from Embedded Crack to Surface Crack

When uncracked ligament of the embedded elliptical crack reaches 0.05t, the embedded crack ($a_1$, $a_2$, e) is converted to a semi-elliptical surface crack (a, c) by the replacement of $a_1 \rightarrow$ c and depth $a_2$ + e $\rightarrow$ a.

4.5 Cyclic Loads

Nineteen kinds of cyclic tensile and bending stresses given in Table 5 are chosen from the design loading conditions of Level A (normal operation condition) and Level B (upset condition) which occur in the beltline portion of PWR pressure vessels listed in the Marshall report [31]. The nineteen loads are applied in the order as listed there.

4.6 Failure Criteria

The failure modes considered here are leakage and break, whose criteria are simply defined as follows :

Break criterion : $K_{max} \geq K_{Ic}$ or $b/c \leq 1$ (10a)

Leakage criterion : $a / t \geq 0.95$ (10b)

where $K_{max}$ is taken to be the largest K value along crack front. For simplicity, break phenomenon after leakage is not considered.

4.7 Fatigue Crack Growth

Only fatigue crack growth based on the Paris' law is assumed, whose coefficients are taken from the fatigue crack growth rate of nuclear pressure vessel steels in water given in the ASME Code Section XI, Appendix A [33] :

$$da/dN \text{ (m/cycle)} = 1.738 \times 10^{-13} (\Delta K)^{5.95} \quad (\text{for } \Delta K < 13.2 \text{ MPa}\sqrt{\text{m}}) \tag{11a}$$

$$da/dN \text{ (m/cycle)} = 5.325 \times 10^{-9} (\Delta K)^{1.95} \quad (\text{for } \Delta K \geq 13.2 \text{ MPa}\sqrt{\text{m}}) \tag{11b}$$

The elliptical or semi-elliptical cracks keep their shape during crack growth, except the case that the convergence criteiron in 4.4 is satisfied. As for elliptical crack, an amount of crack growth per one loading cycle is evaluated in all longer and shorter axis directions, independently.

4.8 Fracture Toughness

Referring to the reduction of the upper shelf Charpy absorbed energy due to neutron irradiation [34] and some experimental data conducted by the JWES-LE subcommittee [4], the time variation of $K_{Ic}$ at 300 °C due to neutron irradiation is formulated as follows :

$$\begin{aligned} 300\ ^{\circ}\text{C}: \quad K_{Ic}(t) &= 135.0 \ (\text{MPa}\sqrt{\text{m}}) \qquad (\text{for } F \leq 0.361) \\ &= 3.29 + 118.71 \times F^{-0.102} \qquad (\text{for } F > 0.361) \end{aligned} \tag{12}$$

where F is a neutron fluence ($10^{19}$ n/cm$^2$). The neutron fluence after a 40 year operation is assumed to be 3 x $10^{19}$ n/cm$^2$ according to that of the beltline portion of the PWR pressure vessels in the Marshall report [31]. According to Eq. (12), the $K_{Ic}$ value reduces by about 19 % due to neutron irradiation during a 40 year operation.

In reality, since the neutron fluence varies along the thickness direction, the neutron fluence F is formulated as a function of the distance d(mm) from the inside surface of plate assumming $F_0$ to be the neutron fluence at the inside surface as [8] :

$$F = F_0 \times \exp(-0.00945 \times d) \quad (13)$$

According to Eq. (13), the neutron fluence at the outside surface is about 15 % of that of the inside surface.

## 5. RESULTS AND DISCUSSIONS

Figure 7 shows time variations of cumulative break and leakage probabilities considering embedded elliptical surface cracks. The total number of samples is 168,384. Leakage probability is by two orders of magnitude smaller than break probability. This means that before reaching leakage criterion of a/t = 0.95, most samples satisfy the $K_{Ic}$ criterion. Leakage probability is almost constant, while the break probability increases gradually. In the case of considering only surface cracks, the break probability was in the order of $10^{-8}$, and the leakage probability was in the order of $10^{-12}$ [13]. The present analysis results are one to two orders greater than such a surface crack case. This seems strange, compared with our intuition such that embedded cracks might have more resistance to failure than surface cracks. As noted in 4.3, the probabilistic density distribution of initial crack size for the embedded cracks was determined referring to that of surface cracks, i.e. the Marshall distribution. According to some preliminary evaluation [5], this means that the former analysis case employs the initial distribution of crack depth with three times larger average value than the surface crack case. This may be the main reason of higher failure probabilities in the embedded crack analysis case. More rational probabilistic density distributions for embedded cracks should be investigated in the further study.

## 6. CONCLUSION

In the present study, we investigated effects of consideration of embeded cracks in PFM analyses. At first, we obtained a new SIF interpolation formula for elliptical crack embedded in cylinder, and also newly derived that for semi-elliptical surface crack which is valid for deeper crack with a/t =0.95. Implementing those formulas, we analyzed one of the PFM round-robin problems, i.e. aged RPV under normal and upset operating condition. Leakage probability is by two orders of magnitude smaller than break probability. The leakage probability is almost constant, while the break probability increases gradually. The present analysis results are one to two orders greater than the surface crack case analyzed in the previous study. This result may be caused due to the fact that an average crack size of embedded crack tends to be greater than that of the surface crack when the same probabilistic distribution of crack size is

employed for both embedded crack and surface crack. More rational probabilistic density distributions for embedded cracks should be investigated in the further study.

## ACKNOWLEDGEMENTS

The authors wish to thank all the members of the PFM subcommittee in the Japan Welding Engineering Society (JWES) for their efforts to perform this work, and also thank the Japan Atomic Energy Research Institute (JAERI) for financial support.

## REFERENCES

[1] G. Yagawa, Structural integrity assessment of nuclear power plants using probabilistic fracture mechanics, Nuclear Eng., 34 (1988) 19-30 (in Japanese).
[2] D. O. Harris and K. R. Balkey, Probabilistic considerations in life extension and aging, Technology for the '90s, ASME PVP Division, pp.243-269, (1993).
[3] K.R. Balkey, N.B. Closky and M.K. Vermaut, Application of risk-based methods to inservice inspection and testing, Trans. 14th SMiRT, Lyon, M05/2, (1997).
[4] JWES, Report of LE Subcommittee, Japan Welding Eng. Society (JWES), JWES-AE-9003, (1990) (in Japanese).
[5] Final Report of RC111 Committee, Japan Society of Mechanical Engineers (JSME), (1995).
[6] JWES Report of PFM Subcommittee, JWES, JWES-AE-9705, (1997) (in Japanese).
[7] D. L. Selby et al., PTS evaluation of the H.B. Robinson Unit 2 nuclear power plant, NUREG/CR-4183, Vols. 1, 2, (1985).
[8] B. A. Bishop, Benchmarking of PFM analyses of reactor vessels subjected to PTS loading, EPRI Research Project 2975-5, Final Report, (1993).
[9] S. Yoshimura, G. Yagawa et al., PFM analyses of LWR's pressure vessels and piping : Quantitative study on influences of distributions of initial crack sizes, Proc. 20th MPA Seminar, Vol.2, pp.44.1-10, (1994).
[10] G. Yagawa, S. Yoshimura, et al., Study on life extension of aged RPV material based on PFM -Japanese round robin, Trans. ASME, J. Pressure Vessel Technology, 117(1995) 7-13.
[11] S. Yoshimura, M.-Y. Zhang and G. Yagawa, Life extension simulation of aged reactor pressure vessel material using PFM analysis on a massively parallel computer, Nuclear Eng. & Design, 158 (1995) 341-350.
[12] G. Yagawa, S. Yoshimura et al., PFM analyses of nuclear pressure vessels under PTS events, Nuclear Eng. & Design, 174 (1997) 91-100.

[13] G. Yagawa and S. Yoshimura, A study on PFM for nuclear pressure vessels and piping, Int. J. Pressure Vessels & Piping, 73 (1997) 97-107.
[14] S. Yoshimura, G. Yagawa et al., PFM analysis for LBB evaluation of Light Water Reactor's piping, J. of Atomic Energy Society of Japan, 39 (1997) 777-787.
[15] G. Yagawa and S. Yoshimura, Probabilistic fracture mechanics analyses of nuclear pressure vessels and piping : A review of Japanese activity, Trans. 14th SMiRT, Lyon, GMW/1, pp.541-552, (1997).
[16] J. C. Newman, Jr. and L. S. Raju, Stress intensity factor equations for cracks in 3D finite bodies subjected to tension and bending loads, NASA -TM- 85793, 1984.
[17] I. S. Raju and J. C. Newman, Stress intensity factors for internal and external surface cracks in cylindrical vessels, Trans. ASME, J. Pressure Vessel Technology, 104 (1982) 293-298.
[18] D. L. Stevens et al., VISA, NUREG/CR-3384, (1983).
[19] F. A. Simonen et al.,VISA-II, NUREG/CR-4486, PNL-5775 RF, R5, (1986).
[20] M. Shiratori, Analysis of stress intensity factors for surface cracks subjected to arbitrarily distributed stresses, Bulletin of Faculty of Eng., Yokohama National University, 35 (1986) 1-25.
[21] S. Yoshimura, J.-S. Lee and G. Yagawa, Automated system for analyzing stress intensity factors of 3D cracks : Its applications to analyses of two dissimilar semi-elliptical surface cracks in plate, Trans. ASME, J. Pressure Vessel Technology, 119 (1996) 18-26.
[22] G. Yagawa, Y. Kitajima and H. Ueda, 3D fully plastic solutions for semi-elliptical surface cracks, Int. J. Pressure Vessels & Piping, 53 (1993) 457-510.
[23] G. Yagawa, Y. Kitajima and H. Ueda, Erratum of [22], Int. J. Pressure Vessels & Piping, 74 (1997) 77-80.
[24] G.-W. Ye, G. Yagawa and S. Yoshimura, PFM analysis based on 3DJ-integral database, Eng. Fracture Mechanics, 44 (1993) 887-893.
[25] G. Yagawa and G.-W. Ye, A PFM analysis for cracked pipe using 3-D model, Reliability Eng. & System Safety, 41 (1993) 189-196.
[26] G. Yagawa, S. Yoshimura and H. Ueda, An estimation scheme for J- and C*- integrals of surface cracks, Proc. Int. Symp. Pressure Vessel Technology & Nuclear Codes & Standards, Seoul, pp.8.15-8.22, (1989).
[27] K. Hojo, G. Yagawa, S. Yoshimura et al., Applications of PFM to FBR components, Nuclear Eng. & Design, 42 (1993) 43-49.
[28] N. Soneda and T. Fujioka, Stress intensity factor influence coefficients of embedded cracks in cylinder, Komae Research Laboratory Report of Central Research Institute of Electric Power Industry (CRIEPI), No. T94037, (1995).
[29] T. Nishioka and S.N. Atluri, Analytical solution for embedded elliptical

cracks and finite element alternating method for elliptical surface cracks subjected to arbitrary loadings, Eng. Fracture Mechanics, 17 (1983) 247-268.
[30] T. Miyoshi, K. Ishii and Y. Yoshida, Database of stress intensity factors for surface cracks in pre/post penetration, Trans. JSME, 56A (1990) 1563-1569.
[31] W. Marshall, An assessment of the integrity of PWR PVs. UKAEA, (1982).
[32] T. Y. Lo et al., Probability of pipe failure of the reactor coolant loop of Combustion Eng. PWR plants, NUREG/CR-3663, UCRL-53500, (1985).
[33] ASME, ASME Boiler & Pressure Vessel Code. Section XI, Appendix A, (1973).
[34] P. Tipping, Study of a possible plant life extension by intermediate annealing of the reactor pressure vessel II : Confirmation by further annealing schedules, Proc.NEA-UNIPEDE Specialist Meeting on Life-Limiting and Regulatory Aspects of Reactor Core Internals and Pressure Vessels, Sweden, (1987).

Table 1 Ranges of parameters for SIF calculations of embedded elliptical cracks

| $a_2/a_1$ | $2a_2/t$ | $e/t$ |
|---|---|---|
| 1, 2/3, 1/2, 1/3 | 0.1 | 0.1, 0.3, 0.5, 0.7, 0.9 |
| | 0.3 | 0.2, 0.35, 0.5, 0.65, 0.8 |
| | 0.5 | 0.3, 0.4, 0.5, 0.6, 0.7 |
| | 0.7 | 0.4, 0.45, 0.5, 0.55, 0.6 |

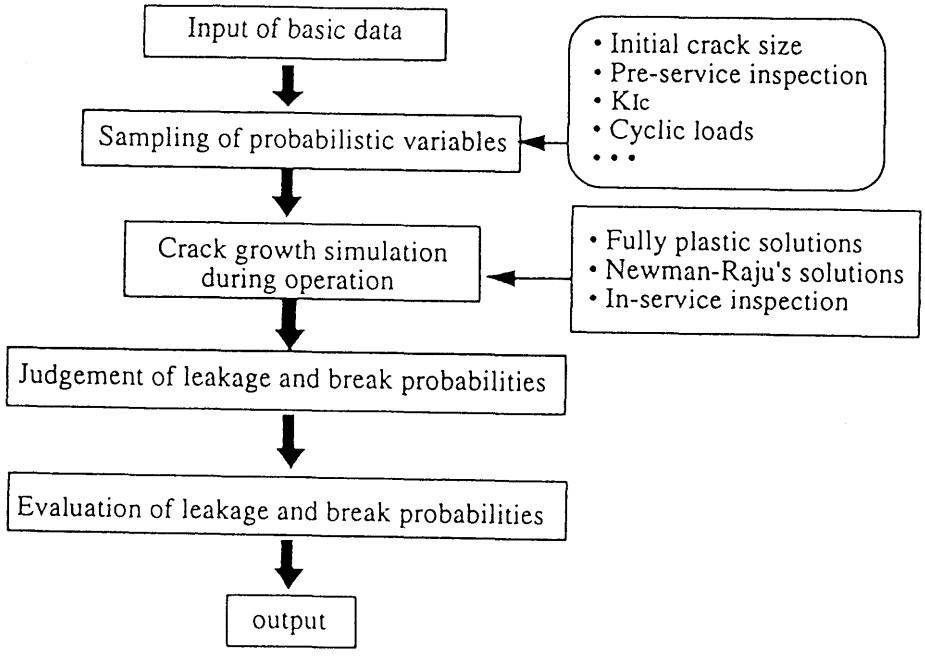


Fig. 1 Flow of typical PFM analysis

Table 2 Coefficients of interpolation functions of influence coefficients for axial embedded cracks

| order of | | | Uniform | | | Linear | | |
|---|---|---|---|---|---|---|---|---|
| $\xi$ | $\eta$ | $\zeta$ | $\pi/2$ | 0 | $-\pi/2$ | $\pi/2$ | 0 | $-\pi/2$ |
| 0 | 0 | 0 | 1.0147e+00 | 1.0155e+00 | 1.0152e+00 | 3.8658e-01 | 5.0793e-01 | 6.2819e-01 |
| 1 | 0 | 0 | -1.7213e-02 | 4.1572e-03 | 2.6449e-02 | 5.0035e-01 | 5.1074e-01 | 5.2024e-01 |
| 2 | 0 | 0 | 1.8667e-01 | 6.9649e-02 | 1.8025e-01 | 5.5523e-02 | 3.5662e-02 | 1.3142e-01 |
| 3 | 0 | 0 | -1.9288e-01 | -1.1752e-02 | 1.7125e-01 | 5.6909e-03 | 2.9000e-02 | 1.9105e-01 |
| 0 | 1 | 0 | -2.1698e-02 | -1.4928e-02 | -2.3164e-02 | -3.6529e-02 | -7.5738e-03 | 1.3820e-02 |
| 1 | 1 | 0 | 1.5948e-02 | -4.4034e-03 | -2.8181e-02 | -1.5644e-03 | -1.0429e-02 | -2.6354e-02 |
| 2 | 1 | 0 | -2.7347e-01 | -9.9909e-02 | -2.7216e-01 | -9.8516e-02 | -5.0299e-02 | -1.8140e-01 |
| 3 | 1 | 0 | 2.0036e-01 | 1.9455e-03 | -2.0939e-01 | -5.6461e-02 | -4.8333e-02 | -2.4892e-01 |
| 0 | 2 | 0 | 1.5750e-02 | 3.0500e-03 | 1.8412e-02 | 1.1349e-02 | 6.4351e-04 | 8.0896e-03 |
| 1 | 2 | 0 | -4.6970e-04 | 1.9621e-03 | 1.9947e-02 | 1.3636e-04 | -2.9167e-03 | 1.8439e-02 |
| 2 | 2 | 0 | 2.1873e-01 | 6.1455e-02 | 2.2561e-01 | 7.9351e-02 | 3.3507e-02 | 1.3379e-01 |
| 3 | 2 | 0 | -1.3285e-01 | 1.8061e-02 | 1.2739e-01 | 8.4364e-02 | 6.2667e-02 | 1.9006e-01 |
| 0 | 0 | 1 | 9.7038e-02 | 6.6901e-02 | 1.0290e-01 | -1.3911e-01 | 3.3090e-02 | 2.3901e-01 |
| 1 | 0 | 1 | -8.9613e-02 | 6.0236e-03 | 1.0542e-01 | -6.1376e-01 | -5.8178e-01 | -5.1643e-01 |
| 2 | 0 | 1 | 1.7963e-01 | 1.8901e-02 | 1.8005e-01 | 5.0811e-02 | 1.2193e-02 | 1.3577e-01 |
| 3 | 0 | 1 | -1.4339e-01 | -5.6146e-03 | 1.5604e-01 | -2.1673e-02 | -1.4836e-03 | 1.3693e-01 |
| 0 | 1 | 1 | -1.3384e-01 | -5.8347e-02 | -1.4206e-01 | -1.0128e-01 | -2.9686e-02 | -3.7667e-02 |
| 1 | 1 | 1 | 8.5542e-02 | -4.6491e-03 | -1.1418e-01 | 1.1636e-02 | -1.9049e-02 | -9.6713e-02 |
| 2 | 1 | 1 | -1.9598e-01 | -3.7515e-02 | -1.8883e-01 | -6.2331e-02 | -1.7043e-02 | -1.3222e-01 |
| 3 | 1 | 1 | 1.1479e-01 | 1.0764e-03 | -1.1203e-01 | 1.0182e-02 | 1.5389e-02 | -7.8487e-02 |
| 0 | 2 | 1 | 1.0946e-01 | 1.1498e-02 | 1.1878e-01 | 5.7687e-02 | 8.4873e-03 | 5.8915e-02 |
| 1 | 2 | 1 | -6.2691e-02 | -9.3455e-03 | 8.9418e-02 | -7.4182e-03 | 9.8546e-03 | 8.2036e-02 |
| 2 | 2 | 1 | 1.5871e-01 | 3.6655e-02 | 1.2966e-01 | 4.8000e-02 | 8.7273e-03 | 8.3907e-02 |
| 3 | 2 | 1 | -7.5636e-02 | 5.1782e-02 | 4.9455e-02 | -3.4909e-03 | -1.1055e-02 | -2.4436e-02 |
| 0 | 0 | 2 | 1.4099e-01 | 7.4737e-02 | 1.5114e-01 | 5.7916e-02 | 3.6893e-02 | 9.0692e-02 |
| 1 | 0 | 2 | -1.0600e-01 | -5.5500e-03 | 9.7064e-02 | -2.6441e-02 | -4.5136e-03 | 8.4450e-02 |
| 2 | 0 | 2 | -3.6196e-01 | -2.1198e-01 | -3.3835e-01 | -1.1674e-01 | -1.0978e-01 | -2.4242e-01 |
| 3 | 0 | 2 | 4.6800e-01 | 3.3818e-02 | -3.5258e-01 | -4.4291e-02 | -8.7491e-02 | -4.5971e-01 |
| 0 | 1 | 2 | -1.8611e-01 | -6.0818e-02 | -1.9751e-01 | -8.1339e-02 | -2.8603e-02 | -1.1073e-01 |
| 1 | 1 | 2 | 1.0966e-01 | 4.5000e-04 | -1.1696e-01 | 3.3627e-02 | -1.2409e-03 | -7.5300e-02 |
| 2 | 1 | 2 | 5.7988e-01 | 2.4246e-01 | 6.0957e-01 | 2.0726e-01 | 1.1604e-01 | 4.0418e-01 |
| 3 | 1 | 2 | -5.2800e-01 | 2.9455e-02 | 5.9106e-01 | 1.3353e-01 | 1.7433e-01 | 6.8247e-01 |
| 0 | 2 | 2 | 1.5001e-01 | 1.8468e-03 | 1.5758e-01 | 6.4005e-02 | 4.1377e-03 | 7.7751e-02 |
| 1 | 2 | 2 | -1.4018e-01 | -3.0000e-03 | 1.2846e-01 | -2.2364e-02 | 1.5546e-02 | 5.4000e-02 |
| 2 | 2 | 2 | -4.4603e-01 | -5.7974e-02 | -5.3673e-01 | -1.3371e-01 | -3.1792e-02 | -2.9081e-01 |
| 3 | 2 | 2 | 3.8400e-01 | -5.6727e-02 | -5.3673e-01 | -2.4436e-01 | -1.9636e-01 | -5.2364e-01 |

Table 3 Coefficients for interpolation for semi-elliptical surface cracks

| i | j | Tension | | Bending | |
|---|---|---|---|---|---|
| | | $\phi = 0$ | $\phi = \pi/2$ | $\phi = 0$ | $\phi = \pi/2$ |
| 0 | 0 | 0.287026 | 0.836913 | 0.473405 | 0.862347 |
| 0 | 1 | 0.773799 | 0.67752 | 0.640619 | 0.313731 |
| 0 | 2 | -0.0226018 | -0.413642 | -0.045655 | -0.206164 |
| 1 | 0 | 1.2256 | 3.68848 | -0.553412 | 0.387558 |
| 1 | 1 | 1.30201 | -8.7632 | 1.45835 | -5.25741 |
| 1 | 2 | -1.42936 | 4.7263 | -1.04671 | 2.61318 |
| 2 | 0 | 0.279154 | -2.16319 | 2.36998 | -1.74584 |
| 2 | 1 | -2.62083 | 6.40039 | -5.0339 | 4.64063 |
| 2 | 2 | 1.82419 | -3.61489 | 2.82114 | -2.36991 |

Table 4 Validity range of interpolation

| | | |
|---|---|---|
| (o) | For all cases | $a/c \geq 0.2$<br>$a/t \leq 0.95$ |
| (i) | Tension: ($\phi = 0$) | $a/t \geq 0.55$ |
| (ii) | Tension: ($\phi = \pi/2$) | $a/t \geq 0.25$ |
| (iii) | Bending: ($\phi = 0$) | $a/t \geq 0.27$ |
| (iv) | Bending: ($\phi = \pi/2$) | $a/t \geq 0.43$ |

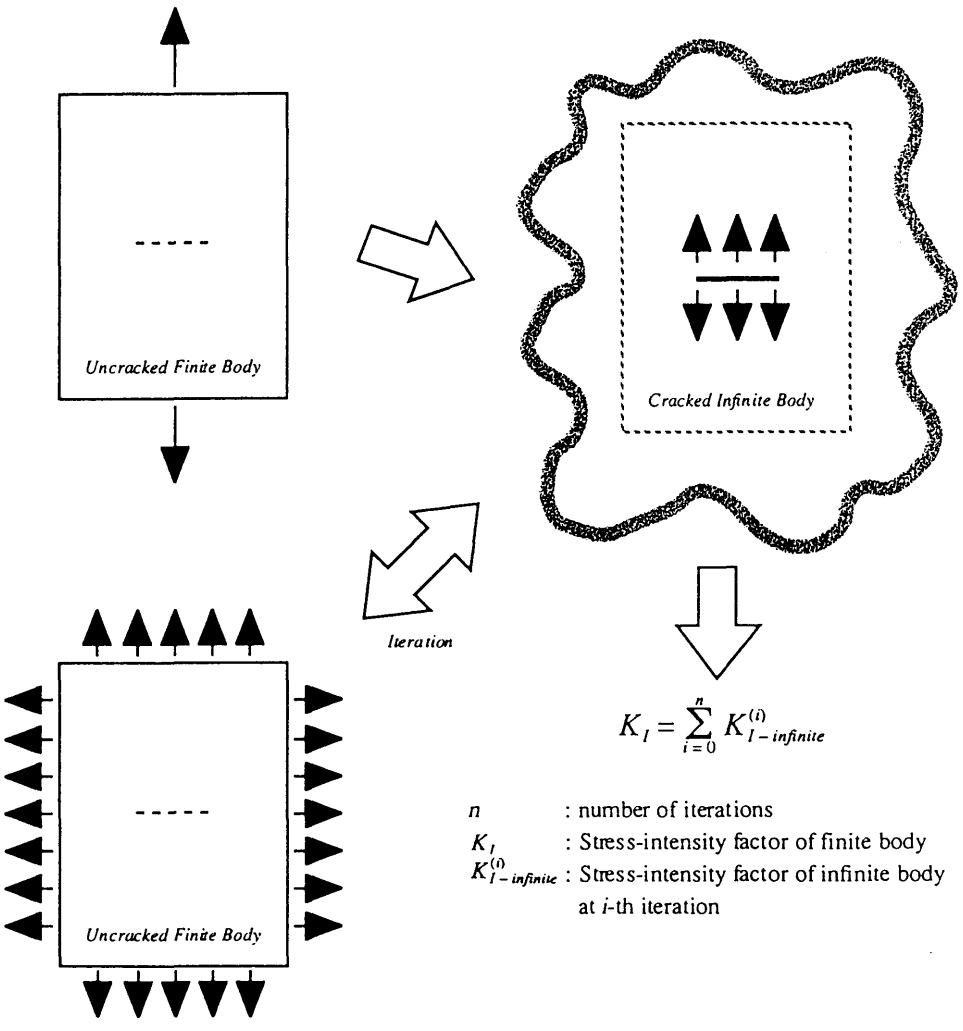


Fig. 2 Algorithm of finite element alternating method

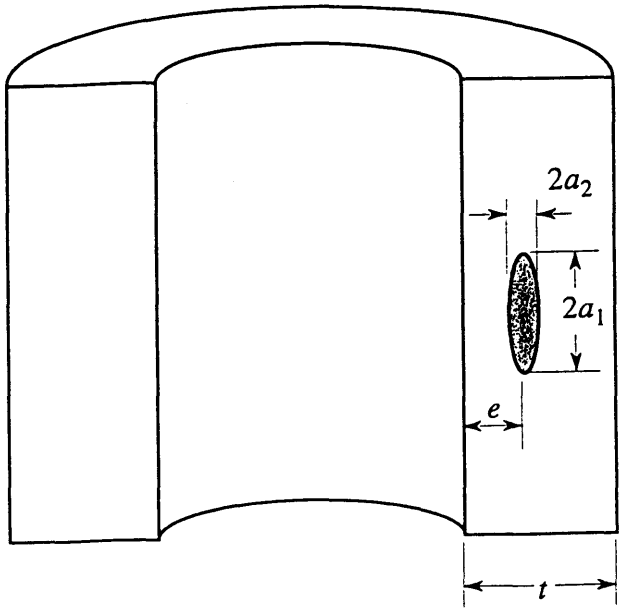


Fig. 3 Axial elliptical crack embedded in cylinder

Table 5 Loading conditions

| Load No. | Design Transient | Applied stress (MPa) | | | | Cycles for 40 years | Estimated cycles | Blocking factor |
|---|---|---|---|---|---|---|---|---|
| | | Tension | | Bending | | | | |
| | | $\sigma_{t,max}$ | $\sigma_{t,min}$ | $\sigma_{b,max}$ | $\sigma_{bmin}$ | | | |
| 1/2 | Heatup-cooldown | 160.9 | 0.0 | 8.0 | 0.0 | 200 | 80 | 2.5 |
| 3 | Unit load-unload | 159.2 | 160.6 | 11.3 | 5.6 | 500 | 20 | 25.0 |
| 4/5 | Plant load-unload | 160.7 | 158.0 | 11.3 | 8.3 | 13200 | 20 | 660.0 |
| 6/7 | Step load change | 164.4 | 157.6 | 5.1 | 5.6 | 2000 | 20 | 100.0 |
| 8 | Steam dump | 167.5 | 150.5 | 4.7 | 6.4 | 200 | 10 | 20.0 |
| 9a | Steady state fluctuations(A) | 160.9 | 158.8 | 8.0 | 5.8 | $1.5x10^5$ | 40 | 3750.0 |
| 9b | Steady state fluctuations(B) | 161.3 | 160.5 | 8.0 | 7.9 | $3.0x10^6$ | 40 | 75000.0 |
| 10 | Feedwater cycling at HS | 154.9 | 162.9 | 16.4 | 1.2 | 2000 | 20 | 100.0 |
| 11/12 | Loop out of service | 167.6 | 160.4 | 6.2 | 6.1 | 80 | 10 | 8.0 |
| 15 | Loss of load | 187.7 | 131.7 | 5.7 | - 7.6 | 80 | 20 | 4.0 |
| 16 | Loss of power | 176.0 | 132.1 | 4.5 | 9.9 | 40 | 10 | 4.0 |
| 17 | Partial loss of flow | 164.7 | 138.2 | 6.0 | 4.7 | 80 | 20 | 4.0 |
| 18a | Reactor trip A | 160.9 | 142.7 | 8.0 | 5.6 | 230 | 20 | 11.5 |
| 18b | Reactor trip B | 160.9 | 114.5 | 8.0 | 17.0 | 160 | 40 | 4.0 |
| 18c | Reactor trip C | 160.9 | 114.5 | 8.0 | 11.0 | 10 | 10 | 1.0 |
| 19 | Inadvertent Depressurization | 160.9 | 9.3 | 8.0 | 52.6 | 20 | 20 | 1.0 |
| 20 | Inadvertent start-up | 167.5 | 142.1 | 10.3 | 8.3 | 10 | 10 | 1.0 |
| 21 | Control rod drop | 160.9 | 131.0 | 8.0 | 9.8 | 80 | 40 | 2.0 |
| 22 | Inadvertent safety injection | 164.0 | 143.7 | 13.1 | 4.6 | 60 | 48 | 1.25 |

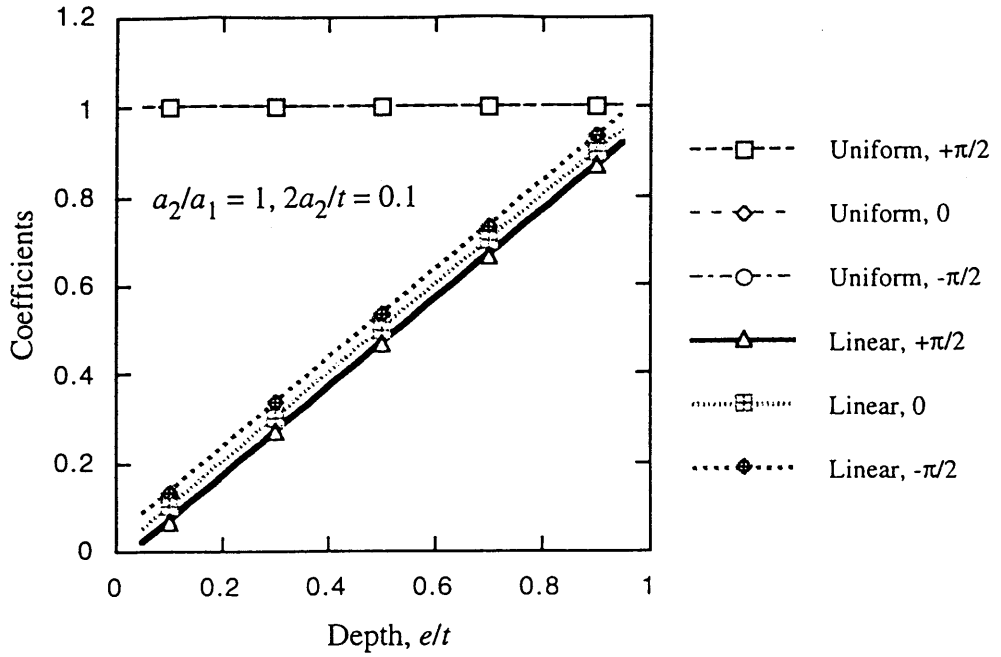


Fig. 4(a) $G_i$ vs. e/t

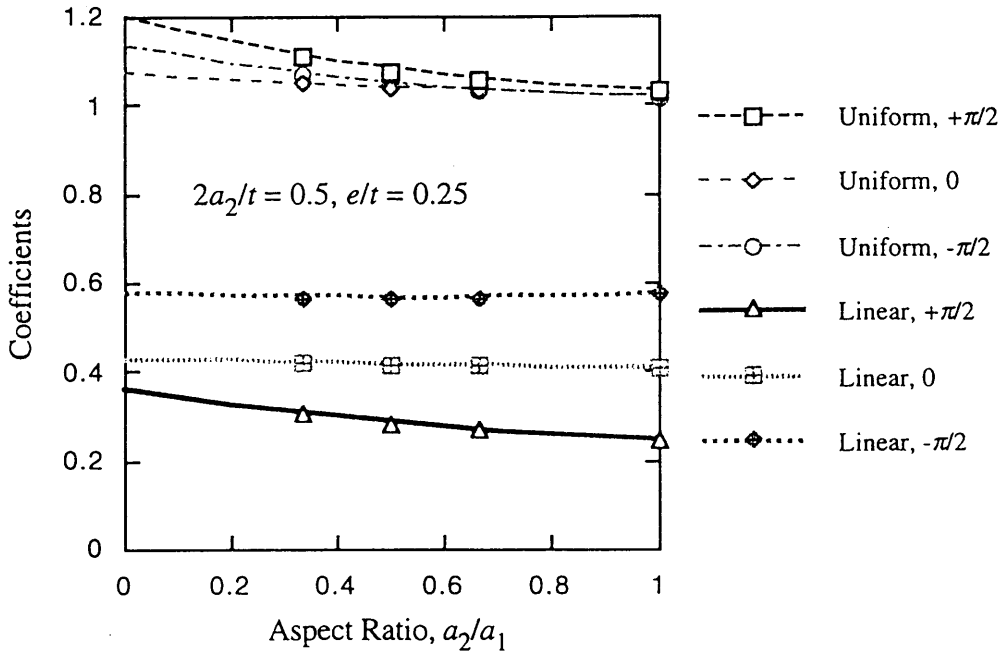


Fig. 4(b) $G_i$ vs $a_2/a_1$

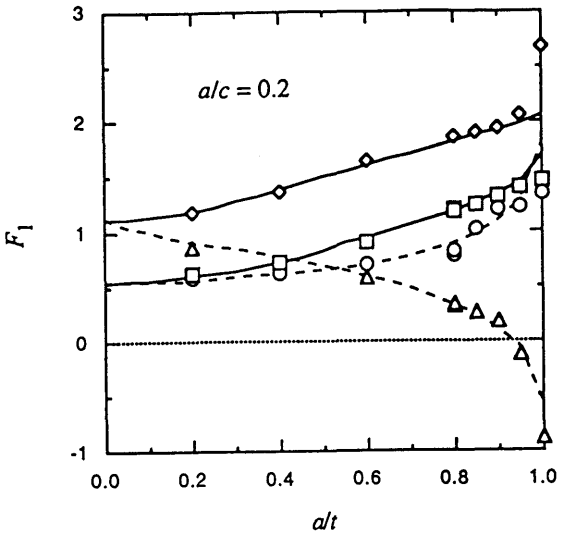


Fig. 5(a) $F_1$ vs a/t (a/c = 0.2)

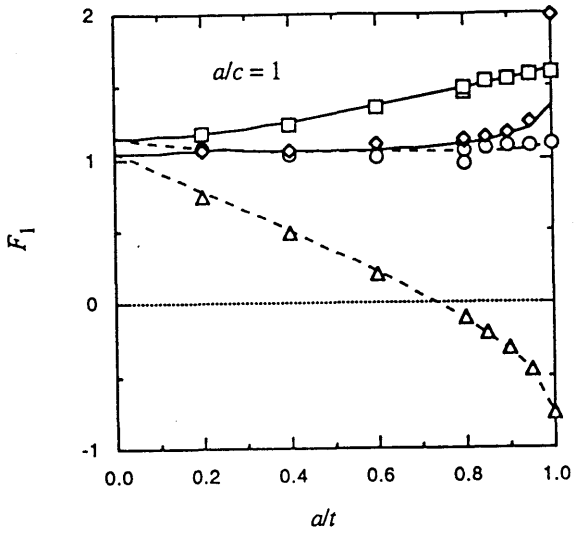


Fig. 5(b) $F_1$ vs a/t (a/c = 1.0)

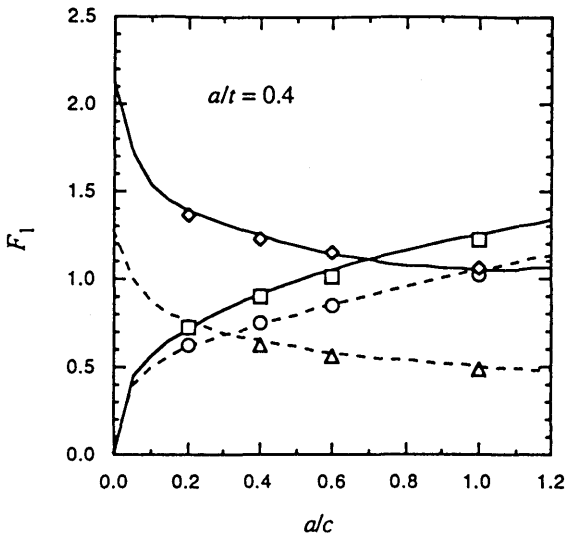


Fig. 5(c) $F_1$ vs a/c (a/t = 0.4)

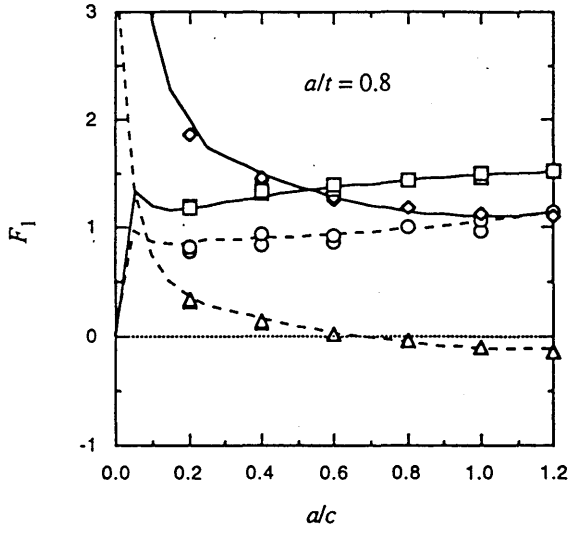


Fig. 5(d) $F_1$ vs a/c (a/t = 0.8)

M: bending moment
$\sigma_b$ = 3M / bt 2 : bending stress

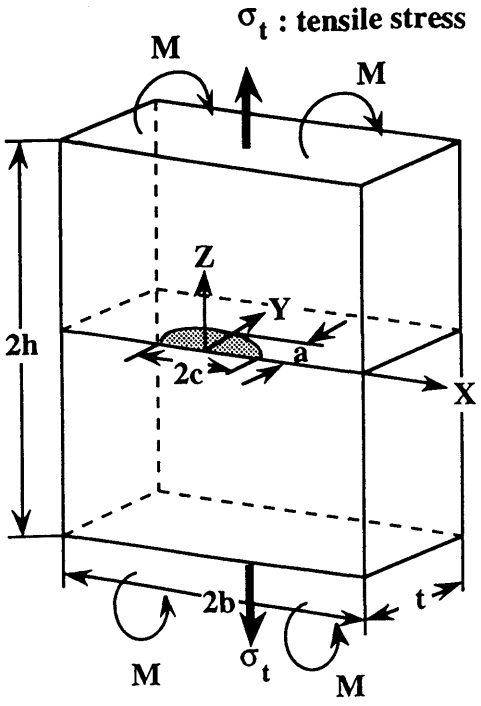


Fig. 6(a) Semi-elliptical surface crack in plate

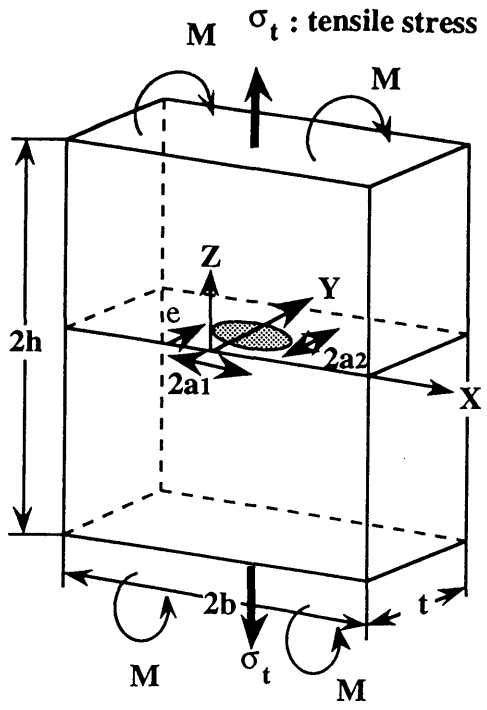


Fig. 6(b) Elliptical crack embedded in plate

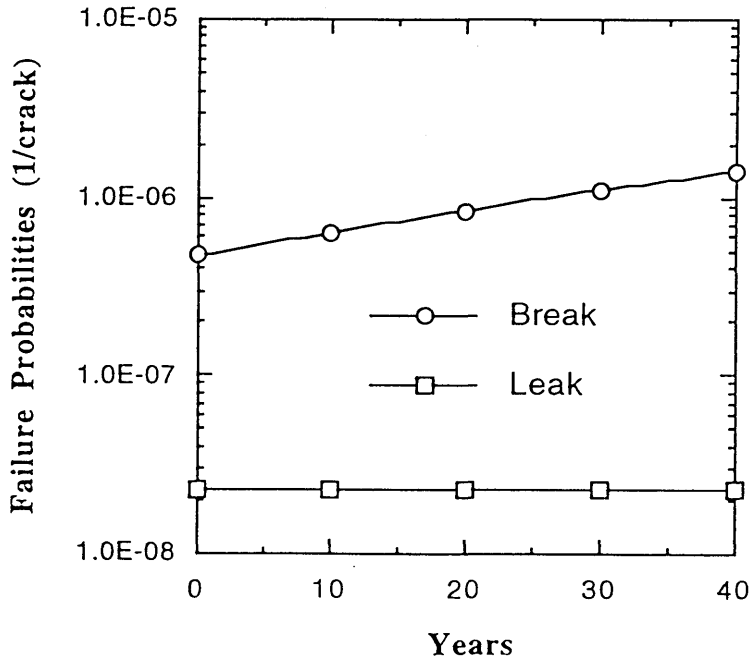


Fig. 7 Failure probabilities vs. operation years

## II-2 Remaining Life Prediction Method Using Operating Data and Knowledge on Mechanisms

Bom Soon Lee, Materials and Corrosion Research Laboratory, Korea Electric Power Research Institute, Korea Electric Power Corporation, Korea

# Remaining Life Prediction Methods Using Operating Data and Knowledge on Mechanisms*

Bom Soon Lee, Han Sub Chung, and Ki-Tae Kim

Materials and Corrosion Research Laboratory
Korea Electric Power Research Institute
Korea Electric Power Corporation, Korea

## ABSTRACT

It is very important to be able to predict the remaining life of components and structures in a power plant, both for nuclear and fossil units. The information needed can be obtained from the controlled laboratory experiments and the plant operating data. On materials degradation, we have accumulated a large amount of data from both sources. However, it is essential to formulate the best methodology to utilize these information so that our needs can be met. In this paper, the methods currently used for remaining life prediction are discussed with typical results. Also discussed are the limitations and the benefits of different approaches along with suggestions for the future R&D directions in this area.

## INTRODUCTION

There are 478 nuclear power plants operating or being built in 32 countries around the world supplying about 17% of the global need for electricity [Ref. 1]. As the nuclear power plants get older, aging becomes an issue, because aging degradation can affect the structural soundness of systems and components. All the nuclear plants around the world should face this issue sooner or later. For instance, United States have the largest number of nuclear power plants in the world, and by the year 2014, 48 commercial nuclear power plants in the United States are projected to reach 40 years of operation [Ref. 2]. The distribution by plant age for the operable USA plants is shown in Figure 1. In managing aging of these plants, good maintenance practices including corrective and predictive ones are required. At the same time, it is very important and necessary to be able to predict the remaining life of a component so that a right decision can be made, in time, among the possible choices of taking no action, repair or replacement. Also, the remaining life estimation will play an important role in the life extension and license renewal processes for the existing nuclear plants.

---

* To be presented at the International Workshop on Integrity of Nuclear Components, Tokyo, Japan (April, 1998)

When a new system or component is designed, the candidate materials are tested under simulated environments so that the right material is selected to assure that the component will last the design life. In this process, the first step is identifying the important parameters that affects the material's performance. Usually, temperature, stress levels, and other environmental parameters are identified in this process. The next step is conducting accelerated tests varying only one parameter at a time while keeping others constant. This experimental approach provides knowledge on the degradation mechanisms even though it is not always successful to understand them with a high level of confidence. This is especially true when multiple parameters are involved.

The predictions based on experimental mechanistic approaches have failed in many cases with the most notable example of Alloy 600, which was believed to last well past the 40 years of design life as a steam generator tube material. During actual operation of nuclear plants, it was discovered that this material was showing several different types of failures modes. The reason for this failure to predict the performance of this material was the lack of knowledge on all the parameters involved in the degradation. Also, the synergetic effects between different parameters are difficult to test in the laboratory.

The operation of a nuclear plant can be considered as a real time experiment under realistic conditions. In fact, we should treat all the nuclear plant operating data as real time (not accelerated) experimental data because we can pull out treasures of failure information from these operating data. If we use these data effectively, we can get complementary information to the experimental results. In this paper, some examples of utilizing operating data are given, and the interrelation between the operating data and experimental data are discussed in the case of steam generator for pressurized water reactors (PWRs).

In utilizing the operating data, we encounter different limitations in predicting remaining life depending on the type of a component, whether it is a component with several subcomponents or rather a simple one. In this paper, to illustrate the differences, globe valves in the containment systems for the Westinghouse PWRs and a steam generator are selected as examples. Globe valves have multi-subcomponents and failure of each different subcomponents cause the failure of the valves. On the other hand, a steam generator has many subcomponents as shown in Figure 2, but the degradation of the tubes is always the life limiting factor for a steam generator. The methods we use to utilize the plant operating data to understand the failure causes and mechanisms are discussed with these two different components.

AGING RESEARCH UTILIZING OPERATING DATA

The United States Nuclear Regulatory Commission (US NRC), Office of Nuclear Regulatory Research has conducted the most extensive research on aging on systems, structures and components (SSCs) of nuclear power plants. This program, entitled "Nuclear Plant Aging Research (NPAR), seeks to improve the operational readiness of systems and components that are vital to nuclear power plants and their safety by understanding and managing aging degradation. Since its inception, the NPAR program has produced a wealth of knowledge on the aging of 19 systems and 29 components. The following were the technical objectives of the program [Ref. 3]:

- o identify and characterize aging effects which, if unmitigated, could cause degradation of SSCs and thereby impair safety,
- o develop supporting data and information to facilitate management of age-related degradation,
- o identify methods of inspecting, surveillance, and monitoring of SSCs, or of evaluating their remaining life to ensure the timely detection of significant effects before safety function is lost,
- o evaluate the effectiveness of storage, maintenance, repair, and replacement practices in mitigating the effects of aging and diminishing the rate and extent of aging degradation,
- o provide technical bases and support for the License Renewal Rule and the license renewal process, and develop a regulatory guide on the format and technical information content for renewal applications.

Usually, for these aging studies, a detailed analysis was performed of the following data bases summarizing the actual operating experience of SSCs:

Nuclear Plant Reliability Data System (NPRDS)
Licensee Event Reports (LERs)
Plant Specific Failure Data.

Analyzing these plant operating data provides information on degradation processes, trend, failure modes, failure causes, and failure mechanisms. The main advantages of using the plant operating data are the large number of data and the fact that these are realistic data. However, since these data are not from the controlled environment, it is not usually possible to identify the exact failure mechanisms. Also, extra caution should

be used in analyzing the data to obtain valid results. For instance, when analyzing valve failure data, similar types of valves should be grouped together.

Figure 3 shows the normalized aging-related failure frequency as a function of age at failure for the globe valves in Westinghouse PWR Containment Isolation function [Ref. 4]. This kind of plot provides information on trend of failure rate as a function of age, but this information cannot be used to make decision on when to replace all the valves. The analysis of failure data provides how and why the valves fail as shown in Figure 4 and 5, respectively. Figure 5 shows that the failures caused by "worn packing" and "worn gasket" increased during the later years, which explains the increase of the failure mode "external leak" shown in Figure 4. Worn or out-of-adjustment packing and worn or damaged gasket result in external leak. The failure due to "aged seat/disk" also increased as the valves got older, which may explain the increase of the failure mode "internal leak".

To obtain more detailed information on the effects of aging on failure causes, the number of failures caused by three major causes were normalized and plotted as a function of age at failure (Figure 6). The frequency curve for the failures caused by worn seats/discs has two peaks at 12 years and 21 years, which explains the peaks at the same ages in the plot for globe valve failures (Figure 3). The failure caused by corrosion product/dirt buildup has a high peak at 3 years, after which the frequency stayed low until it began to increase at 13 years. At 16 to 18 years, many valve failures were caused by worn packing, which explains the peak in the frequency of globe valve failure at 16 - 18 years (Figure 3).

As shown in this example, it is not easy to predict the remaining life of a component which has many subcomponents. However, this kind of operating data analysis provides an important information on when to conduct preventive maintenance to prevent failures. In this example, it was shown that many reported failures were caused by regular maintenance items, such as valve packings. These aging-related failures can be, and should be, prevented by conducting proper scheduled maintenances, which utilizes operating data.

## Prediction of Remaining Life of A Steam Generator

Korea is in the process of replacing steam generators (SGs) at its oldest nuclear plant, Kori 1, which went into commercial operation in 1978. The tubes of these SGs are mill annealed alloy 600, and similar tubes world wide suffered from several forms of degradation over the years. By changing the water chemistry and extensive effort to limit the ingress of aggressive agents, most of the old problems were

solved except the intergranular attack/stress corrosion cracking (IGA/SCC). Degradation of heat transfer tubes is the main issue for the nuclear steam generator life prediction.

As discussed above, several different types of corrosion cause the degradation and failures of steam generator tubes, and both statistical and mechanistic approaches are required in order to predict remaining life of a steam generator with a high level of confidence. Which one is more useful depends on type of degradation, extent of experimental and operational data available, and the extent of mechanistic understanding for the relevant degradation type.

Degradation of steam generator tubes can be considered as an ideal subject for statistical evaluation. Thousands of identical tubes in a steam generator are exposed to same operation condition so that degradation of each tube can be treated as random variable in a statistical sense for a specific type of degradation. In service inspection (ISI) produces tube degradation data during each outage. It is not unusual that a significant amount of defected tubes are identfied at every inspection at the scheduled outage.

Nevertheless, it should be noted that the extent of applicability of statistical approach be limited and be reviewed with care. There have been series of steam generator design improvement by different vendors, and many different models are under operation presently. Any steam generators of a model may not be identical to one another because details of operational conditions, especially water chemistry, vary from plant to plant. Once a life threatening degradation form is identified, each plant start to struggle to control and mitigate the degradation by corrective, preventive, and predictive maintenance efforts, which include for example chemical cleaning, shot peening, corrosion inhibitor, and sludge lancing. Even without the maintenance effort, a steam generator is hardly operated under an identical condition throughout the whole life. Secondary side corrosion of tubes attributed to occasional impurity intrusion into water chemistry is not uncommon. There have been significant improvement of non destructive examination (NDE) techniques for ISI. Improved ISI induces a transient of record by uncovering defects not detected before. In a few instances, it was too late when significant amount of tube degradation data enough to define a statistic trend were available because steam generator replacement or a major sleeve campaign was needed already.

Even though factors listed above limit the applicability of statistical approach, there are still cases where statistical analysis of the operating data plays a key roll in steam generator life prediction. Primary water stress corrosion crack (PWSCC) in roll transition and secondary side inter granular attack / inter granular stress corrosion crack (IGA/IGSCC) in a steam generator with a well controlled water chemistry history

can be a good subject of statistical analysis. PWSCC occurs under a well controlled chemistry condition, almost constant temperature, narrow range of residual stress distribution caused dominantly by manufacturing tolerance. Secondary side IGA/IGSCC is induced by localized impurity concentration inside crevices. The localized impurity concentration may be considered as a part of aging process for steam generators without serious chemistry transients.

## Weibull Function

It has been verified that the Weibull probability distribution function (pdf) is the most appropriate one for interpreting failure trends of steam generator tubes among various pdf's [Ref. 5, 6]. The Weibull pdf is expressed as following:

$$f(t) = \frac{b}{\theta - t_0} \left(\frac{t - t_0}{\theta - t_0}\right)^{b-1} \exp\left[-\left(\frac{t - t_0}{\theta - t_0}\right)\right]^b \qquad (1)$$

,where t ; operation time
$t_0$ ; defect initiation time
b ; Weibull slope
$\theta$; characteristic time

The cumulative Weibull function F(t) $\left(= \int_{t_0}^{t} f(x)\,dx\right)$ can be rearranged as follows,

$$\ln \ln \frac{1}{1 - F(t)} = A + b \ln (t - t_0) \qquad (2)$$

,where $A = -b \ln (\theta - t_0)$

Eqation (1) and (2) denote three parameter Weibull function. If $t_0$ is set to be zero, which is to say the degradation can occur at any time from the beginning of operation, equation (1) and (2) can be modified to two parameter Weibull function. Details of the Weibull function can be found elsewhere [Ref. 5, 6].

Figure 7 shows a Weibull projection of axial PWSCC in the roll transition near top of tubesheet in three steam generators of one of Korean nuclear power plants. 100 % of total 9990 tubes have been inspected every ISI since the fifth regular outage. A tube was defined as cracked when the eddy current inspection detected crack indication, whereas the crack initiation point may be defined as the time when a microscopically small crack has grown to a size big enough to be detected by the current inspection method. An alternative tube repair criteria based on crack length has been adapted rather than the depth based 40% wall thickness criteria for this particular type of

degradation in the unit. Statistical approach can be a valuable tool when the remaining life of these steam generators is to be evaluated.

Crack growth rate data were required to evaluate the remaining life since crack length based repair criteria were adapted. The plant specific crack growth rate could be defined with a high level of confidence by using thousands of crack length data measured by ISI. Each crack growth rate datum was defined as the difference between crack lengths divided by length of operation period between successive ISIs. Figure 8 shows another Weibull projection for which crack initiation point was defined when the crack had grown longer than 5.5 mm. A two parameter Weibull projection fitted well to the data set. Another projection line for tubes with cracks longer than 10 mm, which is a tentative length criterion, could be drawn by using the plant specific average crack growth rate at the crack length of 5.5 mm. This projection contains conservatism since crack growth rate decreases as a crack grows. The curve can be assumed as a future projection of plug ratio when 10 mm length criterion is applied. The life of these steam generators can be estimated against the axial PWSCC in the roll transition when the maximum allowable plug ratio is defined in the unit.

## MECHANISTICAL APPROACHES

While "statistical approaches" are used to estimate the probability of occurrence of an event (e.g., number of SG tubes which has cracks longer than some critical length) by simple extrapolation from credible existing data, "mechanistical approaches" are evaluating the parameters which can affect an event (e.g., crack growth rate in SG tubes) individually and totally, and thereby, preferably setting up a proper model for the event. By using this kind of model with the actual engineering conditions, one can evaluate or predict the possibility of an event.

One of the typical example of mechanistic approaches is the prediction of the stress corrosion crack growth rate of alloy 600 in PWR environment. Of the several models suggested for the SC crack growth mechanism [Ref. 7], following three mechanisms are widely accepted: 1) slip / film rupture / dissolution mechanism, 2) film induced cleavage, 3) hydrogen embrittlement. Different mechanisms, however, may operate in one alloy / environment system with a dominant mode being determined by perhaps small changes in the material, environment, or stressing condition.

According to the slip / film rupture / dissolution mechanism, which is believed most suitable to explain the SCC of SG tubes in PWR, the crack growth rate can be estimated from the relation between the oxidation rates and the stress / strain conditions at the crack tip. These are supported by a good correlation in a number of systems between the oxidation current density (e.g., obtained on a straining surface) and the crack growth rate [Ref. 8. 9].

For a given crack tip environment, corrosion potential, and material condition, the crack growth will be controlled by the change in oxidation charge density with time and the frequency of film rupture at the strained crack tip. As the crack grows, the bare new surface becomes passivated (oxidized). The next crack growth can happen only when the passivated layer (oxide film) at the crack tip ruptures. Therefore, the average crack growth rate, $V_t$, can be related to the oxidation charge density passed between film rupture events, $Q_f$, and the strain rate at the crack tip, $\varepsilon_{ct}$ [Ref. 10]

$$V_t = \frac{M}{zpF} \frac{Q_f}{\varepsilon_f} \varepsilon_{ct} \qquad (1)$$

where: M, $\rho$ = atomic weight and density of the crack tip metal
F = Faraday's constant
z = electrical valence of a metal atom
$\varepsilon_f$ = fracture strain of the film

The oxidation current transient generally shows an initially high bare surface dissolution current density, $i_0$, for a short time, $t_0$, and thereafter decreases according to a power law relationship as the following:

$$i_t = i_0 [t/t_0]^{-n} \qquad (2)$$

where: $i_t$ = oxidation current at time t
t = time
n = constant

Because of this power law relationship, equation (1) can be reformulated as following equation (3). This equation means that the crack growth rate behaviour can be evaluated by the repassivation response "n" value.

$$V_t = f(n) [\varepsilon_{ct}]^n \qquad (3)$$

The effect of "n" on predicted crack growth rate vs. stress intensity is illustrated in Figure 9. There were much efforts to estimate or measure an appropriate "n" value under given temperature, environment, and alloy / microstructure conditions [Ref. 11 - 14]. Figure 10 shows that the range in crack growth data in PWR environments are reasonably predicted by this modeling methodology.

Another example of mechanistic approaches is the evaluation of plugging criteria of a SG tube to prevent tube burst. The plugging criteria of a tube can be fixed by a maximum permissible crack length, $a_0$, which can be obtained according to the following equation:

$$a_0 = a_c - \Delta a_1 - \Delta a_2 \qquad (4)$$

where: $a_c$ = the minimal critical size which causes a fast burst of the tube
Details of $a_c$ assessment can be found elsewhere [Ref. 15].
$\Delta a_1$ = the maximum uncertainty from the dimensioning of the cracks of significant size by means of the inspection technique used
$\Delta a_2$ = crack growth between the two subsequent inspections

By using this criteria with the help of continuous in-service monitoring of primary to secondary leak, a maximum permissible in-service leak criterion also can be set up.

As discussed above, the mechanistic approaches are very successful to formulate the working hypothesis and thereby quantify and validate against real observation for some corrosion problems. However, the diversity of working parameters and yet unknown synergistic effects between them limits the validity of the mechanistic approaches.

## CONCLUSIONS

Experimental data and plant operating data are the two main sources of information that can be used to predict the remaining life of a component. However, only recently, it has been realized that plant operating data can be treated as long term, real time experimental data except that the experimental conditions vary a few times during the real time experiments. In this paper, a few examples of utilizing the both types of data to predict the remaining life of a component were shown and discussed, and the following conclusions may be drawn.

o It is not easy to predict the remaining life of a component which has many subcomponents that fail independantly using the operaing data. However, the anaysis of operating data can provide an important information on when and how to conduct preventive maintenance to prevent failures.

o Weibull statistics is an usuful tool in predicting the remaining life of a component utilizing the operating data as long as it can be assumed that the failure mechanism stay the same.

o The mechanistic approaches are necessary in formulating the working hypothesis, which can be validated by experiments and in some cases by utilizing the

operating data.

o More research should be focused on improving the methods to utilize the operating data to predict the remaining life of a nuclear component, since plenty of operaing data are available, and are still being produced.

REFERENCES


1. IAEA, International Atomic Energy Agency, IAEA-SM-353, 1998.
2. Blahnik, D.E., et al., "Insights Gained From Aging Research," NUREG/CR-5643, BNL-NUREG-52323, March 1992.
3. Vora, J.P., and Vagins, M., "Nuclear Plant Aging Research Program Plan," NUREG/CR-1144, Rev.2, 1991.
4. Lee, B.S., et al, "Aging Assessment of Westinghouse PWR and General Electric BWR Containment Isolation Functions," NUREG/CR-63339, BNL-NUREG-52462, Brookhaven National Laboratory, March 1996.
5. EPRI, NP-7493, "Statistical Analysis of Steam Generator Tube Degradation," 1991.
6. EPRI, TR-103566, "Statistical Analysis of Steam Generator Tube Degradation: Additional Topics," 1994.
7. Parkins, R., British Corr. J., 7, 15, 1972.
8. Ford, F.P., "Stress Corrosion Cracking", in Corrosion Processes, Ed. R.N. Parkins, Applied Science, 1982.
9. Parkins, R., "Environment Sensitive Fracture - Controlling Parameters", Proc., Third Int. Conf. on Mechanical Behaviour of Materials, Vol. 1, p.139-164, 1980.
10. Ford, F.P. and Anderson, P.L., "Practical Application of Knowledge of Mechanisms of EAC in LWRs", Proc., Int. Symp. on Steam Generator Technology Update, KEPRI, Taejon, Korea, December 1997.
11. Thompson, C., et al, "Analysis of A600 and X-750 SCC Cracks", Proc., Alloy 600 Experts Meeting, Arlie, VA, EPRI, Palo Alto, April 6-9, 1993.
12. Thompson, C., et al, "Prediction of PWSCC in Nickel Base Alloys Using Crack Growth Models" Proc., Seventh Int. Symp. on Environmental Degradation of Materials in Nuclear Power Systems - Water Reactors, NACE, p.867-880, 1995.
13. Carey, D.M., et al, "Alloy 600 SCC Growth Measurements in Primary Coolant", Prod., Workshop on PWSCC of Alloy 600 in PWRs, EPRI, November 1994.
14. Angeliu, T, et al, "Repassivation and Crack Propagation of Alloy 600 in 288C Water", Paper 96086, Corrosion/96, NACE, 1996.
15. Flesch, B., et al, "Failure Analysis Module for the EPM Code for PWR Steam Generator Tube Maintenance", Proc., SMIRT 11, Tokyo, 1991.

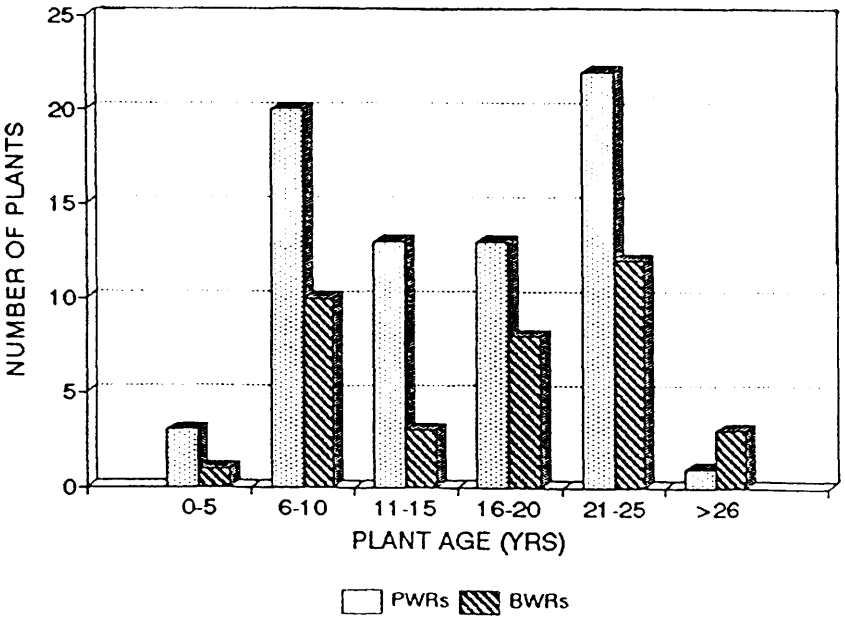


Figure 1 Age distribution of operable plants in the USA

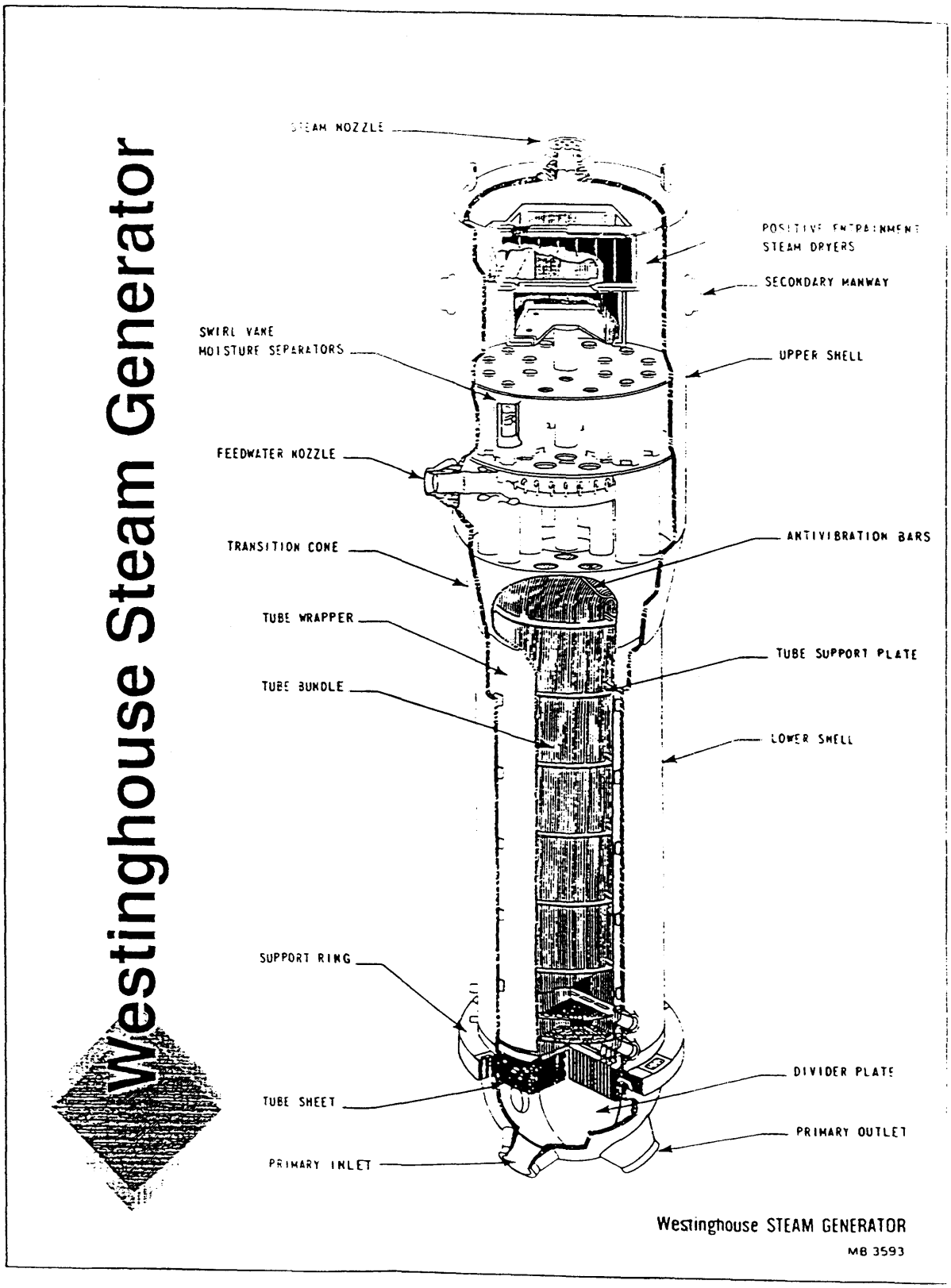


Figure 2 Schematic diagram of a Westinghouse steam generator

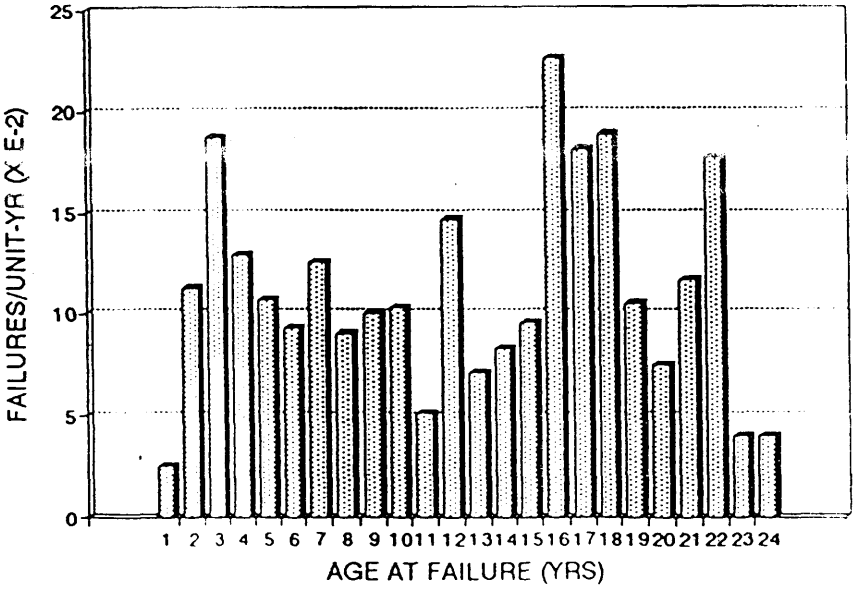


Figure 3 Normalized failure frequency for globe valves in the Westinghouse CI function

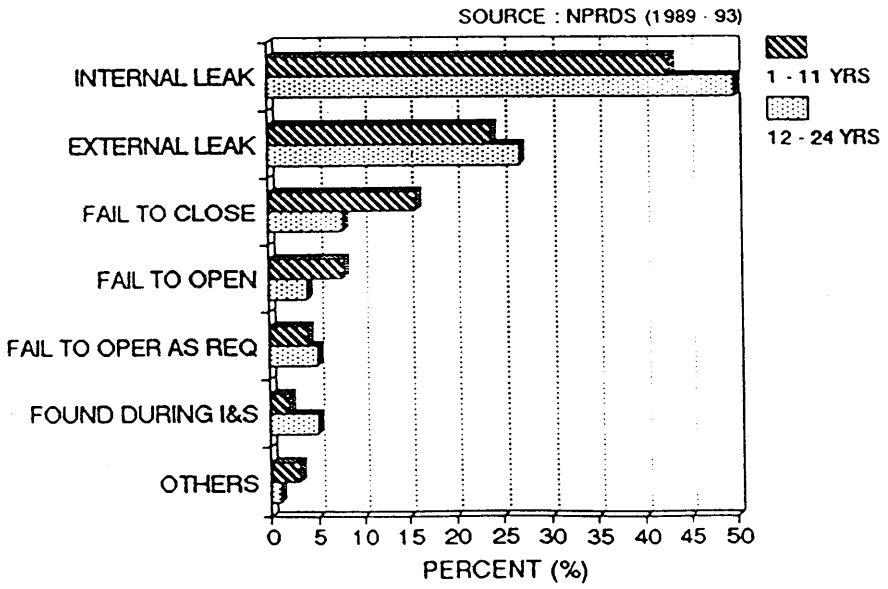


Figure 4 Failure modes for globe valves in Westinghouse PWR CI function during two periods

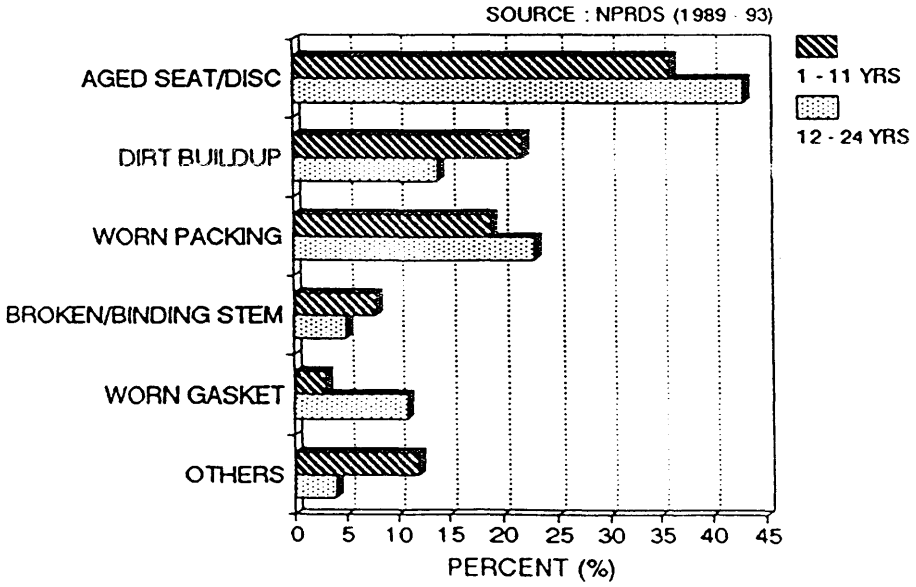


Figure 5 Failure causes for globe valves in Westinghouse PWR CI function

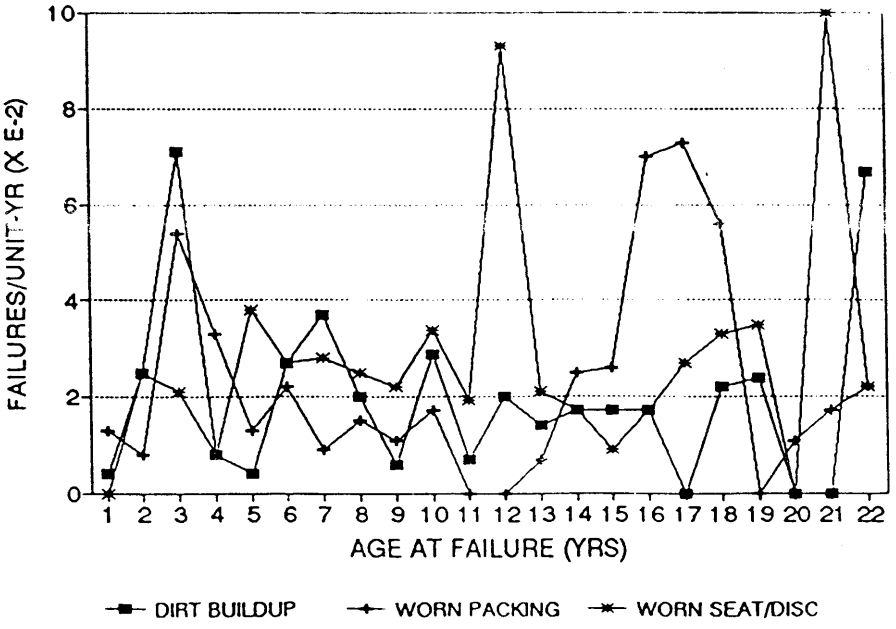


Figure 6 Frequency of globe valve failures caused by major failure causes

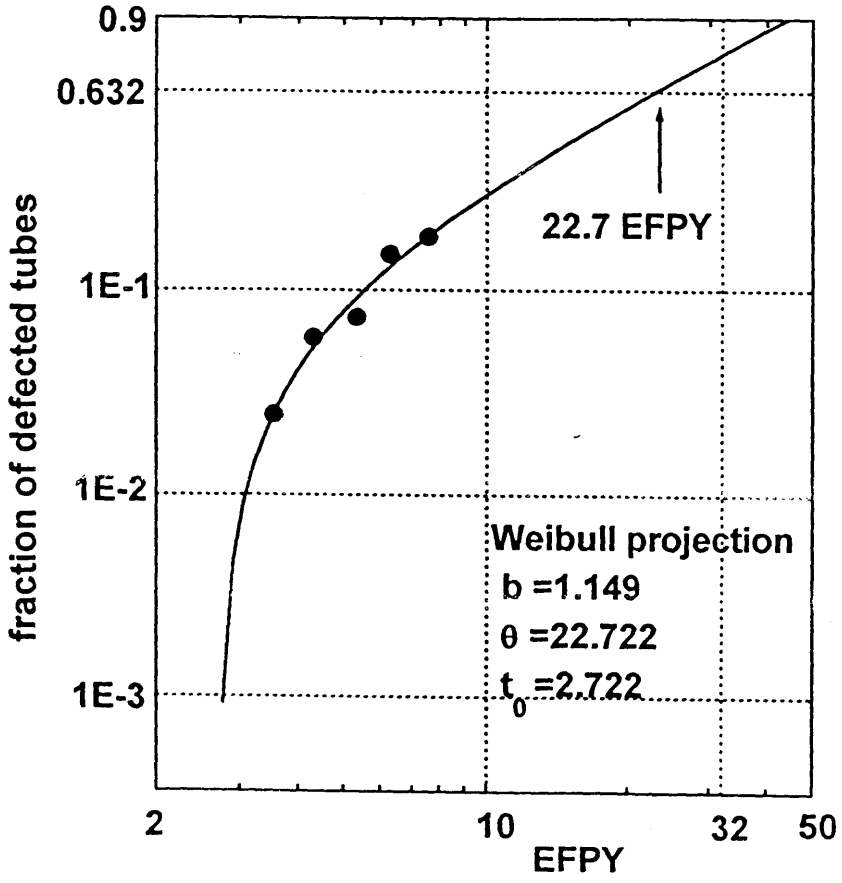


Figure 7 Weibull projection, fraction of tubes cracked vs. EFPY

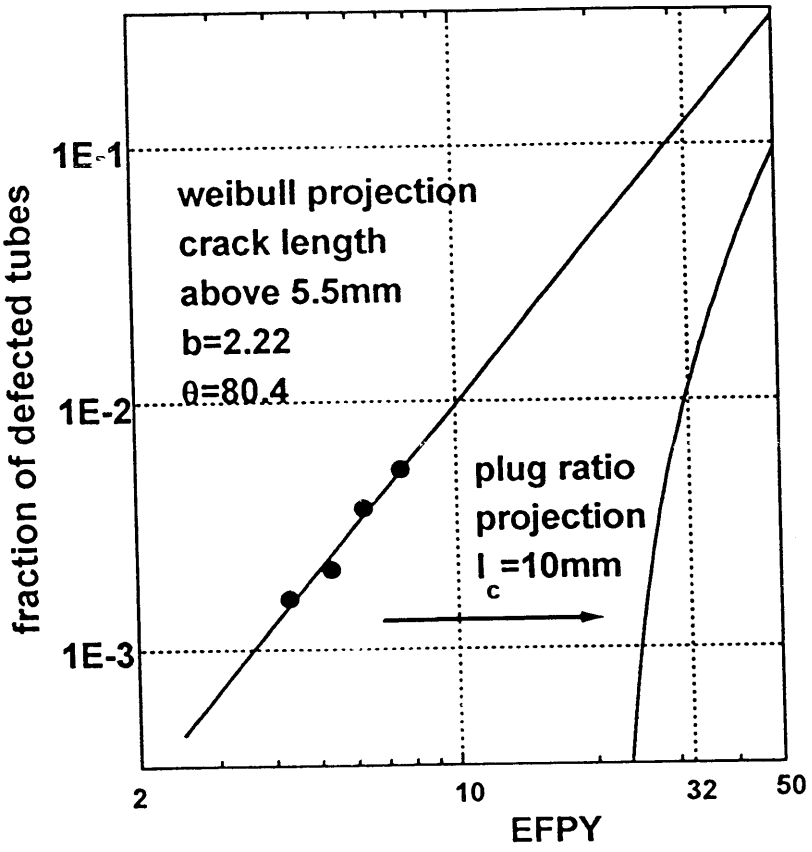


Figure 8 Plug ratio projection using Weibull projection and plant specific crack growth rate data

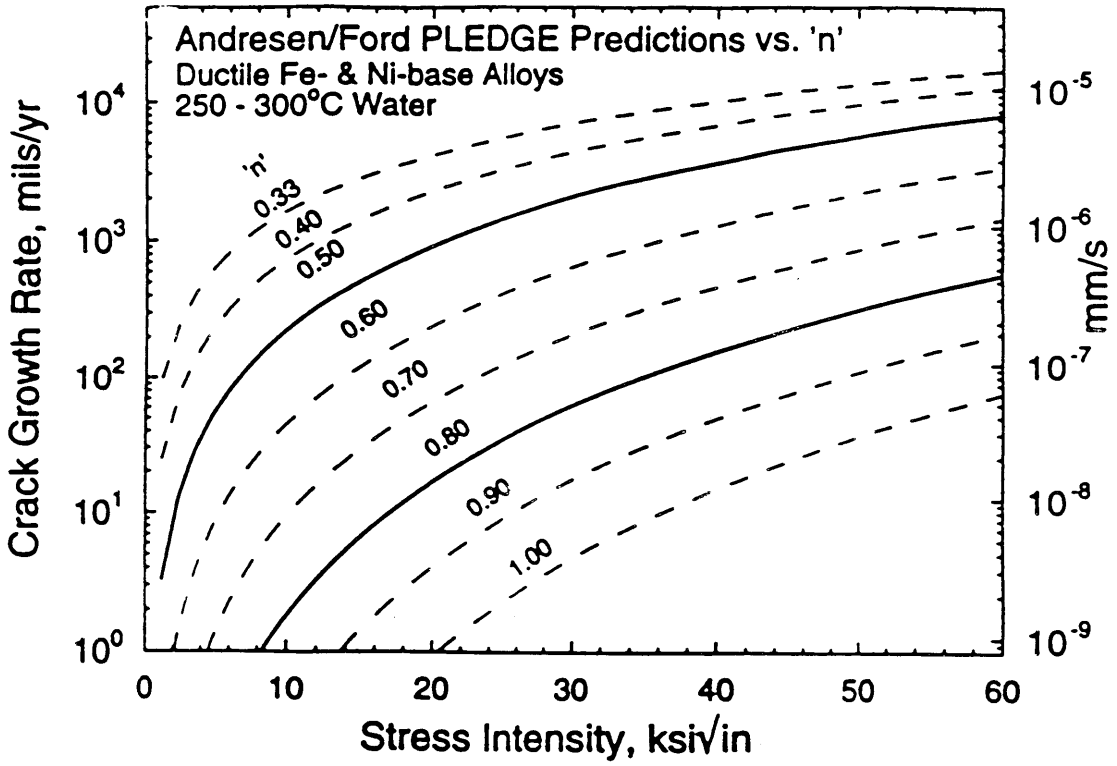


Figure 9 The effect of "n" on predicted crack growth rate for ductile austenitic alloys (Fe and Ni-based) over the range of "n" values considered applicable to 250-300C water. (after [10])

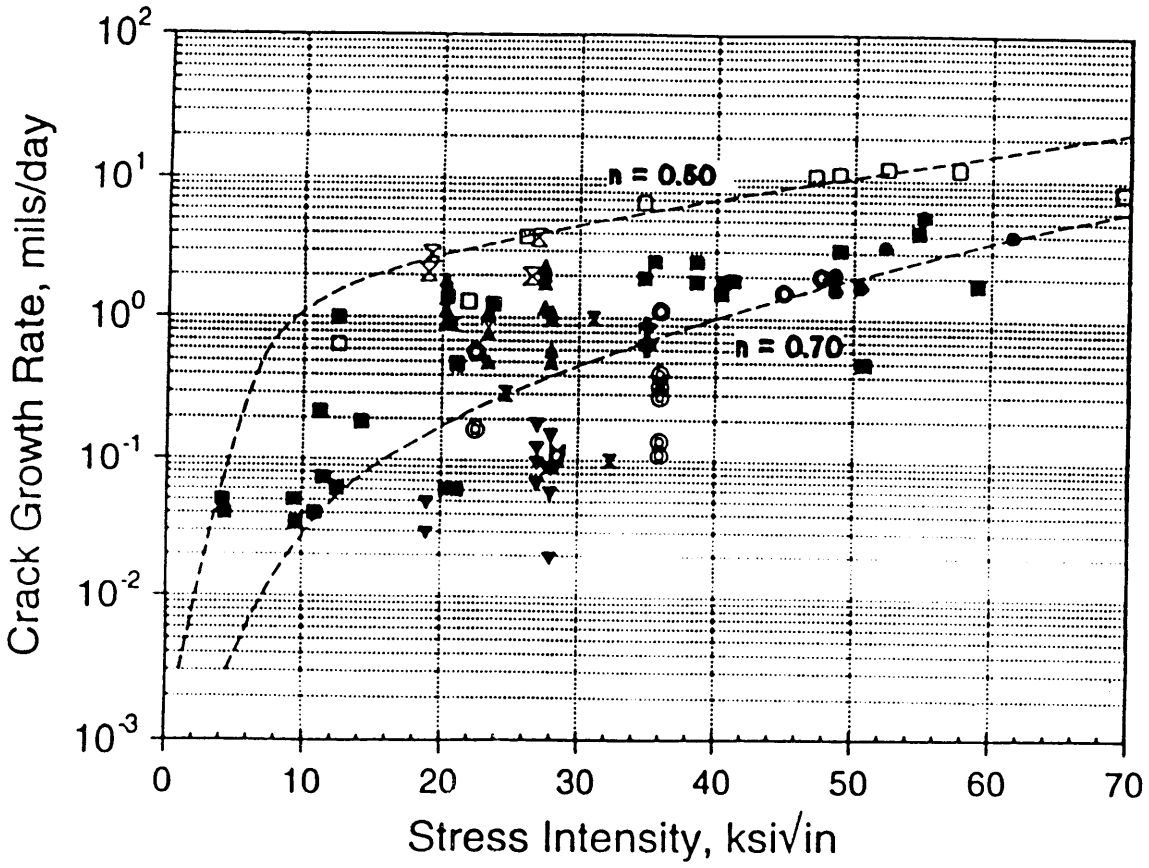


Figure 10 Compilation of Alloy 600 crack growth rate data vs. stress intensity in high temperature deaerated pure water. Model predictions are shown for "n" values of 0.5 and 0.7. (after [10])

II-3 Structural Integrity Assessment of the Reactor Pressure Vessel under the External Cooling Condition

Jong Sung Kim, Yoon Suk Chang, Tae Eun Jin, Korea Power Engineering Company, Inc., Korea

# Structural Integrity Assessment of the Reactor Pressure Vessel under the External Reactor Vessel Cooling Condition

Jong Sung Kim* and Tae Eun Jin*

Key Words : In Vessel Retention, External Reactor Vessel Cooling, Core Melting Accident, Transient State, Finite Element Method, Elastic-Perfect Plastic Behavior, Larson-Miller Curve, Damage Rule

## Abstract

Since the suggestion of External Reactor Vessel Cooling(ERVC), the effects of melting and cooling on the response of structural integrity of the Reactor Pressure Vessel(RPV) under core melting accident conditions have been investigated. This paper describes the vessel response according to the ERVC condition and analysis method. The steady state and transient analysis for the temperature and stress field were performed using ABAQUS. Especially, transient analyses were studied for the variable boundary conditions. To obtain an analogy with real phenomena, the material properties were determined by combining and modifying the existing results considering phase transformation and temperature dependency. The results show that the vessel can be melted if there is no external cooling. Finally, the potential for vessel damage is discussed using the Larson-Miller curve and damage rule.

## 1. Introduction

ERVC(external reactor vessel cooling) has recently been studied and developed as the management strategy for severe accidents[1~3]. In previous studies[4,5] for IVR(in-vessel retention), the extrapolation method was used for the determination of material properties beyond the temperature range presented in the ASME code[6] or the material properties of RPV material not to consider phase transformation and change are used.

But the real material properties are considered to be different from those found by the extrapolation method because material properties, especially thermophysical material properties, are abruptly changed with temperature due to phase transformation. Previous studies[4,5] also utilized the steady state analysis to maintain a constant value of the boundary condition variables for time. However, optimal ERVC time can not be determined

* KOPEC(Korea Power Engineering Company, Inc.)

using steady state analyses. Therefore, the ambiguous conjecture that the reactor cavity would be completely submerged before molten debris reaches the RPV lower head, is presented by those studies.

In this study, however, the material properties for temperature are established like real phenomenon, the boundary conditions are determined to consider the transient state that boundary condition variables - the levels of molten debris/external vessel water, and the temperatures/pressures of molten debris, external vessel water and gas in core - are subjected to change over time. The database and the user subroutine program are constructed in order to determine the material properties of molten debris and the specification of boundary conditions according to transient state. The temperature and the stress analysis are performed for the core melting accident due to large break LOCA by using ABAQUS[7]. Finally, the damage and the structural integrity for RPV are evaluated by using the Larson-Miller curve and damage rule[8]. In addition, the effects of analysis conditions on structural integrity - molten debris quantity, ERVC condition, analysis method and connection condition with RPV upper part - are reviewed.

## 2. Analysis model

### 2.1 Model configuration

The RPV configuration is shown for the case where molten debris and metallic layer are located in the RPV lower head in Fig. 1. The materials of RPV and cladding are SA508 Gr.2 Cl.1[9] and SB166[10], respectively. The thickness of cladding, $t_{clad}$, is 3.175mm.

### 2.2 Chemical composition and material properties

The chemical composition of SA508 Gr.2 Cl.1 is presented in Table 1[9]. The liquidus and solidus temperatures of SA508 Gr.2 Cl.1 are determined to be 1501.04℃ and 1461.09℃ respectively by substituting the chemical composition of Table 1 into Howe's[11] and Kubachewski's[12] correlations. Density $\rho_{RPV}$ is determined from the correlation by Jablonka et al.[13] as shown in Fig. 2. The specific heat, $c_{p,\,RPV}$ and the thermal conductivity, $k_{RPV}$, for temperature are determined from ASME Code[6] and Thomas'

results[14] as shown in Fig. 3 and 4, respectively. The elastic modulus, $E_{RPV}$ and the yield strength, $\sigma_{ys,RPV}$, for temperature are determined from ASME Code[6] and Grill's results[15] as shown in Fig. 5 and 6. Poisson's ratio $\nu_{RPV}$ is determined to be 0.3. The thermal expansion coefficient, $\alpha_{RPV}$, for temperature is determined from ASME Code[6] and Jablonka's results[13] as shown in Fig. 7.

The Larson-Miller curve[16] for SA508 Gr.2 Cl.1 is shown in Fig. 8. $LMP(=0.001T(20+\log t_r))$ is Larson-Miller parameter. $t_r$ is rupture time( *hour*).

The chemical composition of SB166 is presented in Table 2[10]. The liquidus temperature of SB166 is determined to be 1427℃[6]. The thermal conductivity of SB166 for temperature, $k_{clad}$, is determined as shown in Fig. 9[6]. The emissivities of SA508 Gr.2 Cl.1 and SB166, $\varepsilon_{RPV}$, are determined as shown in Fig. 10[17].

Molten debris is assumed to be composed of 72.25%(weight percentage) $UO_2$ and 27.75% $ZrO_2$. The solidus and liquidus temperatures of molten debris are 2536℃ and 2542℃[18], respectively. The density of molten debris, $\rho_{mol}$, versus temperature is determined as shown in Fig. 11[18,19]. The specific heat $c_{p,mol}$ and the thermal conductivity, $k_{mol}$, versus temperature are shown in Fig. 12[18] and 13[18], respectively. The volumetric expansion coefficient, $\beta_{mol}$, for temperature is determined as shown in Fig. 14[18,19]. The viscosity, $\mu_{mol}$, for temperature is as shown in Fig. 15[18,19].

The metallic layer is assumed to be composed of stainless steel. Therefore, emissivity of metallic layer, $\varepsilon_{met}$, is determined to be 0.43[17].

## 3. Boundary condition

### 3.1 Accident scenario

The significant event stage and the time frame for a core melting accident occurs due to large break LOCA and SI(safety injection) failure are presented in Table 3[20].

### 3.2 Boundary condition variable

Boundary condition variables - the levels of molten debris/metallic layer/external vessel water, the temperatures/pressures of molten debris, metallic layer, external vessel water and gas in core, and the decay heat of molten debris - change over time.

Therefore, the applicable boundary condition region and the magnitude of heat transfer coefficient also change according to time.

The levels of molten debris and metallic layer over time, $H_{mol}$ and $H_{met}$, are shown in Fig. 16[20]. The temperatures of molten debris and metallic layer over time, $T_{mol}$ and $T_{met}$, are shown in Fig. 17[20]. The temperature and the pressure of the gas in core versus time, $T_{gas}$ and $P_{gas}$, are shown in Fig. 18 and 19[20], respectively. The level, the temperature and the pressure of external vessel water versus time, $H_{wat}$, $T_{wat}$ and $P_{wat}$, are shown in Fig. 20, 21 and 22[20], respectively. The decay heat of molten debris for time, $Q$, is shown in Fig. 23[20]. The Air temperature outside of RPV, $T_{air}$, is supposed to be maintained at a constant 127℃.

### 3.3 Thermal boundary condition

In transient analysis, the thermal boundary condition of RPV is determined using the following assumptions:

- The heat transfer is assumed to be the one for a quasi-static state.
- The thermal conduction through debris crust and the gap between molten debris and the inner wall of RPV lower head are ignored.
- The temperature distributions of molten debris, metallic layer and external vessel water are uniform over time.
- The heat convection on the RPV inner wall by the metallic layer is assumed to be the one from molten debris. The heat transfer on the RPV inner wall during the period when molten debris and metallic layer exist in the solid state is assumed to be the heat convection from the molten debris.
- The water exists in RPV lower head until 6528sec after the accident but the heat convection is due to the gas in the core conservatively.
- The effect of insulation on the thermal behavior of RPV is not considered.
- The effect of cladding and gas in gap on the heat convection coefficients for the inner wall of RPV lower head are considered by using an equivalent film coefficient[21].

The initial and the thermal boundary conditions for RPV are shown in Fig. 24. The heat transfer mechanism change for time is presented in Table 4. In Table 5, the heat transfer coefficients on the RPV inner and outer walls are presented for the heat transfer except radiation. In Table 6, the radiation heat fluxes on the RPV inner wall are presented according to the magnitudes of RPV inner wall temperature $T_{RPV}$ and

$T_{met}$ during the transient state.

In steady state analysis, the thermal boundary condition of RPV is determined by using the assumptions that the lower head is fully submerged in cavity water prior to the deposition of molten debris on lower head and molten debris is located on lower head from the accident initiation time. The boundary condition variables are fixed over time in steady state analysis.

### 3.4 Mechanical boundary condition

The mechanical boundary condition for the RPV is determined by considering the dead weight effects of molten debris and external vessel water.

The mechanical boundary conditions for the RPV are shown in Fig. 25 where $z_1$ and $z_2$ are the depth from the metallic layer surface and water level, respectively. Unit for pressure is MPa.

## 4. Analysis and Results

### 4.1 Analysis method

The analysis method for temperature and stress analysis is shown in Fig. 26. As shown in Fig. 26, the analysis system consists of a database, an ABAQUS Input File[7] and an user subroutine program[7]. The database presents the material properties of molten debris with temperature. These material properties are presented in section 2.2.2. The ABAQUS Input File[7] assigns the finite element model and configuration, material properties of RPV, boundary conditions, analysis type and output data. The user subroutine program[7] assigns the boundary conditions associated with the time variation of boundary condition variables and links between the database and the ABAQUS Input File.

### 4.2 Finite element model

The finite element for an analysis model is shown in Fig. 27. The numbers of an element and a node are 157 and 5059, respectively. The element property is an 8-node quadratic axis-symmetric element[7]. The finite element model is simplified by the deletion of nozzles because the effects of nozzles on the integrity of RPV lower head are minor. The model is an axis-symmetric model due to the axis-symmetric boundary

conditions and model configuration.

### 4.3 Temperature analysis

Temperature analysis is performed considering molten debris quantity, ERVC condition and analysis method.

The conditions for temperature analysis are presented in Table 7.

The NLT(nondimensional ligament thickness) $\overline{w}$ at MTGP(maximum temperature generation part) versus time are shown for conditions ⓐ and ⓑ in Fig. 28. The NLT $\overline{w}$ means the nondimensional value calculated to divide ligament thickness $w_u$ by initial thickness $w_t$ at MTGP. As shown in Fig. 28, the value of NLT is zero and molten debris penetrates through the thickness of RPV lower head at $5.5 \times 10^3$sec for the case that ERVC is not applied and steady state analysis is performed. However, molten debris does not penetrate in the case that ERVC is applied and steady state analysis is performed.

In cases of condition ⓑ~ⓔ, the NLT $\overline{w}$ at MTGP are shown according to time in Fig. 29. As shown in Fig. 29, the effects of molten debris quantity on NLT at MTGP are minor in the case that ERVC is applied and steady state analysis is performed.

In cases of condition ⓔ and ⓕ, the NLT $\overline{w}$ at MTGP are shown according to time in Fig. 30. The time for transient analysis when the NLT is maintained with constant value is later than the one for steady state analysis. When this steady state is reached, the NLT by transient analysis is less than the one by steady state analysis.

The NLT $\overline{w}$ at MTGP versus time are shown for conditions ⓕ~ⓘ in Fig. 31. The effect of ERVC completion time on NLT is minor for the case that the one is less than 10000sec and the NLT decreases with the increase of one.

### 4.4. Stress analysis

Stress analysis is performed considering the following variables : molten debris quantity, ERVC condition, connection condition with RPV part and analysis method.

The conditions for stress analysis are presented in Table 8.

The hoop stresses at the internal points of MTGP versus time are shown for condition ② in Fig. 32. The hoop stress at MTGP increases with the radial coordinate

$r$ and the maximum value of hoop stress occurs on the outer wall surface of MTGP.

The hoop stresses at the outer wall of MTGP versus time are shown for conditions ②~⑤ in Fig. 33. The hoop stress at the outer wall of MTGP increases with molten debris quantity in the case where ERVC is applied and steady state analysis is performed.

The hoop stresses at the outer wall of MTGP versus time are shown for conditions ⑤ and ⑥ in Fig. 34. The hoop stress at the outer wall of MTGP has almost a constant value irrespective of the connection condition with RPV upper part.

The hoop stresses at the outer wall of MTGP versus time are shown for conditions ⑤ and ⑦ in Fig. 35. The hoop stress at the outer wall of MTGP caused by the transient analysis is smaller than the one by the steady state analysis.

The hoop stresses at the outer wall of MTGP versus time are shown for conditions ⑦~⑩ in Fig. 36. The hoop stress at the outer wall of MTGP versus time decreases with an increase in ERVC completion times.

### 4.5 Damage and integrity evaluation

The conditions for damage evaluation are equal to the ones for stress analysis.

Damage factors are calculated by using the temperature and von-Mises effective stress distributions of RPV, and the Larson-Miller parameter and curve for SA508 Gr.2 Cl.1.

To calculate the cumulative damage factor $D$, the following life-fraction rule[8] is used:

$$D=\Sigma\frac{t_i}{t_{ri}}=1, \tag{1}$$

where $t_i$ is the duration time for specific condition $i$ and $t_{ri}$ is the rupture time for specific condition $i$. The satisfaction of equation (1) means rupture.

The failure times when the average value of the cumulative damage factors of all internal points in the maximum temperature generation part is equal to 1 are presented for various conditions in Table 9. From Table 9, the failure time decreases with an increase of molten debris quantity for the case where ERVC is applied and steady state analysis is performed. The failure time by steady state analysis is smaller than the one by transient analysis as shown in the comparison between the results of conditions ⑤

and ⑦. The failure time decreases with an increase of ERVC completion time.

## 5. Conclusions

The following conclusions are obtained from the structural integrity evaluation performed for RPV subjected to a core melting accident due to large break LOCA:

(1) Molten debris penetrates through the thickness of RPV lower head for the case where ERVC is not applied and steady state analysis is performed.

(2) The failure time decreases with the increase quantity of molten debris for the case where ERVC is applied and steady state analysis is performed.

(3) The failure time by steady state analysis is smaller than the one by transient analysis.

(4) The failure time decreases with an increase of ERVC completion time.

## References


(1) O. Kymaelaeinen, H. Tuomisto and T.G. Theofanous, In-vessel melt retention as a accident management strategy for the Loviisa nuclear power plant, in the 24th WRSM, Bethesda, Maryland, 1996.

(2) T.G. Theofanous et al., In-vessel coolability and retention of a core melt, DOE/ID-10460, Vol.1, U.S. Department of Energy, Idaho Operations Office, 1995.

(3) R.E. Henry et al., Cooling of core debris within the reactor vessel lower head, Nuclear Technology, Vol.101, 1992, pp.385-399.

(4) J.L. Rempe at al., Light water reactor lower head failure analysis, NUREG/CR-5642, EGG-2618, Idaho National Engineering Lab., EG&G Idaho, Inc., 1993.

(5) D. Azordi and P. Gruner, Numerical simulation of a BWR vessel lower head with penetration subjected to a postulated core damage accident, Transaction of the 14th International Conference on Structure Mechanics in Reactor Technology, Lyon, France, 1997, pp.443-450.

(6) ASME boiler and pressure vessel code, Section III, Division 1, Appendices, 1995.

(7) ABAQUS user's manual, Ver.5.6, HKS Inc., 1996.

(8) R. Viswanathan, Damage mechanisms and life assessment of high-temperature components, ASM International, 1989.

(9) ASME boiler and pressure vessel code, Section II, Part A-Ferrous, 1995.

(10) ASME boiler and pressure vessel code, Section II, Part B-Nonferrous, 1995.

(11) A.A. Howe, Estimation of liquidus temperatures for steels, Ironmaking and Steelmaking, Vol.15, No.3, 1988, pp.134-142.

(12) O. Kubachewski, Iron binary phase diagrams, Berlin Springer Verlag, 1982.

(13) A. Jablonka, K. Harste and K. Schwerdtfeger, Thermomechanical properties of iron and iron-carbon alloys: density and thermal contraction, Steel Research, Vol.62, No.1, 1991, pp.24-33.

(14) B.G. Thomas, I.V. Samarasekera and J.K. Brimacombe, Mathematical model of the thermal processing of steel ingots: part 1. heat flow model, Metallurgical Transaction B, Vol.18B, 1987, pp.119-130.

(15) A. Grill, J.K. Brimacombe and F. Weinberg, Mathematical analysis of stresses in continuous casting of steel, Ironmaking and Steelmaking, No.l, 1976, pp.38-47.

(16) G.L. Thinnes, G.E. Korth, S.A. Chavez and T.J. Walker, High-temperature creep and tensile data for pressure vessel steels SA533B1 and SA508-Cl2, Nuclear Engineering and Design, Vol.148, 1994, pp.343-350.

(17) T.G. Theofanous, G. Wang and X. Chen, The emissivity of the steel layer, T.G. Theofanous et al., In-Vessel Coolability and Retention of a Core Melt, DOE/ ID-10460, Vol.1, 1995, I-3-8.

(18) J.K. Hohorst et al., SCDAP/RELAP5/MOD2 code manual, volume 4: MATRO-a library of materials properties for light-water-reactor accident analysis, NUREG/ CR-5273, EGG-2555, Vol.4, R3, EG& G Idaho, Inc., 1990.

(19) C.C. Chu et al. Uncertainty analysis for thermophysical properties used in in-vessel retention analyses, T.G. Theofanous et al., In-Vessel Coolability and Retention of a Core Melt, Appendix L, DOE/ID-10460, Vol.1, 1993, L.1-28.

(20) Korea Power Engineering Company, Inc., Severe accident evaluation report, 1996.

(21) J.P. Holman, Heat transfer, Fourth edition, Tower Press, 1976.

(22) R.J. Witt, Local creep rupture failure modes on a corium-loaded lower head, Nuclear Engineering and Design, Vol.148, 1994, pp.385-411.

(23) M. Jahn and A.A. Emara, High Rayleigh number convection in enclosed fluid layers with internal heat sources, U.S. NRC, NUREG-75/065, 1975.

(24) M. Jahn and H.H. Reineke, Free convection heat transfer with internal heat sources: calculations and measurements," Proc. 5th Int. Heat Transfer Conf., Tokyo, Vol.3, NC-2.8, 1974.

(25) M.N. Ozisik, Heat transfer: a basic approach, McGraw-Hill, Inc., 1985.

Table 1. Chemical composition of SA508 Gr.2 Cl.1[9].

| Composition | C | Mn | Si | Ni | Cr | Mo | V | P | S |
|---|---|---|---|---|---|---|---|---|---|
| weight% | 0.27 max | 0.5 - 1.0 | 0.15 - 0.4 | 0.5 - 1.0 | 0.25 - 0.45 | 0.55 - 0.7 | 0.05 | 0.025 max | 0.025 max |

Table 2. Chemical composition of SB166[10].

| Composition | Ni | Cr | Fe | Mn | C | Cu | Si | S |
|---|---|---|---|---|---|---|---|---|
| weight% | 72.0 min | 14.0 - 17.0 | 6.0 - 10.0 | 1.0 max | 0.15 max | 0.5 max | 0.5 max | 0.015 max |

Table 3. Significant event and time of core melting accident due to LB LOCA[20].

| Event | Time(second) |
|---|---|
| Large LOCA initiation | 0 |
| Reactor scram | 9 |
| Main feed water off | 9 |
| Pressurizer empty | 14 |
| Pressurizer surge line nozzle uncovered | 88 |
| Core uncovery begins | 145 |
| SIT injection begins | 178 |
| CFS valve open | 1800 |
| Max. core temperature exceeds 2,499K | 2840 |
| ERVC complete | 3750 |
| Core support plate failed(relocation of molten debris and metallic layer on lower head begins) | 4000 |
| Core uncovery complete | 4091 |
| Water dryout in lower head | 6528 |

Table 4. Heat transfer mechanism change according to time.

| Transient state | Completion time(sec) | Convection fluid on RPV inner wall | Convection fluid on RPV outer wall | Radiation object on RPV inner wall |
|---|---|---|---|---|
| State 1 | 4000 | Gas in core | Water or air | - |
| State 2 | 6528 | U : gas in core | Water or air | - |
| State 3 | 72000 | B : m.d.<br>U : gas in core | Water or air | m.l. or gas in core |

※Note) B : bottom U : upper m.l. : metallic layer m.d. : molten debris

Table 5. Heat convection coefficients applied for various parts of RPV wall.(unit : W/m$^2$℃)

| Part | Contact wall | Contact object | Value or equation |
|---|---|---|---|
| Lower head | Inner wall | Gas in core | $h_{gas} = 100$ (22) |
| | | Molten debris | $h_{mol,eq}(\theta) = \dfrac{h_{mol}(\theta)}{1 + \dfrac{h_{mol}(\theta)\, t_{clad}}{k_{clad}}}$ (21)<br>$h_{mol}(\theta) = h_{mol}(b_1 \sin^2\theta + b_2)$ (23)<br>$b_1 = \dfrac{9.12(1-\cos\theta_p)}{8 - 9\cos\theta_p + \cos 3\theta_p}$, $b_2 = 0.24$<br>$\theta_p = \cos\left(\dfrac{R - H_{mol}}{R_{xy}}\right)$, $R_{xy} = \sqrt{x_{mol}^2 + (R - H_{mol})^2}$<br>$x_{mol}$ : *x − coord. of contact point between RPV inner wall and molten debris upper limit*<br>$h_{mol} = 0.54 Ra^{0.18}\left(\dfrac{H_{mol} + H_{met}}{R}\right)^{0.26}$ (24), $R = 2371.725mm$<br>$Ra = \dfrac{g\beta_{mol} q\, \rho_{mol}^2 c_{p,mol} R^5}{\mu_{mol}\, k_{mol}^2}$, $g = 9800 mm/\sec^2$<br>$q = \dfrac{Q}{V_{mol}}$, $V_{mol}$ : *volume of molten debris* |
| | Outer wall | Air | $h_{air} = 100$ (22) |
| | | Water | $h_{wat} = 300$ (25)* |
| Cylinder | Inner wall | Gas in core | $h_{gas} = 100$ (22) |
| | Outer wall | Air | $h_{air} = 100$ (22) |
| | | Water | $h_{wat} = 300$ (25)* |

* : the boiling convection coefficient of water on Leidenfrost point under 1atm.

Table 6. Radiation heat flux for transient state and various temperature conditions.(unit : W/m$^2$)

| Condition \ Transient state | | State 3 |
|---|---|---|
| $T_{RPV} < T_{met}$ | $T_{RPV} < T_{gas}$ | $q_{rad,met-R} = \sigma\varepsilon_{met}(T_{RPV}^4 - T_{met}^4)$ |
| | $T_{RPV} > T_{gas}$ | $q_{rad,met-R} = \sigma\varepsilon_{met}(T_{RPV}^4 - T_{met}^4)$<br>$q_{rad,R-gas} = \sigma\varepsilon_{RPV}(T_{RPV}^4 - T_{gas}^4)$ |
| $T_{RPV} > T_{met}$ | $T_{RPV} < T_{gas}$ | $q_{rad,R-met} = \sigma\varepsilon_{RPV}(T_{RPV}^4 - T_{met}^4)$ |
| | $T_{RPV} > T_{gas}$ | $q_{rad,R-met} = \sigma\varepsilon_{RPV}(T_{RPV}^4 - T_{met}^4)$<br>$q_{rad,R-gas} = \sigma\varepsilon_{RPV}(T_{RPV}^4 - T_{gas}^4)$ |

※Note) $\sigma$ : Stefan-Boltzmann constant(=5.669x10$^{-8}$ W/m$^2$℃$^4$)
$T_{RPV}$, $T_{met}$, $T_{gas}$ : Absolute temperatures(K)
$R-met$ : Heat flux from RPV inner wall to m.l.
$met-R$ : Heat flux from m.l. to RPV inner wall
$R-gas$ : Heat flux from RPV inner wall to gas

Table 7. Conditions for temperature analysis.

| Condition mark | ERVC | Molten debris quantity( $\theta_p$) | Analysis method | ERVC completion time(sec) |
|---|---|---|---|---|
| ⓐ | × | 22.5 ° | Steady | - |
| ⓑ | ○ | 22.5 ° | Steady | - |
| ⓒ | ○ | 45 ° | Steady | - |
| ⓓ | ○ | 67.5 ° | Steady | - |
| ⓔ | ○ | 90 ° | Steady | - |
| ⓕ | ○ | - | Transient | 3750 |
| ⓖ | ○ | - | Transient | 7000 |
| ⓗ | ○ | - | Transient | 10000 |
| ⓘ | ○ | - | Transient | 15000 |

Table 8. Conditions for stress and damage analysis.

| Condition mark | ERVC | Molten debris quantity( $\theta_p$) | Analysis method | ERVC completion time(sec) | Connection condition |
|---|---|---|---|---|---|
| ① | × | 22.5 ° | Steady | - | Roller |
| ② | ○ | 22.5 ° | Steady | - | Roller |
| ③ | ○ | 45 ° | Steady | - | Roller |
| ④ | ○ | 67.5 ° | Steady | - | Roller |
| ⑤ | ○ | 90 ° | Steady | - | Roller |
| ⑥ | ○ | 90 ° | Steady | - | Clamped |
| ⑦ | ○ | - | Transient | 3750* | Roller |
| ⑧ | ○ | - | Transient | 7000* | Roller |
| ⑨ | ○ | - | Transient | 10000* | Roller |
| ⑩ | ○ | - | Transient | 15000* | Roller |

* : The ERVC initiation time is 1800sec.

Table 9. The penetration and the failure times for each condition.(unit : $x10^3$ sec)

| Condition | ① | ② | ③ | ④ | ⑤ | ⑥ | ⑦ | ⑧ | ⑨ | ⑩ |
|---|---|---|---|---|---|---|---|---|---|---|
| Penetration time | 5.5 | - | - | - | - | - | - | - | - | - |
| Failure time | - | 74.490 | 59.047 | 42.326 | 21.574 | 21.574 | 37.159 | 34.024 | 31.697 | 23.791 |

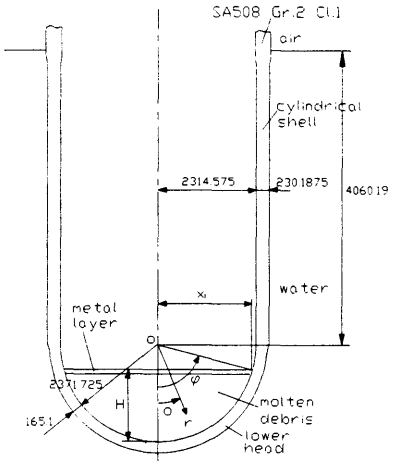


Fig. 1. RPV configuration and composition.

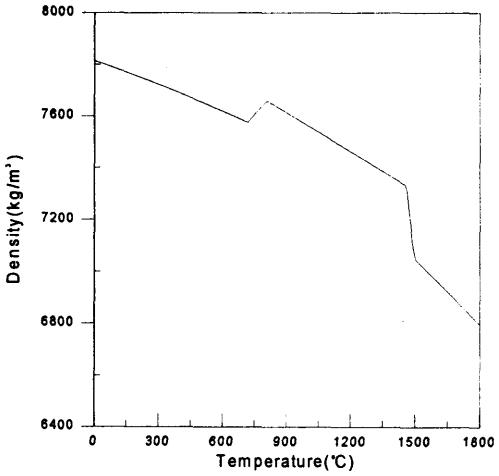


Fig. 2. Density vs. temp.

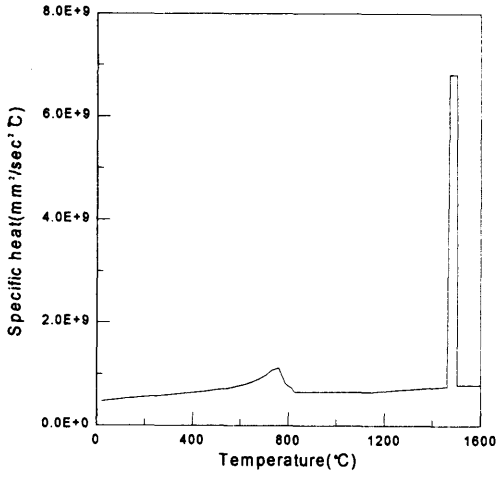


Fig. 3. Specific heat of SA508 vs. temp.

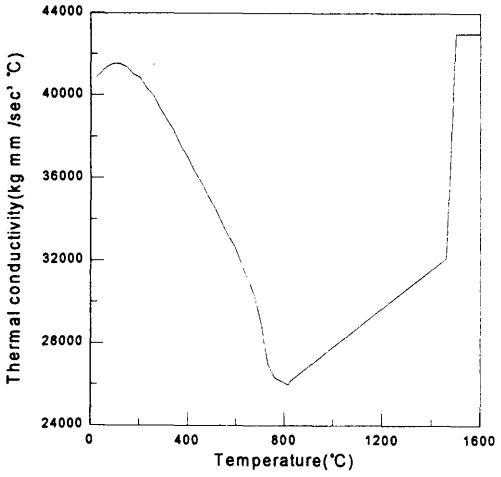


Fig.4. Thermal conductivity of SA508 vs. temp.

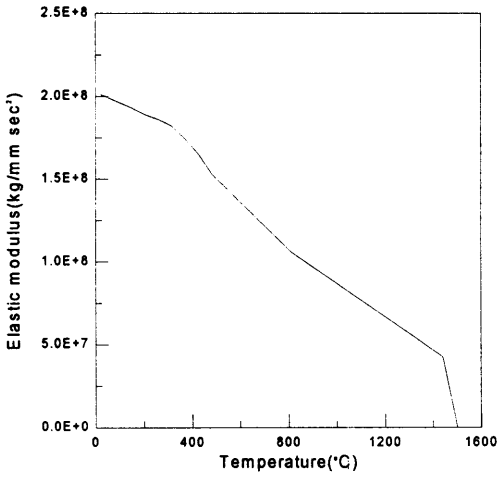


Fig. 5. Elastic modulus of SA508 vs. temp.

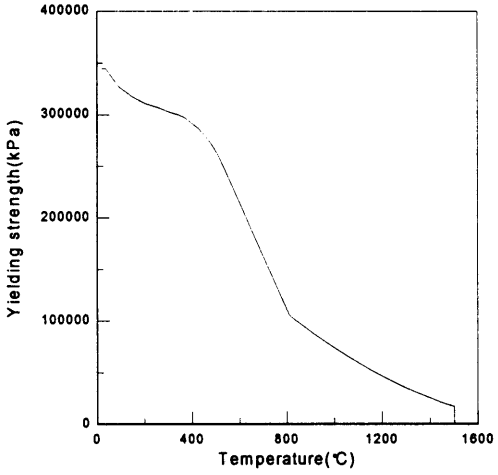


Fig. 6. Yielding strength of SA508 vs. temp.

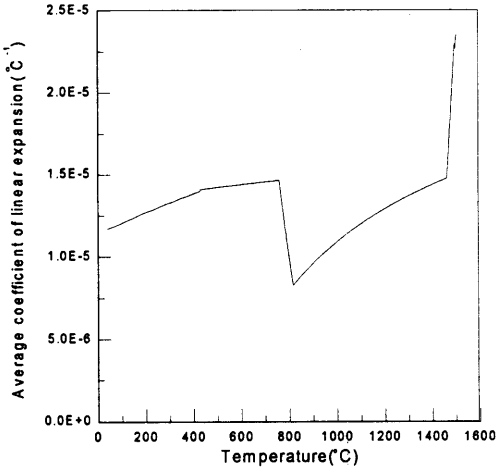


Fig. 7. Average linear thermal expansion of of SA508 coefficient vs. temp.

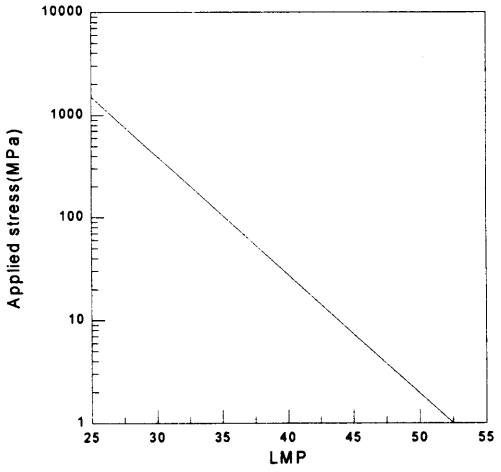


Fig. 8. Larson-Miller curve for SA508 Gr.2 Cl.1.

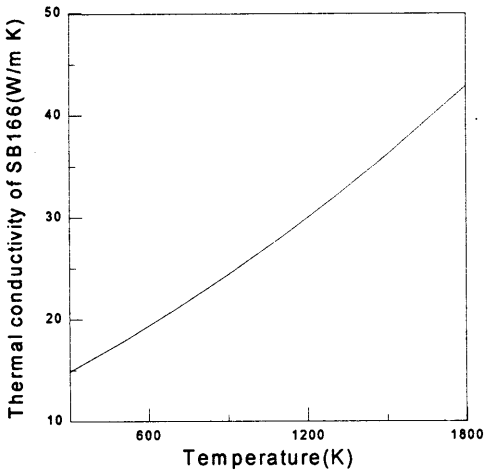


Fig. 9. Thermal conductivity of SB166 vs. temp.

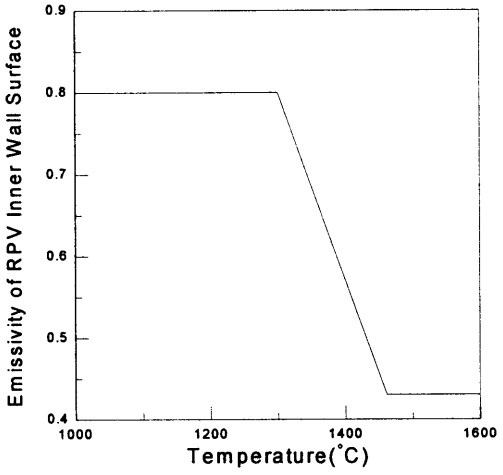


Fig. 10. Emissivity of RPV inner wall vs. temp.

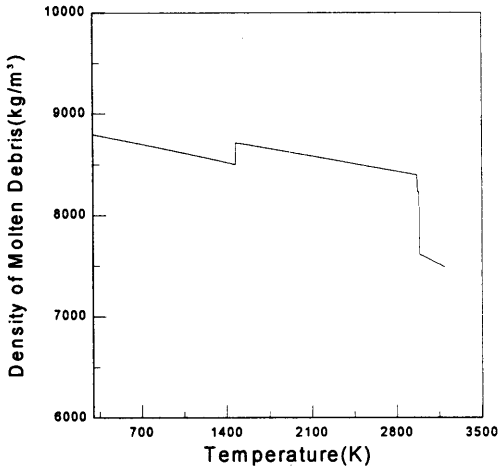


Fig. 11. Density of molten debris vs. temp.

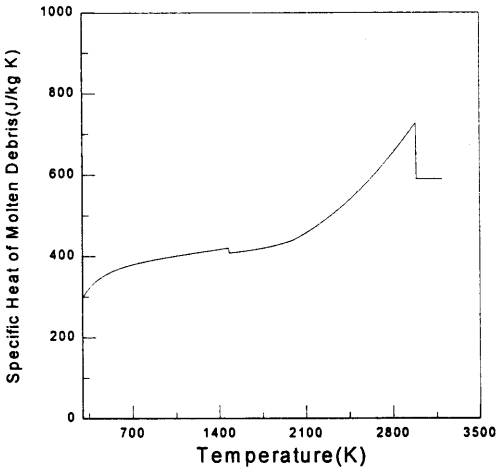


Fig. 12. Specific heat of molten debris vs. temp.

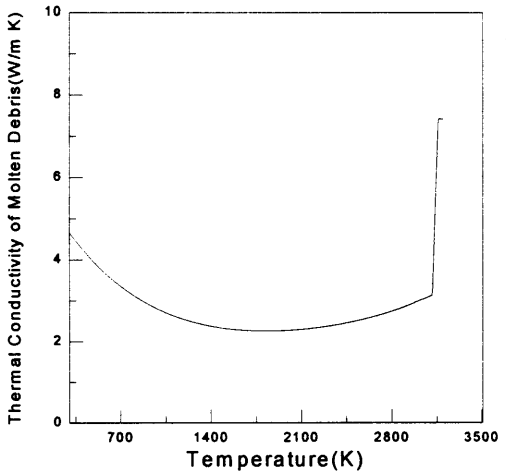


Fig. 13. Thermal conductivity of molten debris vs. temp.

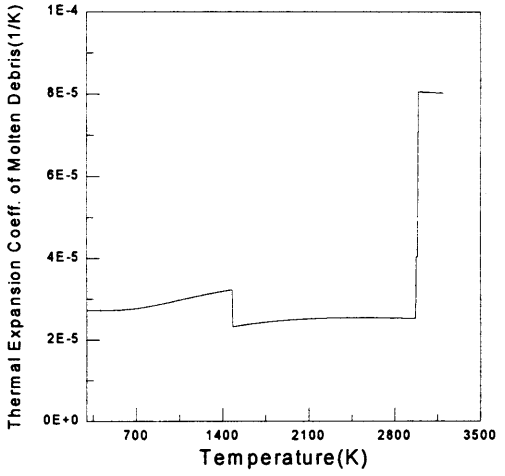


Fig. 14. Volumetric expansion coefficient of molten debris vs. temp.

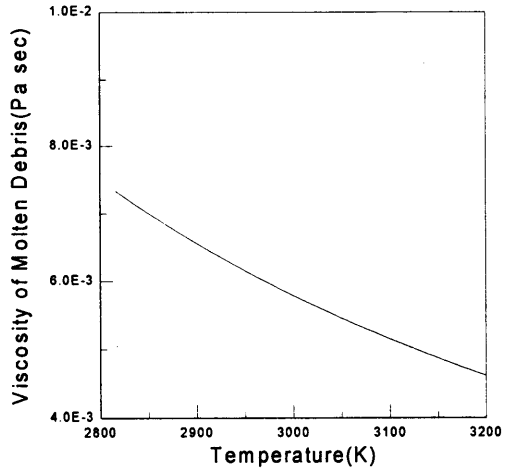


Fig. 15. Viscosity of molten debris vs. temp.

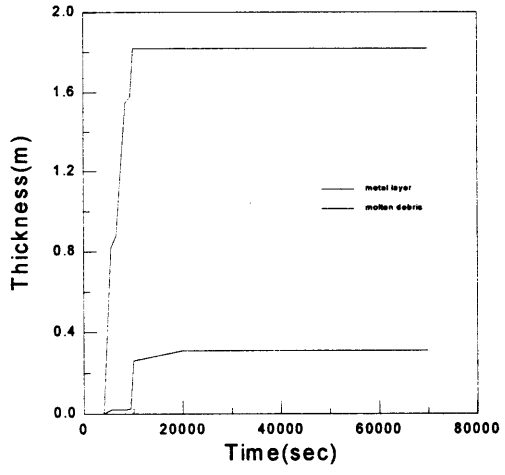


Fig. 16. The levels of molten debris and metallic layer vs time.

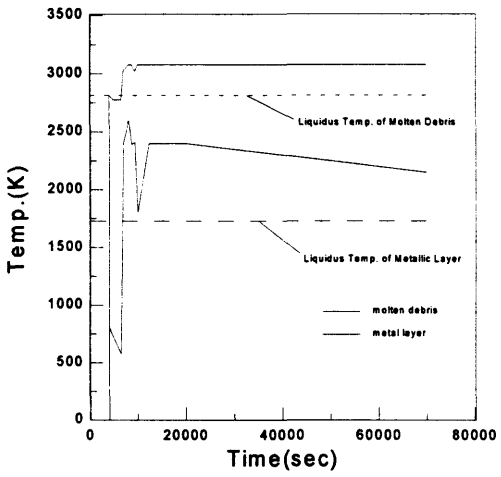


Fig. 17. The temperatures of molten debris and metallic layer vs time.

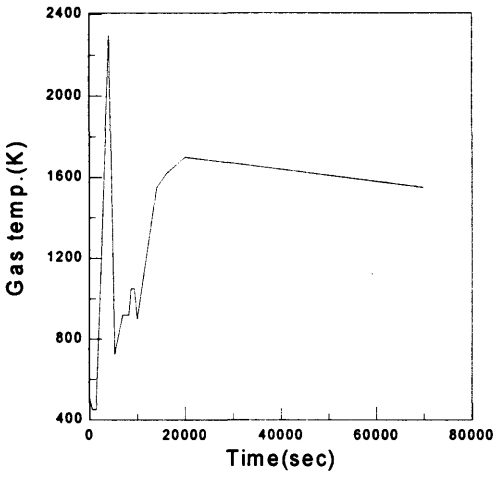


Fig. 18. The temperature of gas in core vs. time.

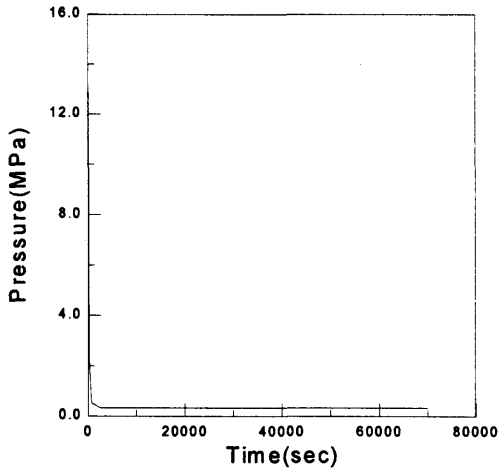


Fig. 19. The pressure of gas in core vs. time.

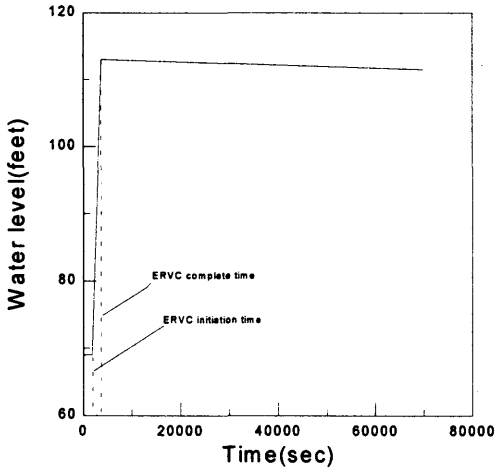


Fig. 20. Water level vs. time.

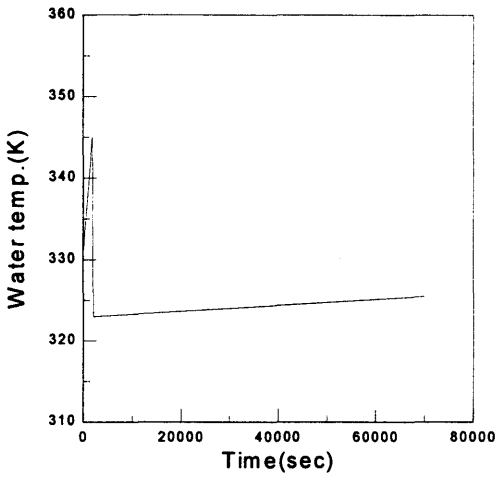


Fig. 21. Water temperature vs time.

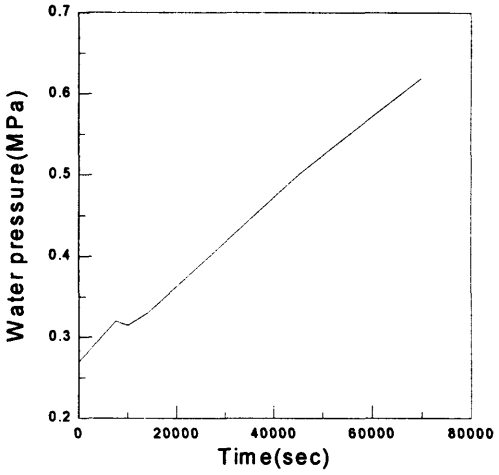


Fig. 22. Water pressure vs time.

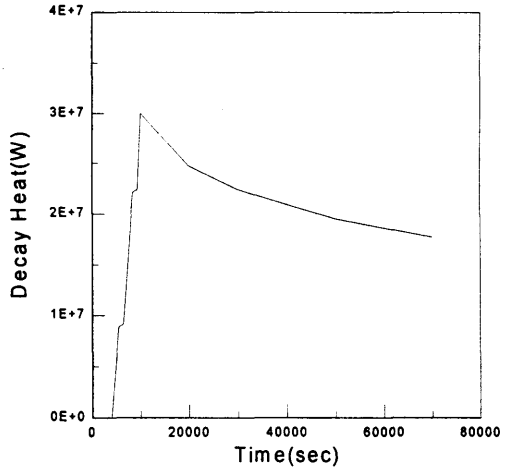


Fig. 23. The decay heat of molten debris vs. time.

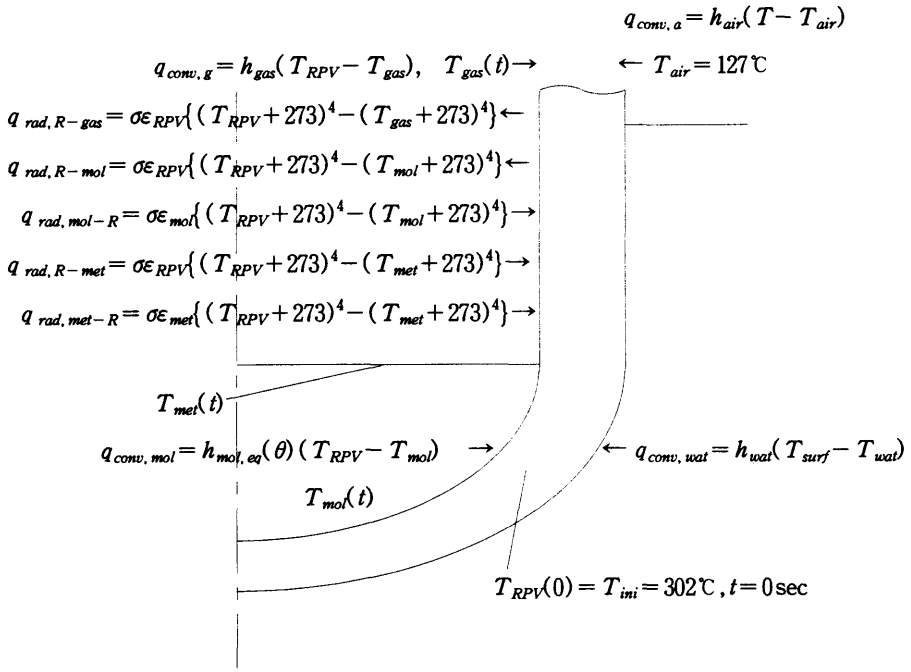


Fig. 24. Thermal B.C. and I.C. for RPV.

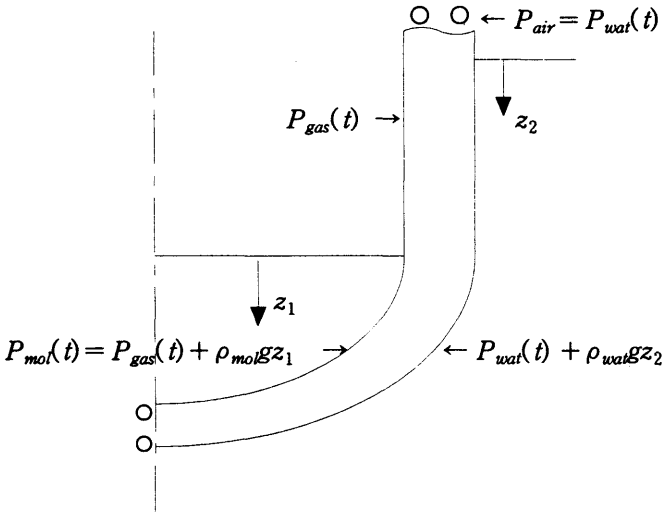


Fig. 25. Mechanical B.C. for RPV.

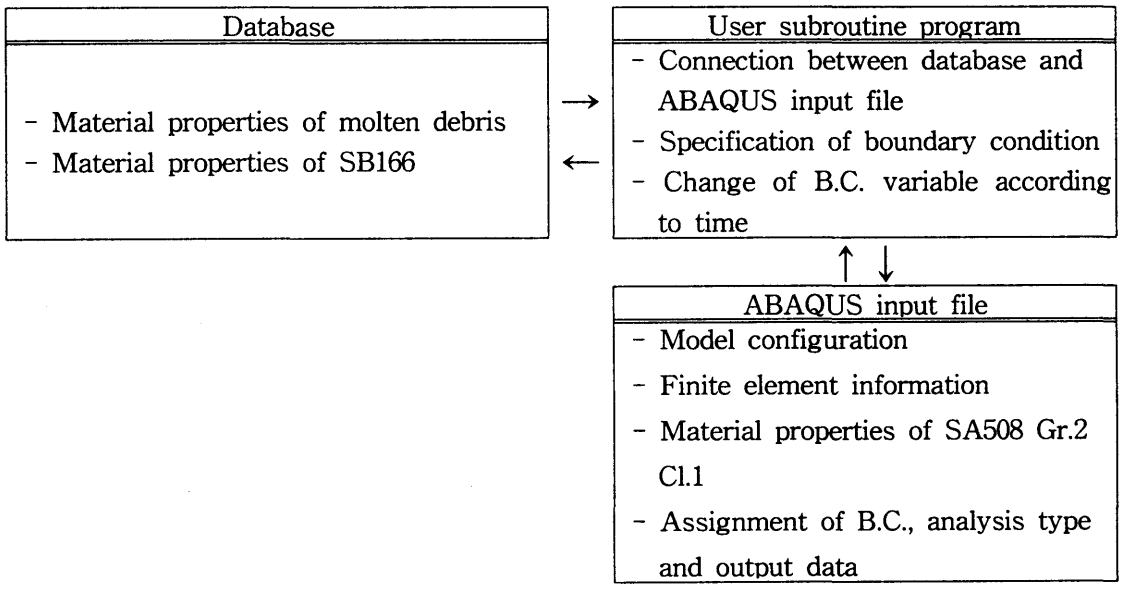


Fig. 26. Analysis mechanism.

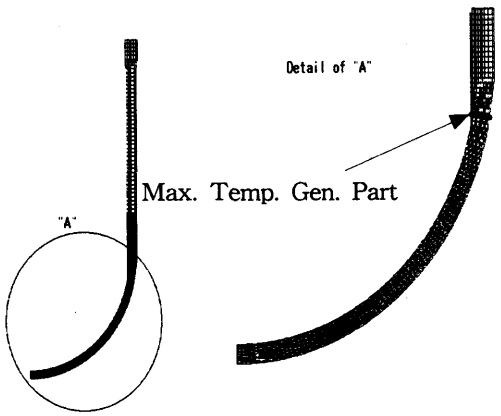


Fig. 27. Finite element model.

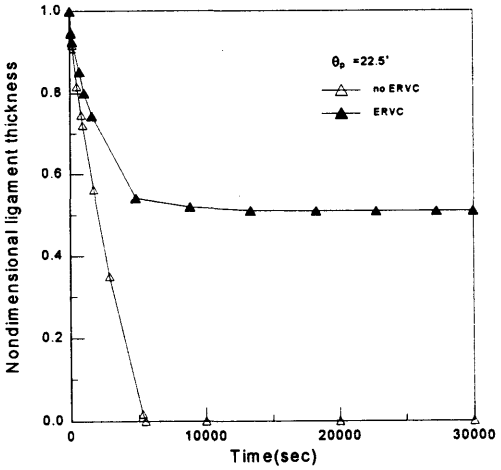


Fig. 28. Nondimensional ligament thickness of maximum temperature generation part vs. time for condition ⓐ and ⓑ.

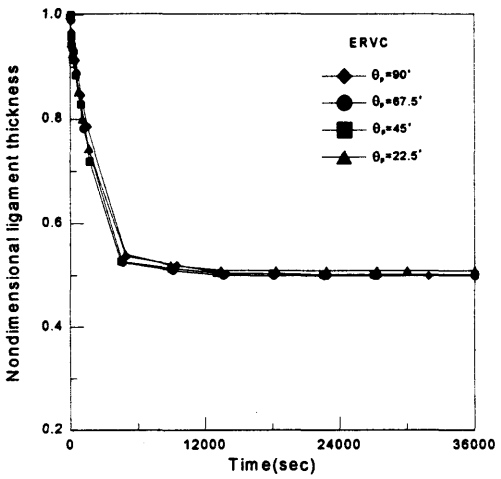


Fig. 29. Nondimensional ligament thickness of maximum temperature generation part vs. time for condition ⓑ~ⓔ.

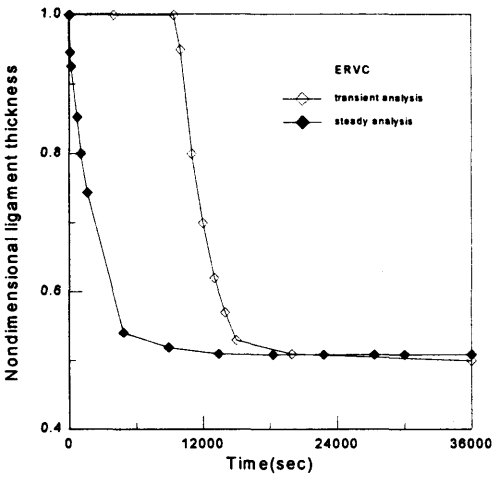


Fig. 30. Nondimensional ligament thickness of maximum temperature generation part vs. time for condition ⓔ and ⓕ.

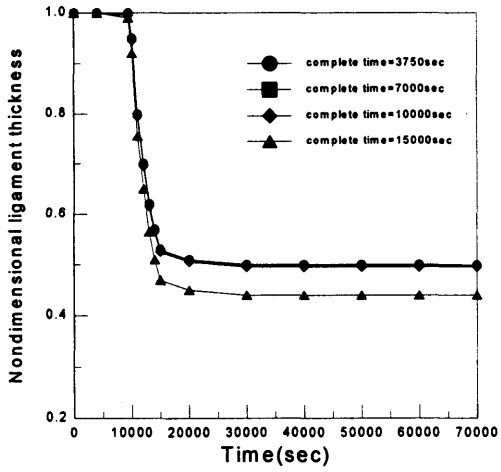


Fig. 31. Nondimensional ligament thickness of maximum temperature generation part vs. time for various ERVC completion times.

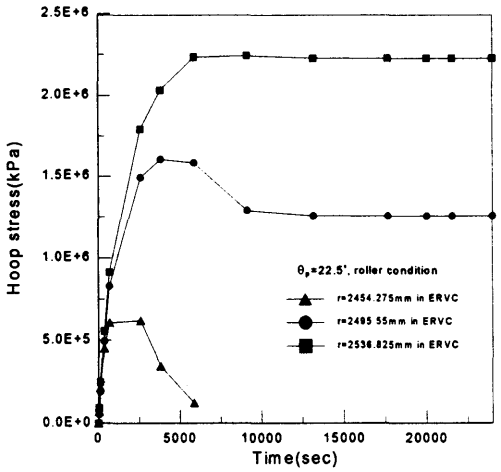


Fig. 32. Hoop stresses at internal points of maximum temperature generation part vs. time for condition ②.

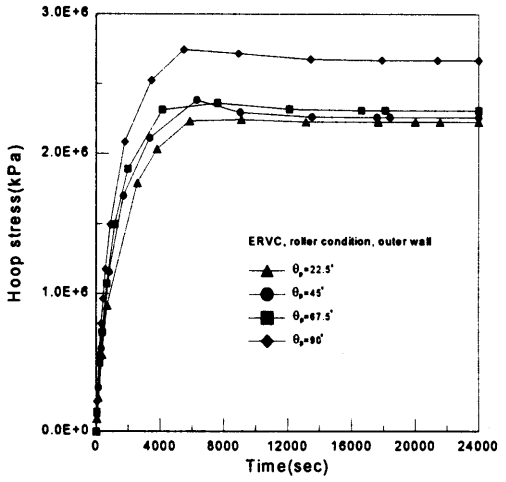


Fig. 33. Hoop stress at outer wall of maximum temperature generation part vs. time for condition ②~⑤.

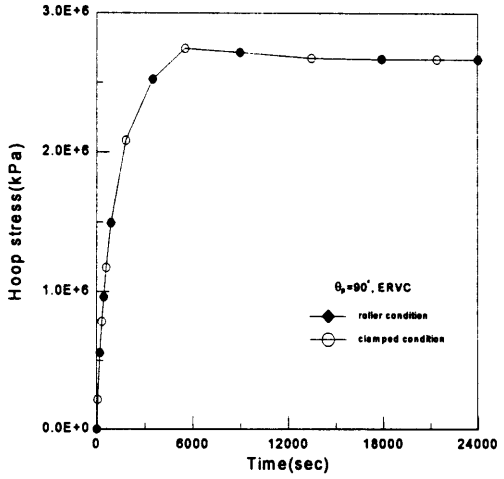


Fig. 34. Hoop stress at outer wall of maximum temperature generation part vs. time for condition ⑤ and ⑥.

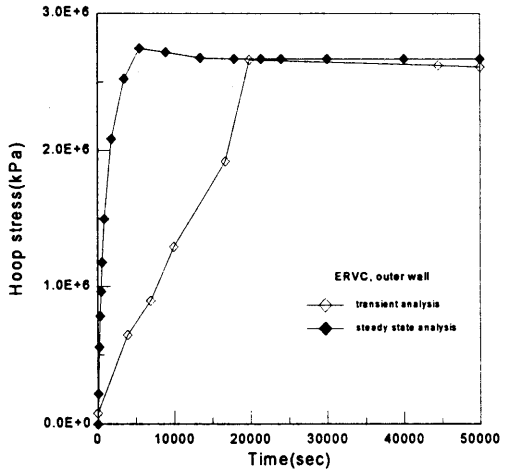


Fig. 35. Hoop stress at outer wall of maximum temperature generation part vs. time for condition ⑤ and ⑦.

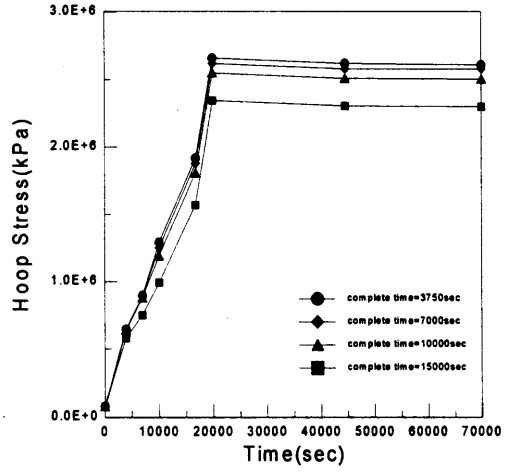


Fig. 36. Hoop stress at outer wall of maximum temperature generation part vs. time for various ERVC completion times.

# Session III

# Plant Experiences

III-1 The Evaluation of IGSCC Problems of Stainless Steel Piping in Taiwan BWR-6 Nuclear Power Plant

Kuen Ting, Department of Nuclear Regulation Atomic Energy Council,Taiwan, Republic of China

# The Evaluation of IGSCC Problems of Stainless Steel Piping in Taiwan BWR-6 Nuclear Power Plant

Kuen Ting

Department of Nuclear Regulation
Atomic Energy Council
Republic of China

## ABSTRACT

Taiwan BWR-6 Kuosheng Nuclear Power Plant Unit 1 implemented the inspection of the IGSCC-susceptible weldments of stainless steel piping in the reactor recirculation, reactor water clean-up, residual heat removal, core spray and feedwater systems. The purpose of this paper is to present the status of the fracture problems in the weldments. The crack growth analysis due to IGSCC and the standard weld overlay design based on the ASME Code Section XI and NUREG-0313 Rev. 2 for the fracture weldments are discussed in detail. Then, the contingent programs including the inspection program, fracture evaluation, the standard weld overlay are completely established to prevent the pipe break during the reactor operation.

## INTRODUCTION

The objective of this paper is to present the intergranular stress corrosion cracking (IGSCC) status of the primary coolant system at BWR-6 Nuclear Power Station (NPS) unit 1 in Taiwan. This work was achieved by identifying all the IGSCC-susceptible systems and the associated weldments. Following the procedures of inspection, evaluation and repair are based on the requirements of the United States Nuclear Regulatory Commission (USNRC) Report NUREG-0313, Rev. 2[1] and Generic Letter 88-01[2].

An inspections have been performed on the various IGSCC-susceptible weldments at BWR-6 NPS unit 1 in Taiwan since 1983. The inspections, since 1987 (EOC-4), have been performed to the requirements of NUREG-0313, Rev.2. The total of 184 weldments which are contained in reactor recirculation, reactor water clean-up, residual heat removal, core spray and feedwater systems are categorized as five groups. However, the inspection frequencies for the various weldment categories were more than the NUREG-0313 requirements during the past 10 years of operation in Taiwan. When a flawed weld is identified during inservice inspection, the flaw evaluation may be performed to meet the requirements of ASME Code Section XI in lieu of repair to justify continued operation for a specified evaluation period. This evaluation is based on the linear elastic fracture mechanics to calculate the IGSCC growth. If the crack growth exceeds the allowable critical length and depth, identified IGSCC in stainless steel may be used standard weld overlay for long-term repair. The design of the standard weld overlay is based on the net section collapse concept. Significant field, and experimental evidence has been assembled to meet ASME Code Case 504-1 [3] for the long term repairs of weld

overlays. The effects of weld overlay on the sustained stress, global mass and global stiffness were also evaluated after each outage repair based on the Generic Letter 88-01 with Supplement 1[4].

During the past 10 years of the operation of Taiwan BWR-6 Unit 1, total of 24 weldments at the recirculation and RHR systems implemented the standard weld overlays. A complete procedures consisting of in-service inspection, flaw evaluation, standard weld overlay and quality control for the IGSCC-susceptible weldments were established in Taiwan. The inspection for these overlayed weldments is continuously conducted during each refueling outage. Due to the long-term inspection, the prevention of the pipe fracture due to IGSCC during the operation can be achieved to maintain the nuclear safety.

## INSPECTION PROGRAM OF IGSCC-SUSCEPTIBLE WELDMENTS

Five systems considered IGSCC-susceptible weldments in in-service inspection program during each refueling outage. These systems are:

1. Reactor Recirculation (RR)
2. Reactor Water Clean-up (RWCU)
3. Residual Heat Removal (RHR)
4. Core Spray (CS)
5. Feedwater (FW)

A total of 184 IGSCC-susceptible weldments were identified for these systems. Figure 1 and 2 present the susceptible weldments on the recirculation, RHR suction and RWCU systems. Other than the nozzle and thermal sleeve welds (KB, KC and TSW welds) all welds comprise of either Type 304 or 316 stainless steel weldments. Some of the weldments in these systems have been solution heat treated. Details of the materials of the N1 (recirculation outlet) and N2 (recirculation inlet) nozzles and safe-end weldments are provided in Figure 3 and 4. The N2 safe-end has a welded thermal sleeve which considered the crevice in this evaluation. Most of the piping of the RHR, core spray and feedwater systems are fabricated with carbon steel and are, therefore, not susceptible to IGSCC. In these systems only, the nozzle welds are considered susceptible since they were partly welded with Inconel 182 material. Details of the materials of the N4 nozzle (feedwater nozzle), N5 (core spray nozzle) and N6 (RHR nozzle) weldments are shown in Figure. 5-7.

Inspection of the various IGSCC-susceptible weldments at BWR-6 unit 1 has been performed since 1983. However, the inspections performed to meet EPRI/USNRC requirements for IGSCC detection and sizing started at 1987 (EOC-4). The inspection frequencies for these weldments were more than the requirements of NUREG-0313, Rev.2, as listed in Table 1.

## INSPECTION RESULTS

No indications were reported at Tawain BWR-6 unit 1 for the first five operating cycles (EOC-1 through EOC-5). However, 10 flawed welds were found during 1989 refueling outage (EOC-6). More than half of fracture welds located at the recirculation loop B (6 of 10). After the fracture analysis, AS-14, BS-J2 and N2G-J2 welds cannot operate during the next fuel cycle. Then, the standard weld overlay repairs (as shown in Figure 8) were applied to 9 welds except BS-J4.

There are ten inlet nozzle-to-safe end weldments between the RR system and Reactor Pressure Vessel. A thermal sleeve is welded to the inside of the safe end and each nozzle. These thermal sleeve-to-safe end weldments within the inservice inspection (ISI) program, are identified as N2A/B/C/D/E/F/G/H/J/K-TSW. During 1991 outage (EOC-7) cracks were detected in four of these weldments (N2A/D/G/H-TSW) and conducted weld overlay repairs. In 1992 outage (EOC-8), six cracks in weldmwnts N2E-TSW were discovered as shown in Figure 9, but a flawed pipe evaluation

determined that this weldment was suitable for continued operation without repair for at least one additional fuel cycle. These cracks in N2E-TSW were observed to grow (as list in Table 2) requiring a weld overlay repair in 1993 outage (EOC-9). Thus, licensee decided to conduct the weld overlay repair for the weldments N2B/C/E/F/J/K-TSW. Table 2 provides a summary of all discovered flawed weldments during each refueling outage and the disposition of these flaws. Recent the 12$^{th}$ refueling outage (1997), four welds N2A-J4, N2C-J4, AD-J5 and AS-J7 of Loop A were still found IGSCC and overlay repairs were conducted. Up to now, only one indication at BS-J4 of RHR system which was identified as the counterbore signal was continuously inspected. All the overlay welds were inspected during each outage. There is no indication to find again.

The stress improvement technique IHSI considered in NUREG-0313, Rev.2 has been applied to 75 welds in the recirculation and RHR system in 1984. Excluded 4 safe-end-to thermal sleeve welds with Inconel 600 creviced design, there were 16 welds with IHSI to discover IGSCC.

The inspection was conducted by the ultrasonic examination. The 1/2 V technique was used during the early stage of the in-service inspection. However, the weld surfaces often were concave due to the shrinkage and grinding. Thus the contact between the sensor and the surface was not fit well to reduce the possibility of the crack detection (see Figure 10(a)). The 1.5V technique as shown in Figure 10(b) was used to extend the inspection scope and increase the reliability of the crack detection.

## FLAW EVALUATION

When the cracks were discovered at the inspection weldments, the fracture evaluation based on the NUREG-0313 Rev. 2 and ASME Code Section XI must be performed to determine the repair works or not.

Flaw evaluations are generally performed using linear elastic fracture mechanics techniques. The applied internal pressure, dead weight, thermal expansion, weld overlay shrinkage and residual stresses were found in the stress reports. With these load combinations and a linear elastic fracture mechanics model for the flaw weldment, the crack tip stress intensity $K_I$ can be determined by the Buchalet-Bamford polynomial fit method[5]. Flaw growth can be determined using the upper bound weld sensitized crack growth data shown in NUREG-0313, Rev.2:

$$\frac{da}{dt} = 3.59 \times 10^{-8} K_I^{2.161}$$

where $da/dt$ denotes the crack growth rate, inches/hr.

The crack was conservatively assumed to have an initial depth $a_0$ equal to the maximum reported depth and the initial length $l_0$ equal to the sum of the individual lengths. Crack growth analysis was performed to determine the final crack depth $a_f$ after 18 months of operation (or 12000hours). The aspect ratio of the crack depth and length $a/l$ was assumed as the same during the crack growth. Then, the final crack length can be calculated as

$$l_f = \frac{a_f}{a_0} l_0$$

Then the allowable flaw size is determined using the criteria in ASME Section XI IWB-3640.

For the case of the inspection data of N2E-TSW as listed in Table 2, the input parameters were expressed as

$a_0 = 0.14"$, $l_0 = 8.1"$, $a_0 / l_0 = 57.85$

Using the crack growth analysis, the final crack depth $a_f$ reached 0.475" after the assumption of 12000 hours operation. Then the final crack length $l_f$ was 27.5". Corresponding to the parameters in IWB-3640, four parameters $l_0/\pi d$, $l_f/\pi d$, $a_0/t$ and $a_f/t$ were used to determine the allowable crack size as shown in Figure 11. The crack size can be tolerate to operate at the next fuel cycle without the repair. However, the significant growth of the fracture weldment was observed during the next refueling outage as displayed in Table 2. Using the fracture analysis, the life prediction of the cracks was only 2000 hours. Thus, the repair work must be necessary for the safe operation during the next fuel cycles.

Weld overlay induced shrinkage stresses were analyzed by ANSYS finite element computer program[6]. The actual weld overlay shrinkages measured after application of each weld overlay were equivalent as the thermal shrinkages at the nodes corresponding to repair welds. This approach is used to simulate the mechanical shrinkage observed in the field.

$$E\alpha\Delta T l = \delta$$

where $l$ is overlay length, $\delta$ is the as-built weld overlay shrinkage. $E$ is Young's modulus and $\alpha$ is thermal expansion coefficient. The equivalent temperature drop $\Delta T$ will input at the nodes corresponding to repair welds.

## WELD OVERLAY REPAIR

Presently, there are 24 welds with weld overlay repairs. All these welds are in the recirculation system. The overlays were designed as " standard" overlays meeting the requirements of ASME Section XI IWB-3640 for overlay sizing. This repair program is to define the managerial and administrative controls for the implementation of Weld Overlay Repairs during outage which are covered the document preparation and review, preparation work, implementation and final reports. The detailed work items are listed as shown in Figure 12. The scope of work addressed by the repair program shall meet the requirements of ASME Section XI and Code Case 504-1. In addition, the scope of work shall comply with the requirements of NUREG 0313 Rev. 2 and Generic Letter 88-01. All piping from the reactor pressure vessel to the first isolation valve was originally constructed in accordance with the ASME Section III identified in the piping system stress report. The design, welder, filler metal procurement, and welding repair shall be performed in accordance with ASME Section XI. Nondestructive examination and testing work shall be performed in accordance with ASME Section V and XI.

The standard overlay design considers the determinations of the thickness and the width. The net section collapse criterion is used to calculate the minimum thickness [7]. 360° circumferential through-wall-crack and safety factor 3 are assumed. The overlay thickness can be calculated by the iterations of the following equations.

$$\beta = \frac{\pi(1 - a/t - P_m/\sigma_f)}{2 - a/t}$$

$$P_b = \frac{2\sigma_f}{\pi}(2 - a/t)\sin\beta$$

where $\sigma_f$ is the material flow stress, $a$ is the crack depth which equals to pipe wall thickness and $t$ is the overlay thickness. An iteration scheme is performed using these equations until the minimum required weld overlay thickness is determined.

The width of the overlay must consider the following conditions:

(1). The width is at least $1.5\sqrt{Rt}$
(2). Inspectability
(3). Cover the crack extension
(4). To minimize possible damage to base material.

The effects of weld overlay on the sustained stress, global mass and global stiffness were also evaluated after each outage repair based on the Generic Letter 88-01 with Supplement 1.

## CONCLUSION

Reported fracture weldments information survey results show that IGSCC is probably the most common aging degradation mechanism for Taiwan BWR-6 austenitic stainless steels piping. The strategy for controlling or mitigating IGSCC is necessary to manage in the future.

Due to the in-sufficient of supply of the high quality Class 1 pipe components, the replacement of the fracture pipe is impractical in Taiwan. Therefore, the fracture analysis and the standard weld overlay repair are the important contingent plant during each refueling outage. These evaluation and the repair works can demonstrate that there is substantial margin for each of these cracked welds under conservative, bounding conditions to allow for continued operation for a minimum of one additional 18month operation cycle. A complete procedures including the inspection program, flaw evaluation, repair and quality control have been established in Taiwan to augment the safety of long-term nuclear operation.

## REFERENCE


1. United States Nuclear Regulatory Commission (USNRC) NUREG 0313, "Technical Report on Material Selection and Processing Guidelines for BWR Coolant Pressure Boundary Piping", Rev. 2, publishing January 1988.

2. United States Nuclear Regulatory Commission (USNRC) Generic Letter 88-01, Subject: NRC Position on IGSCC in BWR Austenitic Steel Piping, dated January 25, 1988, with Supplement 1, dated February 4, 1992.

3. Taiwan Power Company, "Generic Letter 88-01, Supplement 1 Weld Overlay Shrinkage Effect Assessment Report for Second Nuclear Power Station Unit 1993 Outage, ZTP046.0210, 1993.

4. American Society of Mechanical Engineers (ASME) Boiler and Pressure Vessel Code Section XI, "Rules for Inservice Inspection of Nuclear Power Plant Components", 1989 Edition.

5. Buchalet C.B. and Bamford W.H. , "Stress Intensity Factor Solution for Continuous Surface Flaws in Reactor Pressure Vessels", *Mechanics of Crack Growth*, ASTM STP 590, 1976.

6. Desalvo G. and Gormin, *User Information Manual and Theoretical Manual.* ANSYS Engineering System, 1991.

7. Smith E. ,"Theoretical Justification of the Association of a Critical Net-Section Stress with Fracture Initiation at a Crack Tip", *International Journal of Pressure Vessels and Piping*, Vol. 8, 1980, pp. 303-311.

Table 1 Summary of Inspection Schedules for Taiwan BWR Piping Weldments

| Description of Material | | Categ. | Recommend Inspection Schedule | | |
|---|---|---|---|---|---|
| | | | NUREG 0313 | Before 1988 | After 1988 |
| | Resistant Material | A | 25%<br>every 10 years | 100%<br>every 2 refueling cycles | 100%<br>every 10 years |
| Nonresistant Materials | SI within 2 years of operation | B | 50%<br>every 10 years | 100%<br>every 2 refueling cycles | 100%<br>every 2 refueling cycles |
| | SI after 2 years of operation | C | 100%<br>every 10 years | 100%<br>every 2 refueling cycles | 100%<br>every 2 refueling cycles |
| | No SI | D | 100%<br>every 2 refueling cycles | 100%<br>every 2 refueling cycles | 100%<br>every 2 refueling cycles |
| Cracked | Reinforced by weld overlay or Mitigated by SI | E | 100%<br>every 2 refueling cycles | 100%<br>every refueling cycles | 100%<br>every refueling cycles |
| | Inadequate or no repair | F | 100%<br>every refueling cycles | 100%<br>every refueling cycles | 100%<br>every refueling cycles |

Table 2 The Data of Cracks of N2E-TSW Weldment at Two Inspections

| Inspection Schedule | Crack No. | 1 | 2 | 3 | 4 | 5 | 6 | 7 | Analysis Used |
|---|---|---|---|---|---|---|---|---|---|
| 1992, 5 (EOC-8) | Length(in) | 0.7 | 1.7 | 1.7 | 0.3 | 1.5 | 1.6 | 0.6 | 8.1(sum) |
| | Depth(in) | 0.08 | 0.14 | 0.14 | 0.06 | 0.10 | 0.12 | 0.07 | 0.14(max) |
| 1993, 5 (EOC-9) | Length(in) | 0.8 | 2.8 | 2.4 | 0.3 | 1.5 | 1.8 | 1.6 | 11.2(sum) |
| | Depth(in) | 0.15 | 0.18 | 0.18 | 0.15 | 0.15 | 0.15 | 0.15 | 0.18(max) |

Table 3 IGSCC Flaw Records of Taiwan BWR-6 Piping Weldments

| Inspection Schedule | Fracture Weldments | | | | Treatments |
|---|---|---|---|---|---|
| | 10 " | | 20" | | |
| 1989,10(EOC-6) | 5 | N2D-J3,N2J-J4,N2F-J4, N2J-J2,N2G-J2 | 5 | BS-J2,BS-J4, AS-J2,AS-J4, BD-J5 | BS-J4 leave as-is, others were welded overlay |
| 1991, 2(EOC-7) | 4 | N2A/D/G/H-TSW | 1 | AD-J9 | All were welded overlay |
| 1992, 5(EOC-8) | 1 | N2E-TSW | 0 | - | Continuous operation in one fuel cycle |
| 1993, 5(EOC-9) | 0 | | 1 | | N2B/C/E/F/J/K-TSW were welded overlay |
| 1997, 5(EOC-12) | 2 | N2A-J4,N2C-J4 | 2 | AD-J5,AS-J7 | All welds were overlay |

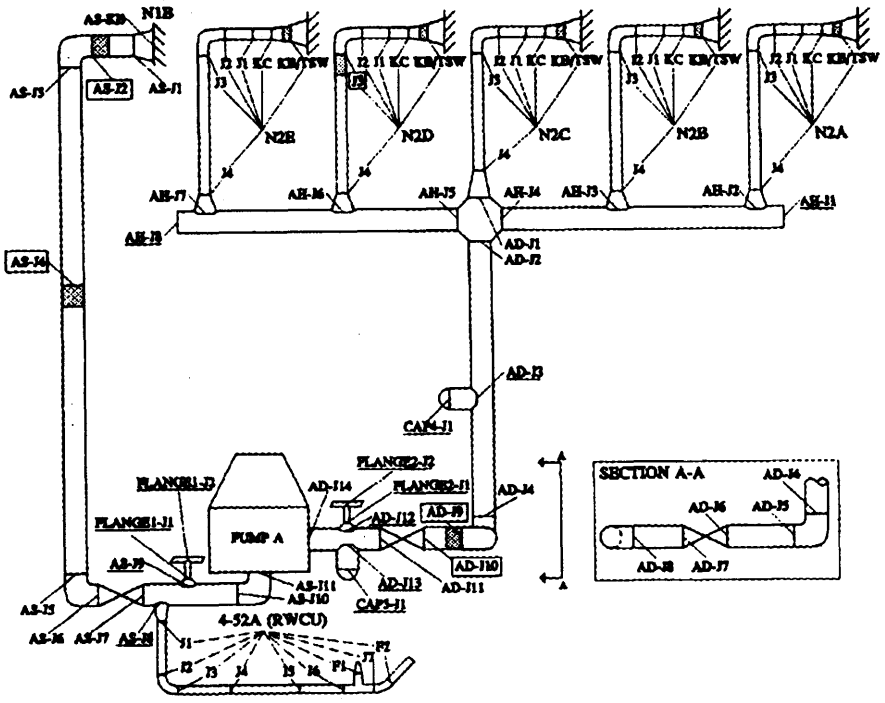


Figure. 1 Loop A welds[3]

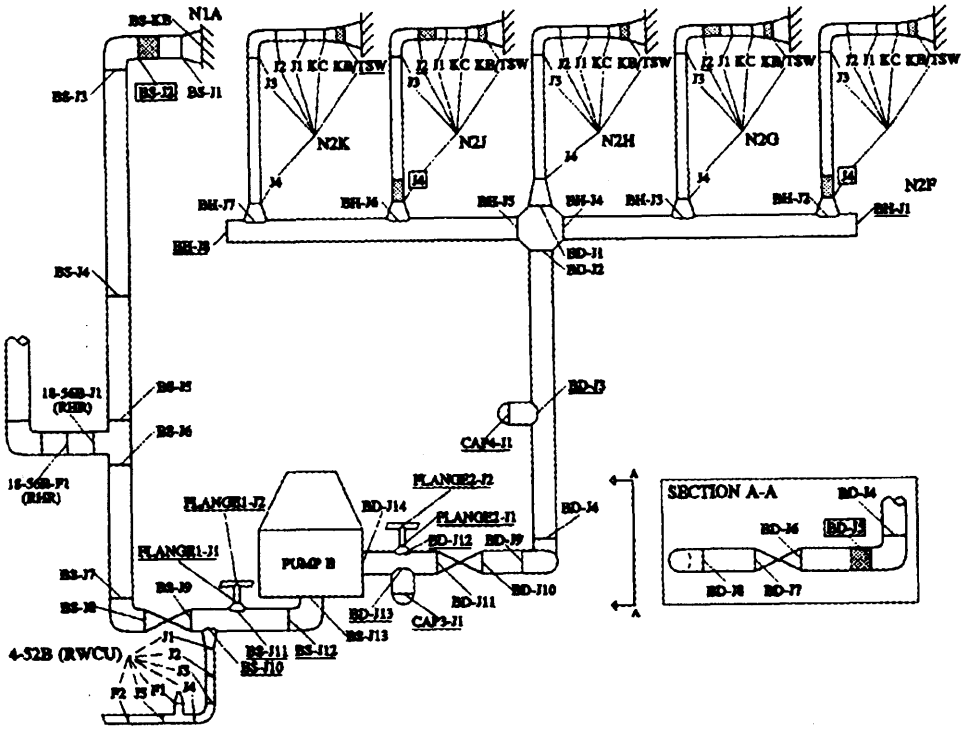


Figure 2 weldments in Loop B

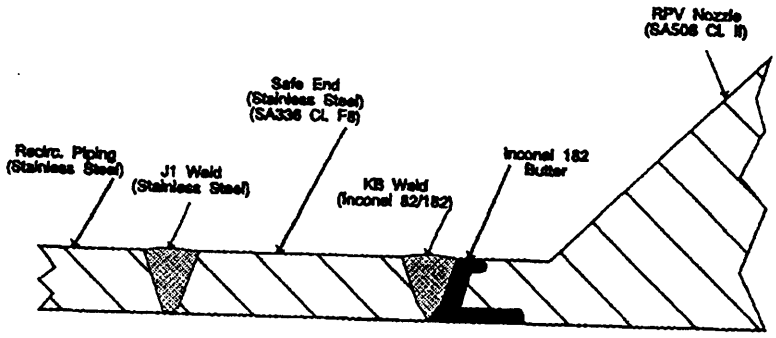


Figure 3. N1 Nozzle and Safe-end Weldments

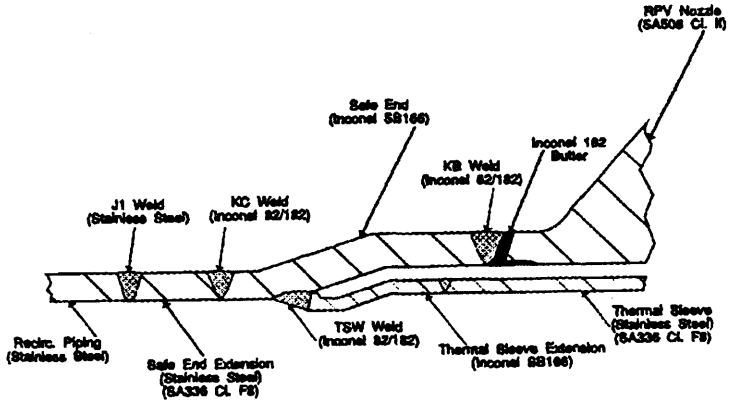


Figure 4. N2 Nozzle and Safe-end Weldments

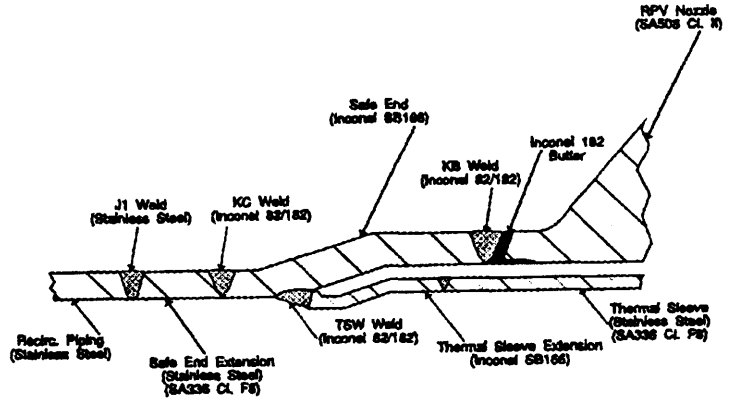


Figure 5 N4 Nozzle Weldments

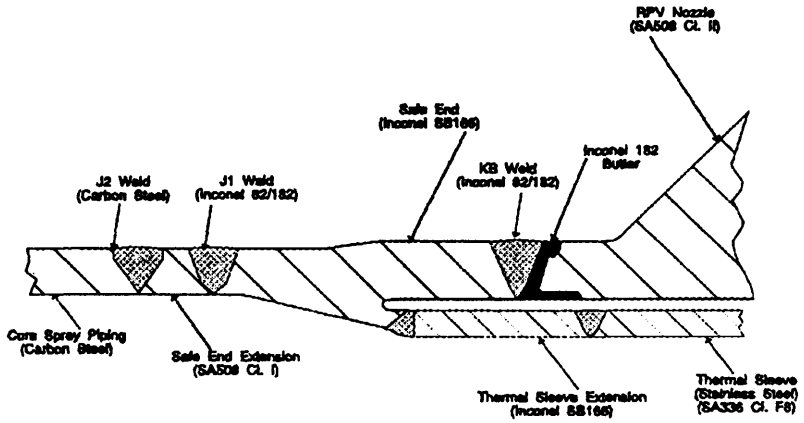


Figure 6. N5 Nozzle Weldments

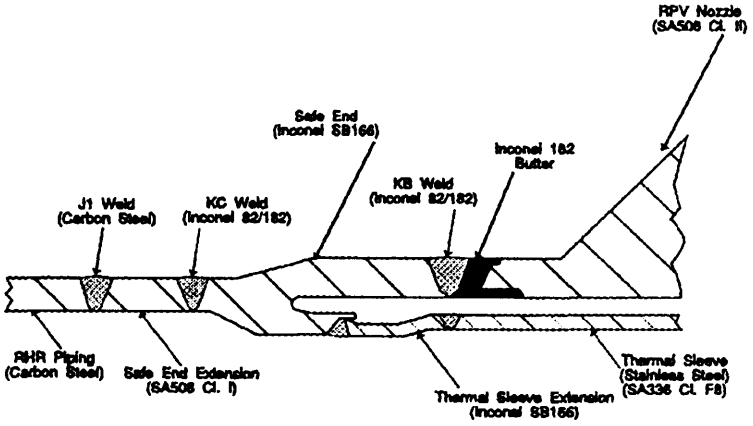


Figure 7. N6 Nozzle Weldments

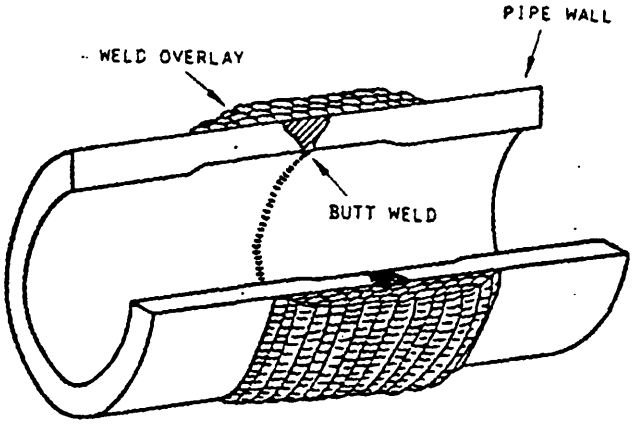


Figure 8 standard Weld Overlay

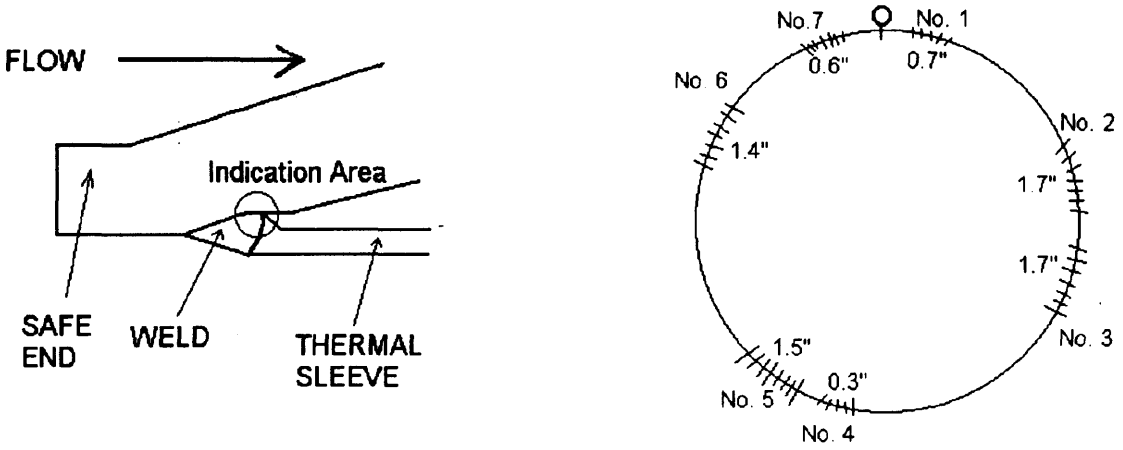


Figure 9 N2E-TSW Weldment Cracks

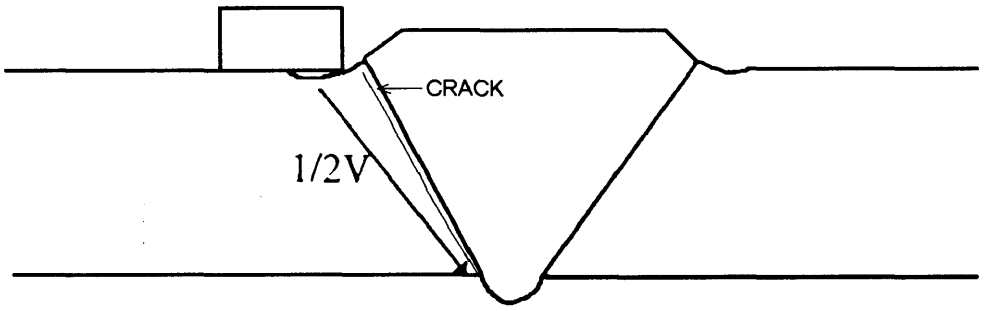


(a) 1/2 V Ultrasonic Examination Technique

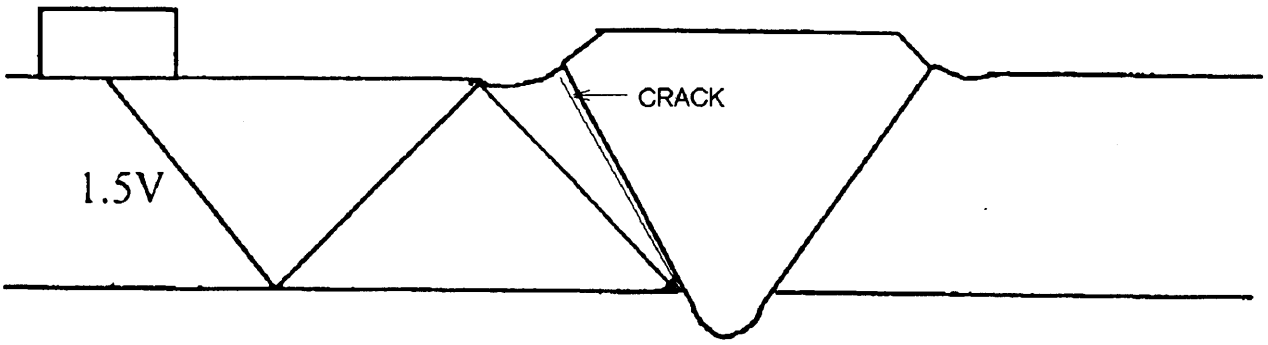


(b) 1.5 V Ultrasonic Examination Technique

Figure 10 1/2 and 1.5 Ultrasonic Examination Technique

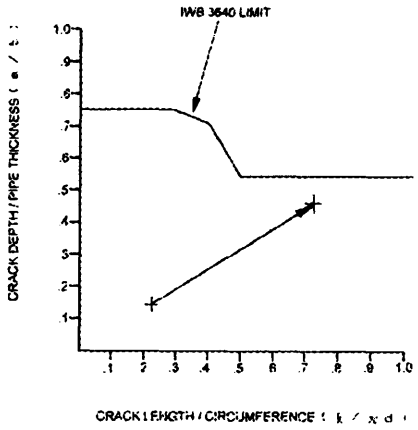


Figure 11 Fracture Mechanics Analysis of N2E-TSW

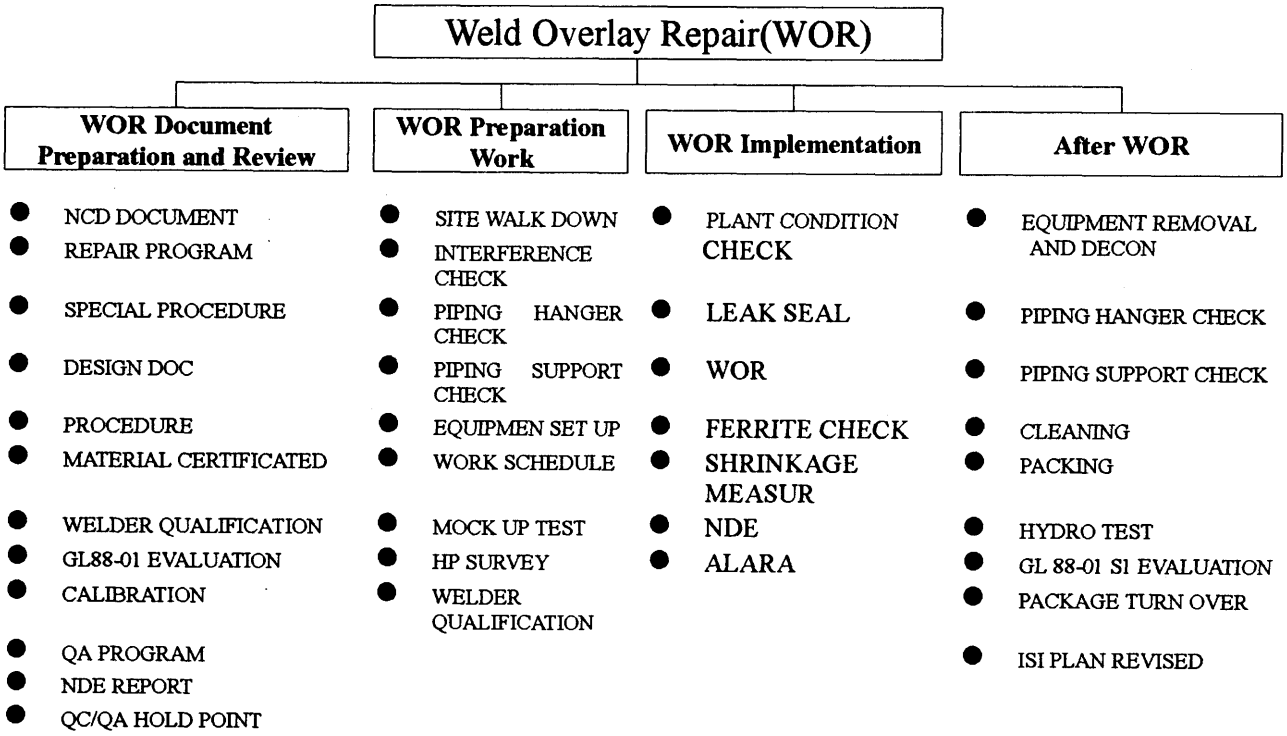


Figure 12 Weld Overlay Repair (WOR) Work Items

III-2 ISI NDE in Korean Nuclear Power Plants

Yi-Hwan (Peter) Jeong, Korea Electric Power Research Institute, Korea

# ISI NDE in Korean Nuclear Power Plants

Yi-Hwan (Peter) Jeong
Hee-Jong Lee
Yong-Sik Kim
Materials & Corrosion Laboratory
Korea Electric Power Research Institute
Taejon, Korea

## Abstract

Structural integrity of nuclear components is important for a safe operation of nuclear power plants. Therefore, the structural integrity should always be maintained by reliable, periodic inservice inspections. Korea Electric Power Company(KEPCO) operates the entire Korean nuclear power plants. Since the safe operation and the inservice inspection(ISI) of the nuclear power plants are under the plant owner's responsibility, Korea Electric Power Research Institute(KEPRI), the R&D division of KEPCO, has established an integrated ISI NDE support system(called, ISI NDE Total Support System: TSS), primarily focused on the inservice inspection of nuclear power plants. And the KEPRI has initiated a long-term plan for the development of key ISI NDE technology that is necessary for an efficient on-site support. This paper describes the KEPRI's TSS and the long-term plan for the key ISI NDE technology development.

## Introduction

Since Kori Unit 1, the first nuclear power plant in Korea, started to generate electricity in 1978, Korea has built twelve nuclear power plants and produces 10gigaWatts of electricity(25% of the total electricity

in Korea, and 9th in the nuclear power generation worldwide). According to the latest survey(Table 1), a total of 336 units at 81 power plants nationwide(including hydraulic, fossil and nuclear) generated over 41gigaWatts of electricity in 1997(17th in the overall power generation worldwide). Over the past years, Korean nuclear power plants showed remarkable improvements in the performance such as drop of unplanned shutdowns and reduction of outages. The nuclear power generation is now a wing of the main source of electricity in Korea. In a long-term, the share of nuclear electricity production will increase to over 45% nationally with the completion of additional nuclear power plants(23 nuclear power plants by the year 2006).

In addition to supplying a quantity of electricity to users, it is also important to supply high-quality, stable(interruption-free) electricity. To supply high-quality, stable electricity, the structural integrity of the nuclear components should be maintained by reliable, periodic inservice inspections.

Table 1. Electricity generated by Korean Power Plants

As of January of 1998 (Unit : MW)

| Type | Hydraulic (7.5%) | | Steam (38.6%) | | Combined Cycle (27.5%) | | Internal Combustion (0.7%) | | Nuclear (25.5%) | | Total | |
|---|---|---|---|---|---|---|---|---|---|---|---|---|
| Co | Unit | Cap. | Unit | Cap. | Unit | Cap. | Unit | Cap. | Unit | Cap. | Unit | Cap. |
| KEPCO | 37 | 2,116 | 52 | 16,578 | 88 | 9,535 | 52 | 265 | 12 | 10,316 | 241 | 38,810 (94%) |
| Others | 81 | 999 | - | - | 14 | 1,500 | - | - | - | - | 95 | 2,499 (6%) |
| Total | 118 | 3,115 | 52 | 16,578 | 102 | 11,035 | 52 | 265 | 12 | 10,316 | 336 | 41,309 (100%) |

Notes: (1) 9th in the nuclear and 17th in the total power generations worldwide.

## PSI/ISI

During the plant operation, plant components are under severe environmental conditions such as high temperature, high pressure, corrosion, mechanical stress and vibration. Therefore, various types of inservice defects or premature failures can occur in the plant components. Such structural failures can cause catastrophic accident. In particular, the component failures in the primary system in the nuclear power plant can cause serious damages to the properties and human lives by radiation exposure. Therefore, periodic inservice inspections should be conducted during the plant operation in order to maintain the structural integrity of nuclear components.

Plant component inspections are classified as preservice inspection(PSI) and inservice inspection(ISI) depending upon whether the inspection is performed at the completion of plant construction or during the plant operation. The PSI is performed to confirm that all structural members of the plant have been constructed safely and properly, and also to acquire initial inspection data that can be compared with the future inservice inspection results. The ISI of nuclear components is generally performed in 10-year period during the plant operation. The PSI and ISI in Korean nuclear power plants are performed according to ASME code Section XI: "Rules for Inservice Inspection of Nuclear Power Plant Components". Because the ASME code mandates that PSI/ISI be performed by nondestructive examination(NDE), the NDE for nuclear component examination is particularly important.

## Status of ISI NDE

During the last several decades, the nondestructive evaluation(NDE) technology for inservice inspection(ISI) in nuclear power plant has been greatly improved. Particularly, with the advancement of computer technology in recent years, the NDE equipment for reactor pressure vessel(RPV), steam generator(SG), turbine, pressurizer, reactor

coolant pump(RCP) and pipings were fully automated and sophisticated. Consequently, the accuracy, the speed and the reliability of the ISI performance were improved accordingly.

However, the KEPCO has been heavily relying on foreign countries in conducting the inservice inspections of the nuclear components due to lack of key ISI NDE technology. Consequently, the ISI operation costs KEPCO a great deal of financial burden. Furthermore, due to lack of the key ISI NDE technology, the KEPCO has not been able to respond to site problems in an efficient and timely manner. Such difficulties of Korean nuclear power plants provided the needed impetus for KEPCO to develop a long-term plan for the ISI NDE technology development and to prepare for the independent operation of inservice inspection of nuclear power plant components.

## ISI NDE Long-Term Plan

The KEPCO, as a utility, is primarily responsible for the safe and reliable operation of the nuclear power plants. Therefore, the KEPCO monitors the periodic inspections of nuclear components performed by domestic and foreign companies. The mission of KEPRI, the R&D division of KEPCO, is to perform the research and development of ISI NDE technology as well as the associated technology transfer. To meet such mission, the KEPRI has established an on-site support system, called ISI NDE total support system(TSS), that can respond to various plant ISI problems in an efficient and timely manner. Furthermore, in order to successfully support the plant ISI operation, the KEPRI has established a long-term plan for the development of key ISI NDE technology(Figure 1). The key ISI NDE technology areas were chosen among the most important technical areas in conducting the on-site ISI support tasks.

The TSS and the key ISI NDE technology development programs contain the following three stages: preparation, independent operation, and

technology transfer stages. The preparation stage(Years 1997-1999) is for the initial development of the essential NDE and the ISI engineering methods that will become the basis of the independent ISI operation. The major NDE equipment will be automated and computerized to improve the efficiency and the speed of the nondestructive examination. The independent operation stage(Years 2000-2002) is for the application of the major ISI NDE technology for the nuclear component examination solely by the domestic teams. Moreover, the plant-required ISI inspectors will be trained and qualified by the domestic training and qualification system(Korean Performance Demonstration Initiative: KPDI). The technology transfer stage(beyond 2003) is for exporting the key ISI NDE technology as well as the services to foreign countries as the opportunity arises.

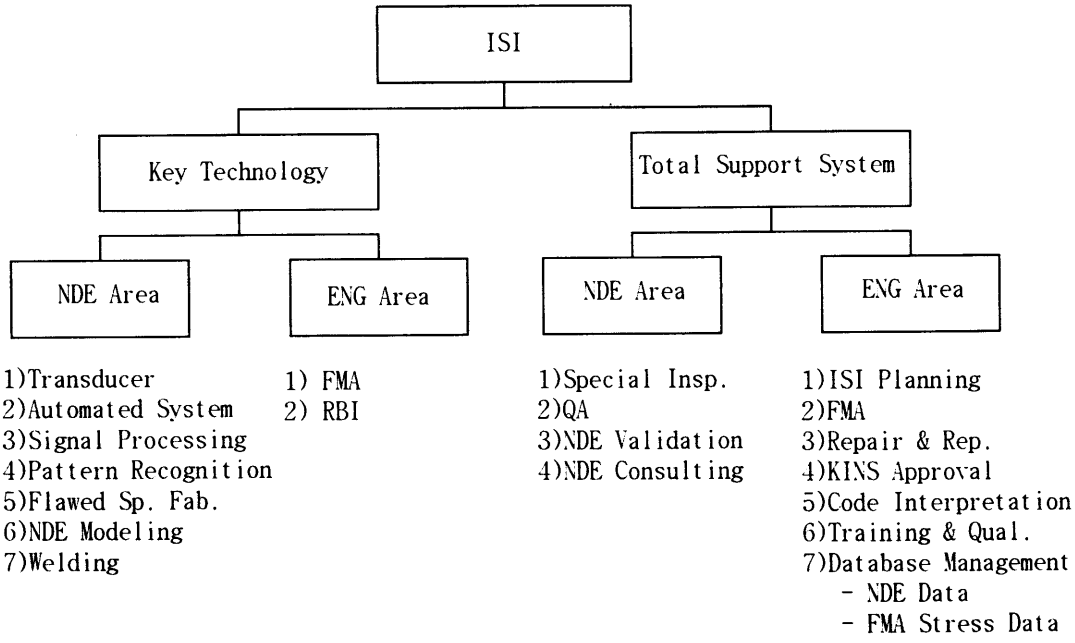


Figure 1. ISI NDE Technology Tree

# ISI NDE Total Support System

The ISI of nuclear components typically include such tasks as ISI planning, nondestructive testing(NDT), quality assurance(QA), fracture mechanics analysis(FMA), and repair or replacement of defective components. And these tasks are being performed according to the rules and the regulations of ASME Boiler And Pressure Vessel Code: e.g., the NDE concepts and the criteria(Section XI), the NDE procedures(Section V), the repair and replacement(Sections III, IX, and XI), etc.. The ISI planning is to plan the overall scope of the ISI operation, the sequence of component examinations, and the associated time schedule. The NDT is for the actual examination of nuclear components using various NDT techniques such as ultrasonics, Eddy current, X-ray, dye penetrant, magnetic particle and visual examination. The quality assurance(QA) is to confirm the accuracy and reliability of the NDT performed by other inspection teams. The FMA is to determine whether the detected flaws of certain sizes could influence the component integrity during the operation. If the flaws could indeed influence the component integrity, then, the FMA determines how long the defective components could be safely operated without repair or replacement. The repair and replacement tasks in TSS are to recommend the repair and replacement methodology for defective components that can satisfy the relevant code requirements. Since the component defects are being found during the ISI, the necessary repair or replacement tasks can not be incorporated into the ISI planning. Therefore, it is necessary to make a prompt, sound judgement at the site for whether the component should be either repaired or replaced depending on the applicable code requirements. And if it has to be repaired or replaced, then, it should be determined which repair or replacement methods should be applied.

In fact, the above ISI tasks require the knowledge and the experience on NDE technology and NDE code requirements in order to perform the tasks in an accurate and proper way. Nevertheless, in the past, some of the tasks were conducted by non-NDE personnel resulted in unnecessary

time delays and expenses to the power plant. Furthermore, the recent development of risk-based ISI technology for nuclear power plant encourages the NDE to establish a new strategy for the ISI application. To meet such demand, the KEPRI has developed the ISI NDE total support system(TSS) that can support various ISI tasks in an efficient, reliable and timely manner(Figure 2). Under the TSS, the NDE experts provide an extended service on the above ISI NDE tasks. Furthermore, the overall ISI tasks can be performed consistently without the conflicts in the data or code interpretations amongst many different groups of ISI personnel. It should be noted, however, the KPERI does not intend to perform the routinely repeated ISI NDE tasks, but to perform a supporting role by conducting advanced or special ISI NDE tasks that require special knowledge and experience on NDE.

Under the TSS, a number of additional NDE-related services are also provided which include NDE valiadation, NDE consulting, approval from regulatory agencies(e.g., KINS in Korea), code interpretation, training & qualification, and database management(NDE data and FMA stress data).

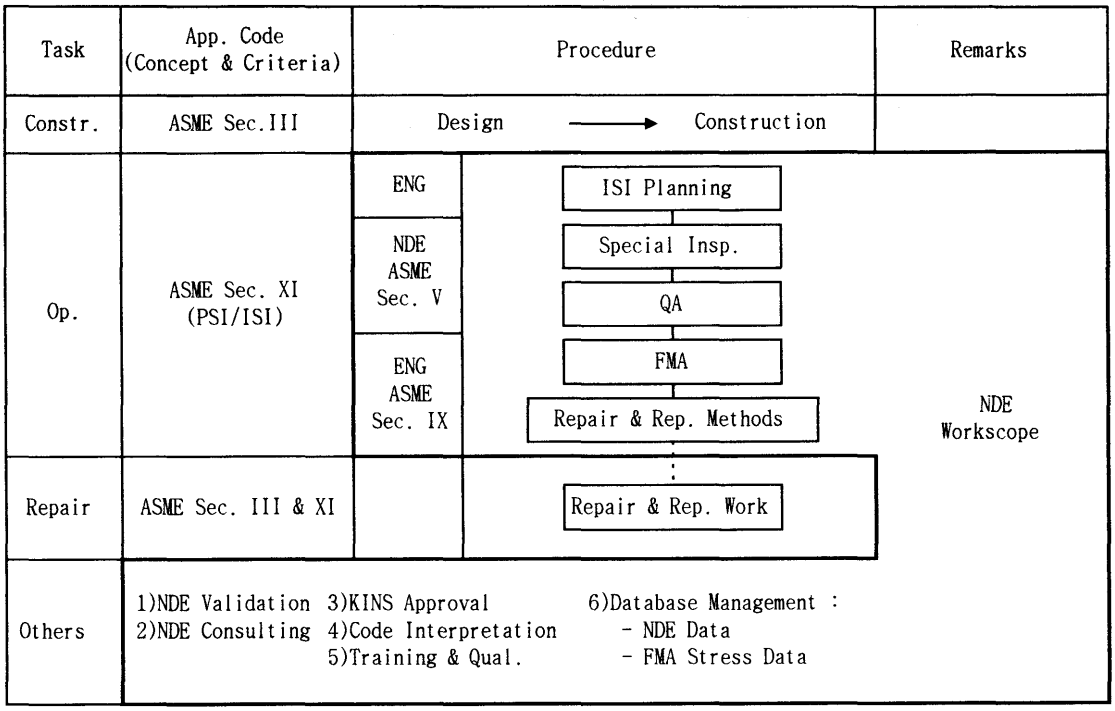


Figure 2. ISI NDE Total Support System

## Key ISI NDE Technology

The ISI site support under the TSS contains a number of key technologies that are essential for a successful application of the TSS to plant ISI. In the past, the KEPCO has been heavily relying on foreign ISI service companies due to lack of the key ISI NDE technology. Consequently, the KEPCO had to manage a great deal of financial burden. In order to alleviate such difficulties of KEPCO, the KEPRI has selected 9 technical areas to develop in parallel with the TSS which include transducer manufacture, NDE systems automation, signal processing, pattern recognition, fracture mechanics analysis(FMA), risk-based inservice inspection(RBISI), flawed-specimen fabrication, NDE modeling, and welding. These technical areas were chosen among the fundamental NDE techniques that are needed for conducting each of the major TSS tasks(Figure 3). Brief descriptions of each area were given below:

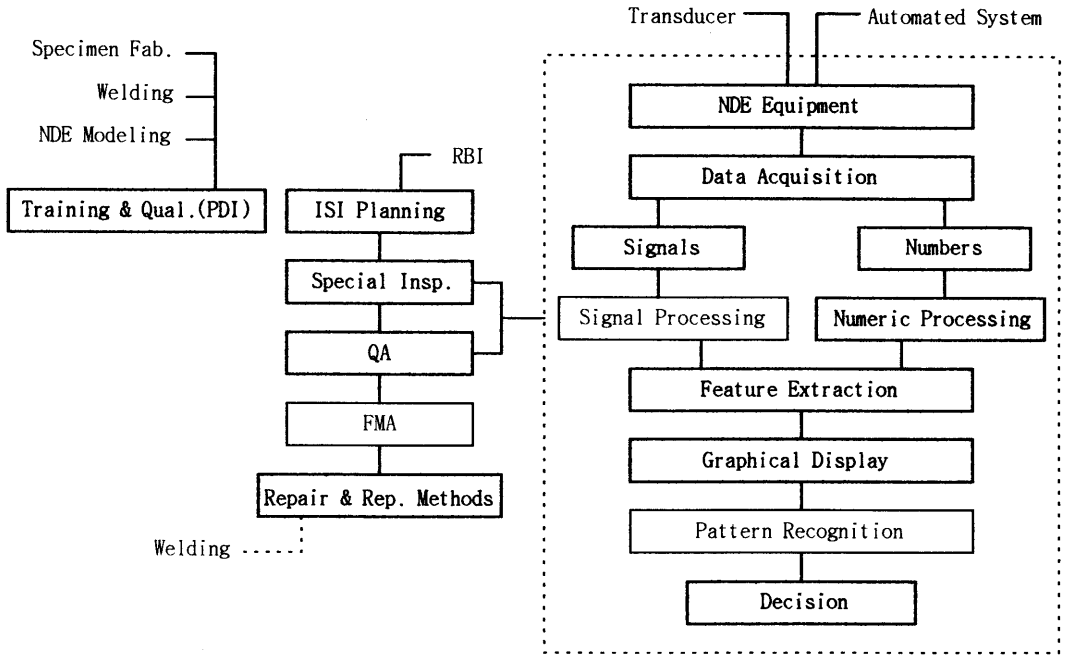


Figure 3. Sources of the key ISI NDE technology

Although the NDE procedure as shown in Figure 3(within dotted line) might be more or less different depending on the testing conditions, the NDE procedure typically includes the following tasks: data acquisition by NDE equipment, (signal or numeric) data processing, feature extraction, graphical display, pattern recognition, and decision. Although the details of each step of the above procedure would be out of the scope of this paper, we could easily recognize the following 4 essential technologies contained in the whole procedure: transducer manufacture, NDE systems automation, signal processing, and pattern recognition:

(1) Transducer Manufacture: As the ISI NDE technology became complex and sophisticated, varieties of transducer types and designs are required to fabricate. To fulfill such needs, the transducer manufacturing capability is an absolute necessity.

(2) NDE Systems Automation: The ever increasing complexity, the

volume and the number of testing components in recent years require the speed, the accuracy, and the reliability of nondestructive examination. To meet such demand, and to keep pace with the fast growing modern NDE technology, the NDE systems automation for the nuclear component examination should be seriously considered.

(3) Signal Processing: Answers for NDE problems are not always contained in the raw data as acquired. For an example, some flaw characteristics are extractable not directly from the ultrasonic flaw signal, but from some other modified data types such as frequency spectrum or transfer function. Such signal processing techniques as FFT, correlation, convolution, filtering, to name but a few, are essential for analyzing the complicated data types.

(4) Pattern Recognition: When the signal processed NDE data is insufficient to extract a reliable answer, the data has to be further relied upon the pattern recognition techniques. Pattern recognitions are mathematical and statistical analysis methods that make decisions based on multiple feature values extracted from the various data types (e.g., linear or nonlinear regression, Bayes decision theory, discriminant function, etc.). As the complexity of NDE data types grows, the need for pattern recognition becomes more absolute.

(5) Fracture Mechanics Analysis(FMA): the nuclear components having defects larger than the code-allowable sizes(in terms of length, depth, width, etc.) should basically be either repaired or replaced. However, the defective components may continuously be operated for an extended period of time only if the safe operation of the defective components is theoretically(using FMA) demonstrated. The KEPRI is in the development process for the stress analysis and FMA programs, and for establishing the stress database for major nuclear components that is necessary to perform the FMA.

(6) Risk-Based Inservice Inspection(RBISI): The ASME Code-based ISI

in nuclear power plant requires to inspect many components having no previous records(or history) of component failure or defect occurring. The risk-based ISI(RBISI) is therefore to avoid such inefficiency by allowing utility to inspect only the components whose probability of failure is ranked high. The component ranking is determined based on the risk level calculated as follows:

Risk = (Core Melt Potential/Pipe Rupture) x (Potential for Pipe Rupture) ----- (1)

where, all terms indicate the probability of occurring.

The RBISI considerably reduces the components to inspect(A 70% reduction has been demonstrated by US plants), and hence, reduces the overall ISI costs as well as the overhaul period. The RBISI is currently being applied only for the pipings in the United States, and further applications of the technique to other major components are currently being considered. The KEPRI had initiated the RBISI development program in 1997(Figure 4). The KEPRI is planning to apply the RBISI to actual Korean nuclear power plants in the year 2001.

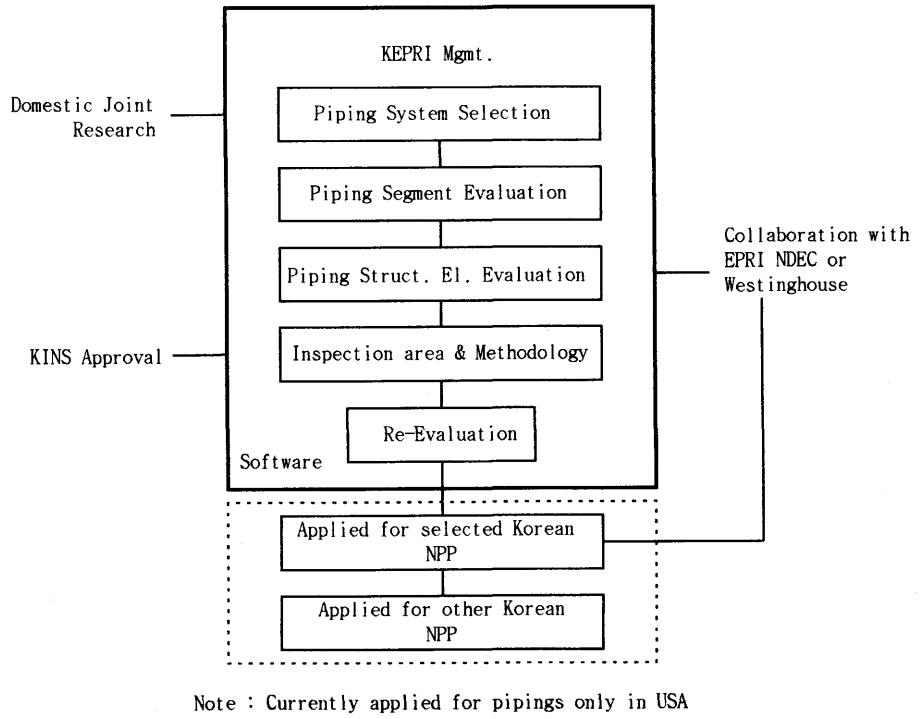


Figure 4. The Approach for KRBISI

The following 3 technical areas(flawed-specimen fabrication, NDE modeling, and welding) are related to the KEPRI's Korean Performance Demonstration Initiative(KPDI) program initiated in 1997(Figure 5). In the past, all ultrasonic inspectors were allowed to inspect nuclear components if they have been qualified once in any certified training and qualification institute. However, because detecting and sizing of flaws of complex shapes(IGSCC, under-clad cracking, etc.) require special skills and experience, the codes(ASME and CFR in the United States) mandated that the performance demonstration of all ultrasonic inspectors be conducted by an integrated qualification process combining the inspector, the procedure, and the equipment, in order to improve the accuracy and the reliability of NDE performance on specific ISI task. The KEPRI is planning to apply the KPDI program to actual Korean nuclear power plants in the year 2001. Brief descriptions of 3 additional technical areas were provided next:

(7) Flawed-Specimen Fabrication: In order to evaluate the ultrasonic inspector's performance, it is required to prepare test specimens containing certain number of flaws of certain sizes as described in the ASME Code Section XI, Appendix VIII. The fabrication of flawed-specimen requires special techniques, and it involves technical know-hows and therefore high fabrication cost. Considering the situation, it would be beneficial to have the specimen fabrication capability in-house to establish the training and qualification system for KPDI.

(8) NDE Modeling: For the application of performance demonstration program(KPDI) to ISI NDE inspectors, the test specimens that represent all nuclear components should be prepared. To meet such requirement, a great number of specimens of an extremely high cost has to be fabricated. However, the use of NDE modeling can help reduce the number of the specimens by theoretically(NDE modeling) demonstrating the equivalency of similar inspection situations. The NDE modeling can also help avoid unnecessary re-training and qualification for the similar inspection situations. In addition, the NDE modeling can be utilized for an

effective education for the theoretical wave propagation.

(9) Welding: The welding techniques are continuously needed to fabricate the test specimens for the inspector's performance demonstration and to develop optimum repair and replacement technology for defective components.

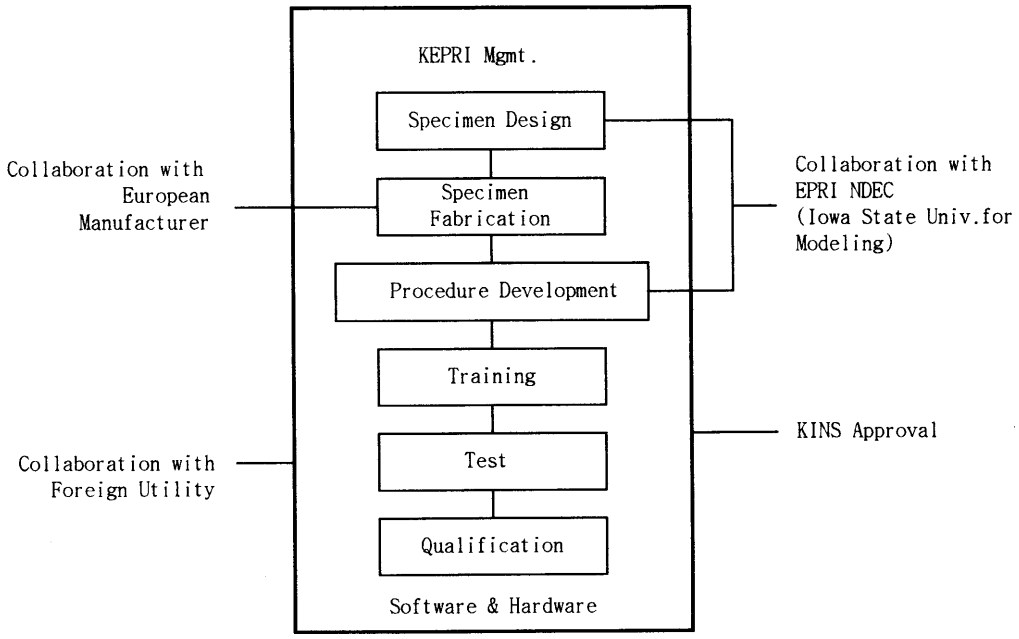


Figure 5. The Approach for KPDI

## Summary

Structural integrity of nuclear components is important for a safe operation of nuclear power plant. Therefore, the structural integrity should always be maintained by reliable, periodic inservice inspections. Since the safe operation and the inservice inspection of the nuclear power plants are under the plant owner's responsibility, KEPRI, the R&D division of KEPCO, has established an integrated ISI NDE total support system(TSS), primarily focused on the inservice inspection of nuclear

power plants. And the KEPRI has initiated a long-term plan for the development of key ISI NDE technology that is necessary for an efficient on-site support. Although KEPRI took the lead in this effort to establish the TSS, the KEPRI intends to collaborate with industry, universities, and research institutes throughout the development process in order to promote the entire Korean ISI NDE technology.

## References

1. Plant Operation Statistics, Korea Electric Power Company, 1997.

III-3 Core Shroud Replacement of Fukushima-Daiichi Unit #3

Jun Matsumoto, Nuclear Power Plant Management Dept.
Tokyo Electric Power Company, Japan

# Core Shroud Replacement of Fukushima-Daiichi Unit #3

J. MATSUMOTO
Tokyo Electric Power Company
1-1-3 Uchisaiwai-cho, Chiyoda-ku Tokyo, Japan

***Abstract***

*The core shroud replacement of a Boiling Water Reactor (BWR) is now in progress at Fukushima-Daiichi Unit #3(1F3) of the Tokyo Electric Power Company (TEPCO) in Japan. The core shroud and other core internal components made of type 304 stainless steel (SS) are replaced with the ones made of low carbon type 316L SS to improve Intergranular Stress Corrosion Cracking (IGSCC) resistance. This project is the first application of the replacement procedure developed for the welded core shroud, and employs various advanced technologies. The outline of the core shroud replacement project and applied technologies are discussed in this paper.*

## 1. Introduction

Since the core shroud cracking was found, the Japanese BWR owners and the plant manufacturers have conducted several R&D programs to establish the countermeasures for core shroud cracking. These countermeasures are repair and mitigation technologies including replacement, bracket reinforcement, tie rod reinforcement, hydrogen water chemistry (HWC), water jet peening, shot peening, and noble metal technologies. When the crack was found in Fukushima-Daiichi Unit #2 (1F2), the core shroud was reinforced by the brackets which had been studied as one of the repair concepts.

The countermeasures for the actual plants should be carefully selected considering effect and applicability of the countermeasures, uncertainty of the developed technologies, estimated cost (tool fabrication and implementation cost, inspection cost through the plant life etc.), estimated schedule, possibility of cracking, political

environment, and so on. Based on the evaluation of these influential elements, TEPCO decided to replace the core shrouds made of 304SS which has relatively higher potential of IGSCC. Among 17 BWR plants owned by TEPCO, four plants have the core shrouds made of 304SS. In accordance with the long term outage schedule, 1F3 was selected as the first plant to replace the core shroud with the one made of 316L SS which has much less potential of IGSCC.

In addition to the core shroud, the majority of the internal components made of 304SS are replaced in the 1F3 project. Those are (1) core shroud, (2) top guide, (3) core plate, (4) core spray spargers, (5) feed water spargers, (6) jet pumps, (7) DP/LC pipe, (8) ICM guide tubes, and internal pipes and nozzle safe ends connected to these components as shown in Figure 1. Prior to the application to 1F3, integrity and reliability of the replacement process were demonstrated by the full scale mock-up test, which was conducted by the Nuclear Power Engineering Corporation (NUPEC).

## 2. Replacement Process

The replacement sequence is shown in Figure 2. After the removal of all fuels and detachable components, inside of the pressure vessel and the remaining internal components were chemically decontaminated. Subsequently, most of the removals are conducted by means of Electrical Discharge Machining (EDM) process under water. Following the removal of all components to be replaced, the new components were installed in reverse order of the removal. Most of the installation process including welding was performed in a dry condition to acquire high quality of the weld. The followings are the major technologies applied to the core shroud replacement process.

### 2.1 Chemical Decontamination

Prior to cutting the core shroud, the chemical decontamination was conducted. The Chemical Oxidation Reduction Decontamination (CORD) process provides a high Decontamination Factor (DF), and generates a small amount of waste in comparison to other decontamination processes. Decontamination solution was circulated by the Primary Loop Recirculation (PLR) pumps, and the dissolved active metal was captured by ion exchange resins (Figure 3). In the core shroud replacement project for 1F3, the oxidation and reduction process was repeated three times in a week. The volume of waste was approximately $5m^3$, and the DF measured under water was approximately 40 at the bottom of the RPV .

### 2.2 Core Shroud Cutting

The old core shroud was cut remotely under water by EDM process. Four EDM-cutting carriages are mounted on the circular track assembly and run individually. Each EDM-cutting carriage has a rotating graphite electrode as shown in Figure 4. A swarf collection hood is attached to the EDM-cutting carriage. After this primary cutting, the old core shroud was transferred under water to the Dryer Separator Storage Pool (DSP) for slicing. The height of the old core shroud in the DSP should be less than 3.5m to assure the shielding effect of water. The old core shroud was cut circumferentially at two elevations so that the height of each old core shroud was less than 3.5m.

After removal of lower half of the old core shroud, the upper face of the remaining shroud support is machined to acquire a sufficient flatness for the welding. Figure 5 shows the machining tool which uses a rotational milling head.

### 2.3 In-vessel Shielding

After the cutting and removal process under the water, the in-vessel shielding was set up to reduce the dose from the radioactive RPV wall. Reduction of radiation dose level during the installation process is important because the new components are welded in a dry condition. Figure 6 shows the shielding panels hanging from the RPV flange. The shielding panels have windows to allow welding the riser pipe and the riser brace without removing the shielding panels.

### 2.4 Core Shroud Installation

Although the design of the new core shroud is improved in the material and welding to increase IGSCC resistance, the basic structural geometry was maintained to assure the same plant performance.

The overall structure of the core shroud in 1F3 is shown in Figure 7. The left side shows a cross section of the new core shroud, and the old core shroud is shown on the right side. The number of welds is reduced because it directly influences the probability of cracking. The new core shroud consists of three forged cylinders (316L SS) with no vertical weld, and a lower ring (alloy 600) with two vertical welds. Totally, seven circumferential welds are decreased to four welds, and twenty-four vertical welds are reduced to two welds.

Figure 8 is the illustration of the weld joint between the lower face of the core shroud and the upper face of the remaining shroud support. The lower face of the new core shroud meets the upper face of the remaining shroud support at a narrow angle to reduce

welding heat input and to shorten welding time in comparison to the old core shroud. In the old core shroud, the joint was welded from inside with the backing ring which formed a crevice. In order to avoid a crevice in the weld joint and to get a smooth configuration of the outside surface, the new core shroud was welded from both sides.

Figure 9 shows the bead sequence of the weld joint. Tungsten Inert Gas (TIG) welding was applied. First, the outer diameter (OD) side was welded, and then the inner diameter (ID) side was welded. Since the distance between the core shroud and the jet pump diffuser is only 70mm at the joint elevation, the OD welding machine is thin to fit the space, and was mounted on the OD track prior to the shroud installation as shown in Figure 10. The filler wire was also attached on the outside of the new core shroud prior to the shroud installation in order to save the space for wire feeding system. The ID welding machines were attached manually after the new shroud installation, and ran on the ID track remotely (Figure 11).

At the development stage of this welding process, the weld joint was evaluated by visual test, penetration test, radiographic test, microstructure, metallography, side bend test, crevice bent beam test (CBB), tensile bond strength test, and measurement of hardness and residual stress. Based on the evaluation, the limit of the essential variables for this welding method was established.

### 2.5 Alignment of the Components

It is important to align the core shroud, the core plate, and the top guide with the CRD housings to secure appropriate motion of the control rods. Figure 12 shows the alignment tool for the new core shroud, core plate and top guide. A laser targeting system is set in the gas purged tube of the alignment tool. The new core plate was aligned with respect to existing CRD housings as shown in Figure 13. Bottom of the alignment tools were set on the top of CRD housings, and top of the alignment tools were fixed in the core plate master holes. The new core plate was aligned checking the location of the core plate master holes and the CRD housings. The new core shroud and the top guide are aligned similarly.

## 3. Waste Management

The removed core shroud and other components were sliced and put into the containers in the DSP. The underwater plasma arc cutting was employed for the slicing process because of its fast cutting speed. The stuffed containers were decontaminated

and transferred to the site bunker pool and the dry storage facility in the site. Although all of the waste is low level radioactive waste, the site bunker pool stores more radioactive waste.

## 4. Conclusion

TEPCO is replacing the core shroud of 1F3 to improve IGSCC resistance. The shroud replacement is considered to be one of the most comprehensive countermeasures to improve IGSCC resistance for all the welds of the core shroud. As of April 1998, the new core shroud has already been installed properly, and the project is under restoration process of other internal components. Subsequently, the core shroud replacement will be performed in several Japanese BWR plants.

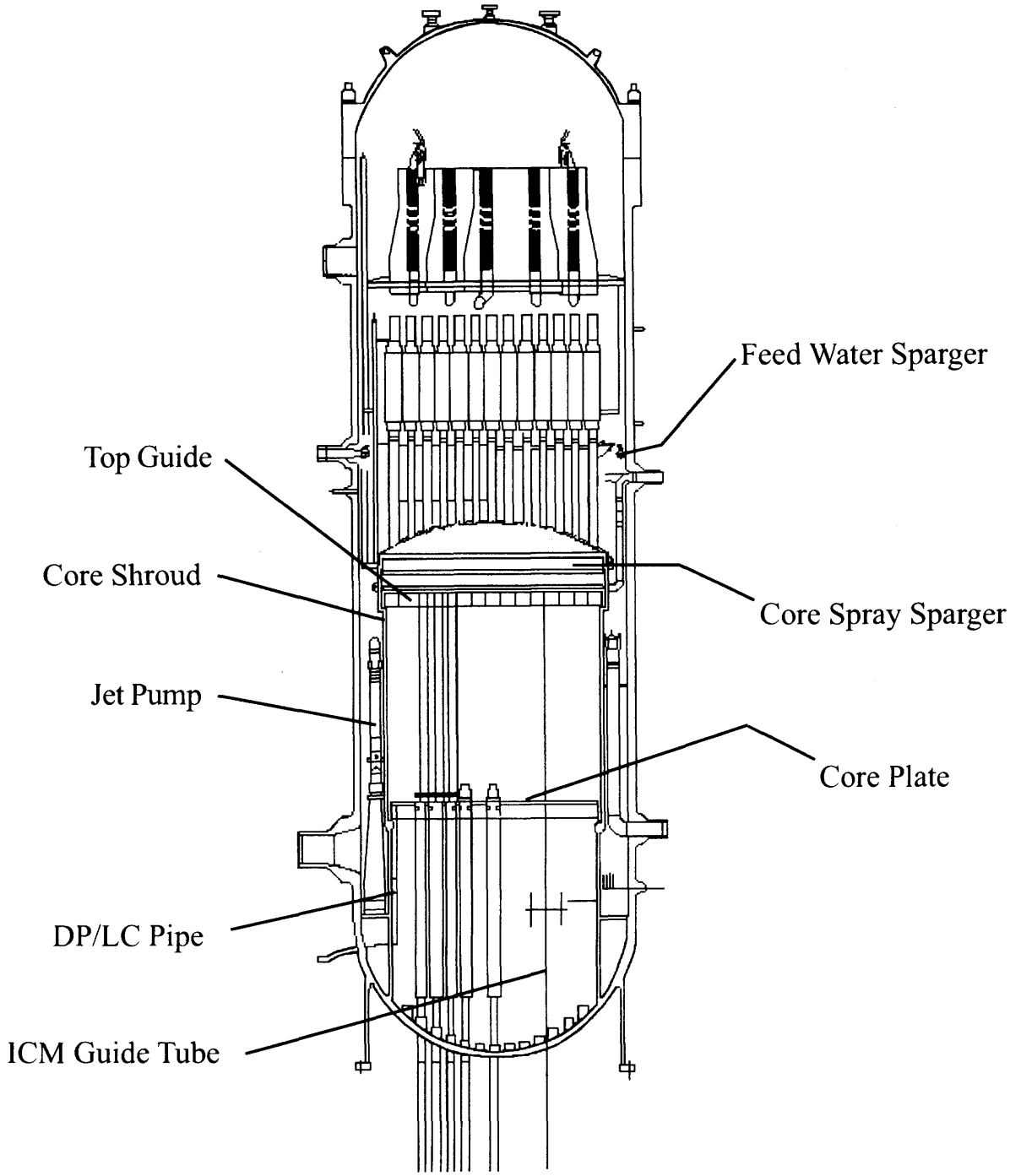


Figure 1 Replaced Components

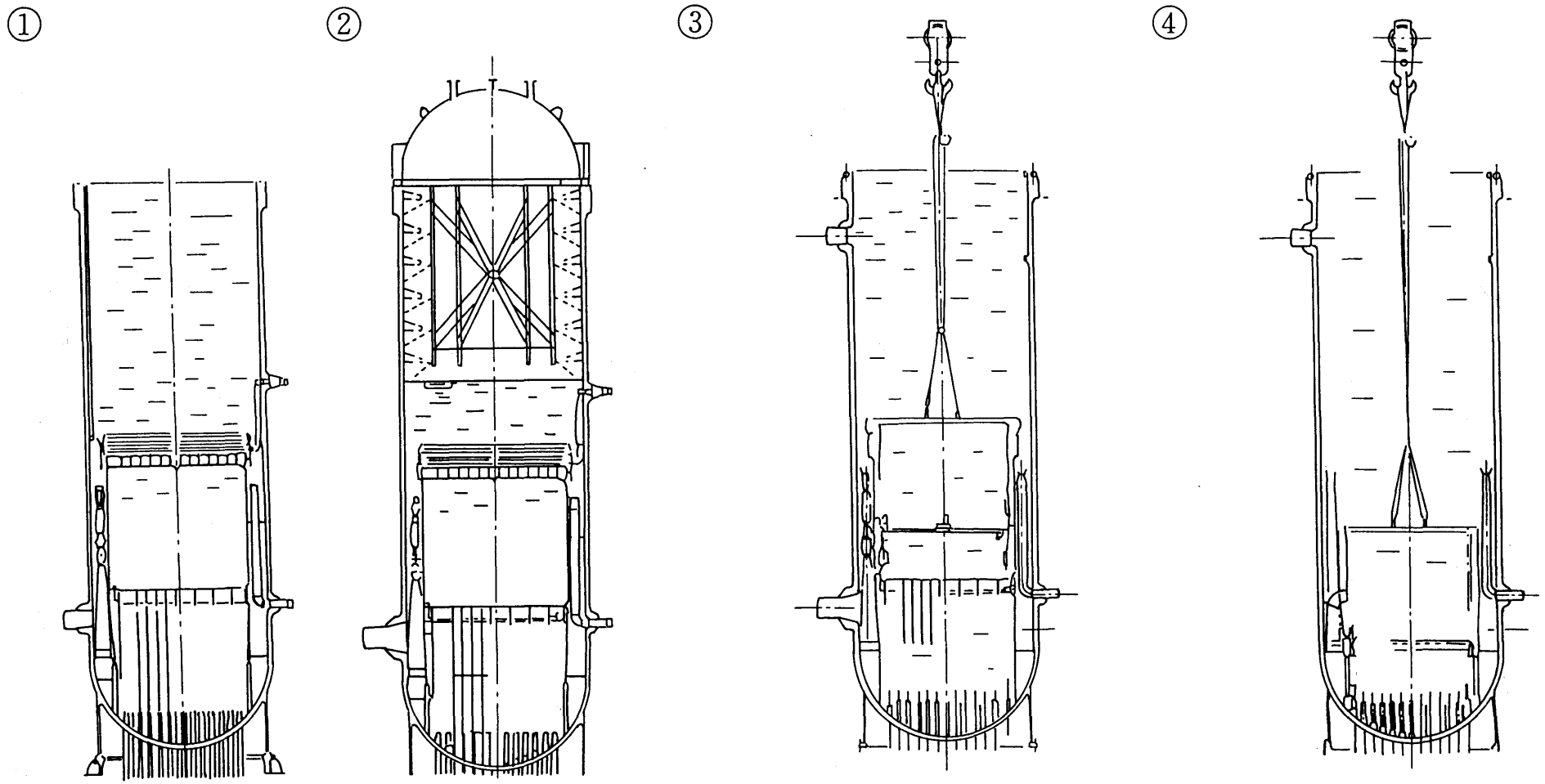


Figure 2 (1) Replacement Sequence

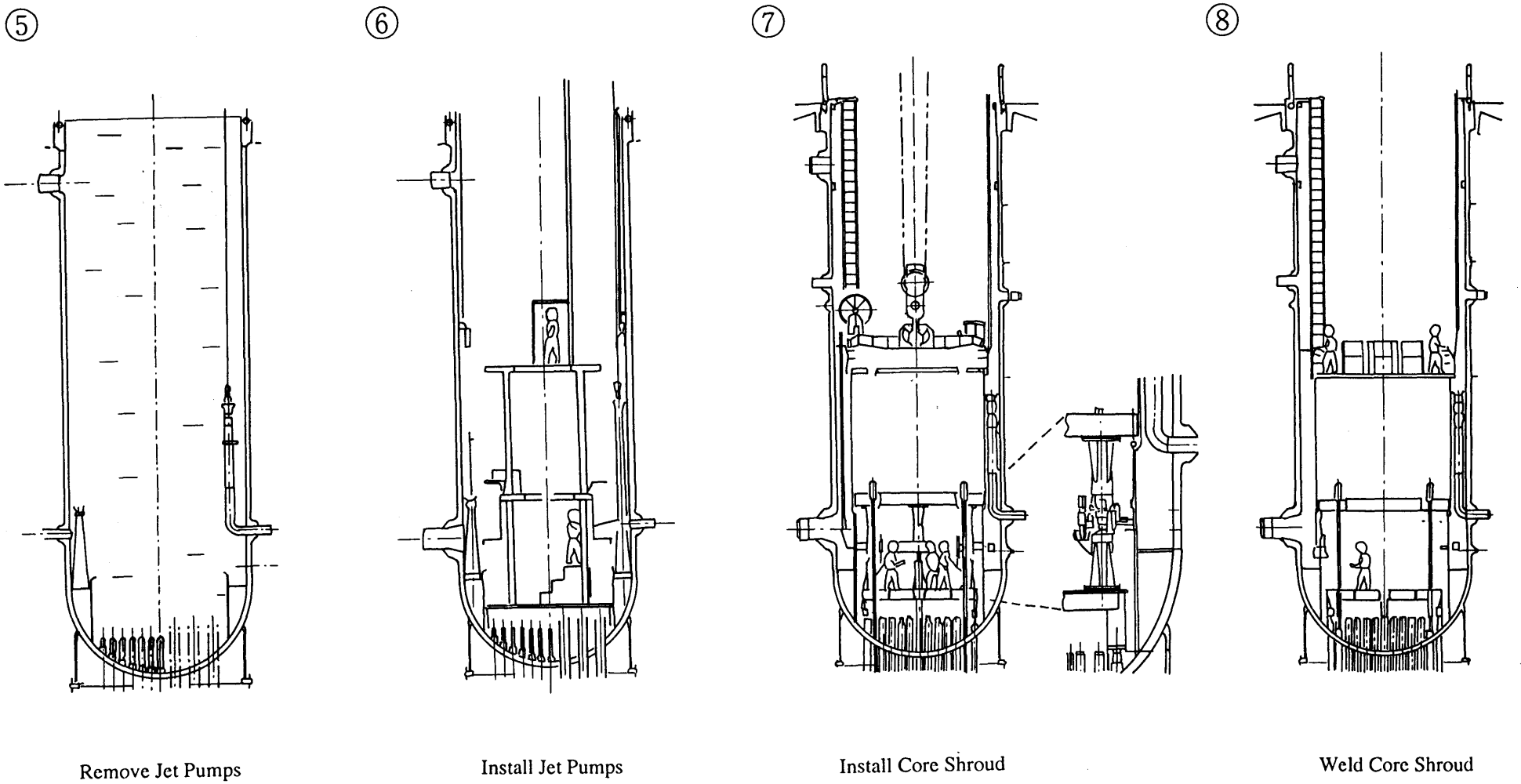


Figure 2 (2) Replacement Sequence

⑨

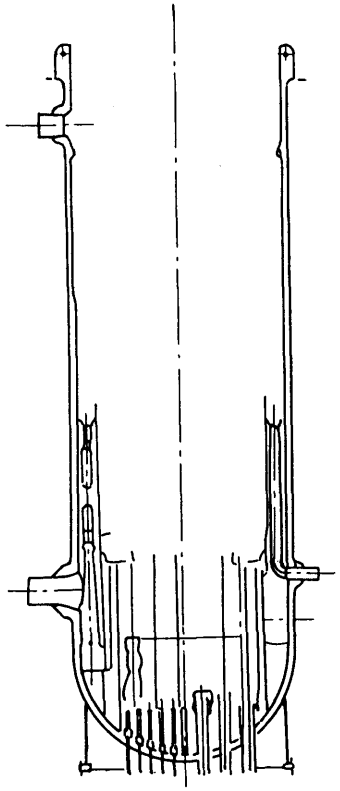

Install DP/LC Pipe,

ICM Guide Tubes

⑩

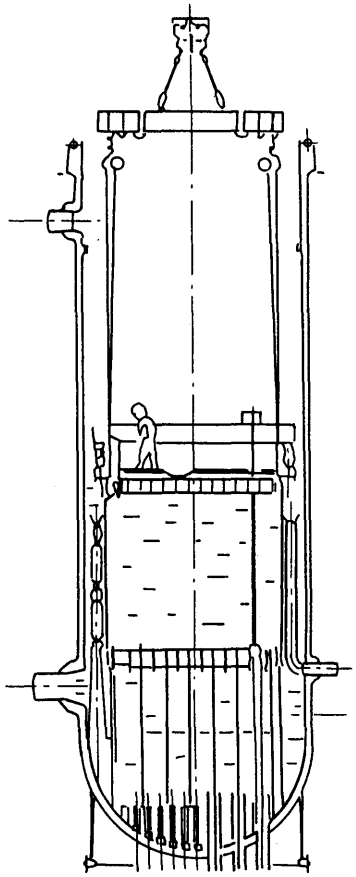

Install Core Plate, Top Guide,

Feed Water Spargers

⑪

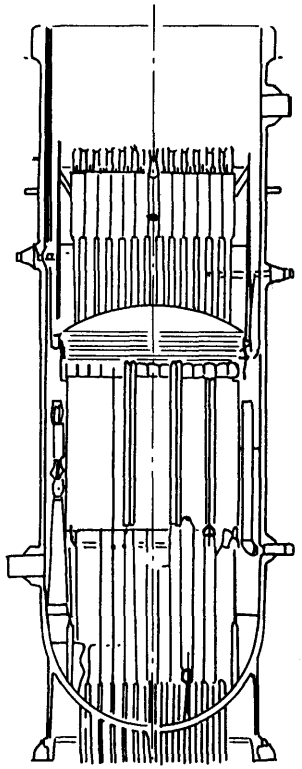

Restore Fuel, Core Components

Figure 2 (3) Replacement Sequence

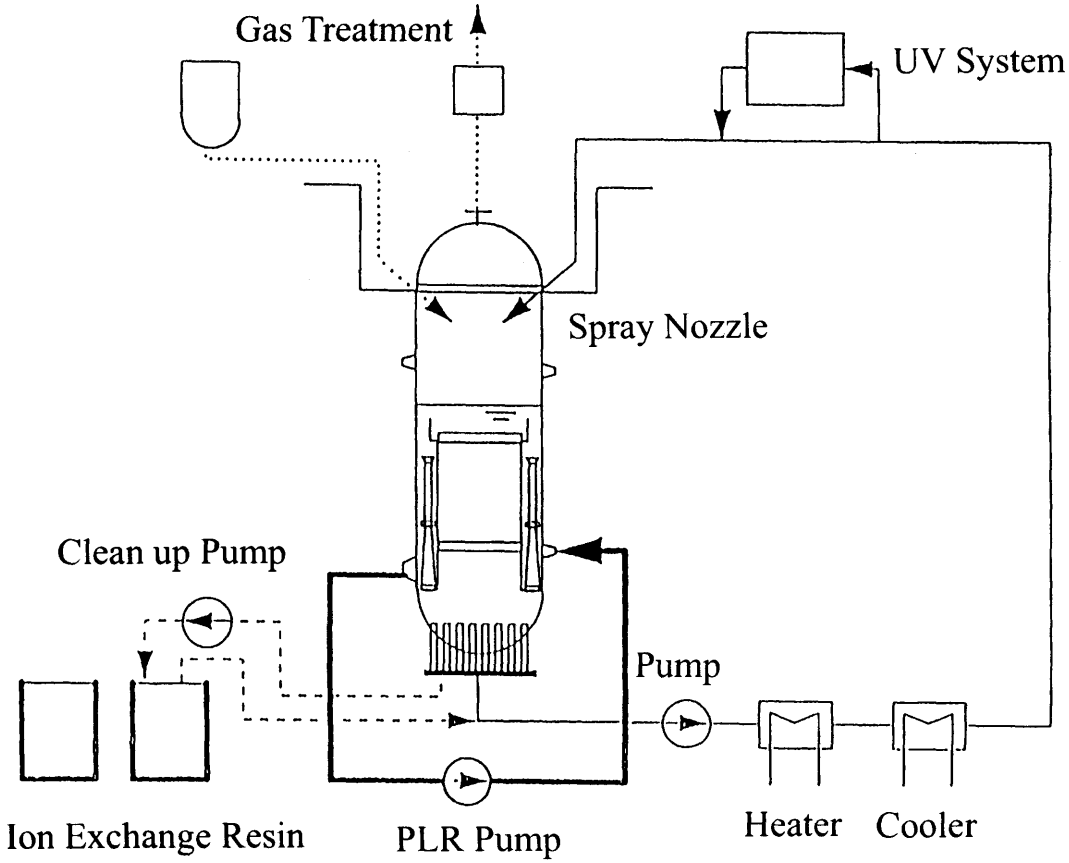


Figure 3 Chemical Decontamination System

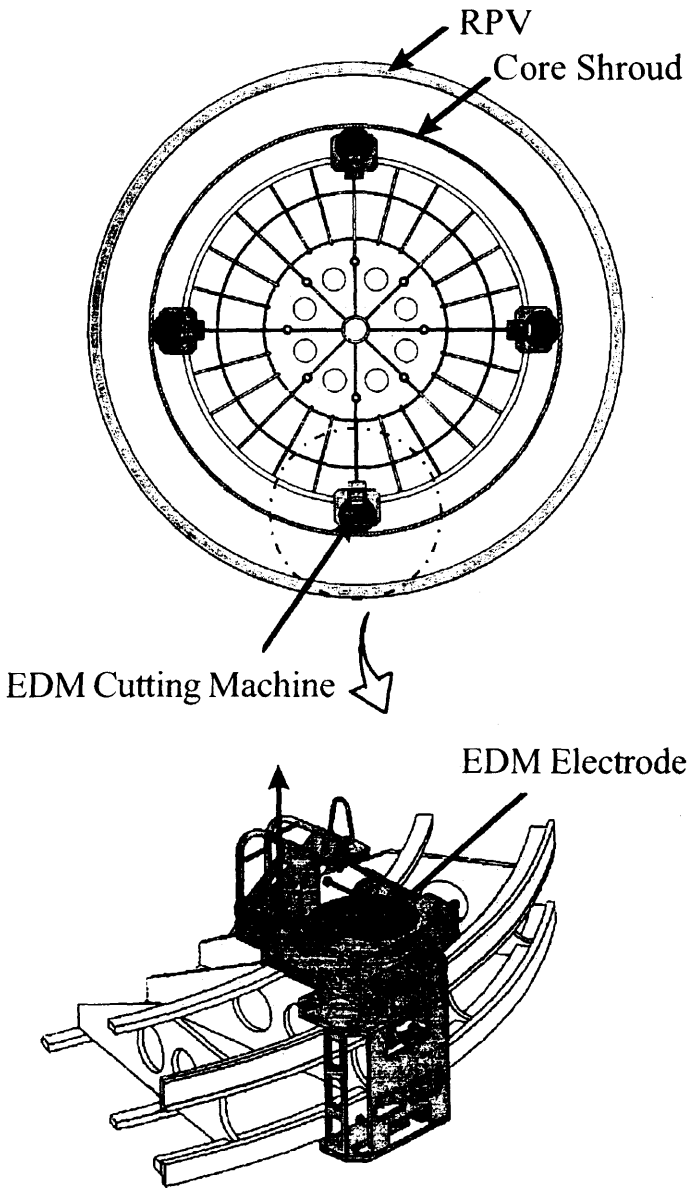


Figure 4 EDM Cutting Machine

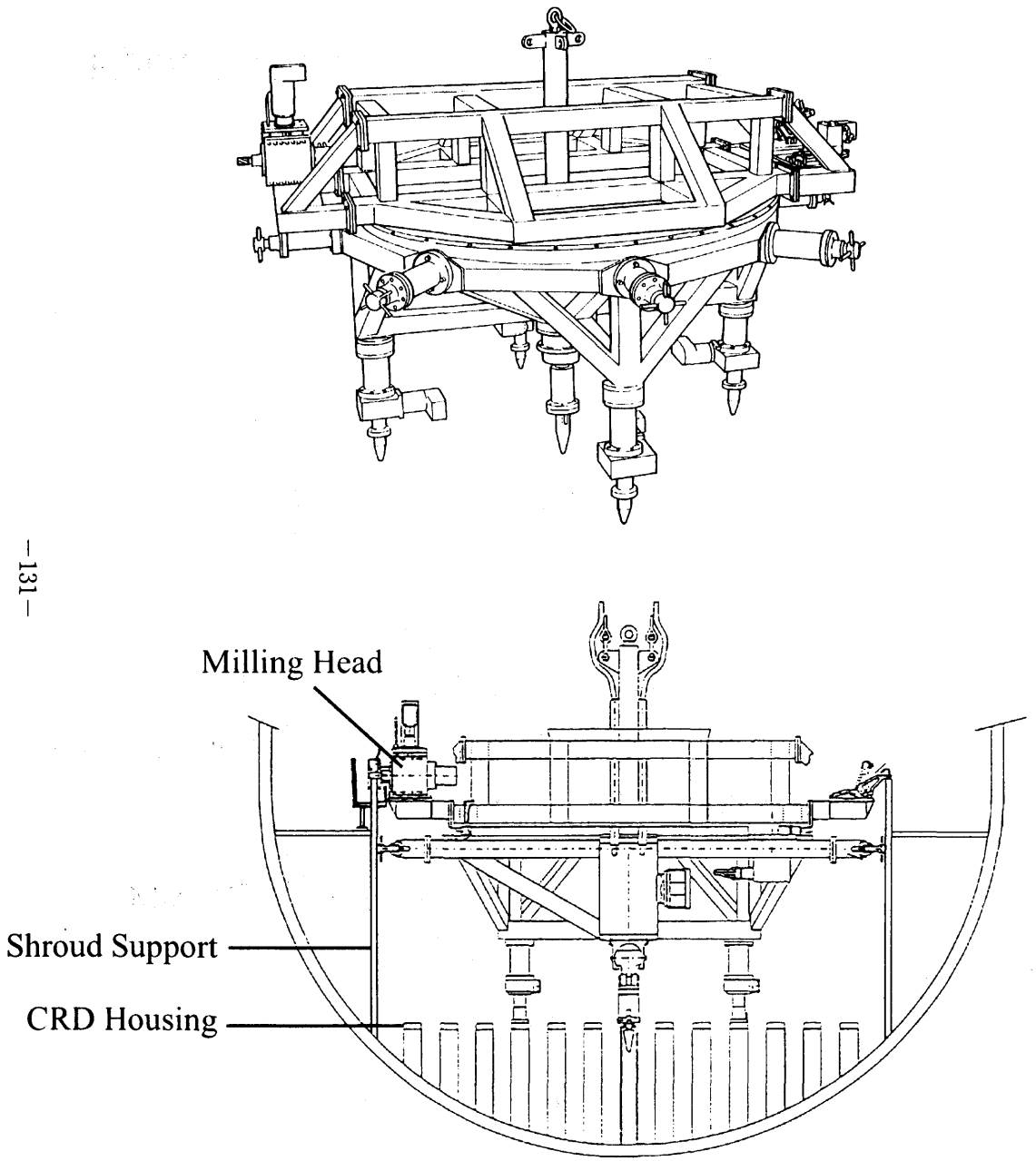


Figure 5 Shroud Support Machining Tool

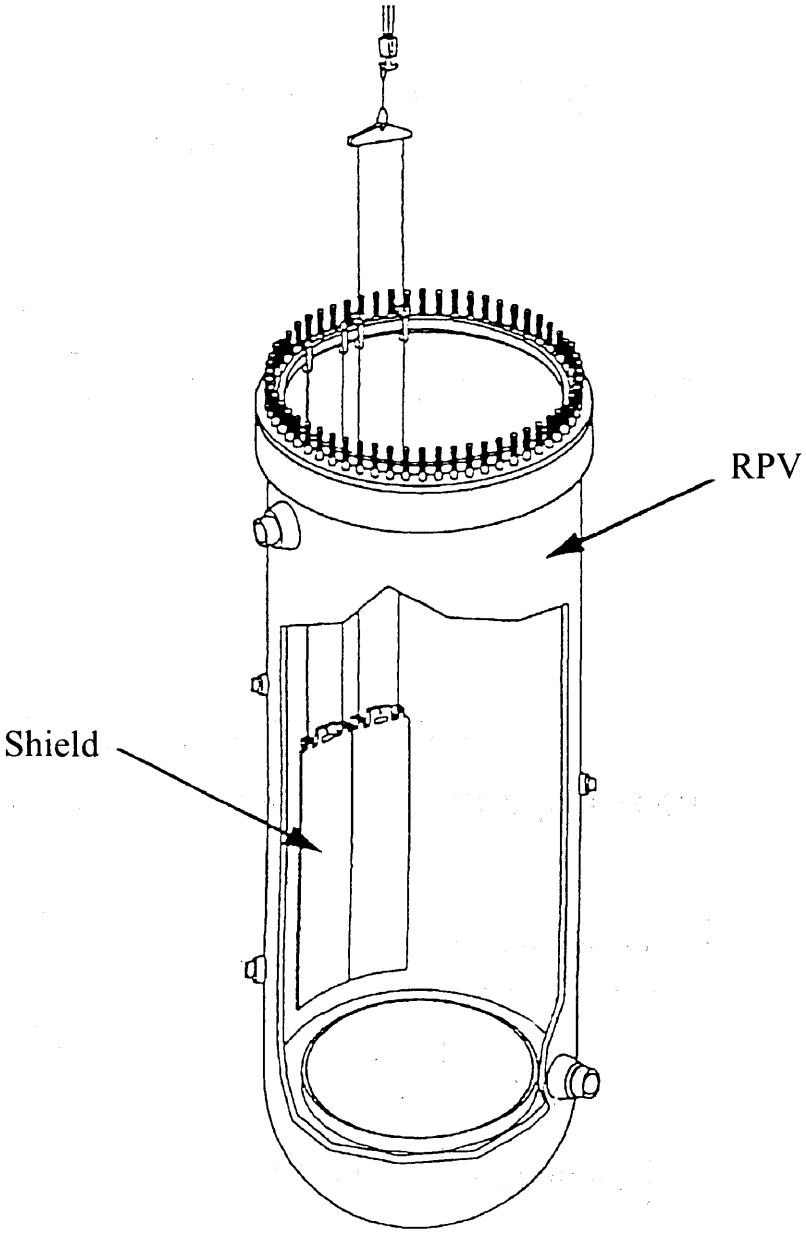


Figure 6 In-Vessel Shielding

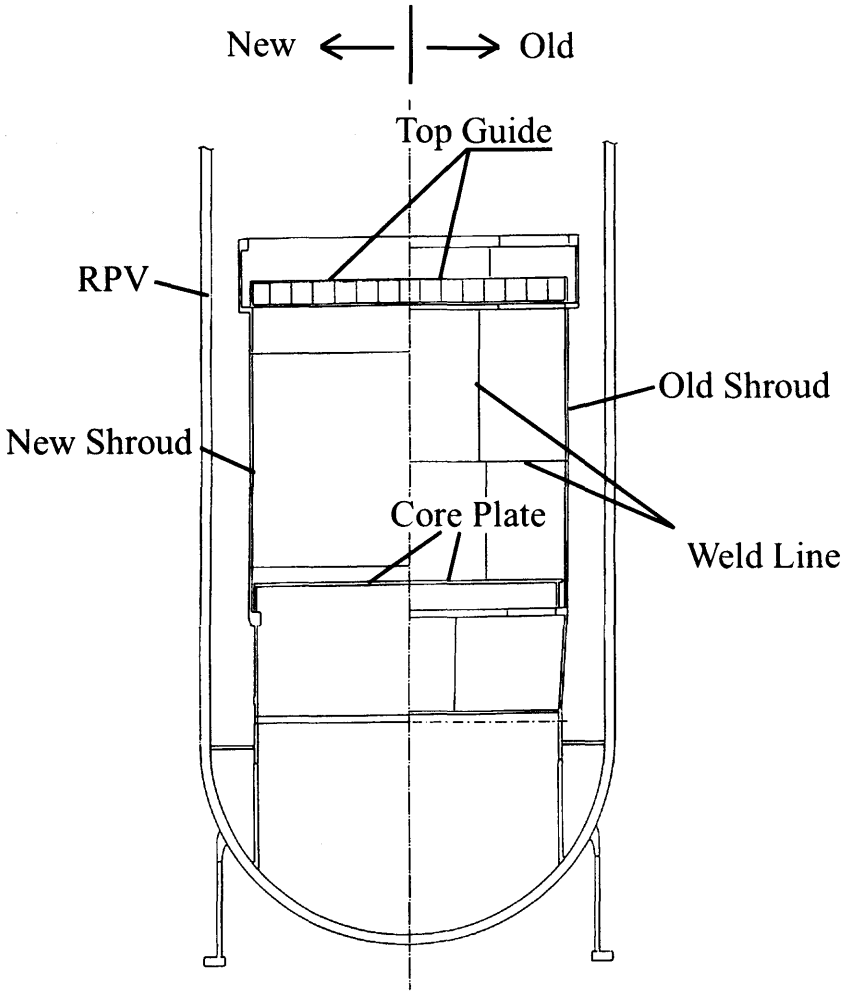


Figure 7 Old and New Shroud Structure

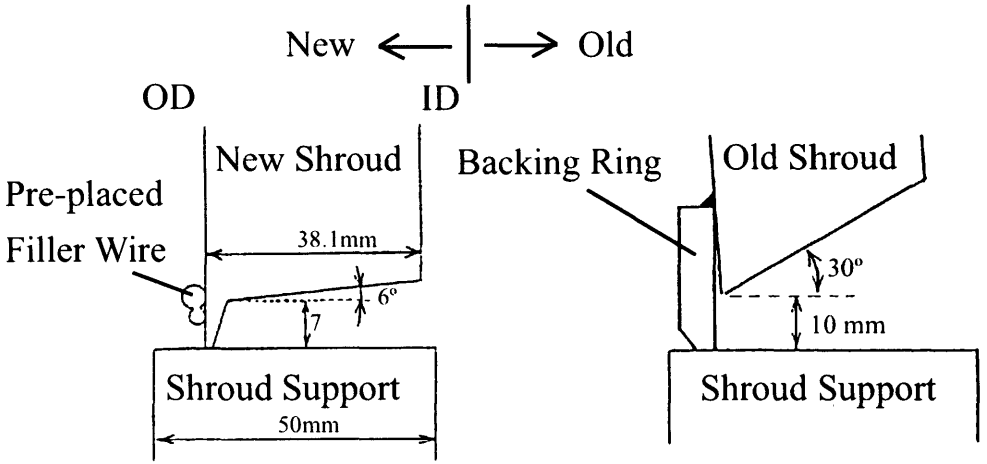


Figure 8 Old and New Design of Joint Between Shroud and Shroud support

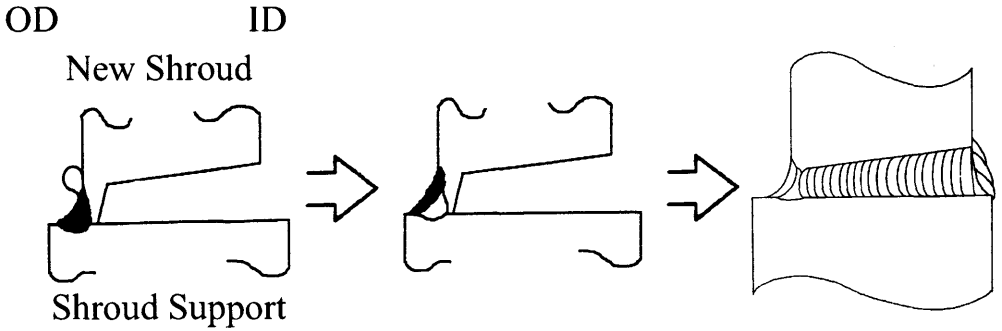


Figure 9 Weld Sequence
(New Shroud / Shroud support)

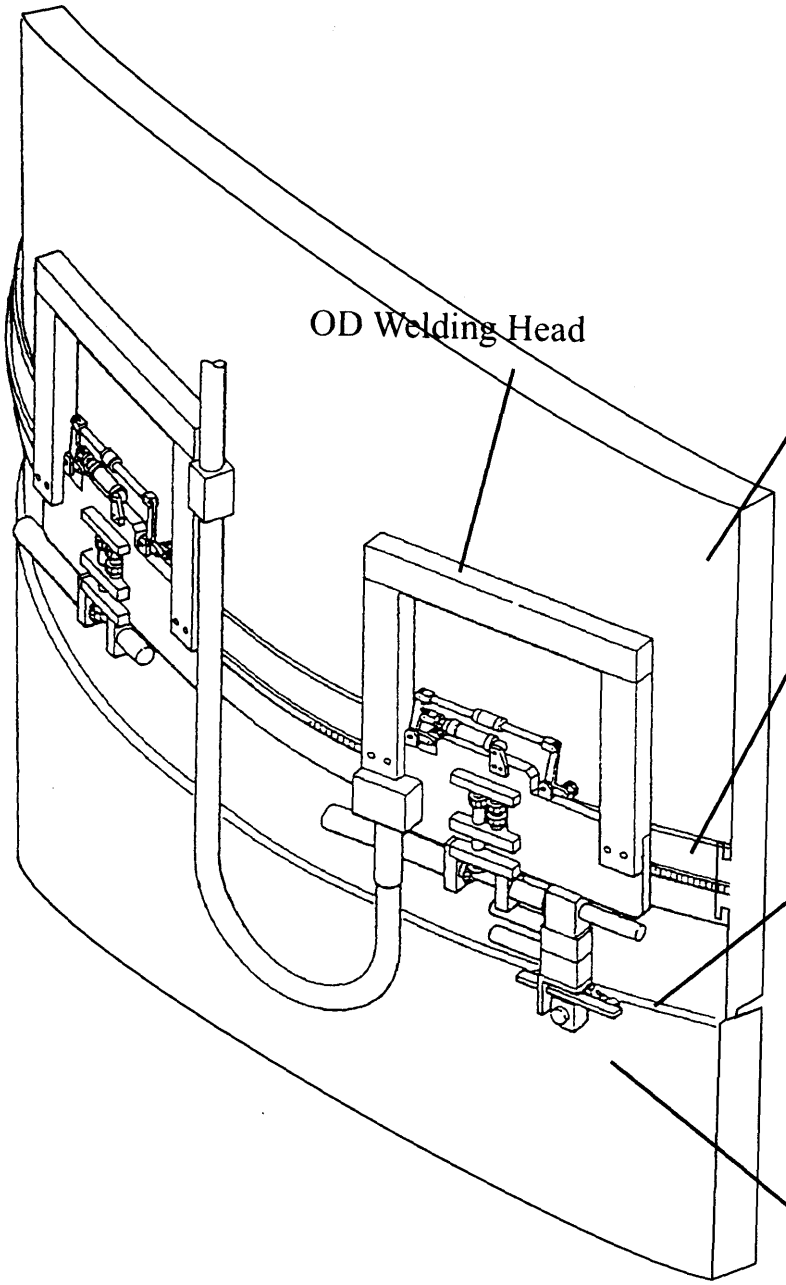


Figure 10 OD Welding Machine

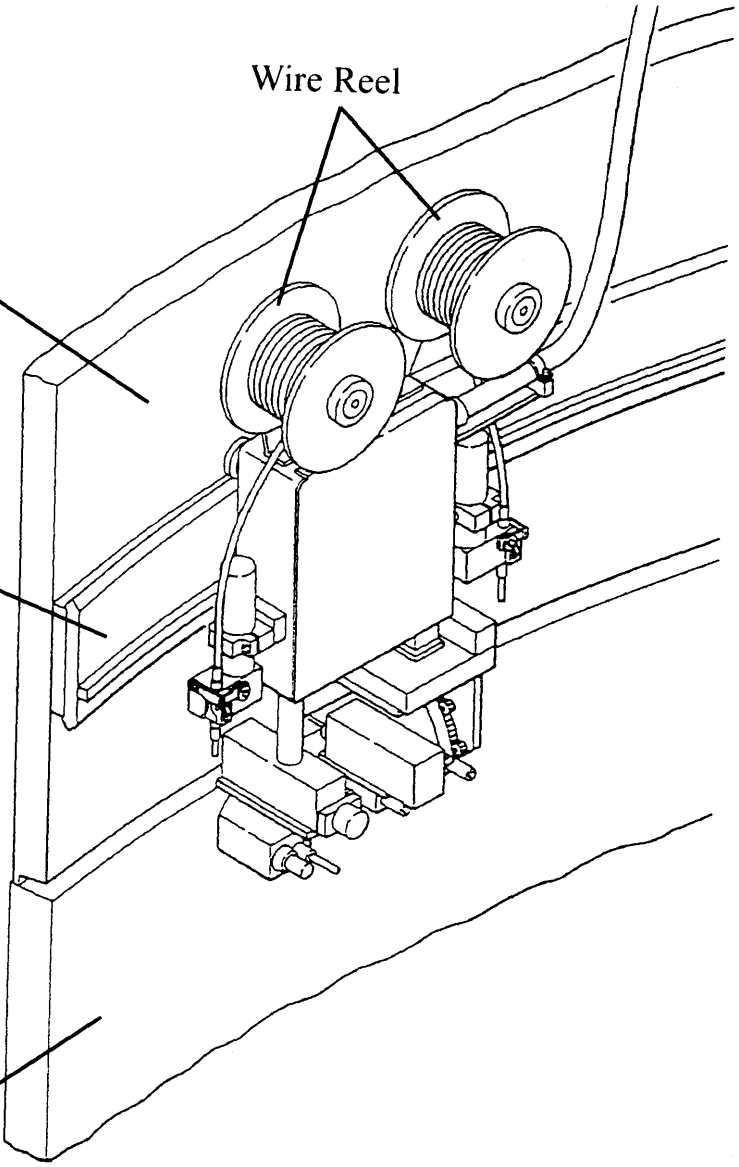


Figure 11 ID Welding Machine

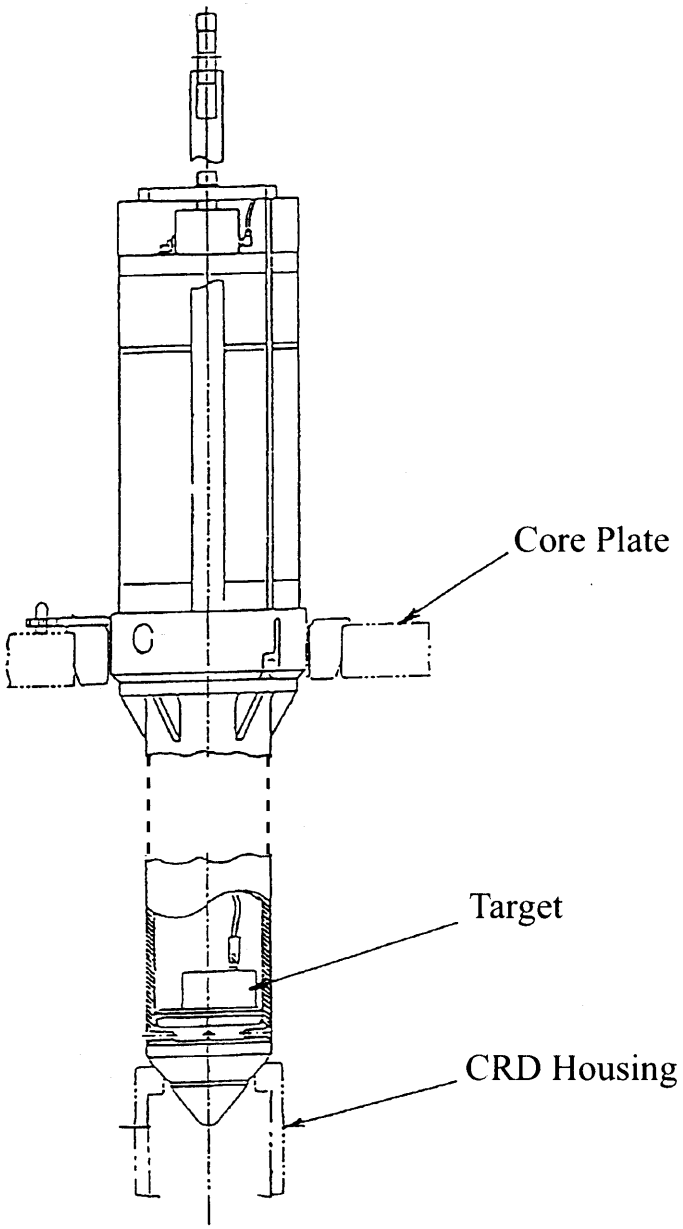


Figure 12 Alignment Tool

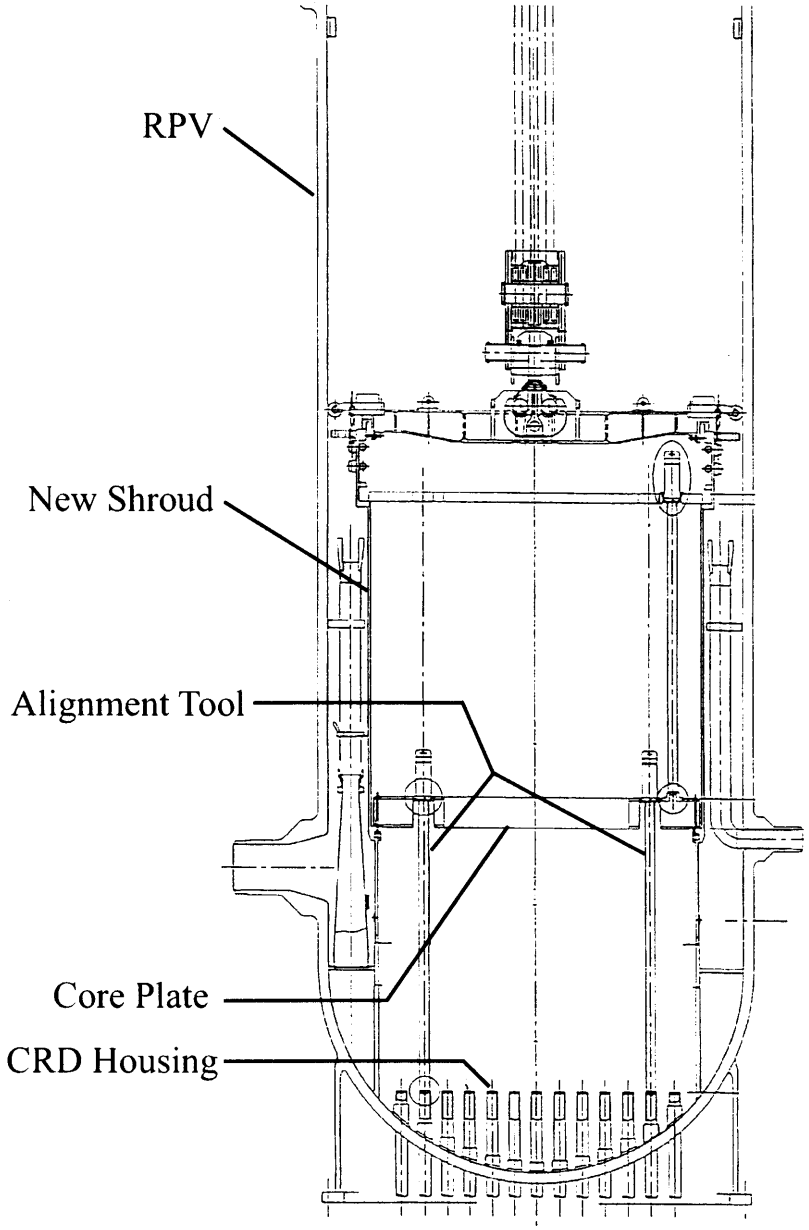


Figure 13 Core Plate Alignment

III-4 The Evaluation of Erosion-Corrosion Problems of PWR Carbon Steel Piping in Taiwan

Kuen Ting, Department of Nuclear Regulation Atomic Energy Council, Taiwan, Republic of China

Yin Pang Ma, Institute of Nuclear Energy Research Atomic Energy Council, Taiwan, Republic of China

# THE EVALUATION OF EROSION/CORROSION PROBLEMS IN TAIWAN PWR CARBON STEEL PIPING

**Kuen Ting**
Department of Nuclear Regulation
Atomic Energy Council
Republic of China

**Yin Pang Ma**
Institute of Nuclear Energy Research
Atomic Energy Council
Republic of China

## ABSTRACT

Taiwan PWR Nuclear Power Plant Units 1 and 2 implemented the measurements of the wall thinning of the carbon steel piping under the request of regulation authority to prevent the events due to the erosion/corrosion since 1989. At the first, the licensee established the comprehensive inspection program by itself. Over 2000 components were inspected per each unit and 300-500 pipe components were examined by ultrasonic testing per scheduled outage. The simple predictive methodology determined the operability of each individual piping component in the next fuel cycle. Based on the inspection results, the susceptible pipe components were established. The implementation of the effective correction management and improved inspection program can improve the safety, as well as the efficiency, of long-term reactor operations.

## INTRODUCTION

Erosion/corrosion is a piping degradation process that induces the pipe wall thinning. The oxide layer on the carbon steel pipe is dissolved by single-phase or two-phase flow in the nuclear power plant[1]. In 1989, the regulatory authority requested the licensee of Taiwan nuclear power plants to develop their own inspection program to prevent the failure of piping due to erosion/corrosion damage. The licensee established a full scope of pipe wall thickness database through "Pipe Wall Thinning Measurement Program"[2]. Over 2000 pipe components were selected per each unit and 300-500 pipe components were examined by ultrasonic testing per scheduled outage. Based on the inspection results and the analytical method, the evaluation of the susceptible pipe components in the licensee inspection program was established during each scheduled outage. This paper will discuss the implementation of this

effective management and the inspection program. The efforts can improve the safety, as well as the efficiency, of long-term reactor operations.

## INSPECTION PROGRAM

In 1989, after a severe piping rupture at Surry nuclear plant, the regulatory authority requested the licensee to develop the plant specific-monitoring program to prevent the failure of piping due to erosion-corrosion damage. The licensee, Taiwan Power Company (TPC), established the comprehensive inspection program to measure the thickness of most of the carbon steel piping components in the balance of the plant. The inspected components consist of straight pipes, elbows, tees and expanders/reducers in the feedwater, condensate, extraction, heater drain and reheater drain systems. The detailed configurations for measured points in each typical component are displayed as Figure 1.

The evaluation method of the inspection program is based on the measured data. The thinning due to erosion/corrosion wear $T_{ec}$ can be calculated as

$T_{ec} = T_l - T_s or T_n - T_s$ (if no inspection data for reference)

$T_{ec}$ =(previous measured thickness)-(present measured thickness)

In which $T_l$ and $T_s$ are the maximum and minimum measured thickness, respectively. $T_n$ is the nominal thickness. The wear rate can be defined as

$W_r = T_{ec} / H$

where $H$ is the operating hours between two inspection intervals. The allowable wear thickness $T_r$ is

$T_r = T_s - T_m$

where $T_m$ is the required thickness from the stress report or by analysis.

Thus, the remaining time of operation , $L_r$ ,can be estimated as

$L_r = T_r / W_r$

The allowable number of remaining fuel cycles, $I_{cal}$ , can then be predicted as

$I_{cal} = L_r / (KO_c)$

where $K$ is safety factor, $1.5 < K < 2.5$ , $O_c$ is the estimated operating hours of the next fuel cycle.

The total number of the selected pipe components was greater than two thousand per PWR unit. However, the capacity of realistic ultrasonic testing was only three to five hundred pipe components per outage. So, one PWR plant needs at least seven outages to examine all selected components and build up the complete database of the wall thinning.

## OBSERVATIONS OF THE INSPECTION

The measured data from four outages have been studied according to the type of the pipe components, such as 90° elbow, 45° elbow, reducer, tee and straight pipe. Figure 2 displays the occurrences of the thinnest thickness versus measured points for all inspected 90° elbows. The position B5 that is the outward bent of the elbow had the majority of the occurrences of the thinnest thickness. Almost 70% of all inspected elbows show that this region is easily erosive owing to the change of the flow direction. This phenomenon is also found in the 45° elbow inspection as shown in Figure 3. The majority of the worst thinning occurs at the location B3 which is the outward bent of the elbow.

For the erosion/corrosion of the reducer, the thinnest thickness locates at the two ends A1, A4, D1 and D4 as shown in Figure 4. The fraction of these locations is approximately 90%.

The distribution of the thinnest thickness is uniform for tee components in Figure 5. According to the experience, B and C sectors are not easily subjected to erosion/corrosion. However, Figure 5 revealed that B and C sectors with 38% are the positions of the thinnest thickness.

From Figure 6 presents the statistical distribution of the measured data for straight pipe. The inlet position is the susceptible location for erosion/corrosion as anticipated.

## THE EVALUATION OF THE POTENTIAL RISK OF THE CARBON STEEL PIPING UNDER EROSION/CORROSION

The ultrasonic inspection program of carbon steel piping due to erosion/corrosion was comprehensive. An analytic method to evaluate the potential risk of the carbon steel piping subjected to erosion/corrosion is necessary. Berge's model[3] assumed the soluble iron species production and mass transfer effect on the erosion corrosion rate. Thus, the total erosion/corrosion rate $V_C$ is expressed as:

$$V_C = \frac{K_1 K_2}{K_1 + K_2}(C_{eq} - C_\infty)$$

where $C_\infty$ is the soluble ferrous ion concentration at the bulk water; $K_1$ is the reaction constant which depends on fluid velocity and water temperature; $K_2$ is mass transfer coefficient which depends on the Sherwood number $Sh = \alpha_1 \mathrm{Re}^{\alpha_2} Sc^{\alpha_3}$, Re and Sc are the Renolds number and Schmidt number, respectively; $\alpha_1$, $\alpha_2$ and $\alpha_3$

are constants which depend on the pipe component geometry. $C_{eq}$ is the equilibrium soluble ferrous ion concentration at the oxide layer which depends on the pH value and the coolant temperature. In present work, $C_{eq}$ is expressed as

$$C_{eq} = \alpha_4 \exp[\frac{-(T-\alpha_5)^2}{\alpha_6}] + \alpha^7$$

where these constants are dependent of pH values.

The calculation results of the present model are in good agreement with the referenced data from the previous experimental works [4-6] as shown in Figure 7, 8 and 9. The parameters studied here are simulation to the realistic environments of PWR nuclear power plants. The values of pH, the fluid temperature and fluid velocity in PWR are ranged from 8.9 to 9.5, $300°C$ to $500°C$ and 1m/sec to 4m/sec. The presented model also shows the good relations with the measured data of the PWR realistic conditions ranging from $120°C$ to $230°C$ and the velocity over 1m/s.

Based on the predicted analysis, the carbon steel piping system, such as condensate system, feedwater system, main steam system, extraction steam system and drain system, are categorized into 36 groups to evaluate the potential relative risk of the pipe systems of the PWR plant under the attack of erosion/corrosion. The first column of Table 1 shows the categorized groups which are divided by the critical component. For example, the critical components of the feedwater system consider as feedwater pump, HP heater 1 and 2, steam generator. Thus, the feedwater system is categorized as three groups to evaluate the behaviors with erosion/corrosion. The pipe diameter, flow rate, steam quality nominal thickness and allowable thickness are the input parameter for the prediction of the rate of erosion/corrosion and the life of the carbon steel pipe components as listed in the last two column of Table 1. The superscripts "*" notes "the not-used-normally" pipe components which are not used during normal operation. The pipes from the 3rd stage feedwater heater dump to the condenser are the most dangerous pipes for not-used-normally pipes, if the upstream level control valves of the pipe components are leaking, the water flashing in the level control valves due to the high pressure gradient across the valves may cause the wall thickness of the down stream pipe components to thin and exceed the limitation within one fuel cycle[7].

## RESULTS AND DISCUSSIONS

Based on the prediction as mentioned above, the damage of the two-phase pipe

components is worse than the single-phase pipe components. The extraction lines from the high pressure turbine to the first stage feedwater heaters in which the steam quality is ranges from 88% to 95% were the high risk of the erosion/corrosion. The pipe components in the following pipes are also highly susceptible, such as:

(1). from the 4th stage feedwater heaters to the 3rd stage feedwater heaters,
(2). from the 3rd stage feedwater heaters to feedwater pumps,
(3). from the drain pumps to the feedwater pumps,
(4). from the 2nd stage feedwater heaters to the drain tank,
(5). from the drain tank to the drain pumps,
(6). from the 2nd reheater to the first feedwater heaters.

Table 2 describes the records of the replacements of the pipe components during each outage. The extraction lines and the exhaust lines are the highly replacement rate which are consistent with the predicted work as shown in Table 1.

## CONCLUSION

The actual operating conditions in the nuclear power plants cannot be effectively controlled as stringently as in the laboratory, and the analytical predictions and inspection program are not so reliable as anticipated. To avoid the erosion/corrosion damage, the current inspection program should be improved by a proper analytical method and engineering judgment.

The present work provides a pipe erosion/corrosion inspection program and analytical method to assist the relevant engineers in making engineering judgment and to find out the susceptible pipe components and to evaluate the relative potential risk of the pipe components. The results are helpful for the engineers to renew and audit the monitoring prioritization of the pipe components.

REFERENCE

1. U.S. Nuclear Regulatory Commission Bulletin 87-01, "Thinning of pipe walls in nuclear power plants," July 9, 1987.
2. Taiwan Power Company, Nuclear power plant pipe wall monitoring program, NED-NPS-0001, R2, TAIPOW, June, 1989.
3. J.P. Berge et al., Effect of chemistry on corrosion-erosion of steels in water and wet steam, Proceeding of 2nd Conference on Water Chemistry, BNES, 1980.
4. ASM International Handbook Committee, Metals Handbook, 9th edition, Vol.13, Corrosion.
5. J.P. Goffin, Thickness measurements of pipes submitted to erosion and corrosion problems in the steam, feedwater and condensate systems of the Doel 1 and 2 power plants, International Atomic Energy Agency (IAEA) Specialist Meeting on

Erosion/Corrosion, September 12-14, Vienna, Austria, 1988.
6. M. Bouchacourt, Flow assisted corrosion in power plants-part 1: The EDF research program, International Atomic Energy Agency (IAEA) Specialist Meeting on Erosion/Corrosion, September 12-14, Vienna, Austria, 1988.
7. H.J. Chao and Y.P. Ma, User's manual for nuclear power plant pipe erosion/corrosion data base system, INER-1215, May, 1994.

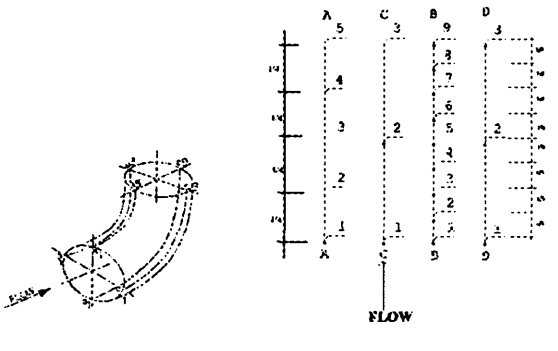


(a) 90° elbow

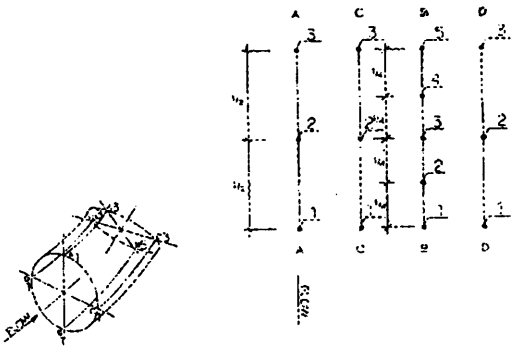

(b) 45° elbow

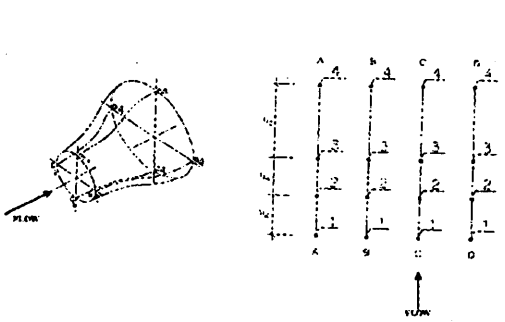

(c) reducer

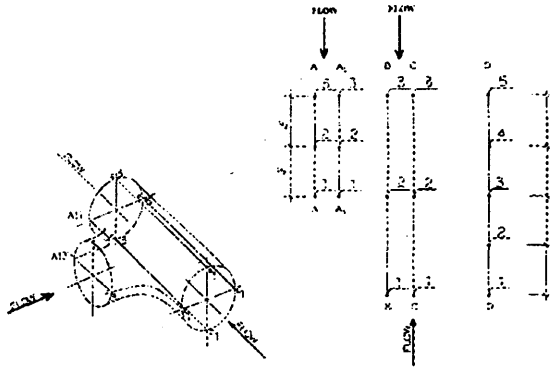

(d) tee

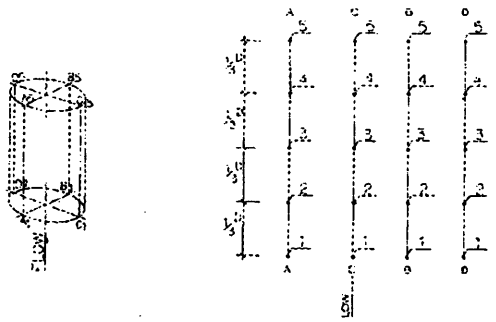

(e) straight pipe

Figure 1. Detailed configurations for measured points in inspection components

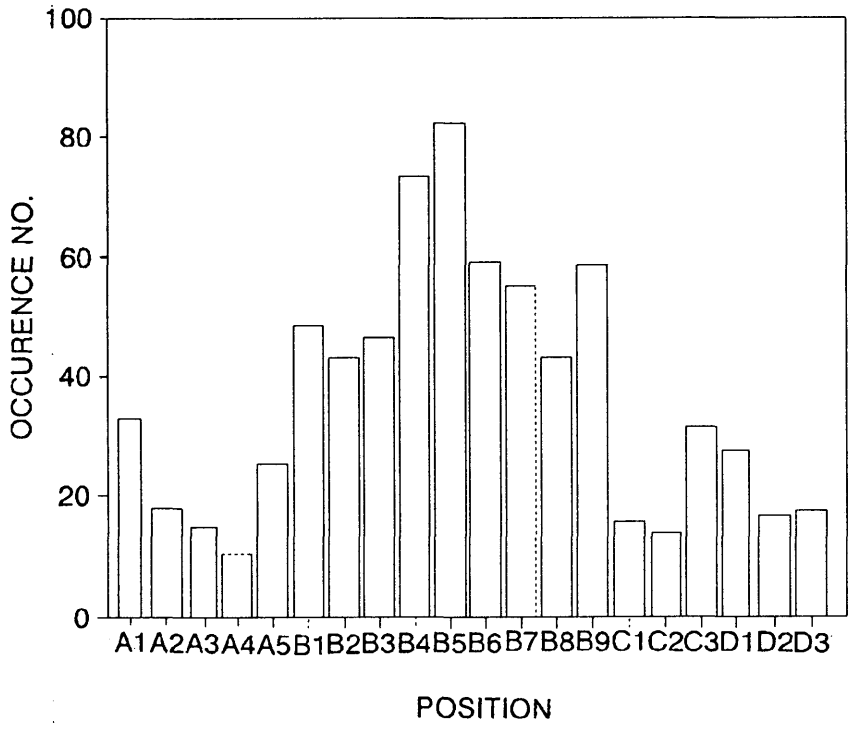


Figure 2. Statistical analysis of the measured thinnest position for 90° elbow

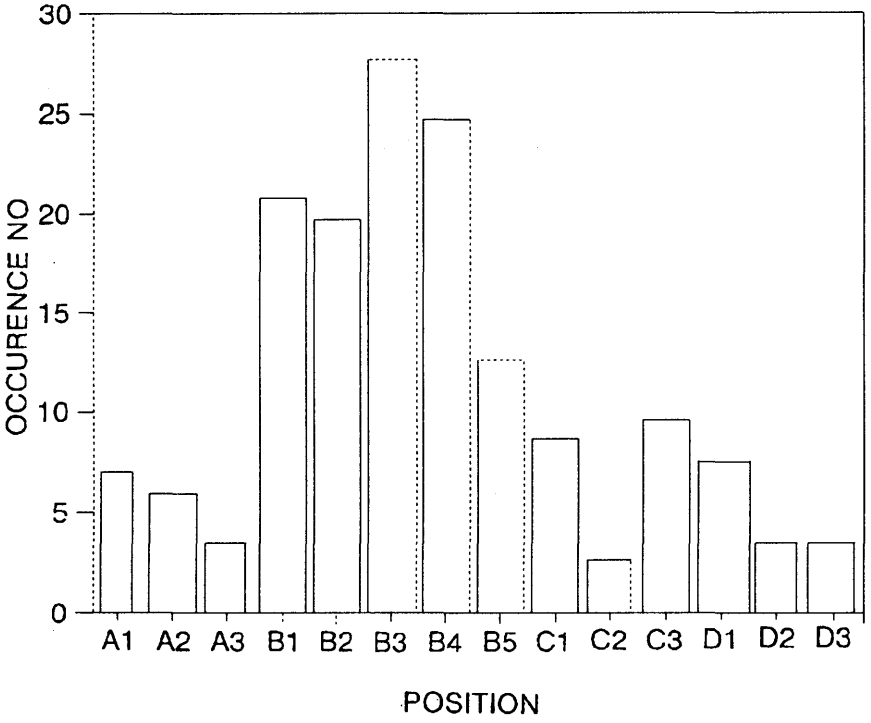


Figure 3. Statistical analysis of the measured thinnest position for 45° elbow

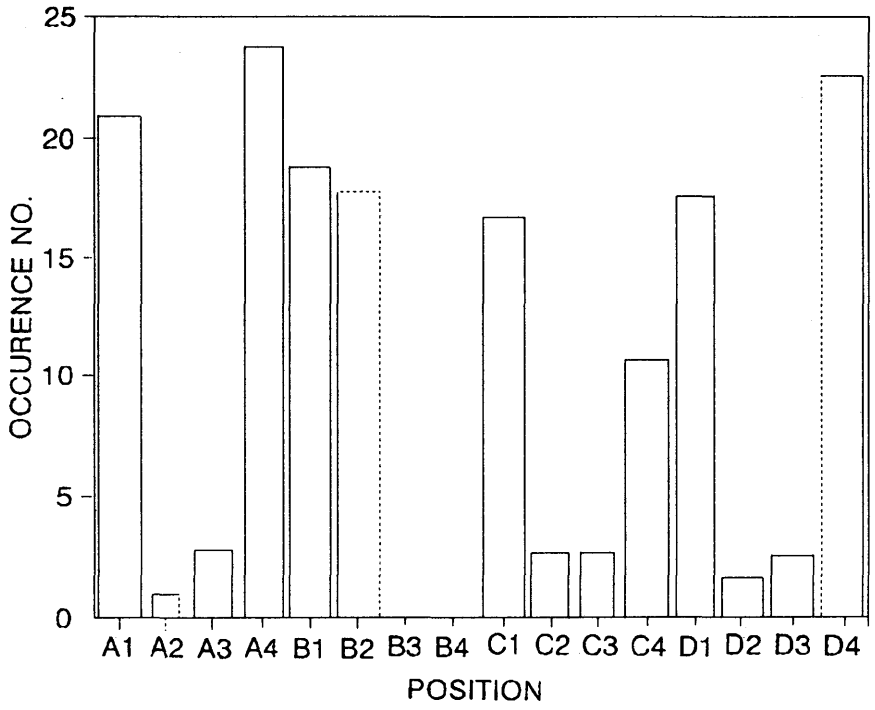


Figure 4. Statistical analysis of the measured thinnest position for reducer

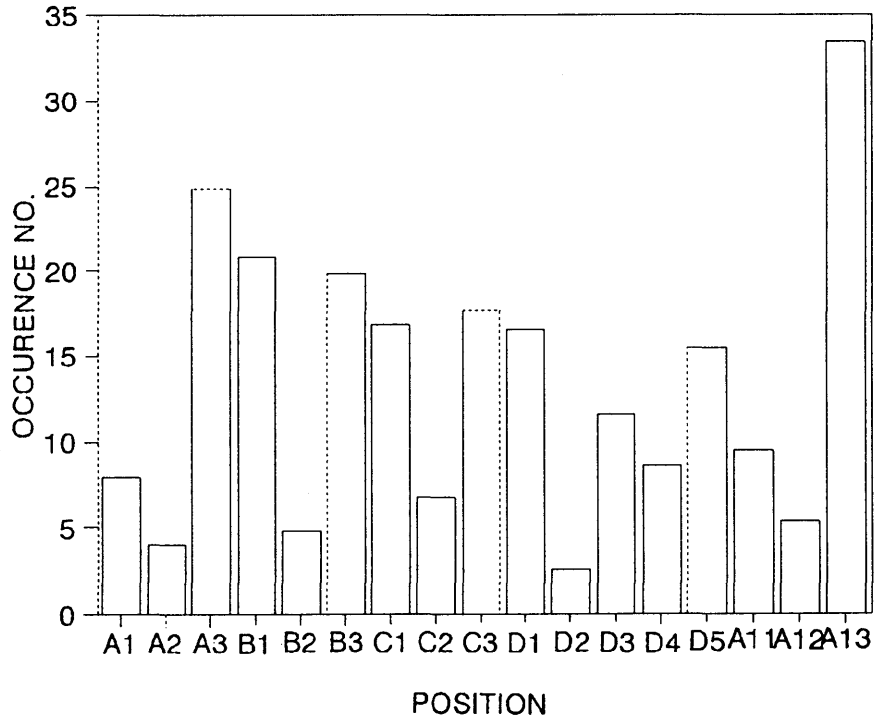


Figure 5. Statistical analysis for the measured thinnest position for tee

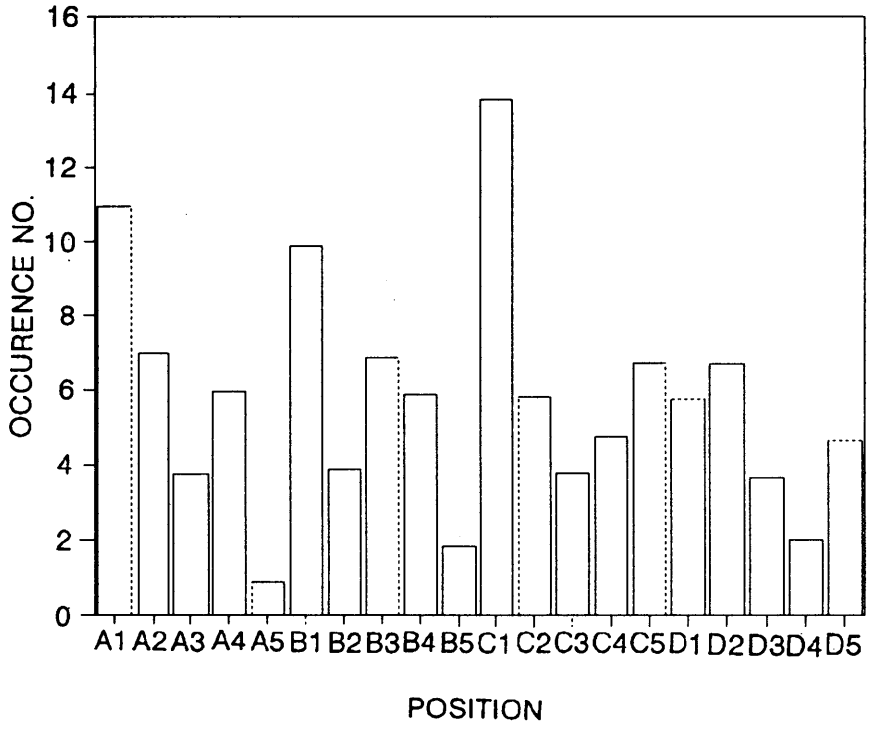


Figure 6. Statistical analysis of the measured thinnest position for straight pipe

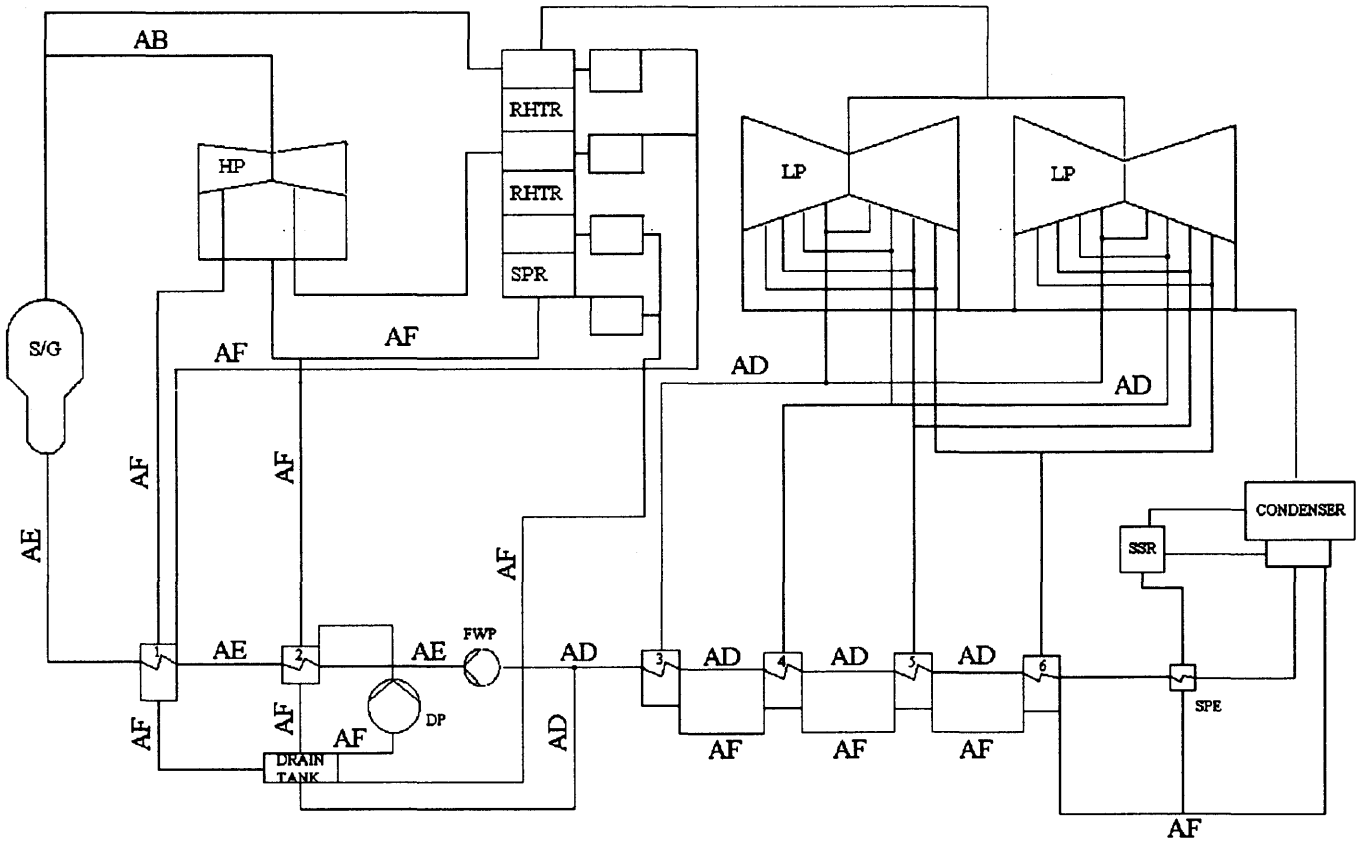


Figure 7. The sketch of the balance of plant for PWR nuclear power plant

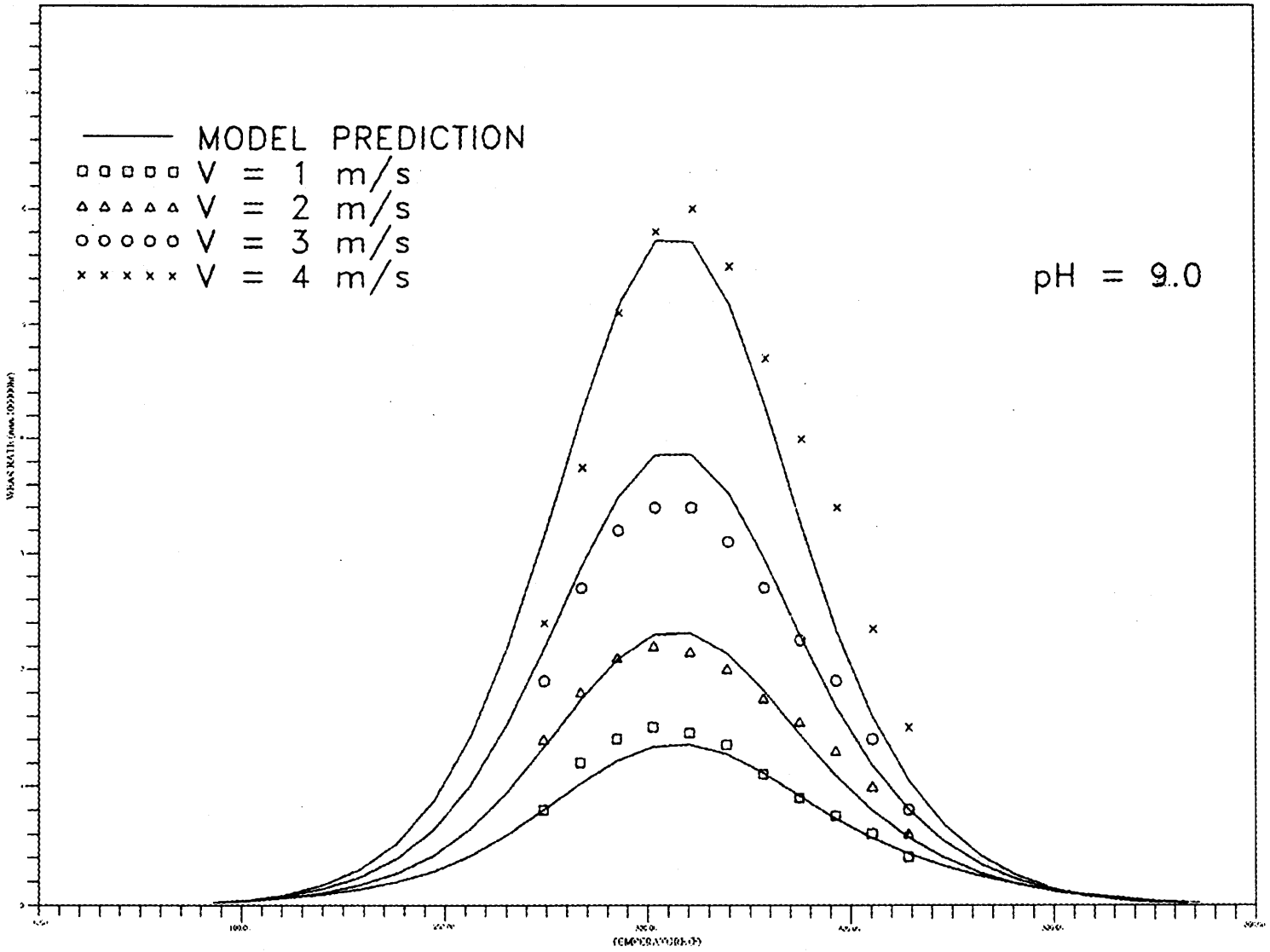


Figure 8. Comparison of wear rate between calculation and experimental data versus temperature for low velocity (Experimental data from reference[6])

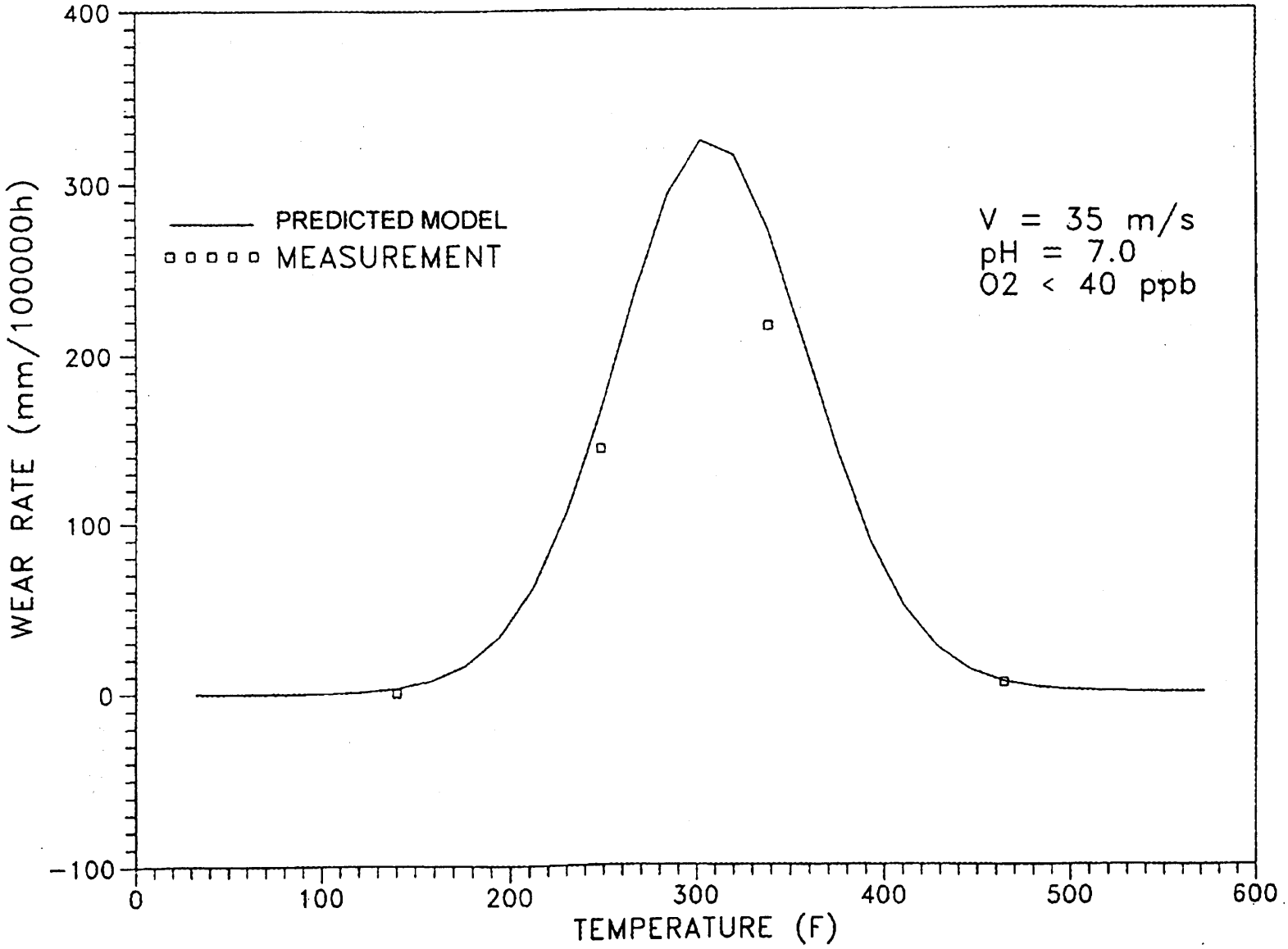


Figure 9. Comparison of wear rate between calculation and experimental data versus temperature for high velocity [Experimental dada from reference(5)]

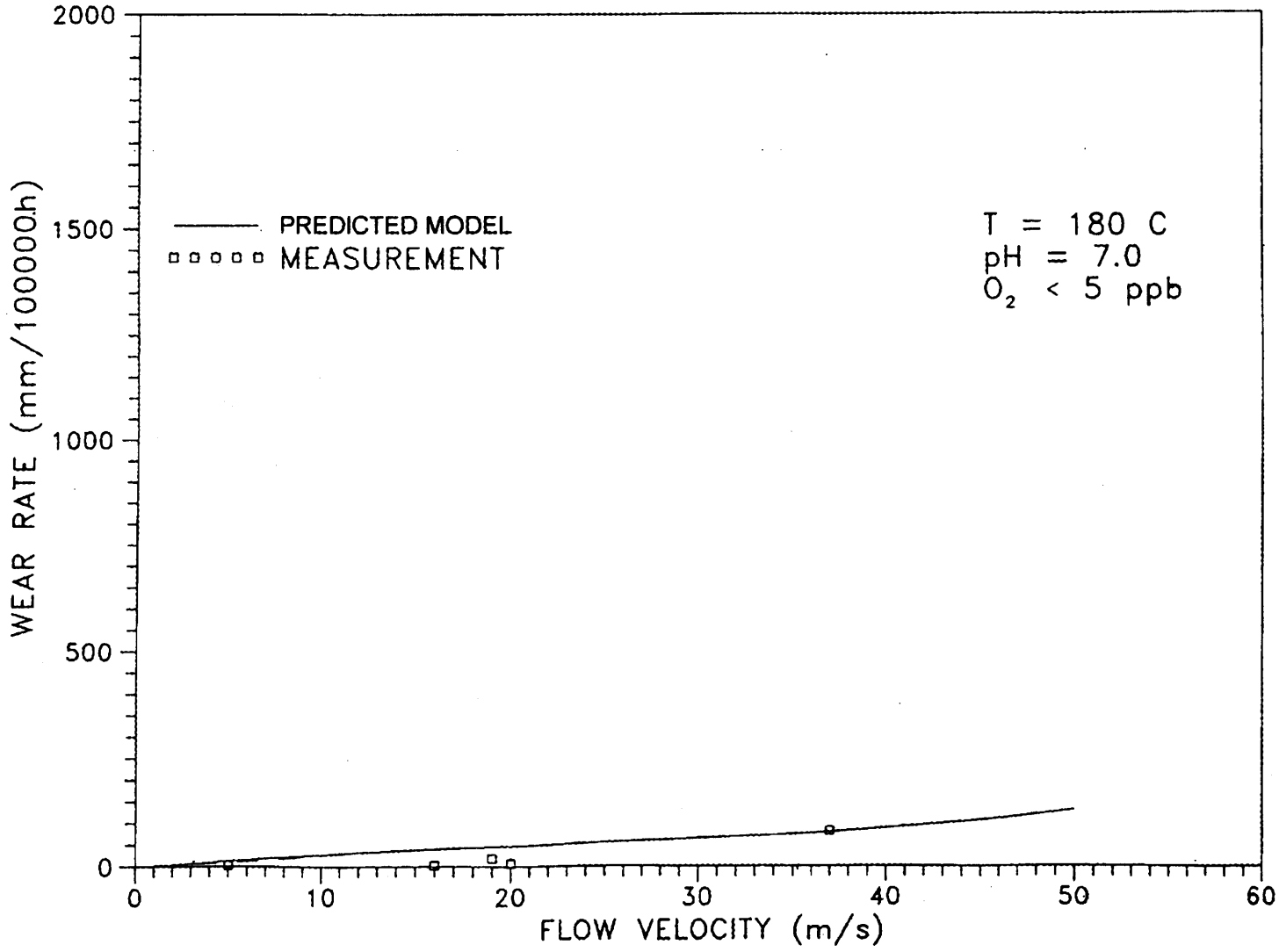


Figure 10. Comparison of wear rate between calculation and experimental data versus flow velocity

# Table 1 Risk Category of Piping due to Erosion/Corrosion

| | Diameter (inch) | Reference Temperature (°F) | Reference Flow Rate (ft/sec) | Steam Quality (%) | Nominal Thickness (mils) | Minimum. Thickness (mils) | Predicted .erosion/corrosion Rate(mil/yr) | Usable time (years) |
|---|---|---|---|---|---|---|---|---|
| 1.condenser to condensate pump | 30 | 103 | 3.1 | 0 | 375 | 101 | <1 | >40 |
| 2.condensate pump to steam packing exhauster | 24 | 103 | 18.8 | 0 | 687 | 601 | <1 | >40 |
| 3.steam packing exhauster to the LP heater 6 | 24 | 105 | 18.8 | 0 | 687 | 601 | <1 | >40 |
| 4.LP heater 6 to LP heater 5 | 20 | 178 | 14.2 | 0 | 593 | 519 | <1 | >40 |
| 5.LP heater 5 LP heater 4 | 20 | 229 | 14.2 | 0 | 593 | 519 | 2.75 | 27 |
| 6.LP heater 4 to LP heater 3 | 20 | 297 | 15 | 0 | 593 | 519 | 7.81 | 9.5 |
| 7.LP heater 3 to feedwater pump | 30 | 335 | 19.3 | 0 | 750 | 656 | 9.15 | 10.3 |
| 8.feedwater pump to HP heater 2 | 20 | 346 | 19.5 | 0 | 1281 | 1121 | 9.90 | 16.2 |
| 9.HP heater 2 to HP heater 1 | 20 | 374 | 19.9 | 0 | 1281 | 1121 | 5.84 | 27.4 |
| 10.HP heater 1 to steam generator | 20 | 438 | 20.9 | 0 | 1281 | 1121 | 1.33 | >40 |
| 11.steam generator to HP turbine | 26 | 540 | 34.9 | 99.9 | 1250 | 1094 | <1 | >40 |
| 12.Main steam extracted to MSR reheater 2 | 10 | 540 | 8.00 | 99.9 | 500 | 437 | 1.07 | >40 |
| 13.HP turbine extracted to MSR reheater 1 | 10 | 469 | 18.4 | 94 | 365 | 298 | 12.58 | 5.3 |
| 14.HP turbine extracted to HP heater 1 | 16 | 445 | 24.5 | 92 | 375 | 328 | 26.25 | 1.8 |
| 15.HP turbine extracted to HP heater 2 | 18 | 382 | 13.2 | 88 | 375 | 236 | 61.18 | 2.3 |
| 16.MSR reheater 2 exhaust to drain tank 2 | 10 | 540 | 3.2 | 10 | 500 | 437 | <1 | >40 |
| 17.MDR reheater 1 exhaust to drain tank 1 | 12 | 470 | 3 | 10 | 375 | 328 | 1.56 | 30 |
| 18.MSR reheater drain to MSR drain tank | 16 | 385 | 6.4 | 10 | 375 | 218 | 6.97 | 22.5 |
| 19.MSR reheater drain tank 2 drain to HP heater 2 | 10 | 445 | 34.3 | 13.5 | 365 | 255 | 10.49 | 10.5 |
| 20.MDR reheater drain tank 1 drain to HP heater 1 | 6 | 445 | 8.8 | 3.85 | 280 | 168 | 2.6 | >40 |
| 21.MSR drain tank drain to heater drain tank | 10 | 385 | 6.2 | 0.2 | 365 | 215 | 4.2 | 35.7 |
| 22.HP heater 1 drain to heater drain tank | 14 | 385 | 9.3 | 0.6 | 375 | 260 | 6.2 | 18.5 |
| 23.HP heater 2 drain to heater drain tank | 14 | 385 | 1.9 | 28 | 375 | 260 | 9.59 | 12 |
| 24.heater drain tank to heater drain pump | 16 | 370 | 8.4 | 0 | 375 | 28.6 | 6.53 | 13.6 |
| 25.heater drain pump to feedwater pump | 16 | 370 | 17.3 | 0 | 500 | 437 | 15.73 | 4 |
| 26.LP heater 3 drain to LP heater 4 | 8 | 303 | 6.8 | 0.5 | 322 | 97 | 9.19 | 24.5 |
| 27.LP heater 4 drain to LP heater 5 | 14 | 236 | 10.6 | 0.55 | 375 | 129 | 6.64 | 37 |
| 28.LP heater 5 drain to LP heater 6 | 18 | 172 | 14.8 | 0.57 | 375 | 141 | 1.76 | >40 |
| 29.LP heater 6 drain to condenser | 16 | 113 | 30.8 | 0.95 | 375 | 110 | <1 | >40 |
| 30.LP heater 5 drain to condenser | 14 | 172 | 34.2 | 6.8 | 375 | 117 | 5.44 | >40* |
| 31.LP heater 4 drain to condenser | 10 | 236 | 5.1 | 13 | 365 | 114 | 6.06 | >40* |
| 32.LP heater 3 drain to condenser | 8 | 303 | 98.7 | 19.9 | 322 | 107 | 416.7 | 0.52* |
| 33.HP heater 1 drain to condenser | 12 | 388 | 8.1 | 29 | 406 | 297 | 18.9 | 5.8* |
| 34.MSR drain tank drain to condenser | 10 | 381 | 25.8 | 28.2 | 365 | 135 | 77.6 | 3.0* |
| 35.reheater drain tank 1 drain to condenser | 6 | 470 | 26.3 | 37.12 | 280 | 94 | 11.13 | 16.7* |
| 36.reheater drain tank 2 drain to condenser | 8 | 540 | 14 | 44 | 322 | 114 | <1 | >40* |

Table 2 Replacement Records of Piping due to Erosion/Corrosion

| Unit 1 | | | | | | | | Unit 2 | | | | | | | |
|---|---|---|---|---|---|---|---|---|---|---|---|---|---|---|---|
| Inspection Interval | No. of Replaced Components | No. of Replaced Components in Systems | | | | | | Inspection Interval | No. of Replaced Components | No. of Replaced Components in Systems | | | | | |
| | | AB | AC | AD | AE | AF | FA | | | AB | AC | AD | AE | AF | FA |
| EOC-3 | 1 | | 1 | | | | | EOC-3 | 1 | | | | | 1 | |
| EOC-4 | 2 | | | 2 | | | | EOC-4 | 1 | | | | | 1 | |
| EOC-5 | 6 | | | 1 | | 5 | | EOC-5 | 4 | 3 | | | | 1 | |
| EOC-6 | 13 | 1 | 2 | 2 | | 8 | | EOC-6 | 18 | 1 | 2 | | | 15 | |
| EOC-7 | 27 | 2 | 3 | 5 | | 17 | | EOC-7 | 34 | 2 | 8 | 1 | 1 | 22 | |
| EOC-8 | 11 | | 1 | 1 | | 9 | | EOC-8 | 15 | 4 | 4 | 1 | 2 | 4 | |
| EOC-9 | 29 | | | | | 29 | | EOC-9 | 21 | | 1 | 2 | | 18 | |
| EOC-10 | 26 | | 6 | 3 | | 15 | 2 | EOC-10 | | | | | | | |
| Total | 115 | 3 | 13 | 14 | 0 | 83 | 2 | Total | 94 | 10 | 15 | 4 | 3 | 62 | 0 |

AB: Main steam system

AC: Main steam drain system

AD: Condensate system

AE: Feedwater system

AF: Feedwater heater extraction and drain system

FA: Auxiliary main steam system

2.EOC: End of Cycle

# Session IV

# Piping and LBB

IV-1 Development of Modified Piping Evaluation Diagram for LBB Application

Y.J.Kim, Y.Z.Lee & N.S.Huh, Dept. of Mechanical Engineering, Sung Kyun Kwan Univ., Suwon, Korea
C.R.Pyo, Dept.of Mechanical Engineering, Induk college, Seoul, Korea
J.S.Yang, Korea Electric Power Research Institute, Daejon, Korea

# Development of Modified Piping Evaluation Diagram for LBB Application to Korean Next Generation Reactor

**Y.J. Kim[a], Y.Z. Lee[a], N.S. Huh[a], C.R. Pyo[b], J.S. Yang[c]**

**[a]School of Mechanical Engineering, Sung Kyun Kwan Univ., Suwon, Korea**
**[b]Dept. of Mechanical Engineering, Induk Inst. of Technology, Seoul, Korea**
**[c]Korea Electric Power Research Institute, Daejon, Korea**

Recently, the Piping Evaluation Diagram (PED) is accepted in nuclear industry for an efficient application of Leak-Before-Break (LBB) concept to piping system at an initial piping design stage. The objective of this paper is to develop the modified PED which can account for the variation of the material properties of the PED development stage and those of the assembly stage. For this purpose, a parametric study was performed to investigate the effect of stress-strain curve on the detectable leakage crack length and the effect of fracture resistance curve on the LBB allowable load. Finite element analyses were also performed to investigate the effect of stress-strain curve on the LBB allowable load. Finally a modified PED was proposed as a function of crack length and the allowable safe shutdown earthquake load. The LBB analyses based on the modified PED are in good agreement with those based on the traditional PED. By adopting the modified PED, the variation of material properties can be considered in the LBB analysis and the computing times required for the application of LBB during the design process can be considerably reduced.

## 1. INTRODUCTION

The Leak-Before-Break (LBB) concept has been accepted as a justifiable approach for designing nuclear piping systems with the elimination of massive protective measures due to the pipe rupture design requirement. If the LBB concept is applicable to nuclear piping design, the construction cost can be significantly reduced by eliminating unnecessary pipe whip restraints and jet impingement devices. In order to apply the LBB concept to piping system, the nuclear piping design should meet all the criteria specified in NUREG 1061, Vol. 3[1] and Standard Review Plan 3.6.3[2]. Current LBB analyses on nuclear piping system are based on the plant-specific loads due to the geometry of the piping system and the operating condition of concerned piping system. Therefore, if the analysis results do not meet the LBB criteria, all the piping routing should be changed until the results are satisfactory. In performing LBB evaluation, highly specialized knowledge in fracture mechanics is required and lengthy period of time is required due to its complicated procedures and methods.

Recently, numerous studies have been reported on the applicability of LBB during the initial piping design stage. The "Allowable Load Window" using the maximum and the minimum moment of each piping was proposed by Nana and Yoon[3]. The "PED (Piping Evaluation Diagram)" using the Normal OPeration (NOP) load and the Safe Shutdown Earthquake (SSE) load was also proposed by Fabi et al.[4]. Swamy et al.[5] proposed the

"BAC (Boundary Analysis Curve)" using the stress at the normal operating condition and the maximum stress. Y.J.Kim et al.[6] developed the "PEDs" using the NOP load and the SSE load and applied for the safety injection and the shutdown cooling line in Korean Next Generation Reactor (KNGR). These diagrams were developed prior to the piping design and can be used for the evaluation of critical points for the LBB requirements in the piping system. Thus the iterative process of design to modification regarding the LBB applicability can be eliminated.

According to the current LBB criteria, the final LBB evaluation should be performed using the archival material properties. However, the PED may have to be modified to account for the difference between the material properties of the PED development stage and those of the assembly stage. The objective of this paper is to develop a modified PED which can account for the variation of the material properties and apply them to the safety injection line and the shutdown cooling line in KNGR.

## 2. DEVELOPMENT OF NUCLEAR PIPING MATERIAL DATABASE

NUclear PIping Material database (NUPIM database) was constructed prior to the development of the modified PED. The objective of NUPIM database is to obtain the material properties such as stress-strain curves and fracture resistance curves required for the modified PED. In designing nuclear piping systems, a plenty of material properties should be considered, and thus the development of NUPIM database which covers about 500 test data was essential.

Searching a material property in NUPIM database can be easily done owing to the hybrid database which is connected to the DBMS (DataBase Management System). This DBMS searches the selected item from the stored material properties. The material properties stored in database was obtained from domestic material test programs such as YGN 3&4[7], UCN 3&4[8] and the dynamic test for carbon steel[9].

Search index of database consists of material name, welding method, yield stress, pipe thickness, temperature, pipe size et al. In order to provide various material properties, a statistic calculation module with plenty of raw data has been attached to the database. Therefore, not only the material raw data but also pre-processed second hand material data can be easily obtained using NUPIM database.

## 3. PROCEDURE FOR DEVELOPING MODIFIED PED

### 3.1 General procedure

The general methodology and criteria used for developing the modified PED are based on NUREG 1061, Vol. 3 and SRP 3.6.3. The material properties required for the development of the modified PED were obtained from NUPIM database which consists of previous domestic LBB test results. Generally, the worst case material properties (worst stress-strain curve and worst fracture toughness) are used in the analysis for ensuring the conservatism of the LBB analysis. In this paper, an additional margin for the consideration of archival material properties, which are usually obtained at the final stage of the design process, was added by applying three different stress-strain curves in the LBB analysis. Different fracture resistance curves considering archival material properties were also used in the analysis.

Fig. 1 illustrates the analysis procedure applied for the modified PED development. In the

first step of the analysis, each piping was grouped by system, material, size, and geometry. In the second step, the NOP load range was established. In the third step, the Detectable Leakage Crack (DLC) length was calculated. In the fourth step, the applied *J*-integral for the DLC and twice the DLC length was computed. In the fifth step, from the applied *J*-integral and the material *J*-integral, *J/T* analyses were performed to find the instability point of the crack. In the sixth step, the SSE load range was calculated in accordance with the NUREG 1061, Vol. 3. Finally, the modified PED was developed as a function of crack length (the DLC and twice the DLC) and the allowable SSE load.

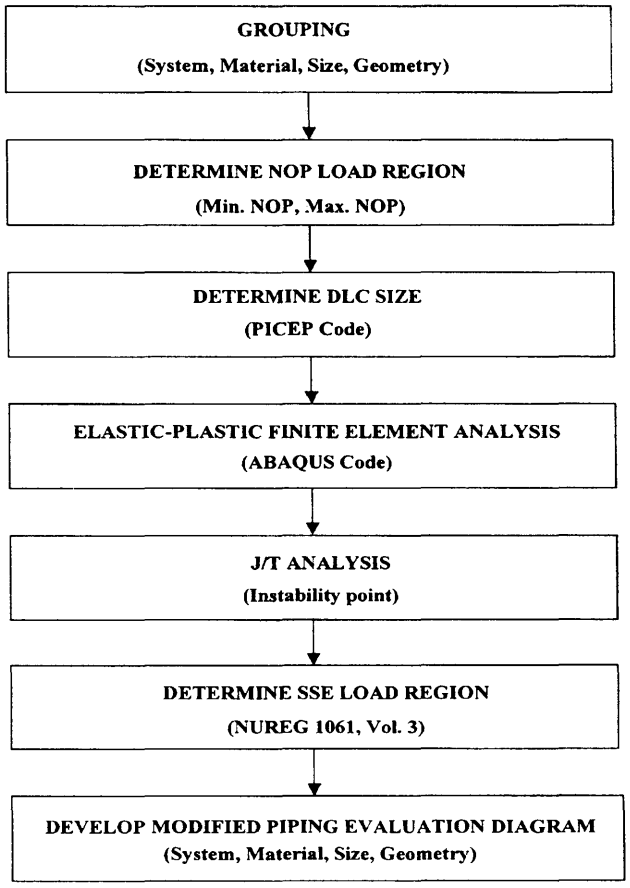


Fig. 1 Procedure for development of the modified PED

3.2 Grouping for LBB analysis

The LBB analyses were performed on the safety injection line and the shutdown cooling line in KNGR, which are classified by material, size and operating temperature as listed in Table 1. The minimum and the maximum NOP load ranges were set as wide as possible to apply to the KNGR, based on the actual load observed from the currently operating nuclear power plants.

3.3 Analysis of detectable leakage crack

For a given NOP load level, the DLC length which produces the 10 gpm leak rate was calculated by PICEP code[10] based on the NOP load and three different stress-strain curves; namely upper bound, best-fit, and lower bound. In order to assess the crack stability, two steps were involved. One is to assess the stability of a crack length equal to twice the DLC under (NOP+SSE) load, and the other is to assess the stability of a crack length equal to the DLC under $\sqrt{2}$ (NOP+SSE) load. Three dimensional elastic-plastic finite element analyses were carried out for both the DLC and twice the DLC using the commercial finite element program, ABAQUS[11]. Considering the symmetric condition, only one quarter of the pipe was modeled as shown in Fig. 2. A four-point bending condition was applied to create tensile crack opening mode at the crack tip area.

Table 1 Grouping for characteristics of each system

| Group | System | Material | O.D. (mm) | Thickness (mm) | Temp. (°F) |
|---|---|---|---|---|---|
| 1 | SI | SA312 TP304 | 356 | 9.5 | 122 |
| 2 | SI | SA312 TP316 | 356 | 35.7 | 565 |
| 3 | SI | SA312 TP316 | 273 | 28.6 | 565 |
| 4 | SI | SA312 TP316 | 324 | 33.3 | 120 |
| 5 | SC | SA312 TP316 | 406 | 40.5 | 621 |

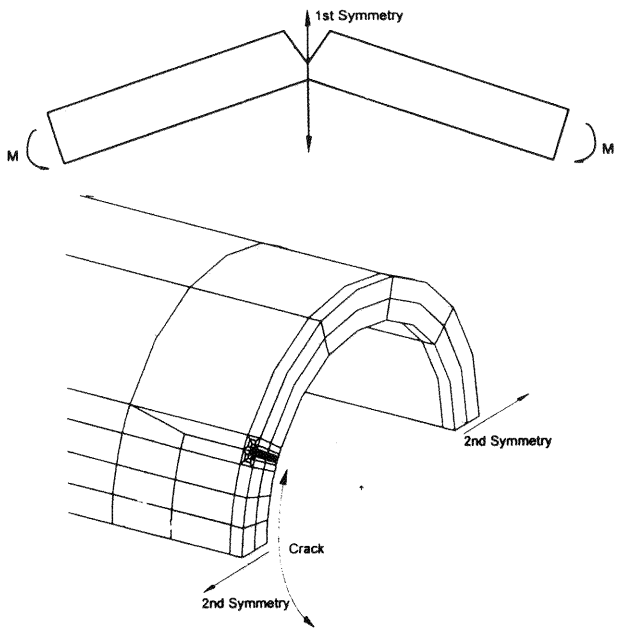


Fig. 2 Three dimensional mesh design for finite element analysis

3.4 Crack stability evaluation

For the crack stability evaluation, the *J*-integral / Tearing modulus (*J/T*) method was used. For a stable crack growth, the material's tearing modulus ($T_{mat.}$) must be greater than the tearing modulus ($T_{app.}$) obtained from the applied load. The instability point may be found by plotting $J_{app.}$ versus $T_{app.}$ and $J_{mat.}$ versus $T_{mat.}$ on a single figure. The material *J-R* curves can be obtained as following from the *J-R* data for weld metals.

$$J_{mat.} = C_1(\Delta a)^{C_2} \tag{1}$$

And differentiating Eqn. (1) with the crack length, the material tearing modulus can be obtained as follows:

$$\left.\frac{dJ}{da}\right|_{mat.} = C_1 C_2 (\Delta a)^{C_2 - 1} \tag{2}$$

In this paper, various $C_1$ and $C_2$ values were used for the development of the modified PED. The *J/T* curves for applied load were obtained as follows. In the first step, from the result of finite element analysis, the applied *J*-integrals for crack lengths of $a-\delta$, $a$, and $a+\delta$ as well as $2a-\delta$, $2a$, and $2a+\delta$ were determined for the applied load. The crack length increment, $\delta$, was assumed as 10% of crack length. In the second step, an equation for the *J* was postulated as a function of crack length $(a)$ as following.

$$J_{app.} = c_1 a^2 + c_2 a + c_3 \tag{3}$$

And also by differentiating Eqn. (3) with crack length, the applied tearing modulus was obtained as shown in the following equation.

$$\left.\frac{dJ}{da}\right|_{app.} = 2c_1 a + c_2 \tag{4}$$

Finally, the *J/T* analyses were performed to find the instability point of the crack by applying following equation.

$$\frac{dJ_{app.}}{da}(=T_{app.}) < \frac{dJ_{mat.}}{da}(=T_{mat.}) \tag{5}$$

Fig. 3 shows a typical *J/T* evaluation diagram.

3.5 SSE load

The SSE load for the modified PED was calculated in accordance with NUREG 1061, Vol. 3[1]. For the DLC length, safety factor of $\sqrt{2}$ was applied on the load as following.

$$M_{total} = \sqrt{2}[M_{NOP} + M_{SSE} + M_{etc}],$$

$$SSE\ Load = (M_{SSE} + M_{etc}) = \frac{M_{total}}{\sqrt{2}} - M_{NOP} \tag{6}$$

And for twice the DLC, safety factor was not applied on the load as following.

$$M_{total} = [M_{NOP} + M_{SSE} + M_{etc}],$$
$$SSE\ Load = (M_{SSE} + M_{etc}) = M_{total} - M_{NOP} \tag{7}$$

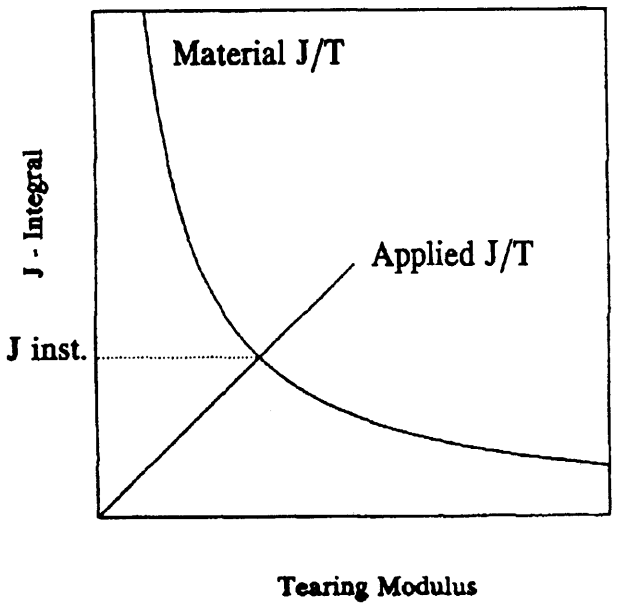


Fig. 3 J/T evaluation diagram

## 4. VERIFICATION OF ANALYSIS METHOD AND FE MODEL

The proposed modified PED method depends on the finite element analysis. Therefore, the finite element analysis procedure involved in this method should be appropriate for piping analysis. In order to verify the finite element analysis procedure, the modified PED method was applied to a piping system and compared with the experimental data.

### 4.1 Fracture test for through-wall circumferential cracked pipe

An extensive experimental program for the fracture evaluation of stainless steel flux welded pipe was conducted by Battelle[12]. Seven full-scale pipes (four pipes with through-wall circumferential cracks and three pipes with circumferential internal surface cracks) were tested at 288°C considering the nuclear piping operational condition. The experiment covered three different pipe outer diameters of 168.3mm, 413mm, and 711.2mm. For each pipe, the crack initiation load and the maximum load were measured. One of the seven experimental data was selected for the verification of the proposed modified PED method. Fig. 4 shows the schematic illustration of the piping test, and the specific dimensions are listed in Table 2. The loading condition was four point bending, and the internal pressure was not considered.

A finite element model was designed to simulate the Battelle pipe test. The crack initiation

load and the maximum load were calculated from the finite element analysis, and compared with those from the experimental data. Fig. 5 and Fig. 6 show the stress-strain curve and the fracture resistance curve for the pipe used in the fracture test, respectively. In order to evaluate the effect of planform size on the analysis result, the fracture resistance curves for the three different planform sizes of 1T, 3T and 9.5T CT specimen were applied, respectively. The crack initiation load was predicted based on the $J_{IC}$ values which are listed in Table 3.

Table 2 Summary of pipe geometry and experimental result

| Material | SA358 TP304 |
|---|---|
| Weld Type | SAW |
| Outside Diameter (mm) | 413 |
| Wall Thickness (mm) | 26.2 |
| Crack Length, % of Pipe Circumference | 36.4 |
| Crack Initiation Load (kN-m) | 195 |
| Maximum Load (kN-m) | 380 |

Table 3 Results of J-R tests for SA358 TP304 stainless steel

| SPEC_ID | Size | B[(a)] (mm) | W[(b)] (mm) | SG[(c)] (%) | $J_{IC}$ (kJ/ m$^2$) |
|---|---|---|---|---|---|
| A45W_2 | 1T | 25.0 | 50.0 | 0.0 | 120.0 |
| A45W_3 | 3T | 26.0 | 152.0 | 0.0 | 133.0 |
| A45W_6 | 9.5T | 29.0 | 483.0 | 0.0 | 524.0 |

(a) The specimen thickness.
(b) The specimen width.
(c) The side-grooving percentage.

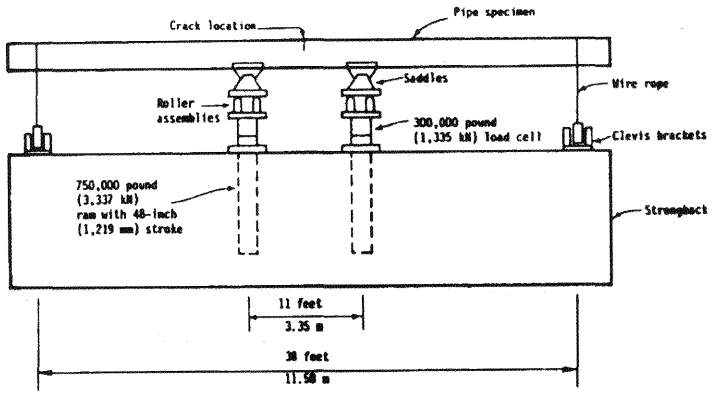


Fig. 4 Schematic of test frame used in pipe fracture experiment

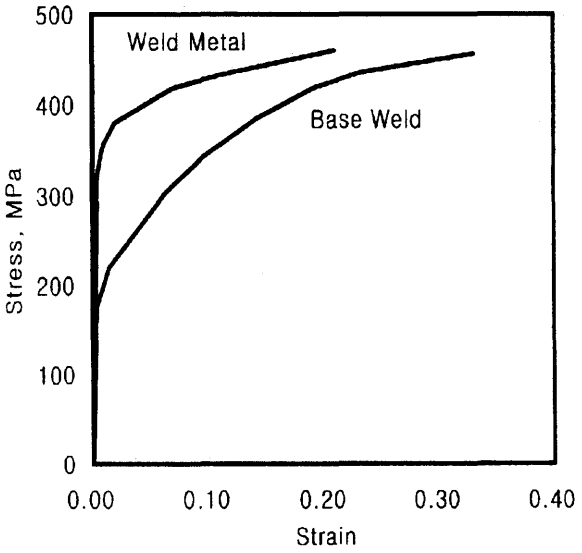


Fig. 5 Stress-strain curves for TP304 stainless steel base metal and weld metal

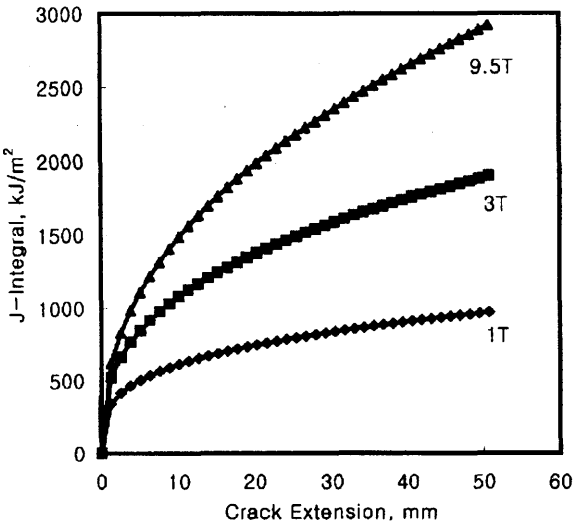


Fig. 6 J-R curves for TP304 stainless steel

4.2 Analysis method

In order to evaluate the effect of the pipe weldment on the crack behavior, three different material properties were considered in the finite element analysis as follows. In the first model, the full pipe was modeled as the all-base metal. In the second model, the full pipe was modeled as the all-weld metal. The final model was designed with combination of the weld metal and the base metal considering the actual weldment observed from the pipe as illustrated in Fig. 7. The crack initiation load was determined from the point satisfying the following equation.

$$J_{app.}(a, P) = J_{IC} \tag{8}$$

In calculating the maximum load, the *J/T* analysis was used.

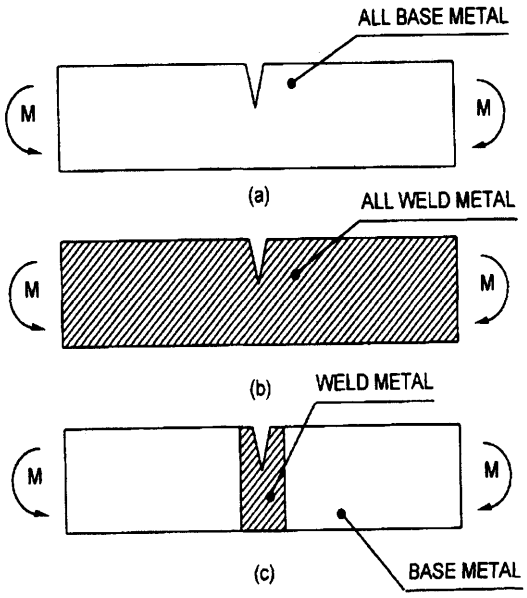


Fig. 7 Schematics of pipe with circumferential through-wall crack, for (a) all-base metal, (b) all-weld metal, and (c) weldment pipe

4.3 Analysis results

Fig. 8 shows the resulting *J* values with increasing moment for three different cases. While the variation of *J* values was similar for the all-base metal and the weldment analyses, the all-weld metal analysis produced much different applied moment versus *J*-integral curve. That is, even the crack was embedded on the weldment, the deformation behavior of the cracked pipe was governed by the base metal. This implies that the base metal has a greater effect on the elastic-plastic crack behavior than the weld metal[13].

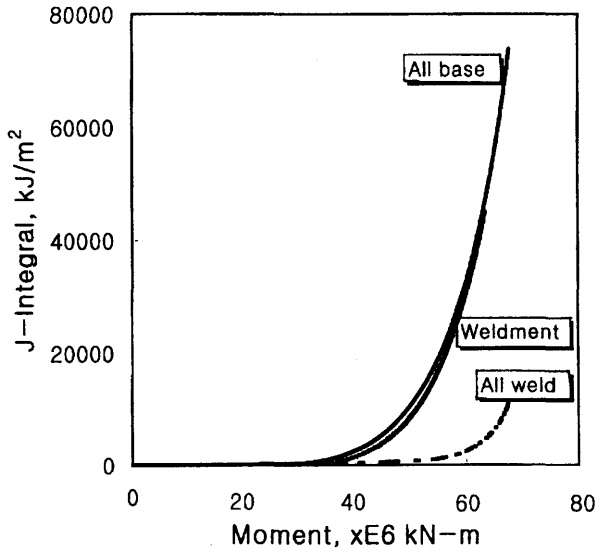


Fig. 8 Comparison of applied moment vs. J-integral curves for all-base metal, all-weld metal, and weldment pipe

Fig. 9 shows the calculated crack initiation loads for three different cases using Eqn. (8). Three different $J_{IC}$ values obtained from the 1T, 3T and 9.5T CT specimens were applied and compared with the experimental data. As shown in Fig. 9, the analysis results based on the $J_{IC}$ values from the 1T CT specimen showed the best agreement with the test results. The analyses based on the all-base metal and the weldment pipe showed better agreement with the experimental results than the all-weld metal analysis.

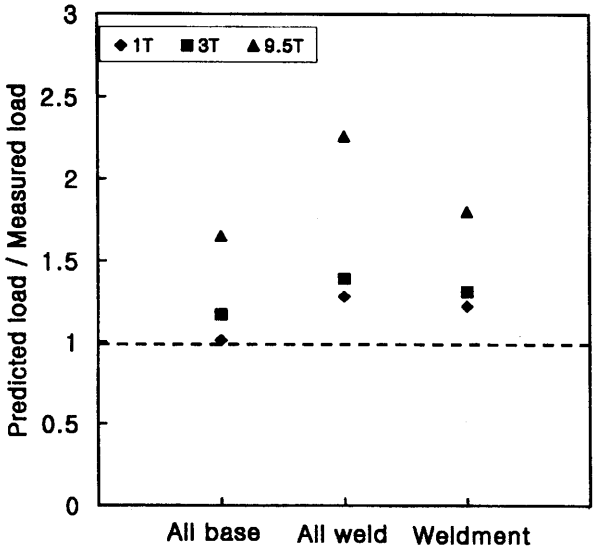


Fig. 9 Comparison of crack initiation loads for all-base metal, all-weld metal, and weldment pipe

Fig. 10 shows the resulting maximum loads for three different analyses. Three different fracture resistance curves were used for respective case. As shown in Fig. 10, the analysis results for the all-base metal and the weldment pipe showed a good agreement with the experimental results. For the all-base metal model, the maximum load predicted based on the fracture resistance curve from the 9.5T CT specimen produced a better agreement than that from the 1T CT specimen. It can be seen that the pipe fracture behavior can be simulated more realistically by adopting the fracture resistance curve for the 9.5T CT specimen due to the size effect, as shown in Fig. 11. The analysis based on the all-weld metal showed much higher values than the experimental data for all cases. As mentioned above, the base metal produces more significant effect on the elastic-plastic crack behavior, and thus this all-weld metal model is not appropriate. As a result, the finite element analyses with the all-base metal and the weldment piping provided a good agreement with the experimental data. In particular, the analyses with the all-base metal produced slightly more conservative results than those with the weldment piping. Considering the conservatism involved in LBB application, the current LBB analysis based on the all-base metal was proved to be appropriate.

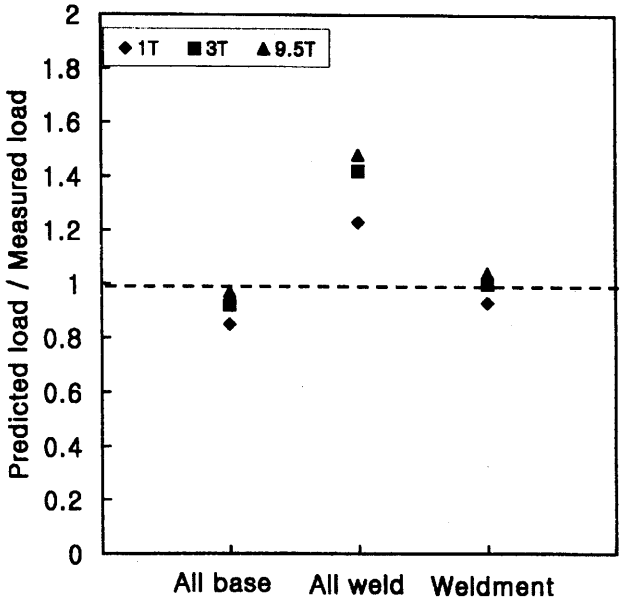


Fig. 10 Comparison of maximum loads for all-base metal, all-weld metal, and weldment pipe

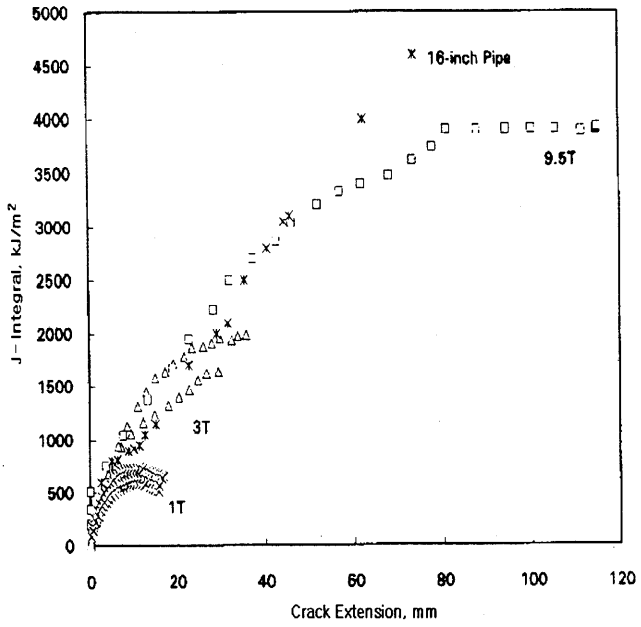


Fig. 11 Comparison of TP304 stainless steel J-R curves from various plane size CT specimens & pipe experiments

## 5. RESULTS AND DISCUSSIONS

Fig. 12 - Fig. 17 are some of the analysis results for the safety injection and the shutdown cooling line. Fig. 12 and Fig. 13 show the modified PEDs for Group 1 in case of the DLC and twice the DLC, respectively with varying $C_1$ values. Fig. 14 and Fig. 15 show the modified PED of the DLC and twice the DLC, respectively with varying $C_2$ values. Fig. 16 and Fig. 17 also show the modified PED of the DLC with varying $C_1$ and $C_2$ values, respectively for

Group 5. Here, the $C_1$ and $C_2$ values are the power law constants obtained from the material tests as shown in Eqn. (1). In order to extend the applicability of the modified PED, the $C_1$ and $C_2$ values were ranged $\pm 50\%$ in these figures. Also the actual LBB design point for previously designed plant[14] is indicated by " ■ " in the modified PEDs. This point is placed below the lower bound curve in both the DLC case and twice the DLC case. A considerable amount of margin between the actual load and the LBB allowable load was obtained. From these figures, the analysis result obtained by using the lower bound stress-strain curve was the lowest one, and thus proved that the current LBB analysis procedure is conservative. It can be seen from Fig. 12 - Fig. 15 (Group 1) that the $C_1$ value has the most significant effect on the allowable SSE load while the $C_2$ value has negligible effect. It was also observed from Fig. 16 and Fig. 17 (Group 5) that the $C_2$ value has some effect on the allowable SSE load while the effect of the $C_2$ value is less than that of the $C_1$ value. Therefore, the $C_1$ value has more significant effect on the allowable SSE load than the $C_2$ value. In addition, broader allowable SSE load region was obtained for Group 5 which has larger outer diameter and thickness. It was observed that the applicability of LBB can be extended with increasing pipe size.

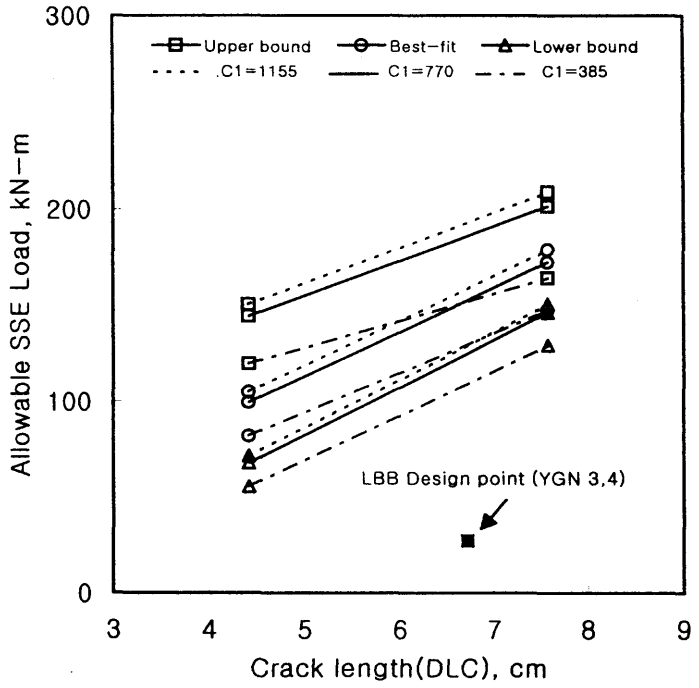


Fig. 12 Modified piping evaluation diagram for Group 1 (DLC, $C_2$=0.3)

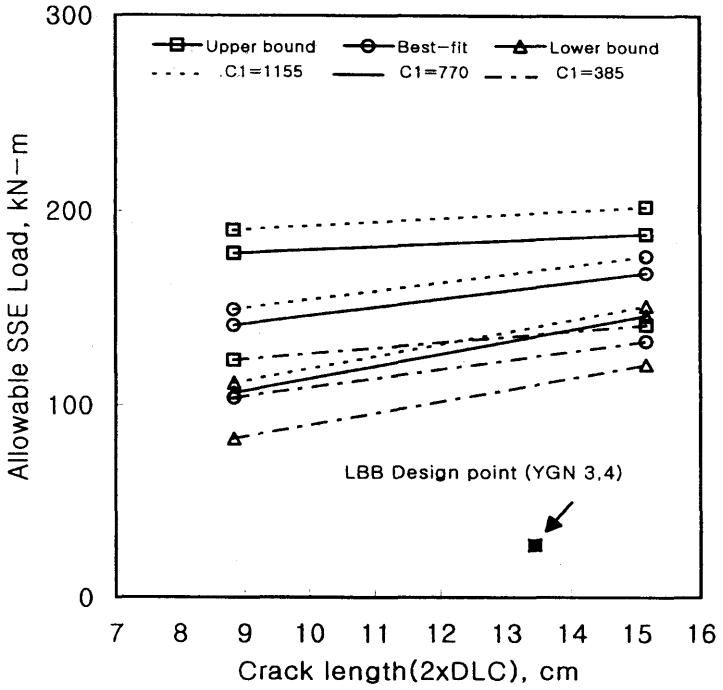


Fig. 13 Modified piping evaluation diagram for Group 1 (2xDLC, $C_2$=0.3)

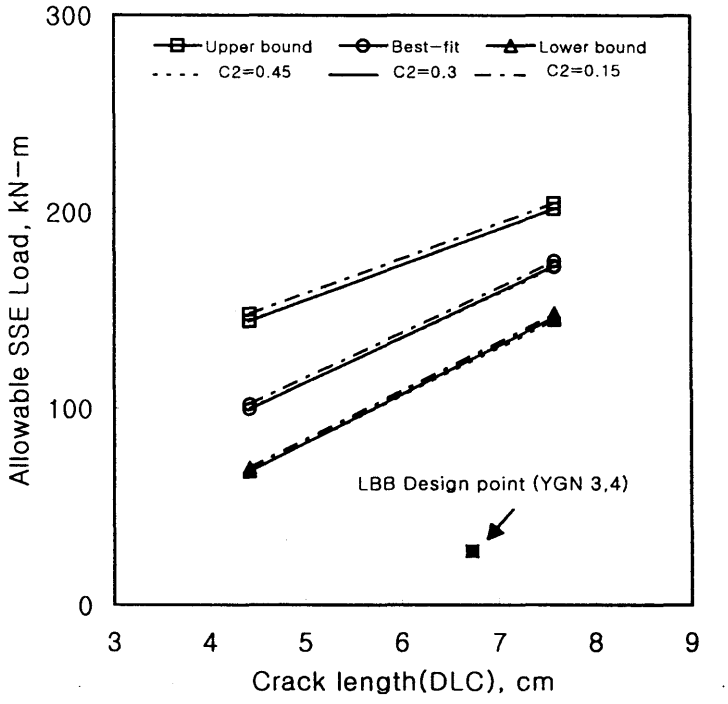


Fig. 14 Modified piping evaluation diagram for Group 1 (DLC, $C_1$=770)

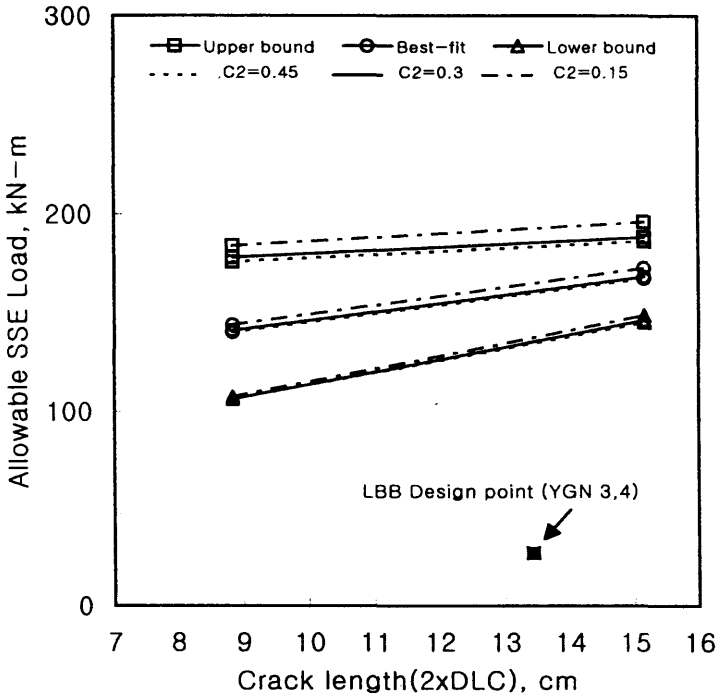


Fig. 15 Modified piping evaluation diagram for Group 1 (2xDLC, $C_1$=770)

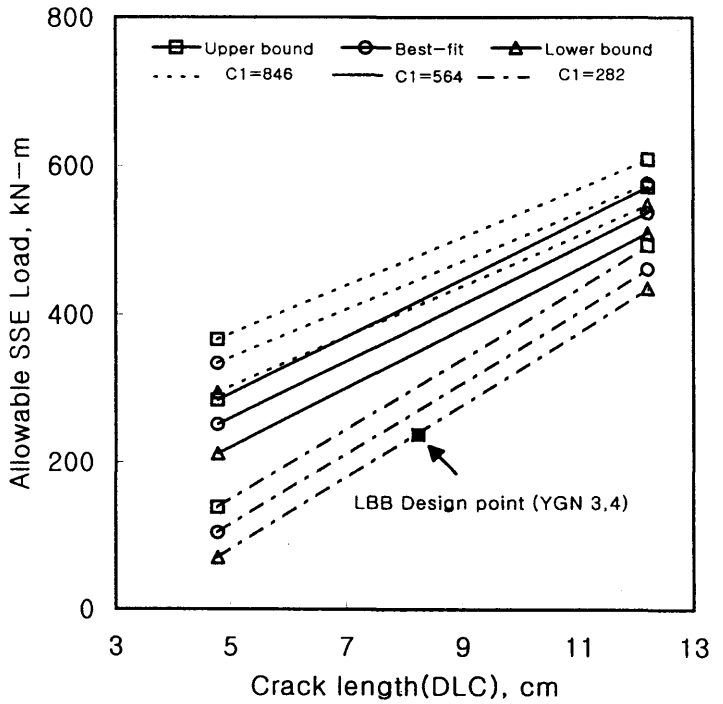


Fig. 16 Modified piping evaluation diagram for Group 5 (DLC, $C_2$=0.6)

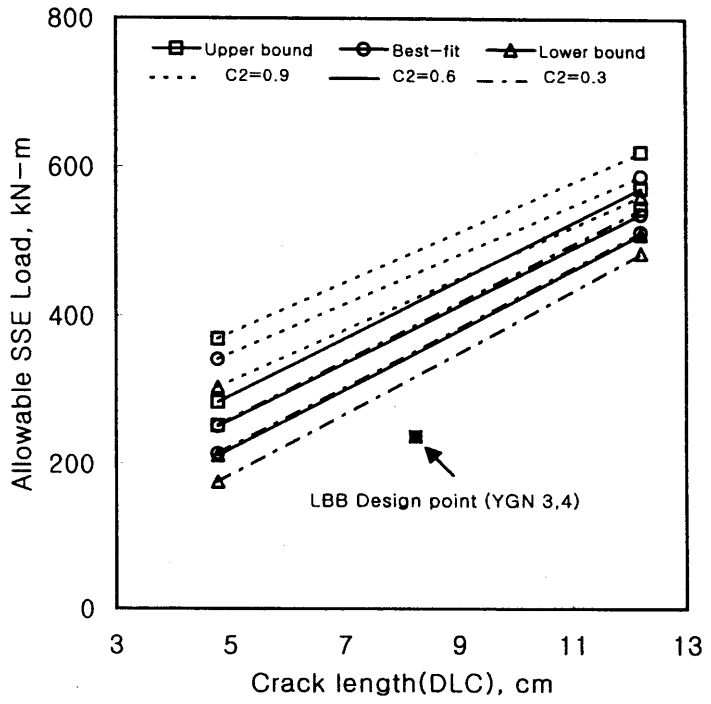


Fig. 17 Modified piping evaluation diagram for Group 5 (DLC, $C_1$=564)

## 6. CONCLUSION

Following conclusions were obtained from the development of the modified PEDs for the safety injection piping and the shutdown cooling piping in Korean Next Generation Reactor.

(1) The modified PED which can account for the variation of material properties in assessing applicability of LBB during the initial piping design process was proposed, and developed for the safety injection and the shutdown cooling piping in KNGR.
(2) The most conservative results were obtained with the lower bound stress-strain curve.
(3) The $C_1$ value produced more significant effect on the allowable SSE load than the $C_2$ value.
(4) The range of LBB application was extended with an increase in diameter and thickness of a pipe.

## 7. REFERENCES

[1] "Evaluation of Potential for Pipe Break," *NUREG 1061, Vol. 3*, USNRC, 1984
[2] "Leak Before Break Evaluation Procedure," *SRP 3.6.3*, USNRC, 1987
[3] A.D. Nana, K.K. Yoon, "Leak-Before-Break Allowable Load Windows Approach," *1994 ASME Conference, PVP-Vol. 287*, pp. 35-41, 1994
[4] R.J. Fabi, D.A. Peck, "Leak-Before-Break Piping Evaluation Diagram," *1994 ASME Conference, PVP-Vol. 283*, pp. 111-115, 1994
[5] S.A. Swamy, P.R. Mandava, D.C. Bhowmick, D.E. Prager, "LBB Consideration for A

New Plant Design," *NEA/CSNI/R(95)18, Vol. 1*, pp. 199-205, 1996
[6] N.S. Huh, J.H. Lee, Y.J. Kim, C.R. Pyo, S.D. Park, "Development of Piping Evaluation Diagram for LBB Application to Safety Injection and Shutdown Cooling Piping," *Proc. of the Korean Nuclear Society Autumn Meeting, Vol. II*, pp. 697-702, 1996
[7] Y.J. Kim, C.S. Seok, "Stress-Strain and Fracture Resistance Characteristics of Primary Piping Weld Materials for Younggwang 3/4 Nuclear Power Plants," S.K.K.U. Research Report, 1992
[8] Y.J. Kim, C.S. Seok, "LBB Test Evaluation of Secondary Piping Materials for Ulchin 3/4 Nuclear Power Plants," S.K.K.U. Research Report, 1996
[9] Y.Y. Earmme et al., "Study of Effect of Dynamic Strain Aging on Fracture Toughness for Main Steam Line Piping of Nuclear Power Plant," KAIST Research Report, 1996
[10] D.M. Norris, B. Chexal, "PICEP : PIpe Crack Evaluation Program," *EPRI Report NP 3596-SR*, 1987
[11] ABAQUS User's manual, Hibbitt, Karlsson & Sorensen, Inc., 1996
[12] G. Wilkowski et al., "Analysis of Experiments on Stainless Steel Flux Welds," *NUREG/CR-4878*, 1987
[13] B.R. Ganta, D.J. Ayres, "Analysis of Cracked Pipe Weldment," Palo Alto, CA. *EPRI NP-5057*, 1987
[14] "Final Safety Analysis Report (YGN 3/4)," Technical Report, KOPEC, 1993

## IV-2 Fracture Mechanics Evaluation for The Cast Duplex Stainless Steel after Thermal Aging

Shigeru Urata, Manager of Nuclear Safety Engineering Section Kansai Electric Power Co. Inc., Japan

# FRACTURE MECHANICS EVALUATION FOR THE CAST DUPLEX STAINLESS STEEL AFTER THERMAL AGING

Shigeru Urata

The Kansai Electric Power Company, Osaka, Japan.

Abstract

For the primary coolant piping of PWRs in Japan, cast duplex stainless steel which is excellent in terms of strength, corrosion resistance, and weldability has conventionally been used. The cast duplex stainless steel contains the ferrite phase in the austenite matrix and thermal aging after long term service is known to change its material characteristics.

It is considered appropriate to apply the methodology of elastic plastic fracture mechanics for an evaluation of the integrity of the primary coolant piping after thermal aging. Therefore, we evaluated the integrity of the primary coolant piping for an initial PWR plant in Japan by means of elastic plastic fracture mechanics.

The evaluation results show that the crack will not grow into an unstable fracture and the integrity of the piping will be secured, even when such through wall crack length is assumed to equal the fatigue crack growth length for a service period of up to 60 years.

## 1. INTRODUCTION

For the primary coolant piping of PWRs in Japan, cast duplex stainless steel (ASME SA351 Gr CF8M or equivalent) has been applied. This cast duplex stainless steel contains a ferrite phase of about 5 to 25% in the austenite matrix in order to improve its characteristics of corrosion resistance, strength, weldability, etc.

In the cast duplex stainless steel, the ferrite phase is gradually separated within the operating period at the PWR operation temperature (at about 300 °C), and that causes changes in its material characteristics.

An aging of the material tends to increase its tensile strength but reduces its fracture toughness. The degree of the toughness reduction becomes more significant with increasing ferrite content and the rate of

toughness reduction increases with rising temperature. Both of these tendencies are mitigated with the aging progress.

The present paper summarizes evaluation results on integrity of the primary coolant piping after thermal aging for initial PWR plant in Japan.

## 2. CRACK STABILITY ANALYSIS

### 2.1 Evaluation Method

Fracture toughness of the primary coolant piping decreases due to thermal aging under long-term plant operation, but this fracture type is considered to be a ductile fracture because ductile crack growth is recognized in the material test data after thermal aging. Therefore, it is appropriate to apply elastic plastic fracture mechanics for an evaluation of the stability of the assumed crack.
The evaluation flow is shown in Fig. 1.

### 2.2 Selection of Evaluating Location

Material toughness, which represents fracture resistance, will be reduced with increasing ferrite content and also with increasing operating temperature. In addition, a high temperature causes a large fracture force due to thermal bending moment. Therefore, the hot leg piping at the reactor vessel outlet nozzle was selected as the location to be evaluated since both temperature and imposed load are severer and ferrite content is relatively high in the evaluating plant.

### 2.3 Evaluation of Crack Growth

The size of the fatigue crack is calculated under the condition that the assumed initial defect on the piping inside surface grows due to the stress cycles applied by the plant operation.

(1) Evaluation Conditions

(a) Size of Initial Defect

The size of the initial defect was conservatively assumed, with a sufficient margin, to be about twice the size of the detectable single defect. Namely, the initial defect was assumed to be a

semi-elliptical, circumferential defect on the piping inside surface and its size to be 0.2t (depth) × 1.0t (surface length), where "t" is the wall thickness.

(b) Stress Cycle Used in Crack Growth Analysis

The stress cycle was produced on the basis of the transient conditions with consideration of the actual operating status of the plant.

(c) Fatigue Crack Growth Law

The fatigue crack growth law is represented by the following equations provided on the basis of the test data under the PWR primary coolant environment [1]:

$$da\,dN = C\,Keff^{m} \quad \cdots\cdot (1)$$

$$Keff = Kmax\,(1-R)^{0.5} \quad \cdots\cdot (2)$$

$$R = Kmin\,Kmax \quad \cdots\cdot (3)$$

Where,

| | | |
|---|---|---|
| da dN | : | Fatigue crack growth rate [mm cycle] |
| C | : | Constant = $7.0 \times 10^{-10}$ |
| m | : | Constant = 4.0 |
| Keff | : | Effective stress intensity factor range [MPa$\sqrt{}$m] |
| Kmax, Kmin | : | Maximum, minimum stress intensity factors [MPa$\sqrt{}$m] |
| R | : | Stress ratio |

2) Evaluation Results

The results of the fatigue crack growth analysis are shown below. It reveals that the fatigue crack growth rate is low and the crack does not penetrate the pipe wall (67.4mm thick) even after long-term plant operation.

1) Assumed initial crack size

Depth : 13.6 mm

Length : 67.4 mm

2) Crack size after plant operation of 60 years

Depth : 26.5 mm

Length : 108.8 mm

## 2.4 Crack Stability Evaluation

(1) Evaluation Method

Fracture toughness of the primary coolant pipe decreases after thermal aging, but this fracture type can be considered to be a ductile fracture because a ductile crack growth is recognized in its material tests. Therefore, elastic plastic fracture mechanics are to be applied for an evaluation of the stability of the assumed crack. Concretely, the crack stability is evaluated with the J integral value (Japp), which shows a fracture force in comparison to the fracture toughness value (Jmat), which shows the fracture resistance of the material after thermal aging.

(2) J Integral Value (Japp)

J integral value is calculated with the stress analysis by using the finite element method on the basis of the design load and the crack length for evaluation.

(a) Design Load

Loads imposed on the piping are those initiated under the normal operating condition and also those caused by S1 earthquake (maximum design earthquake).

(b) Analysis Model

For the analysis, the finite element model is applied to the elbow on the outlet side (high temperature side) of the reactor vessel with a circumferential crack on the inside surface.

Fig. 2 shows the finite element model used for the analysis.

The crack growth analysis was conducted with the assumption of an initial crack on the basis of the number of transients during the operating period of 60 years. Then, the calculated surface crack length was conservatively converted into the through wall crack which length is assumed 1.6t as shown in Fig. 1 for the crack stability evaluation.

(c) Analysis Results

Fig. 3 shows the analysis results for the Japp value at the evaluating location.

(3) The Fracture Toughness Value (Jmat)

The Jmat value was determined by the lower bound curve of toughness (-2 σ lower bound curve) obtained with the toughness prediction model (H3T Model : Hyperbolic-Time Temperature Toughness) on the basis of the ferrite content at the evaluating location.

(a) The H3T model

The H3T model expresses the relation of $J_{IC}$ and $J_6$ to the aging time with the following hyperbolic function as shown in Fig. 4.

$$M = A + \frac{B}{t + C} \quad \cdots\cdots (4)$$

where

M : Toughness ( $J_{IC}$ or $J_6$) kJ $m^2$

t : Aging time. Hours

A : Fully aged toughness kJ $m^2$

B : Constant relating to aging temperature

C : Constant relating to aging time

Now. it is assumed that B = exp (D T + Co) and D = Q R. where T is the aging temperature (K). Co is a constant and R is gas constant. When T is Ti. B is Bi. When T = Tj. B is Bj. Then.

$$Bi \quad Bj = \exp [D (1 \quad Ti - 1 \quad Tj) ] \quad \cdots\cdots (5)$$

$$Bi \quad Bj = \exp [Q \quad R (1 \quad Ti - 1 \quad Tj) ] \quad \cdots\cdots (6)$$

The activation energy Q (kJ mole) obtained from temperature dependence of B is defined to be the embrittlement activation energy.

On the other hand. the initiation activation energy F is defined from temperature dependence of initiation time of tertiary embrittlement $t_F$. namely

$$t_{Fi} \quad t_{Fj} = \exp [F \quad R (1 \quad Ti - 1 \quad Tj)] \quad \cdots\cdots (7)$$

The Q and F values obtained from the $J_6$ changes for the test materials aged at 290, 325, 350 and 400 C are about 100 to 180 kJ mol. From this, it is considered that the result will be conservative when 100kJ mol is used.

Fig. 5 shows the Flow chart of the toughness prediction model.

First, the data for the aging temperature of 400 C is fitted with the H3T model to obtain the constant A (the fully aged toughness).

With this constant A fixed, the data for aging at 300 and 350 C are fitted with the H3T model to obtain the constants B and C at the aging temperatures of 300 and 350 C.

By obtaining relation of the above-obtained constants A, B, and C to chemical composition, the prediction expression can be obtained.

Table 1 shows examples of the prediction formulas obtained for $J_{IC}$ and $J_6$ at 325 C which are constant A for the prediction model. We have been modifying these formulas by increaseing data further.

Table 1 Prediction formulas of constant A for the toughness prediction model

(Temp.: 325℃)

| | Prediction Formula | Standard Error : σ |
|---|---|---|
| $J_{IC}$HT ($KJ\,m^2$) | Log $J_{IC}$=3.29609−0.05297× $F^{o}{}_{o}$ | 0.25184 |
| $J_6$HT ($KJ\,m^2$) | Log $J_6$=3.66985−0.04904× $F^{o}{}_{o}$ | 0.14899 |

$F^{o}{}_{o}$ : Ferrite content ($^{o}{}_{o}$) by ASTM A800

In evaluating the integrity of duplex stainless steel components after thermal aging, it is important to predict the J-Δ a curve. When the $J_{IC}$ and $J_6$ values at an optional aging condition are obtained, the J-Δ a curve can be obtained by the following expression with the above prediction model by giving the flow stress :

$$J = C1 \quad (\Delta a)^{C2} \quad \cdots\cdots\cdots\cdots\cdots\cdots\cdots\cdots\cdots\cdots\cdots\cdots\cdots\cdots \quad (8)$$

(b) Jmat value for evaluation

The ferrite content of the evaluating location was calculated by the method described in ASTM A800 with the chemical compositions on the material certificate.

Fig. 6 shows the Jmat value (-2 $\sigma$ lower bound value) obtained by the ferrite content at the evaluating location.

(4) Crack Stability Evaluation Results

The circumferential surface crack obtained on the basis of the fatigue crack growth analysis after the service period of 60 years was conservatively converted to the circumferential through wall crack of the same length. In order to estimate the stability of this assumed crack, the Japp and Jmat values obtained in Items (2) and (3) above were compared in Fig. 7.

Fig. 7 shows that $J_{IC} > Japp$ even after the service period of 60 years.

Therefore, even when fatigue crack growth is assumed after the service period of 60 years, the evaluation shows that any ductile crack will not be initiated under the design load conditions, and the integrity of the primary coolant piping is confirmed to be secured with sufficient margin.

## 3. CONCLUSION

Integrity evaluation was conducted by means of the elastic plastic fracture mechanics for the primary coolant piping after thermal aging in an initial PWR plant.

The results show that, even when fatigue crack growth is assumed after a service period of 60 years, the crack is estimated to be stable and the integrity of the piping is confirmed to be maintained in consideration of the thermal aging of cast duplex stainless steel after long-term plant operation.

## REFERENCES

1) Kanasaki, H, et.al. "Fracture toughness and fatigue crack growth of PWR materials in Japan" ICONE-1.

2)Suzuki, I. et.al. "Long term thermal aging of cast duplex stainless steels" ICON-4.

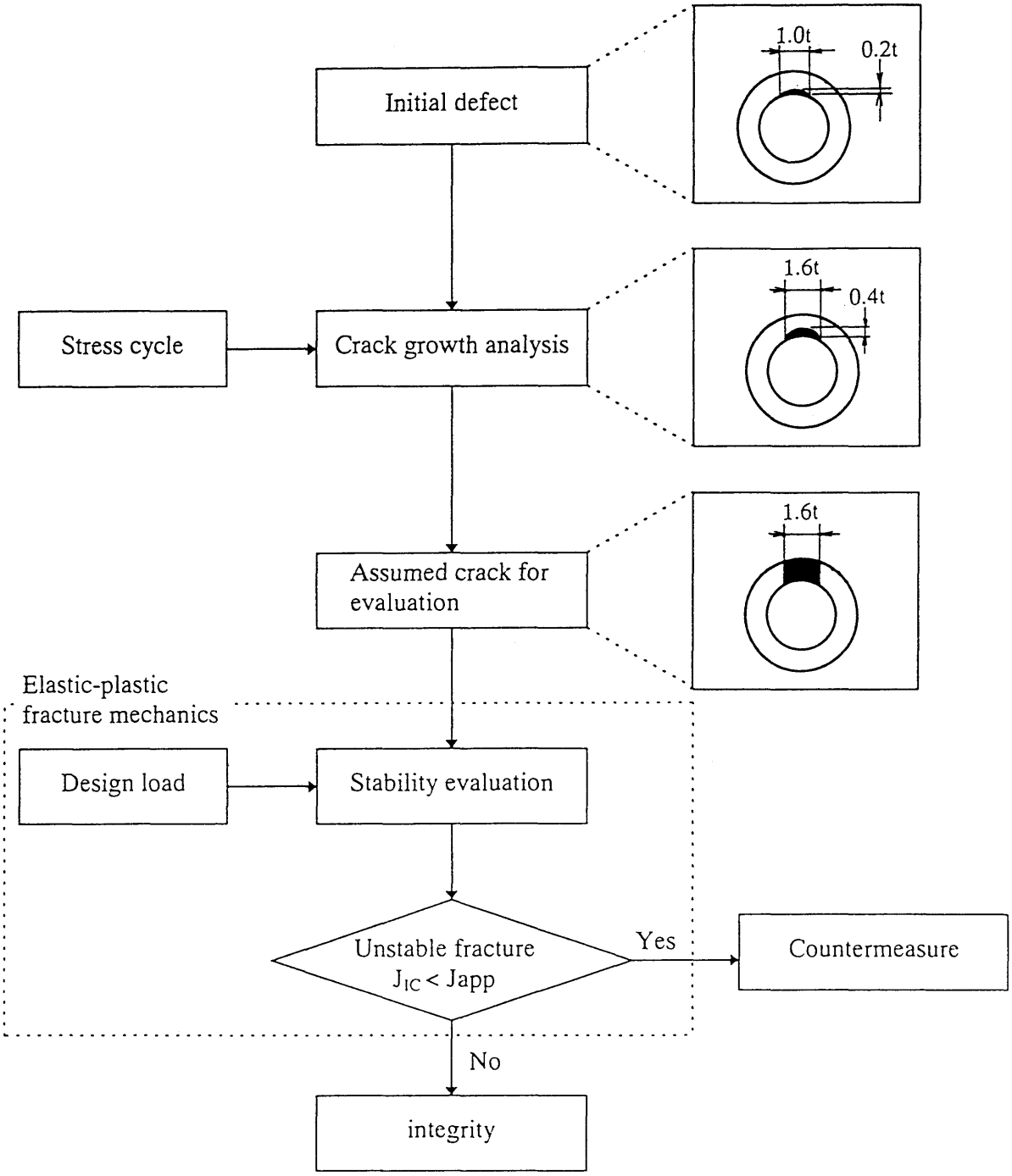


Fig. 1 Evaluation Flow for Thermal Aging

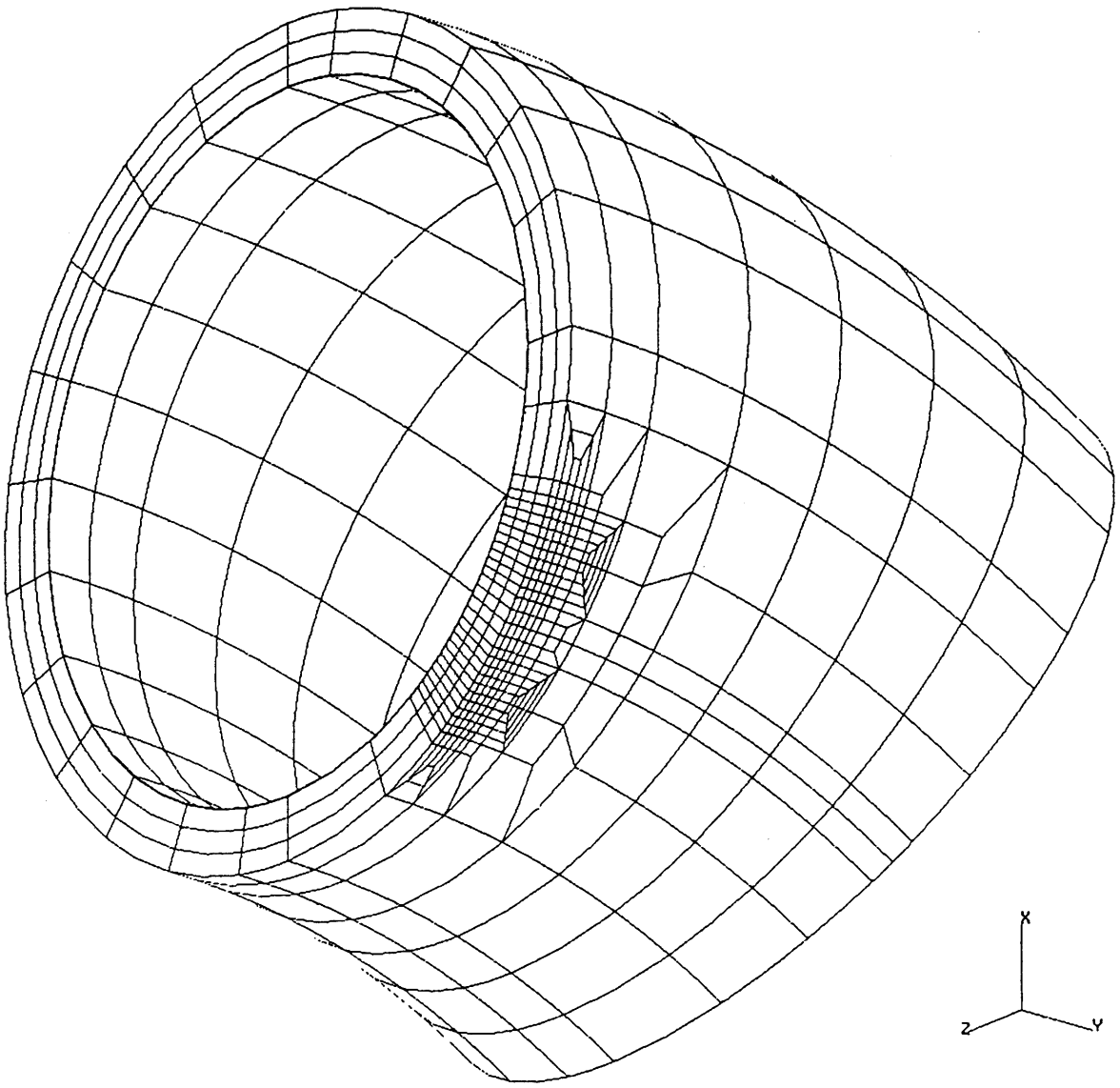


Fig. 2 Elemental Division Diagram

(Crack length : 2c = 2t)

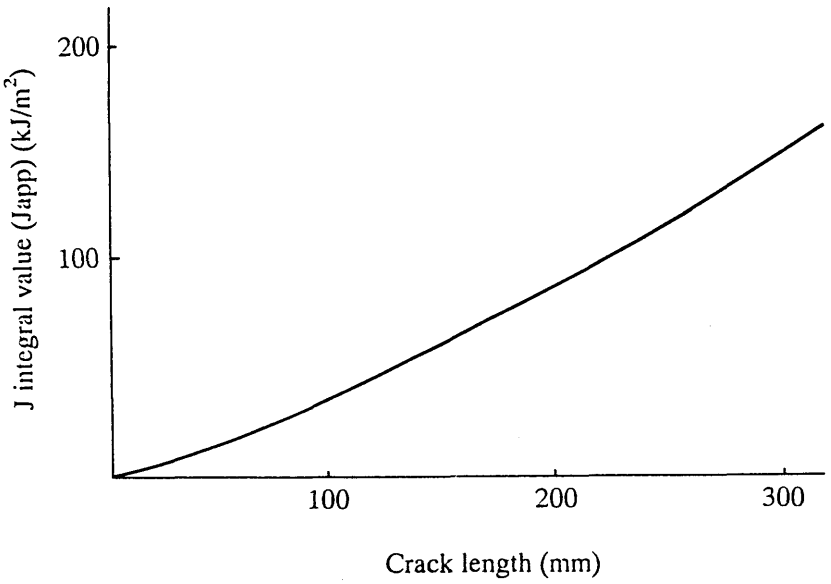


Fig. 3 J Integral Value at Evaluation Position

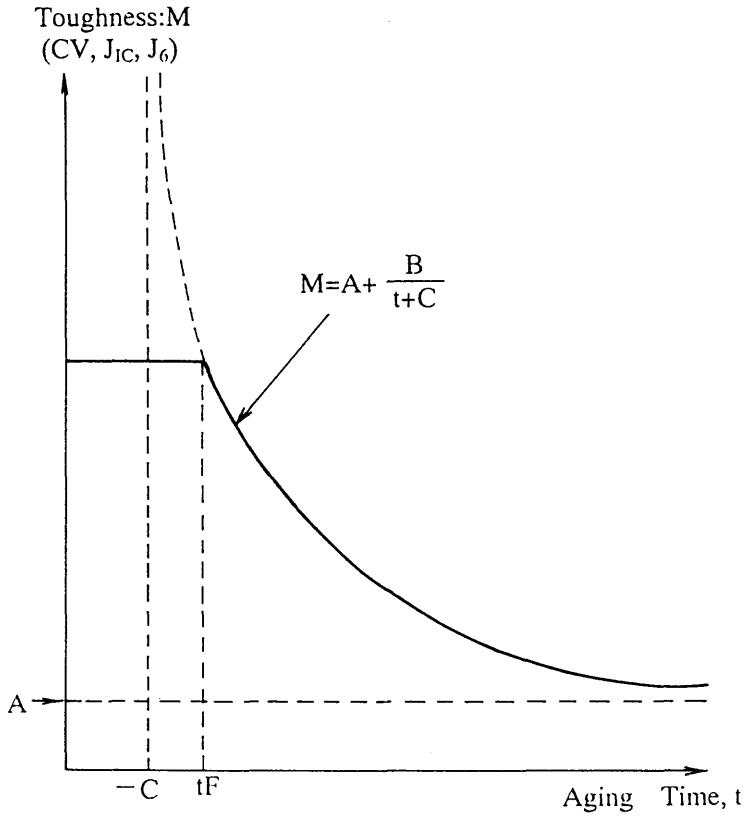


Fig. 4 Schematic illustration of the toughness prediction model

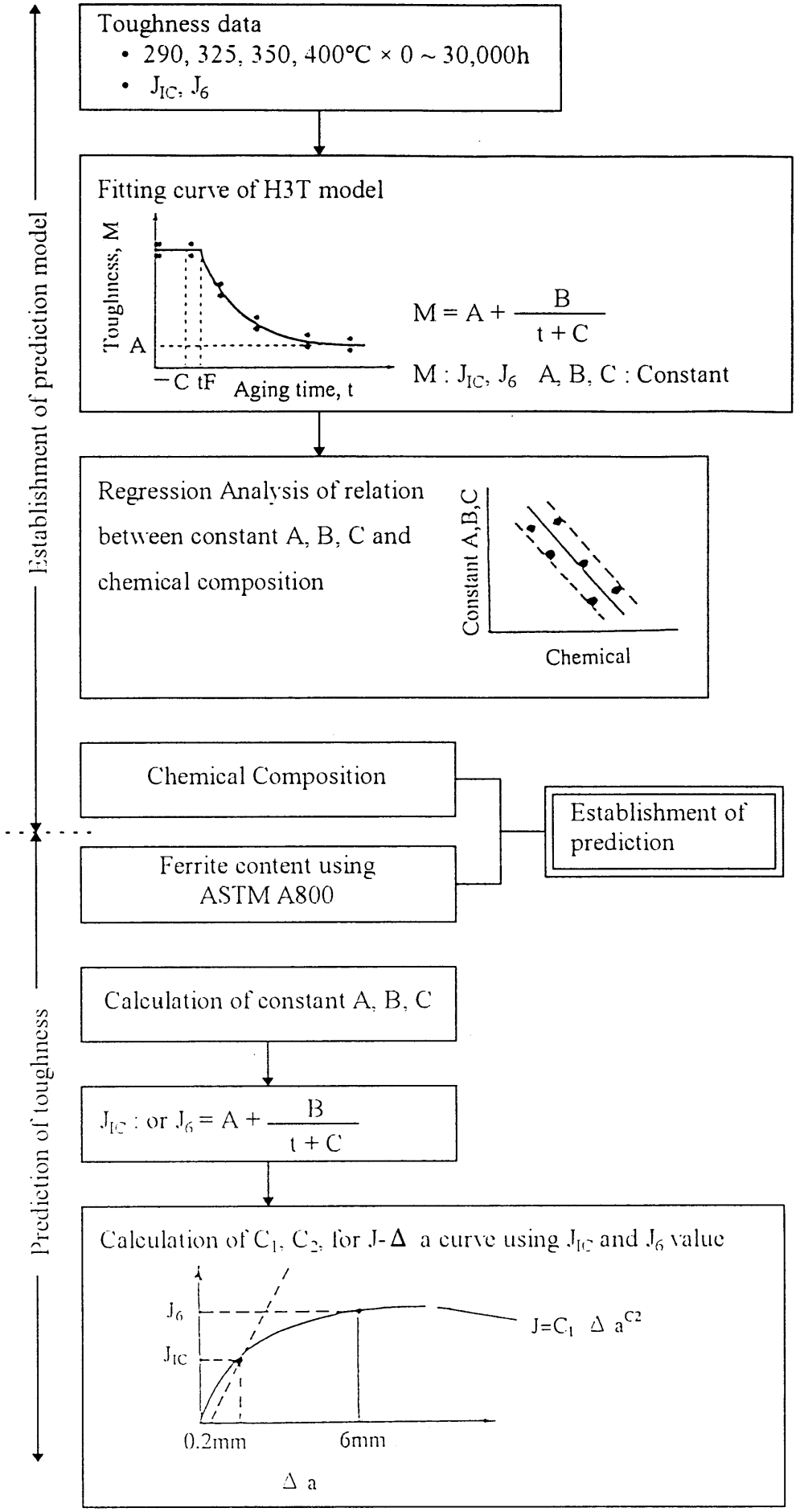


Fig. 5 Flow chart of the toughness prediction model

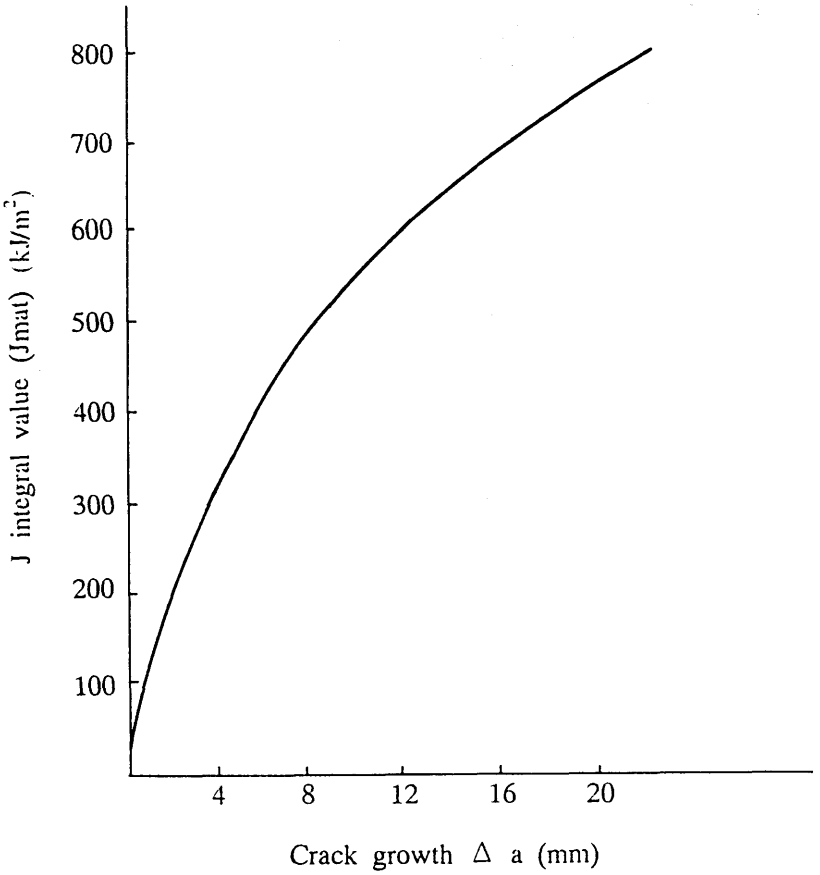


Fig. 6 J-Δ a Curve (Hot Leg Pipe Material)

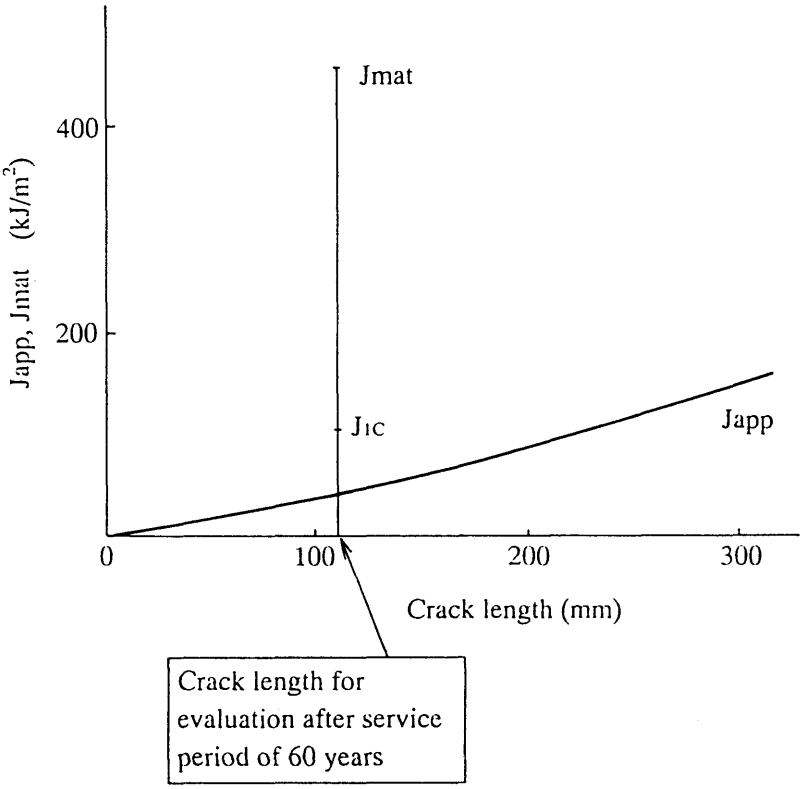


Fig. 7 Crack Stability Evaluation Diagram

IV-3 Fracture Behavior of Carbon Steel Pipe with Local Wall Thinning Subjected to Bending Load

Katsumasa Miyazaki & Satoshi Kanno, Mechanical Engineering Research Laboratory, Hitachi Ltd., Japan

Masayuki Ishiwata & Kunio Hasegawa, Hitachi Works, Hitachi Ltd., Japan

# Fracture Behavior of Carbon Steel Pipe with Local Wall Thinning Subjected to Bending Load

**Katsumasa Miyazaki, Satoshi Kanno,**
Mechanical Engineering Research Laboratory, Hitachi Ltd.
Ibaraki, Japan

**Masayuki Ishiwata and Kunio Hasegawa**
Hitachi Works, Hitachi Ltd.
Ibaraki, Japan

1-1, Saiwai-cho 3-chome, Hitachi-shi, Ibaraki-ken, 317 Japan

## ABSTRACT

To evaluate the structural integrity of power plant piping, monotonic bending tests were conducted on 4-inch diameter full-scale carbon steel pipe specimens with local wall thinning. The local wall thinning was simulated as a eroded part. Eroded part was subjected to tensile or compressive stress caused by applied bending load. The deformation or fracture behavior at maximum moments was classified into three types. When eroded part was subjected to tensile stress, ovalization and crack initiation was occurred. When eroded part was subjected to compressive stress, local buckling occurred. When fracture behavior was ovalization or local buckling, the applied load decreased slightly form the maximum load. On the other hand, in the case of crack initiation, the applied load was abruptly decreased from the maximum load, because of circumferential crack propagation. The relationships between applied load and load line displacement for eroded pipes were compared with those for cracked pipes. The maximum loads and total displacement for the eroded pipes were higher than those for circumferentially cracked pipes. Maximum moments predicted using a net section stress approach gave overly conservative evaluation for pipe specimens with local wall thinning. Safety margin for locally thinned pipes was discussed compared with the design maximum load. The safety margin in this paper were roughly more than 2 times.

## 1. INTRODUCTION

Carbon steel is used extensively in piping systems in power plants. High temperature and high pressure water and steam flow at high velocities through these pipes. Erosion / corrosion has caused wall thinning in high-energy carbon steel piping. It is important to evaluate the strength of piping with local wall thinning to maintain the integrity of the piping systems.

Burst and bending tests were performed on 6-inch diameter carbon steel pipes with local wall thinning by JAERI (Japan Atomic Energy Research Institute). From the experiment, it was found that fracture load was high, when locally thinned thickness of a pipe was the minimum required wall thickness defined in terms of design pressure (JAERI Report, 1993).

ASME (American Society of Mechanical Engineers) has considered the need to provide appropriate guidance to system engineers on the subject on erosion and erosion/corrosion in ferritic piping (Deardolff A. F., 1990). New criteria for acceptability of localized wall

thinning of piping components have been developed for inclusion in the ASME Boiler & Pressure Vessel Code, Section XI (ASME B&PV code, 1997a).

This study was undertaken in order to clarify the fracture behavior and strength of carbon steel pipes containing simulated local wall thinning to erosion/corrosion. Deformation and fracture load for locally thinned pipes were compared with those for cracked pipes. The maximum moments were compared with the plastic collapse moments based on net section criteria. In addition, safety margins were discussed using design maximum load.

## 2. EXPERIMENTAL PROCEDURE

### 2.1 Material

The materials used in the experiments were carbon steel pipe called "Carbon steel pipe for high Pressure Service, STS 410" in JIS (Japanese industrial Standards) , which are commonly used in coolant piping systems of nuclear power plants in Japan. The carbon steel, STS410 is similar to ASME A333 Gr.6. The yield strength and ultimate strength at ambient temperature were 326 MPa and 490 MPa, respectively for STS410.

### 2.2 Pipe Specimens

Full-scale experiments were performed on 4-inch diameter schedule 80 carbon steel pipes made of STS410 with local wall thinning. The pipe geometry and dimensions of local wall thinning are shown in Figure 1 and Table 2. The local wall thinning was machined on the inside of STS410 pipe. All local wall thinning to simulate erosion/corrosion thinning was done by grinder machining. The eroded depth means metal loss depth in the thickness direction and the eroded angle was a circumferential wall thinning angle. The eroded length was an axial local wall thinning length which was roughly equal to the diameter of the 4-inch pipe .

### 2.3 Load Conditions

A static bending load without internal pressure was applied by four-point loading until maximum load appeared. The bending test apparatus was shown in Figure 2. The major span and minor span, respectively, were 960 mm and 300 mm. Displacement velocity at cross head was 0.1 mm/s. The total elapsed time from start of loading until fracture ranged from 10 to 20 minutes. The experiments were conducted at ambient temperature.

The eroded area of the local wall thinning was located such that its center coincided with the plane of maximum bending moment. There were two types of bending loads; for the majority of specimens, bending tensile stresses were applied to the locally eroded areas, bending were applied to the locally eroded areas of the other pipe specimens. Figure 2 showed an example of a pipe in which the tensile stress occurred at the eroded thinned area.

## 3. TEST RESULTS

### 3.1 Load - Displacement Curves

The maximum moments for all specimens are shown in Table 2. Eight pipe specimens applied tensile stress at locally eroded area, and two others applied compression stresses by four-point bending. In Table 2, the plastic collapse moment calculated based on net section

stress criteria and fracture behavior, described in detail later, were also listed.

The load-displacement curves for STS410 pipe specimens with local wall thinning subjected to tensile stress were shown in Figure 3. The fracture behavior was discussed later, the eroded pipes subjected to tensile stress at eroded area showed two types of fracture behavior. One was ovalization, and the other was crack initiation with local necking at the eroded part. For Figure 3 (a), fracture behavior was ovalization (Specimens No. TP-5, TP-6 and TP-7). When fracture behavior was ovalization, the relationship between applied load and load line displacement remained the same in spite of difference of eroded area configuration. The maximum load was observed at about 80 mm in load line displacement.

For Figure 3 (b), fracture behavior was crack initiation (Specimens No. TP-3, TP-4 and TP-8). When the crack was initiated, the applied load dropped abruptly. In this case, the displacements of these specimens, after maximum load was applied, were very small, because crack propagated in the circumferential direction.

Load-displacement curves for pipe specimens (Specimens No. TP-9 and TP-11) subjected to bending compressive stresses were shown in Figure 4, compared to the curves for the same local wall thinning geometry when tensile stress caused by bending moment was applied. In Figure 4 (a), normalized eroded depth, $d/t$ was 0.5 and eroded angle, $2\theta$ was $180^\circ$ . On the other hand, normalized eroded depth, $d/t$ was 0.8, erode angle, $2\theta$ was $180^\circ$ , in Figure 4 (b). The maximum loads for TP-9 and TP-11, where compressive stress was applied to the eroded area, were less than those for the specimens subjected to tensile stress. However, applied loads decreased slightly with increasing the displacement.

### 3.2 Fracture Behavior

When a local eroded area in a pipe was located on the tensile stress side, two types of fracture behaviors occurred at the maximum moments. When the eroded depth was shallow, ovalization occurred at the maximum moment. The fracture behavior of such an eroded pipe (specimen No. TP-6), occurring ovalization was shown in Figure 5. Crack initiation and growth at the eroded area were not observed at or after maximum moment. The load slowly decreased after maximum point accompanying deformation of ovalization. Total displacement was significantly large, when ovalization occurred.

When the eroded depth was deep, local necking was observed first, then a crack initiated around the maximum load. The fracture behavior of the pipe (specimen No. TP-4) with deep eroded depth was shown in Figure 6. Local necking appeared in the local wall thinning area around the maximum load as shown in Figure 6 (a), and a crack initiated in the local necking area and propagated circumferentially as shown in Figure 6 (b). Total displacement after crack initiation was relatively small, and the load abruptly decreased. The crack initiation part after pipe fracture test was shown in Figure 7. The crack initiation point agreed with the maximum eroded part. When the applied load increased, the maximum eroded part was necked. The crack initiation occurred, because of locally rupture at the maximum eroded part.

When the local eroded area was subjected compressive stress, local buckling occurred in the locally thinned area. Figure 8 is a photograph of local buckling (specimen No. TP-11), which was taken after the un-loaded.

## 4. ANALYSIS OF EXPERIMENTS

### 4.1 Fracture Behavior at Maximum Load

Fracture behavior of pipes with local wall thinning can be classified into three types at maximum load in case of receiving a monotonic bending moment; ovalization, local necking-crack occurrence and local buckling .

When the eroded area in a pipe was subjected to tensile stress, ovalization or crack initiation occurred at the maximum load. The ovalization or crack initiation depended on the initial geometry of local wall thinning. The boundary between the ovalization and the crack initiation was illustrated in Figure 9. When eroded angle was large and depth was deep, local necking and crack initiation was observed. Crack was initiated at the maximum moment and propagated circumferentially after the maximum moment was reached. When the eroded area was short and thin, the pipe occurred ovalization at maximum moment, and showed a large degree of deformation.

Pipes containing a local erosion area with short angle and shallow depth showed high strength and a large degree of deformation. It seems reasonable to accept such eroded sizes below the straight line in Figure 9. It is conceivable that those were allowable local wall thinning sizes caused by erosion corrosion.

When the eroded area in a pipe was subjected to compressive stress, local buckling occurred at and after the maximum moment, as shown in Figure 8. Although pipes subjected to compressive stress showed slightly less strength than with those subjected to tensile stress, the degree of pipe deformation was large.

### 4.2 Comparison of Cracked Pipes

Four-point monotonic bending experiments were have been done on the same diameter carbon steel pipes with circumferential cracks at ambient temperature (Miyazaki, et al., 1996). Testing machine and bending apparatus used for these experiments were the same as those shown in Figure 2. Also, the cracked pipes were made of the same material as the eroded pipe discussed in this paper.

The load-displacement curves for pipes with cracks, compared with the curves for pipes with local wall thinning, called eroded pipes, were shown in Figure 10. The cracks were through wall and part-through wall cracks. The crack angle and the eroded angle for both pipes were $2\theta = 60^{\circ}$ . The maximum loads and total displacement for the eroded pipes were higher than those for circumferentially cracked pipes.

### 4.3 Net Section Stress Approach

Fracture strength for a circumferentially cracked carbon steel pipes could be predicted by net-section stress approach (Kanno, et al., 1993). When the crack depth is $d$, and crack angle is $2\theta$, the plastic collapse moment $P_c$ based on net section stress criteria is estimated by,

$$M_c = 2\sigma_f R^2 t(2\sin\beta - \frac{d}{t}\sin\theta) \quad (1)$$

$$\beta = \frac{1}{2}(\pi - \frac{d}{t}\theta) \quad (2)$$

$$P_c = \frac{M_c}{4(L_{out} - L_{in})} \quad (3)$$

where $M_c$ is the plastic collapse moment, $t$ is the nominal wall thickness, $\theta$ is the eroded half angle, $R$ is the pipe mean radius, $\beta$ is the neutral angle of the pipe, $\sigma_f$ is the flow stress, $l_{out}$ was the major span and $l_{in}$ was the minor span of the test apparatus. The flow stress was usually used as an average value of yield strength $\sigma_y$ and ultimate strength $\sigma_u$. That is, the flow stress is defined as,

$$\sigma_f = \frac{\sigma_y + \sigma_u}{2} . \qquad (4)$$

Maximum load $P_{max}$ for circumferentially cracked carbon steel pipes can be accurately estimated from the plastic collapse moment calculated by Equations from (1) to (3).

Maximum moment, $P_{max}$ obtained in cracked pipe test and plastic collapse moment, $P_c$ calculated by Equations from (1) to (3) was compared in Figure 11. The base material, STS410, used for cracked specimens was the same as that of the eroded pipes. The monotonic four-point bending tests using cracked pipe were performed at ambient temperature and at 265℃ (Miyazaki, et al., 1996). The maximum load obtained from cracked pipe test was slightly larger than plastic collapse load. It means that maximum load for a cracked pipe subjected to a bending moment can be predicted conservatively by Equations from (1) to (3).

The same technique was applied for locally eroded pipes, using Equations from (1) to (3). Plastic collapse load calculated from Equation from (1) to (3) was also listed in Table 2. The relationship between maximum moment obtained from eroded pipe fracture tests and the plastic collapse moment was shown in Figure 12. When fracture behavior was ovalization, the ratio of maximum load to plastic collapse load, $P_{max}/P_c$ was about 1.2. On the other hand, in case of crack initiation at eroded part subjected tension and local buckling at eroded part subjected compression, $P_{max}/P_c$ was about from 1.25 to 1.85.

The ratio of maximum load to plastic collapse load, $P_{max}/P_c$ , when occurring crack initiation, was higher than that, when occurring ovalization. It means that maximum moments will be overly conservative, when applying the Equations from (1) to (3) for locally eroded thinned pipes.

### 4.4 Safety Margin

The primary stress for a pipe caused by a bending moment is designed to be less than 1.5 $S_m$ where $S_m$ is the design stress given by ASME Boiler & Pressure Vessel Code Section III (ASME B&PV Code, 1997b) and MITI (Ministry of International Trade and Industry) Notification No. 501. The design stress $S_m$ was 137N/mm$^2$ for STS410. Then, 1.5$S_m$ = 206 N/mm$^2$ for STS410 and 188 N/mm$^2$ for STS370. The maximum design load, $P_D$ is given by,

$$M_D = 1.5 S_m \times Z \qquad (5)$$

$$P_D = \frac{M_D}{4(L_{out} - L_{in})} \qquad (6)$$

where $M_D$ is the design moment, $Z$ is the section modules of the pipe. The maximum design load for 4-inch diameter carbon steel, STS410 were calculated using Equation from (5) to (7) as,

$$P_D = 88 \text{ kN} \quad \text{for STS410 (4B, Schedule 80)} \qquad (7)$$

The maximum moments in Table 2, the safety margins for eroded pipes tested in this paper were shown to be roughly more than 2 times.

## 5. CONCLUSIONS

Monotonic bending tests were conducted on 4-inch diameter full-scale carbon steel pipe specimens with local wall thinning at ambient temperature. It is concluded as follows;

1) Fracture behavior and sequence of fracture process for locally eroded pipes could be classified into three types; deformation of ovalization, local necking - crack initiation - propagation when tensile stress is applied to the eroded area, or local buckling during loading in case of compressive stress at the eroded area. It is conceivable that the locally eroded sizes caused ovalization are allowable.

2) Fracture strength and total deformation of pipes with local wall thinning pipes were higher than for the cracked pipes with the same depth and angle.

3) Net-section stress approach gives an overly conservative evaluation for pipes containing locally wall thinning, as eroded area. The ratio of maximum load to plastic collapse load, $P_{max}/P_c$ , when occurring crack initiation, was higher than that, when occurring ovalization. It means that maximum moments will be overly conservative, when applying the Equations from (1) to (3) for locally eroded thinned pipes.

4) When comparing the maximum design moment, pipes with locally wall thinning have more than twice the safety margin compared with design load, even when eroded depth is 80 % of pipe wall thickness.

## REFERENCES

ASME, 1997a, "ASME Boiler & Pressure Vessel Code Sec. XI, Rules for Inservice Inspection of Nuclear Power Plant Components".

ASME, 1997b, " ASME Boiler & Pressure Vessel Code Sec. III, Rules for Construction of Nuclear Power Plant Components".

Deardorff, A. F. and Bush, S. H., 1990, "Development of ASME Section XI Criteria for Erosion-Corrosion Thinning of Carbon Steel Piping", *ASME PVP*, PVP-Vol-186, NDE-Vol.7, pp.71-75.

Japan Atomic Energy Research Institute, 1993, "Technical Report on the Piping Reliability Tests at the Japan Atomic Energy Research Institute (Japanese)", JAERI-M, 93-076, pp.104-115, May.

Kanno, K., Kimoto, H., Hayashi, M., Ishiwata M., Gotoh, N., Miura, N., Fujioka, T., and Kahima K., 1993, "Low Cycle Fatigue Crack Growth and Ductile Fracture Under Dynamic /Cyclic Loadings for Japanese Carbon Steel Piping : Part I - Experimental Study", *ASME PVP*, PVP-Vol. 266, pp.171-174.

Miyazaki, K., Kanno, S., Ishiwata, M., Gotoh, N., Miura, N., and Kashima K., 1996, "Fracture behavior under Monotonic and Low Cycle Loading in Carbon Steel Pipes and Welded Pipe Joints with a Defect" , *ASME PVP*, PVP-2 Fatigue and Fracture Vol.1, Book No. H01051-1996.

Table 1 Geometry of local wall thinning.

| Specimen No. | Outer Diameter OD (mm) | Inner Diameter $t$ (mm) | Eroded Depth $d$ (mm) | Eroded Depth $d/t$ | Eroded Angle $2\theta$ (deg.) | Eroded Length $\ell$ (mm) |
|---|---|---|---|---|---|---|
| TP-1 | 114.3 | 8.6 | 1.7 | 0.20 | 180 | 100 |
| TP-2 | | | 4.3 | 0.50 | 180 | |
| TP-3 | | | 6.9 | 0.80 | 180 | |
| TP-4 | | | 6.9 | 0.80 | 90 | |
| TP-5 | | | 3.0 | 0.35 | 180 | |
| TP-6 | | | 4.3 | 0.50 | 90 | |
| TP-7 | | | 4.3 | 0.50 | 60 | |
| TP-8 | | | 6.9 | 0.80 | 60 | |
| TP-9 | | | 4.3 | 0.50 | 180 | |
| TP-11 | | | 6.9 | 0.80 | 180 | |

Table 2 Test results for eroded carbon steel pipes subjected to monotonic bending

| Specimen No. | Eroded Depth $d$ (mm) | Eroded Depth $d/t$ | Eroded Angle $2\theta$ (deg.) | Eroded Length $\ell$ (mm) | $P_{max}$ *1 (kN) | $P_c$ *2 (kN) | $P_D$ *3 (kN) | $P_{max}/P_c$ | $P_{max}/P_D$ *4 | Applied Load Form at Eroded Part | Fracture Behavior |
|---|---|---|---|---|---|---|---|---|---|---|---|
| TP-1 | 1.7 | 0.20 | 180 | 100 | 240 | 211 | 88 | 1.14 | 2.74 | Tension | Ovalization |
| TP-2 | 4.3 | 0.50 | 180 | | 233 | 160 | | 1.45 | 2.66 | | Crack Initiation |
| TP-3 | 6.9 | 0.80 | 180 | | 179 | 97 | | 1.85 | 2.04 | | Crack Initiation |
| TP-4 | 6.9 | 0.80 | 90 | | 203 | 158 | | 1.28 | 2.32 | | Crack Initiation |
| TP-5 | 3.0 | 0.35 | 180 | | 235 | 187 | | 1.26 | 2.69 | | Ovalization |
| TP-6 | 4.3 | 0.50 | 90 | | 227 | 191 | | 1.19 | 2.60 | | Ovalization |
| TP-7 | 4.3 | 0.50 | 60 | | 234 | 206 | | 1.14 | 2.67 | | Ovalization |
| TP-8 | 6.9 | 0.80 | 60 | | 231 | 185 | | 1.25 | 2.64 | | Crack Initiation |
| TP-9 | 4.3 | 0.50 | 180 | | 204 | 160 | | 1.28 | 2.33 | Compression | Loacal Buckling |
| TP-11 | 6.9 | 0.80 | 180 | | 171 | 97 | | 1.77 | 1.95 | | Loacal Buckling |

*1 $P_{max}$ : Maximum Load, *2 $P_c$ : Plastic Collapse Load, *3 $P_D$ : Design Load, *4 $P_{max}/P_D$ : Safety Margin

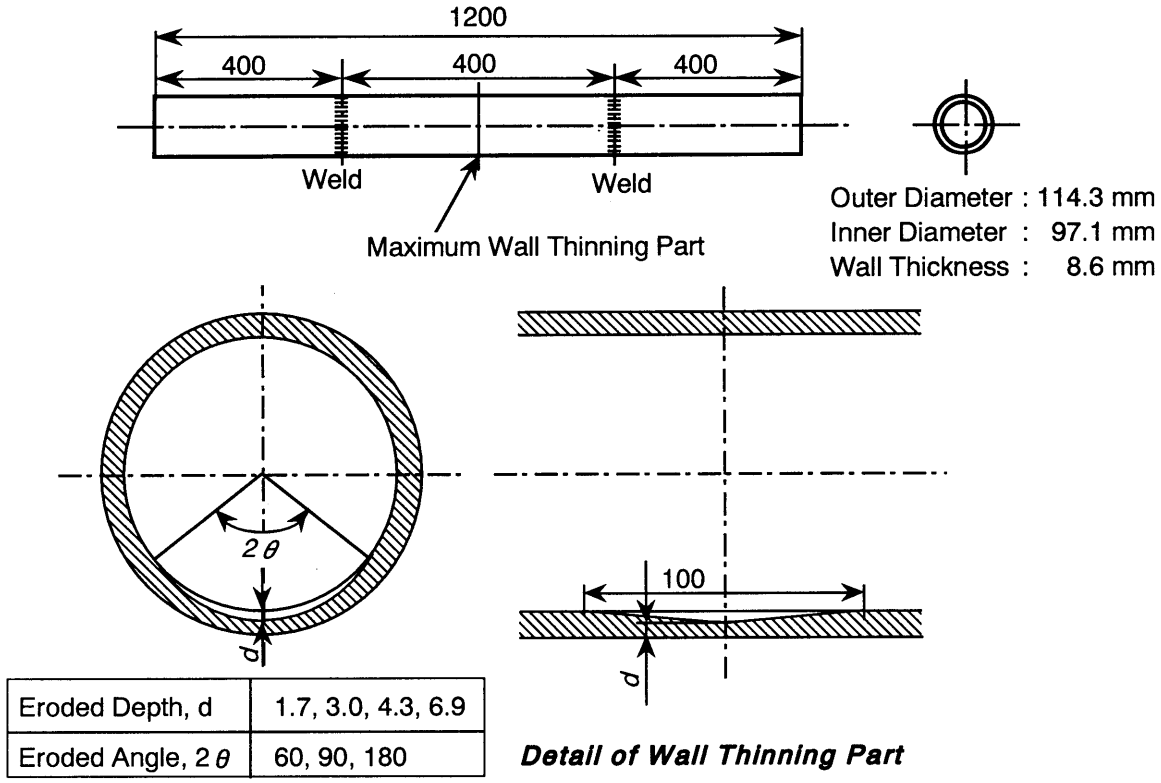


Fig. 1 Geometry of pipe specimen with local wall thinning.

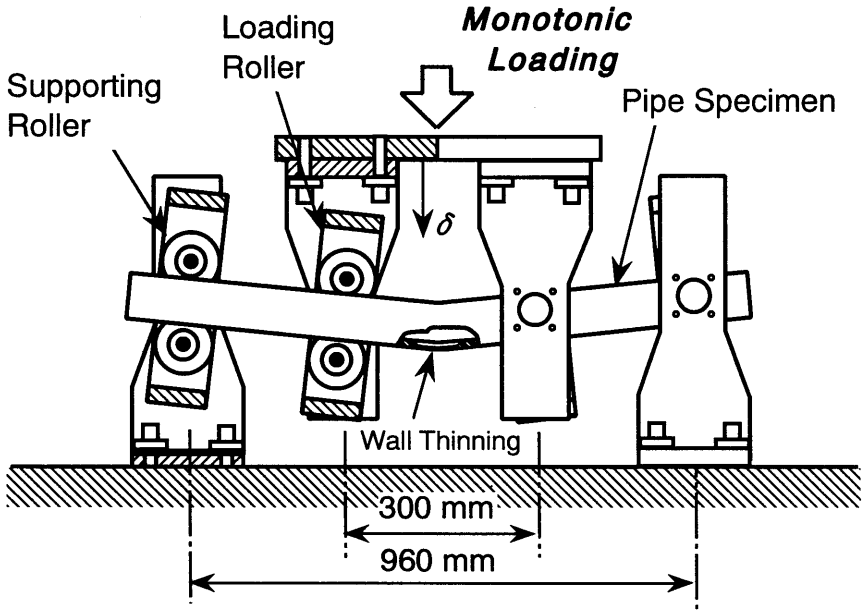


Fig. 2 Monotonic four-point bending test machine.

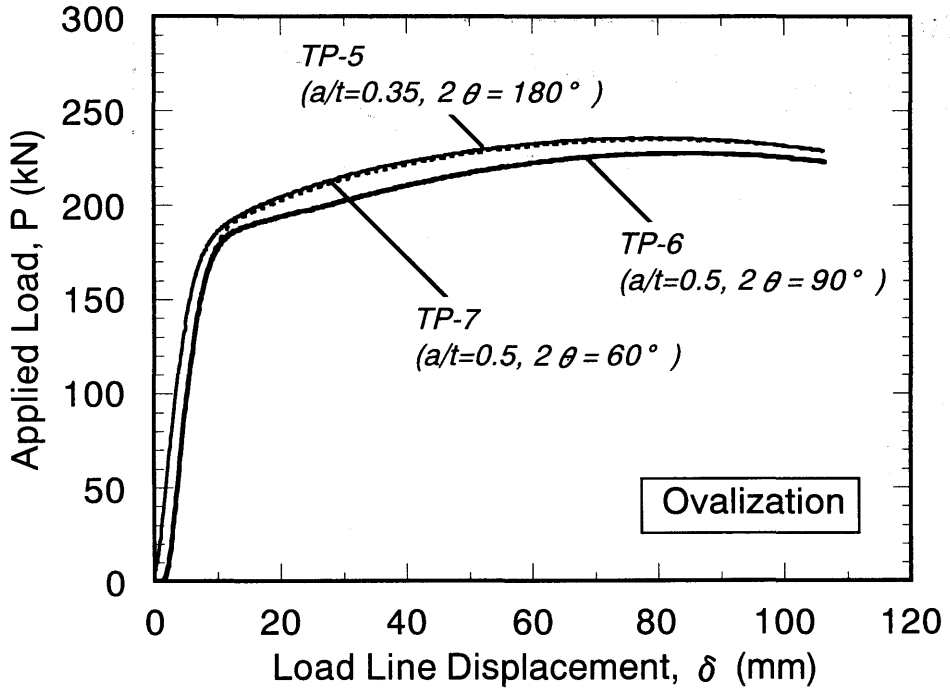


(a) Ovalization

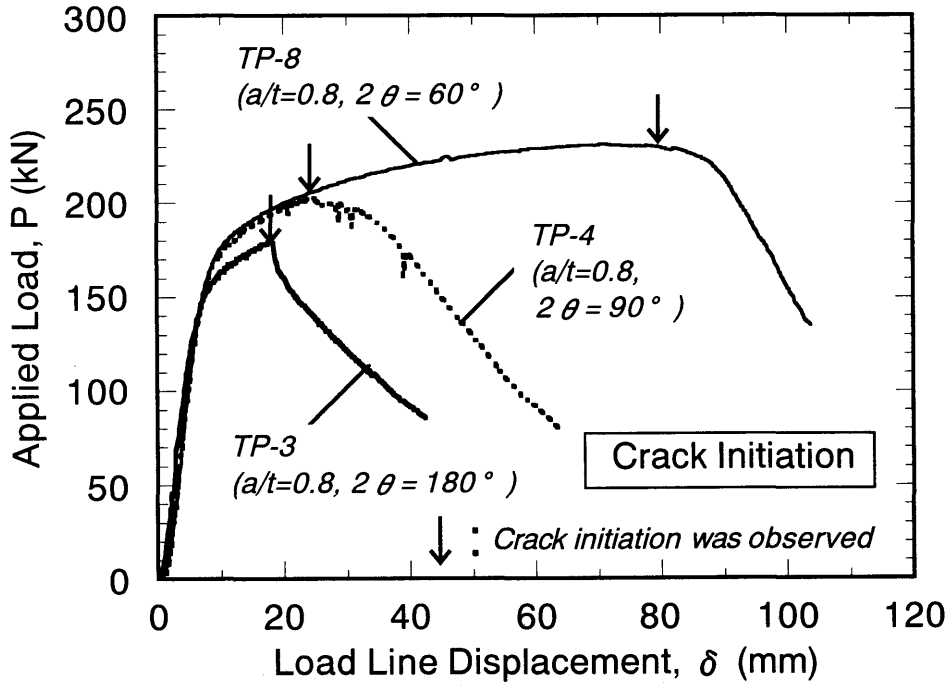


(b) Crack initiation

Fig. 3 Load-displacement curves for locally thinned pipes subjected to tensile stresses.

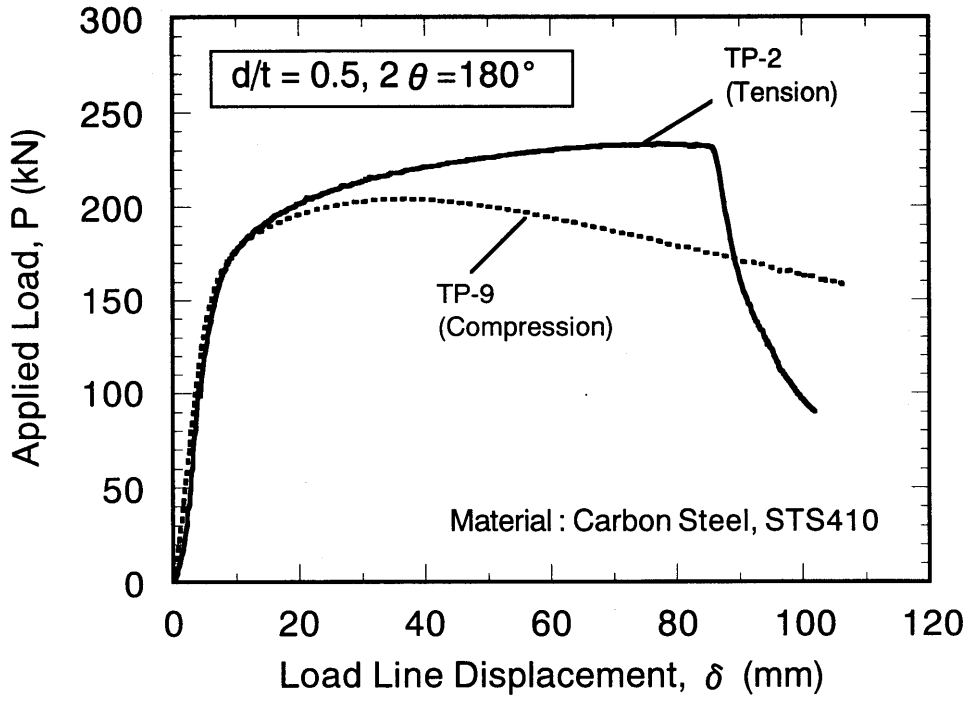


(a) Eroded depth $d/t$ = 0.5, Eroded angle 2θ = 180°

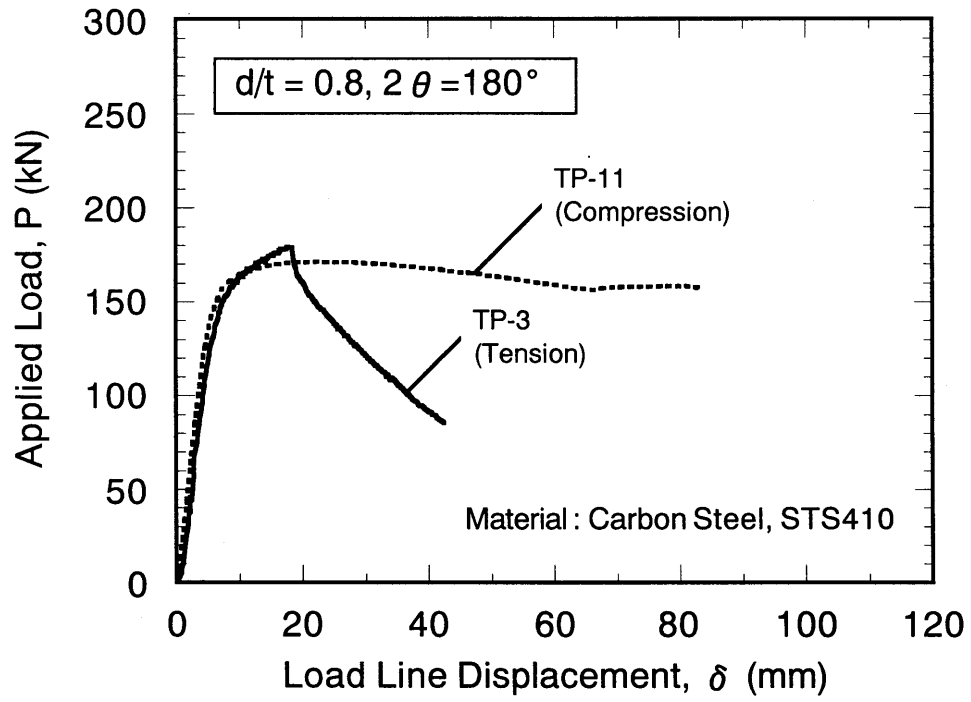


(b) Eroded depth $d/t$ = 0.8, Eroded angle 2θ = 180°

Fig. 4 Load-displacement curves for locally thinned pipes subjected to compression stresses compared to those for pipes subjected to tensile stresses.

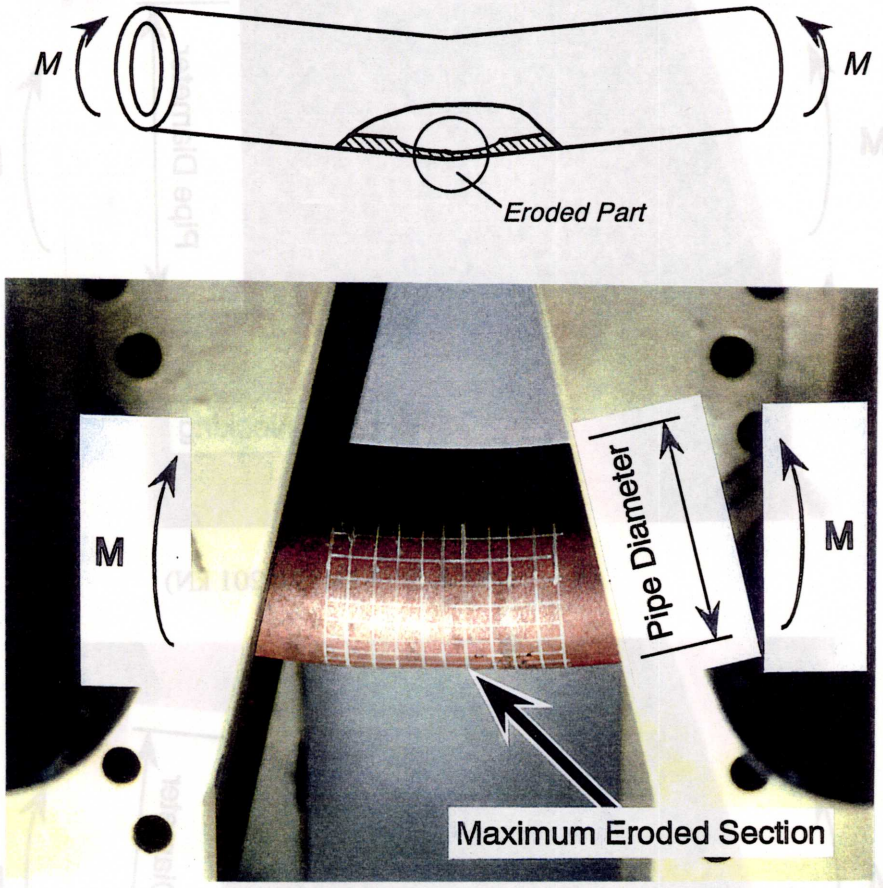


Fig. 5 Fracture behavior of a pipe with a locally thinned area subjected to tensile stress (Fracture behavior : Ovalization, Specimen No. TP-6, Eroded depth $d$ = 4.3 mm, Eroded angle $2\theta = 90^\circ$ , Eroded axial length $\ell$ = 100 mm).

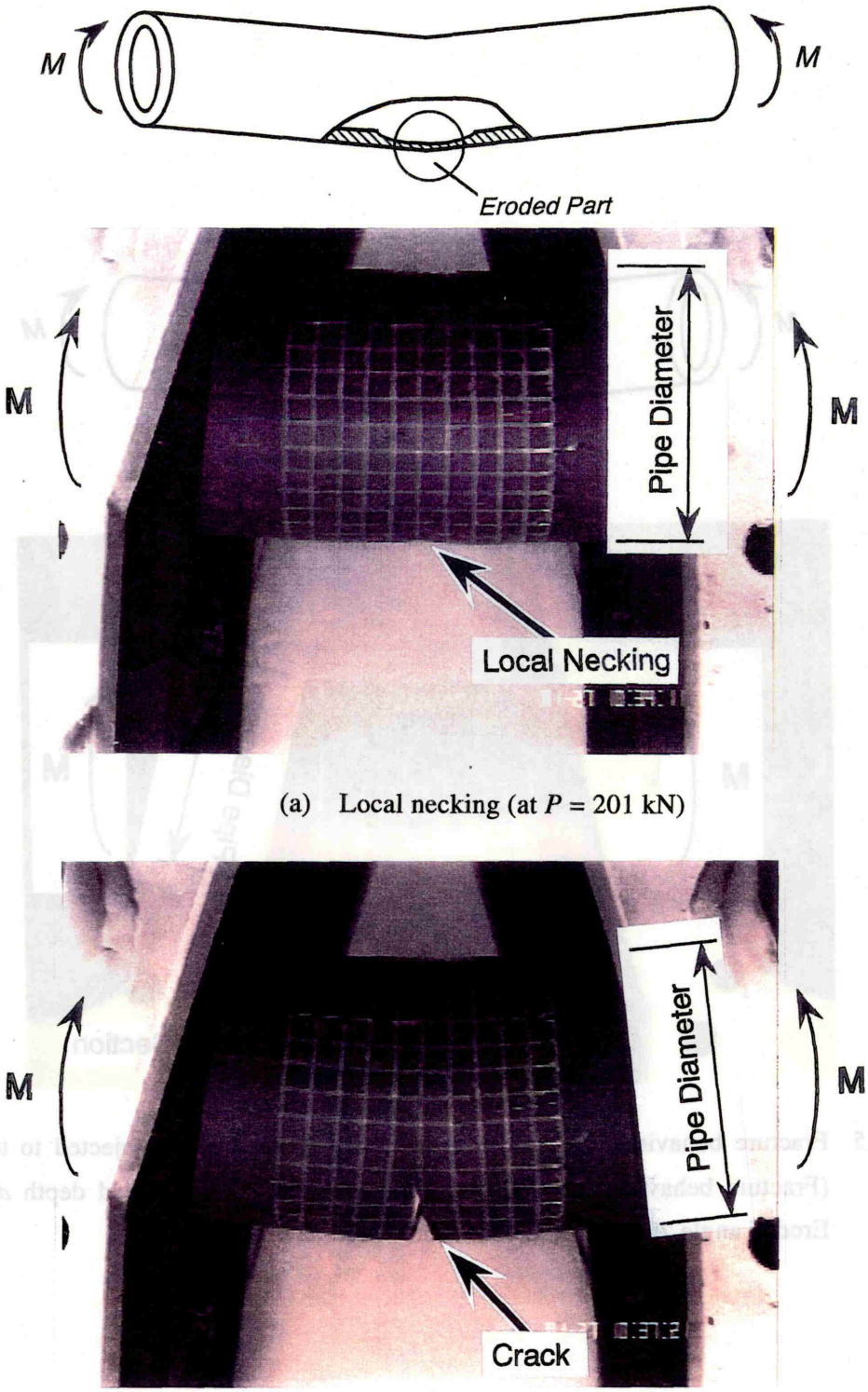


(a) Local necking (at $P$ = 201 kN)

(b) Crack propagation (at $P$ = 161 kN)

Fig. 6 Fracture behavior of a pipe with a locally thinned area subjected to tensile stress. (Fracture behavior : Crack initiation, Specimen No. TP-4, Eroded depth $d$ = 6.9 mm, Eroded angle $2\theta = 90^\circ$ , Eroded axial length $\ell$ = 100 mm).

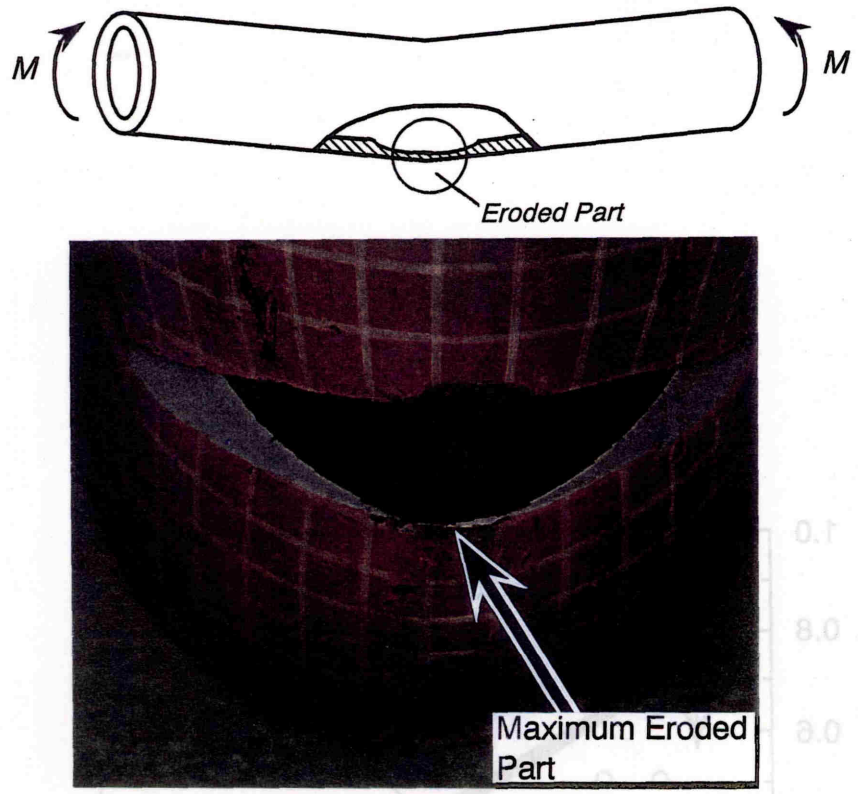


Fig. 7 Crack initiation part of a pipe with a locally thinned area subjected to tensile stress. (Fracture behavior : Crack initiation, Specimen No. TP-4, Eroded depth $d$ = 6.9 mm, Eroded angle $2\theta = 90^{\circ}$ , Eroded axial length $\ell$ = 100 mm).

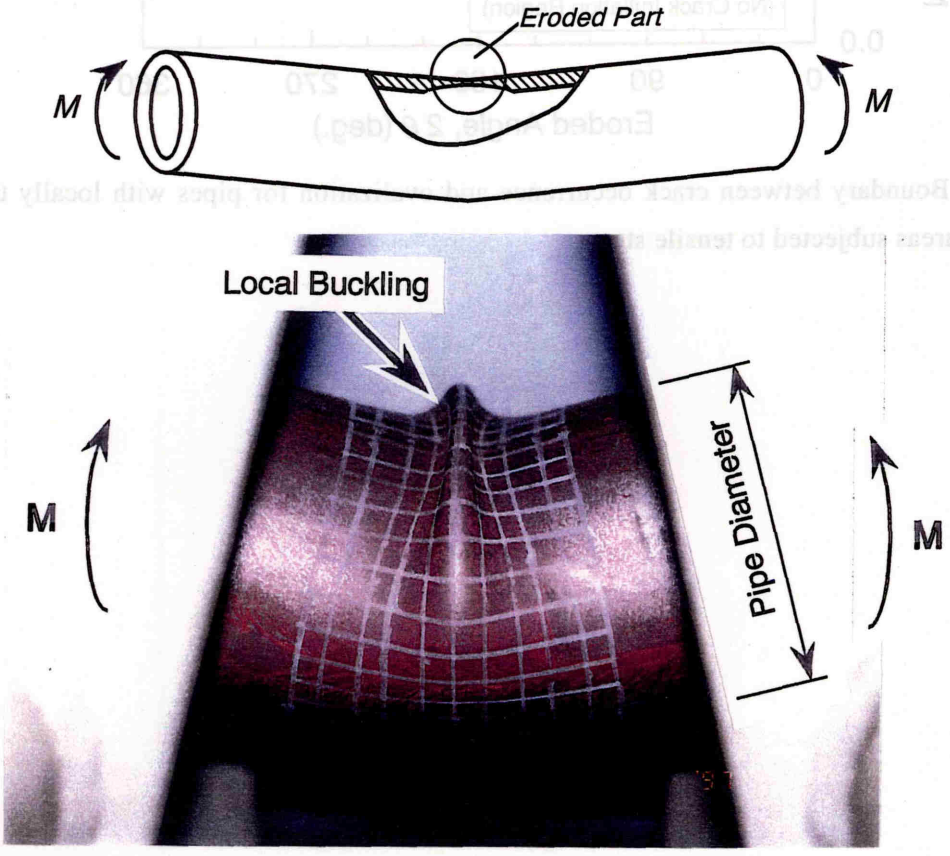


Fig. 8 Fracture behavior of a pipe with a locally thinned area subjected to compressive stress.

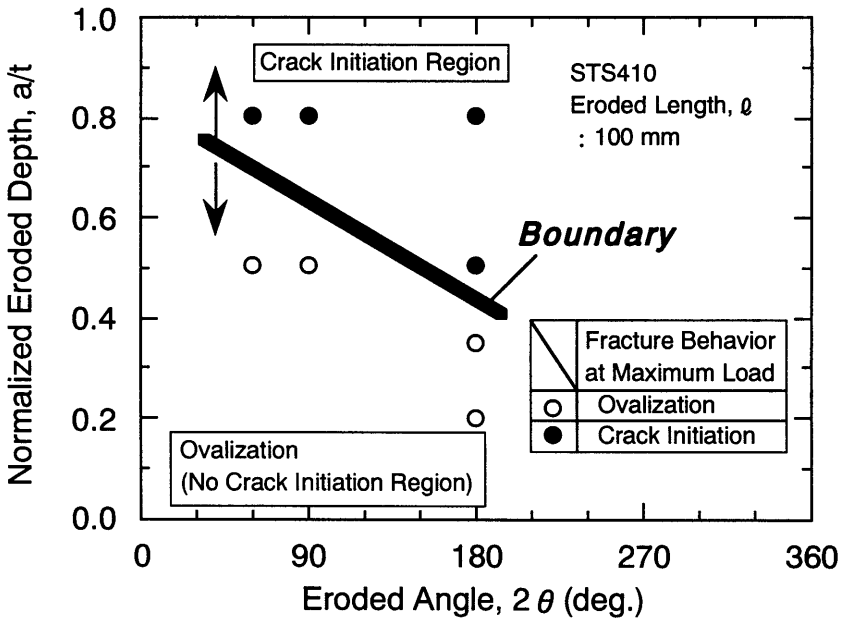


Fig. 9 Boundary between crack occurrence and ovalization for pipes with locally thinned areas subjected to tensile stress.

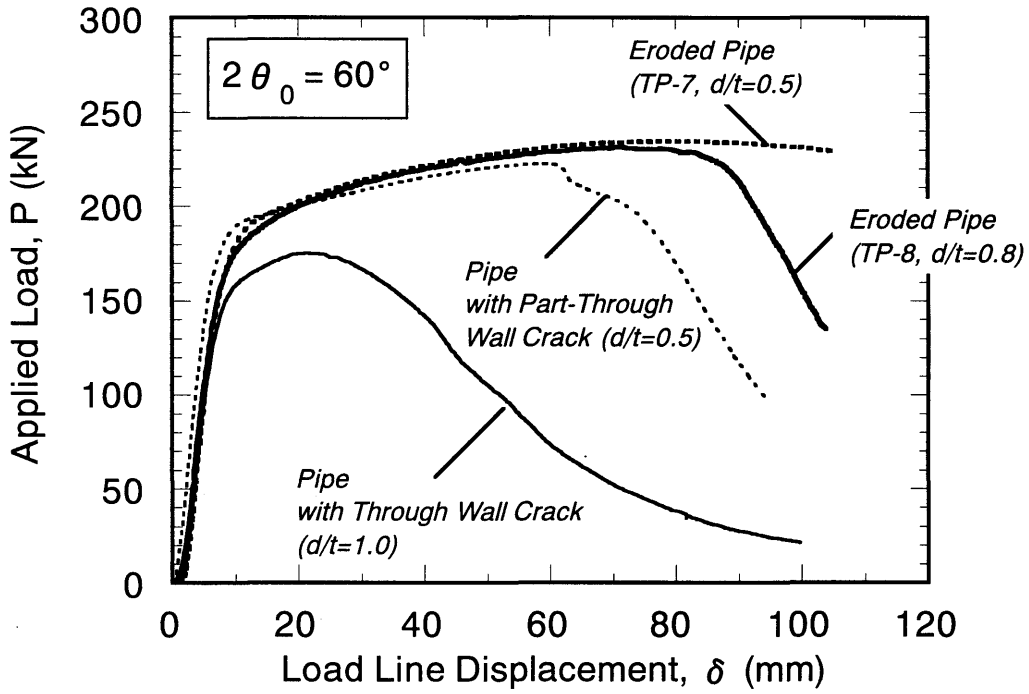


Fig. 10 Comparison of load-displacement curves between cracked pipes and locally thinned pipes. (Eroded angle, $2\theta = 60°$ )

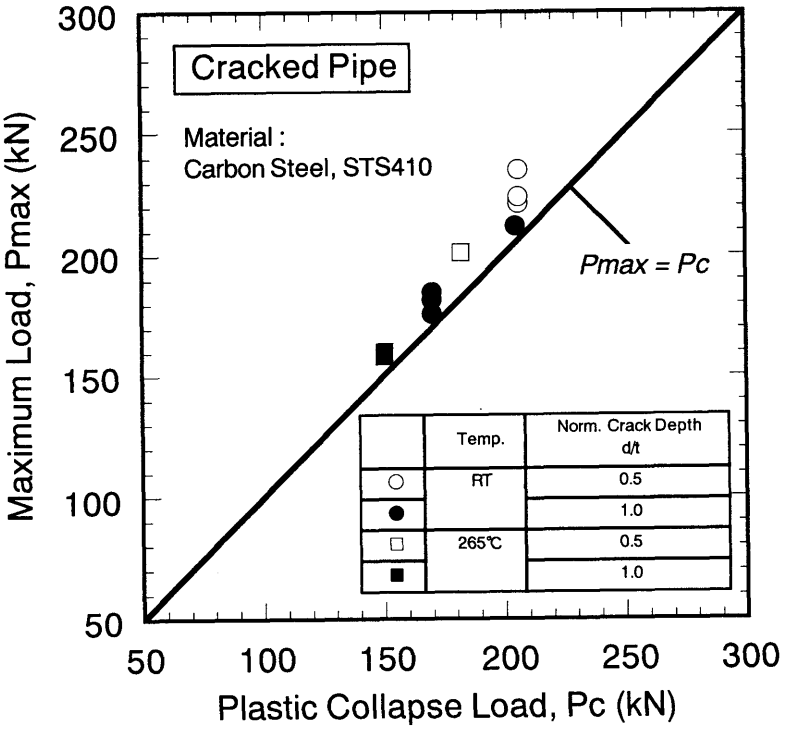


Fig. 11 Comparison of the maximum load, $P_c$ with the plastic collapse load, $P_{max}$ for cracked pipes.

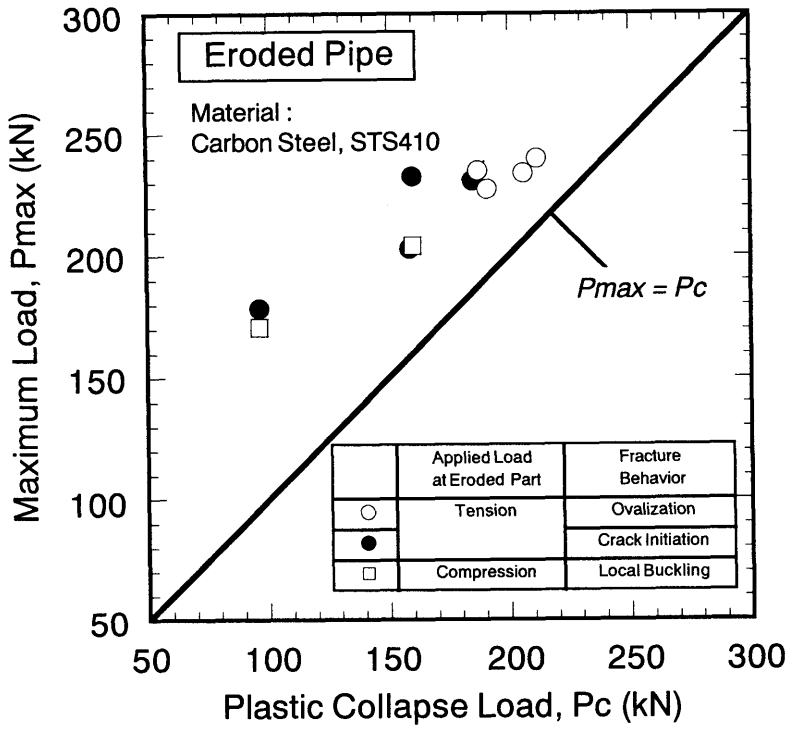


Fig. 12 Comparison of the maximum load, $P_c$ with the plastic collapse load, $P_{max}$ for eroded pipes.

IV-4 Leak-Before-Break Assessment of CANDU Pressure Tube Considering Leak Detection Capability

Youn-Won Park and Yeon-Ki Chung, Korea Institute of Nuclear Safety, Korea

# Leak-Before-Break Assessment of CANDU Pressure Tube Considering Leak Detection Capability

Youn-Won Park and Yeon-Ki Chung
Korea Institute of Nuclear Safety
19 Kusung-dong Yousung-ku Taejon, Korea, 305-338

**Abstract**

The LBB(Leak Before Break) concept is employed as defense in depth in CANDU reactors in order to avoid an unstable failure in pressure tubes. The LBB in pressure tubes can be satisfied when detection, confirmation, and location of the leak are carried out and the reactor is placed in a depressurized condition before the crack exceeds critical crack length. Leak detection and location is provided by the Annulus Gas System. Therefore, the input parameters for LBB analysis, such as leak detection and leak location capabilities, should be made available through AGS in-situ test. Recently, a simulated moisture injection test has been performed in one of the CANDU reactors in Korea, and the LBB assessment was performed using the test results. Only leak detection capability is considered for LBB analysis; the leak location is ruled out because of lack of information in the AGS response vis-à-vis leak location procedure. In this paper LBB assessment is presented using both the leak detection and leak location capability.

## 1. Introduction

Since several incidents of leaking in the pressure tubes in the CANDU reactors have been experienced, significant efforts have been made to improve the pressure tube integrity through design, material, and fabrication upgrades during last decade.

However, delayed hydride cracking (DHC) is still believed to be the major potential threat to pressure tube integrity. To cope with the likelihood of loss of pressure tube integrity due to such DHC, Leak-Before-Break (LBB) is used as a defense-in-depth. The flaw acceptance criteria for pressure tubes, provided by the Fitness For Service Guidelines, (FFSG)[1] requires demonstration that DHC will not occur from flaws in pressure tubes when the hydrogen equivalent concentration exceeds the Terminal Solid Solubility (TSS) for dissolution at full power operating condition, and that if the flaw was propagated by DHC, unstable rupture of the pressure tube is avoided by LBB.

The LBB concept requires timely detection, confirmation of leak, and appropriate operator action to shut the reactor down to a cold depressurized state before the growing crack exceeds the critical crack length (CCL). Since the typical CANDU reactor consists of 380 to 480 pressure tubes, even though a leak is detected in time and the reactor is cooled down, it is not so easy to locate the tube concerned. This is because once the reactor is in a depressurized condition, the crack closes and the leak is near impossible to find. Unless the leaking tube is identified, an entire core inspection is necessary at a cold state. This is very difficult, time consuming, and expensive. Therefore, leak detection and leak location are important from an integrity viewpoint as well as economical standpoint. Normally, only the leak detection is considered in the LBB analysis because there is not enough data for leak location tests[2]. During the pre-operational test of Wolsung unit 2, a complete set of tests for leak detection

and leak location using simulated moisture injection was conducted; these results accounted for LBB analysis for Wolsung units 2, 3 and 4 in Korea.

## 2. Concept of Leak-Before-Break Assessment of CANDU Pressure Tubes

### CANDU Reactor

A CANDU reactor consists of a large tank, called calandria, containing $D_2O$ moderator at 70°C, and is penetrated by 380 horizontal fuel channels each 6 m long. Each channel consists of a pressure tube containing fuel and coolant $D_2O$ at a pressure of 10Mpa and at a temperature ranging from 260°C at inlet to 300°C at outlet. The pressure tubes surrounded and insulated from the cold moderator by a calandria tube. The space between the pressure tube and the calandria tube is filled with recirculating $CO_2$ gas, which is called Annulus Gas System (AGS). The pressure tubes are made from cold-worked Zr-2.5Nb with a wall thickness of 4 mm and an inside diameter of 103 mm. The calandria tubes are made from annealed Zircaloy-2 with a wall thickness of 1.4 mm and an inside diameter of 129 mm. The pressure tubes are rolled into the end fittings at each end of the fuel channel. The residual stress produced by the rolled joint fabrication process is still considered as a potential cause of developing DHC, even though it has been remarkably reduced by using a zero clearance rolled joint[3].

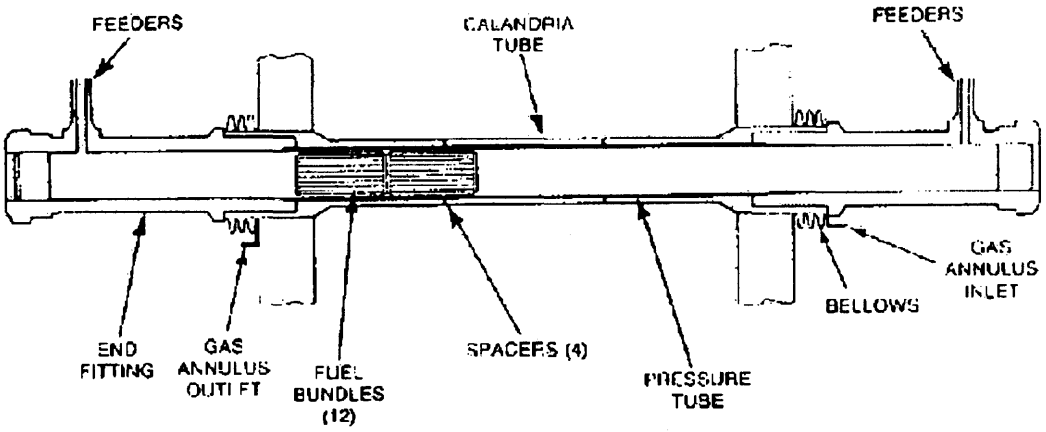


Fig. 1 : CANDU Fuel channel

### Delayed Hydrided Cracking

While the fatigue crack growth which is considered as a principal cracking mechanism for PWR reactors is an order of $10^{-8}$ m/cycle, the crack growth by DHC is an order of $10^{-4}$ m/cycle. Thus the contribution of DHC to crack growth is much more dominant, so that only DHC is taken into account for LBB analysis of pressure tubes. The principal mechanism of DHC is as follows [2] :

Once nucleated, the crack grew in the radial-axial plane under the hoop tensile stress when hydrides were present as the reactor temperature was below Terminal Solution Solubility (TSS) of hydrogen. When the reactor was hot, the hydrides dissolved and crack growth stopped; but, the crack surfaces were oxidized by heat transport of $D_2O$. During later shutdowns the hydrides reprecipitated and the cracking recommenced. When the reactor was again returned to power the hydrides redissolved, the cracking stopped and the crack

oxidation continued, with the newest part of the crack having the oxide with the smallest thickness. Eventually the crack growth in the radial direction led to penetration of the tube wall so that the heavy water of the pressurized heat transport water leaked into the annulus gas system.

## Reactor Operating Condition

Because the Reactor Outlet Header (ROH) pressure is the PHTS pressure parameter for reactor operation, all the reference pressure values are expressed in terms of the ROH pressure taking pressure drop into account. The reactor operating conditions at FPH, ZPH, and ZPC are presented in table 3. For pressure and temperature to be used in LBB analysis, the pressure drops from the pressure tube inlet and outlet to the ROH were derived for every 5°C increments from 40°C to operating temperature, by using linear interpolation[4].

Table 1 : Reactor Operating Conditions and Design Pressures at Different Locations[4]

| Location | Operating Condition | | | | | |
|---|---|---|---|---|---|---|
| | FPH (100%) | | ZPH (0%) | | ZPC (0%) | |
| | Pressure (Mpa) | Temperature (°C) | Pressure (Mpa) | Temperature (°C) | Pressure (Mpa) | Temperature (°C) |
| RIH | 11.3 | 266.5 | 8.4 | 261.0 | 11.7 | 37.8 |
| PTI | 11.1 | 266.5 | 8.1 | 261.0 | 11.4 | 37.8 |
| PTO | 10.3 | 312.1 | 7.3 | 261.0 | 10.2 | 37.8 |
| ROH | 10.0 | 310.0 | 7.0 | 261.0 | 10.0 | 37.8 |

## Parameters for Leak-Before-Break Analysis

The LBB analysis means that when an unlikely leak through-wall DHC crack occurs, throughout the period of time needed for leak detection, confirmation, location and finally placing the reactor in a cold depressurized state, the growing crack length is always less than the critical crack length in order to assure that the probability of an unstable pressure tube rupture is extremely low.
Therefore, the LBB analysis integrates the AGS response to leakage from an assumed through-wall DHC crack with the change in crack velocity and critical crack length as the reactor goes from full power to a cold depressurized condition. The actual station operating procedures should be used to analytically simulate the sequence of events (SOE) following the crack penetration of pressure tube. The parameters needed for the LBB analysis are as follows [1]:

1) Maximum crack length at penetration (Lp)
From the LBB view point, the crack dimensions at onset of leakage is very important. This is estimated to be around four times the normal thickness [1]. Lp of 20 mm is used in this analysis based on the recommendation of FFSG.

2) Delayed Hydride Cracking Velocity (DHCV)
Conservatively, upper bound values of DHCV in axial direction are used:

$$V_a = 5.2 \times 10^{-3} \exp(-41445/RT) \qquad (1)$$

3) Critical Crack Length (CCL)

The half-critical crack length (c), as a function of temperature, stress, fluence, and hydrogen concentration, can be determined from the following equation:

$$c = \frac{K_c^2 \pi}{8\sigma_f^2 \ln[\sec(\frac{\pi M \sigma_h}{2\sigma_f})]} \qquad (2)$$

$$\sigma_f = \frac{\sigma_y + \sigma_u}{2} \qquad \sigma_h = P(\frac{r_i}{w} + 1)$$

$$M = [1 + 1.255(c^2/(r_m w)) - (0.0135(c^4/r_m w) - (0.0135(c^4/(r_m w)^2]^{1/2}$$

4) Leak Rate

A correlation of $D_2O$ leak rate (kg/hr) with crack length (mm) is given:

$$Q = -11.2 + 0.0014(2C_{max})^3 \qquad (3)$$

where, $2C_{max}$ = maximum axial crack length (mm)

This equation is based on PHTS operating conditions of 6MPa and 250°C. Thus, specific conditions other than 6MPa and 250°C, leak rates can be determined using scaling coefficients.

5) Station Response to Moisture in AGS

The time needed to detect, confirm, and locate the leak should be provided. Following the first leak at penetration, the time necessary for initiating the rate of rise alarm is taken from the AGS performance test carried out at Wolsung unit 2 in May 1997. The AGS performance test and its results will be described later on.

6) Pressure tube dimension

For a conservative approach, pressure tube dimensions were taken from expected values after 15 years of operation [4]. Installed thickness is based on the minimum specified dimension of 4.19 mm, subtracting both the corrosion allowance of 0.140 mm and wear allowance of 0.064 mm. Dimensions after 15 years of operation are made by considering an additional wall thinning of 0.149 mm and a diametral creep strain of 2.1%. The wall thickness is also made by considering a local wear of 0.028 mm due to the annulus spacer rolling. At the end of 15-year service, the wall thickness is 3.83 mm, the maximum inner radius is 53.37 mm, and the mean radius is 57.20 mm.

## Assumptions used for LBB analysis[5]

1) The most likely area for DHC crack to occur is inboard of the rolled joint; because of relatively high residual stress. The crack growth in one direction should be stopped due to restraint when the crack arrives at the rolled joint. However, to be conservative, the DHC crack growth is assumed in both directions throughout the event.
2) The crack is to propagate at the upper bound crack velocity
3) A lower bound estimate of critical crack length and fracture toughness is used
4) The pressure tube leak occurs in the longest AGS channel and the AGS is operated in very low recirculation flow. This leads to a longer moisture detection time.
5) There are sufficient hydrides at power for crack growth to occur.
6) The pressure tube dimension of 15 years in operation is used for accounting for the wear and corrosion allowances, and the diametral creep and wall thinning.

## 3. Leak Detection and Location Capability Test

Leak detection in a pressure tube is provided by the Annulus Gas System (AGS). The AGS circulates dry $CO_2$ gas in the annular space between the calandria tubes and pressure tubes. The fuel channel annuli are connected in a series/parallel configuration to form a closed loop as shown in Figure 2. There are 44 inlets connected, in parallel, to the recirculating gas supply system and 44 outlets connected, in parallel, to the drain and the suction side of the recirculating compressors.

A total of ten tests were completed[6]. Seven were moisture injection tests to determine system dew point versus time response with continuous injection until the dew point increased to -10°C. Three of the ten tests were to measure the change in dew point response to leaking valve in and out process. The main purpose of the leak location test was to qualify the AGS abnormal operating procedure to be used for identifying leak channels.

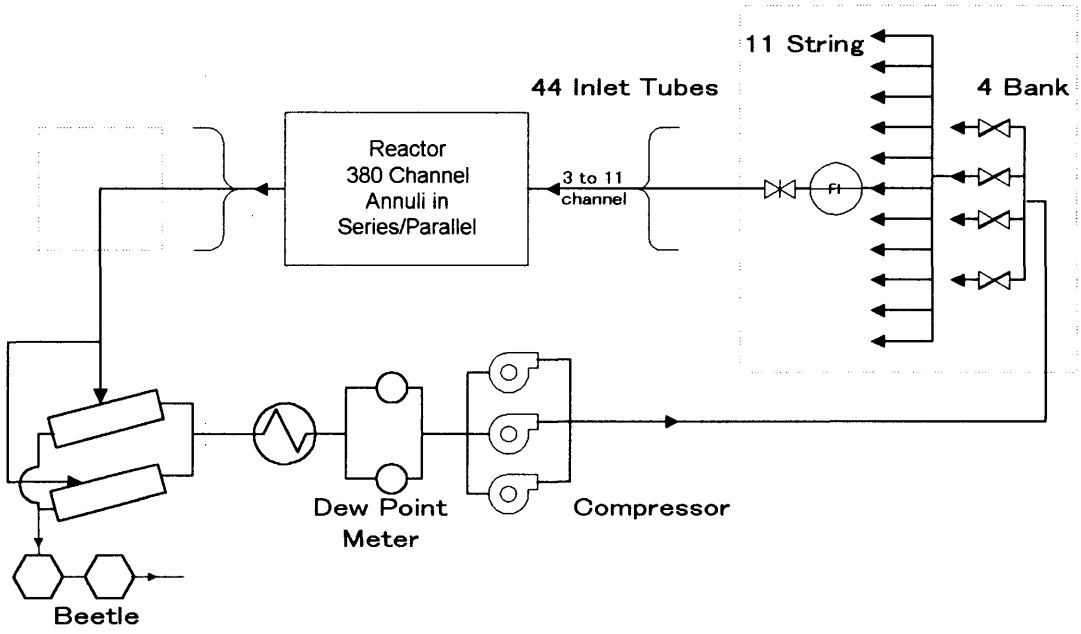


Fig. 2 : Annulus Gas System Configuration

### Leak Detection Test

Of the seven moisture injection tests, three tests were conducted with the Primary Heat Transport System (PHTS) cold and four tests with PHTS Zero Power Hot (ZPH). Table 1 shows the test matrix for leak detection and leak location.

*Test 1, 2, and 3*

The first injection was carried out in the main circuit at the downstream of the compressors and upstream of the gas distribution manifolds. The injected $D_2O$ and $CO_2$ gas was therefore distributed to all the 44 strings. The purpose of these tests was to investigate dew point versus

time response and the dew point's rise rate under several conditions including flow rate, string length, operating modes, and so on. The test results show that there are several peaks which are related to the first wave of moisture from three channel, five channel, seven channel, and so on. Interestingly, using these results, a relative flow resistance from different numbers of channels can be drawn out. The flow rate of each string was calibrated to be the same and the lengths from the injection point to the first channel inlet of each string were almost the same. Therefore, the differences in time in Fig. 3 come from the elapse time necessary for passage through different numbers of fuel channels, the following relation can be derived. Note this relation is applicable to a hot reactor condition because it is only response ratio for geometrical lengths.

$(3C + L)/V = 0.6$ for 3 channels
$(5C + L)/V = 0.92$ for 5 channels

where C = equivalent length of one fuel channel, L = length from injection point to first channel inlet of each string plus length from outlet of last channel to dew point meter, and V=gas velocity.

Therefore, the time required to pass through one fuel channel is equivalent to the time, multiplied by 1.33, necessary for traveling path L. Using this conversion factor the response of an 11 channel string can be drawn out to be 1.88 hr and comparing this value with the test result of 1.89 hr shows that such conversion is acceptable.

As shown in table 1, in test 2 and 3, injection was into one of eleven channel strings which are the longest strings at Wolsung unit 2. Test 2 was carried out with a flow rate of 2.6 L/s and test 3 with 5.1 L/s. The resulting Rate of Rise alarm was initiated at 2 hours and at 1.5 hour respectively.

Table 1 : Matrix of AGS Performance Tests

| | Test No. | Simulated Leak Rate (g/h D2O) | AGS Operating Modes | | | Injection Location | | | PHTS Condition Comments |
|---|---|---|---|---|---|---|---|---|---|
| | | | 1 CP | 2 CP | Purge | 11 CH | Main Circuit | 3 CH | |
| Cold | 1 | 12.8 | X | | | | X | | Cold, Depressurized |
| | 2 | 2.9 | X | | | X | | | Cold, Depressurized |
| | 3 | 3.3 Inject 2.8 Inject + Purge | | | X (inject with purge on) | X | | | Cold, Depressurized |
| | 3A | 2.5 | X | | | X | | | Cold, Depressurized Leak Location Test |
| Hot | 4 | 1.25 Inject 1.50 Inject + Purge | X | | X | X | | | Zero/Low Power Hot |
| | 5 | 3.05 | | X | | X | | | Zero/Low Power Hot |
| | 5A | 2.34 | X | | | X | | | Zero/Low Power Hot Leak Location Test |
| | 5B | 3.04 | | X | | X | | | Zero/Low Power Hot |
| | 6A | 2.48 | X | | | | | X | Zero/Low Power Hot |
| | 6B | 2.4 | X | | | | | X | Zero/Low Power Hot Leak Location Test |

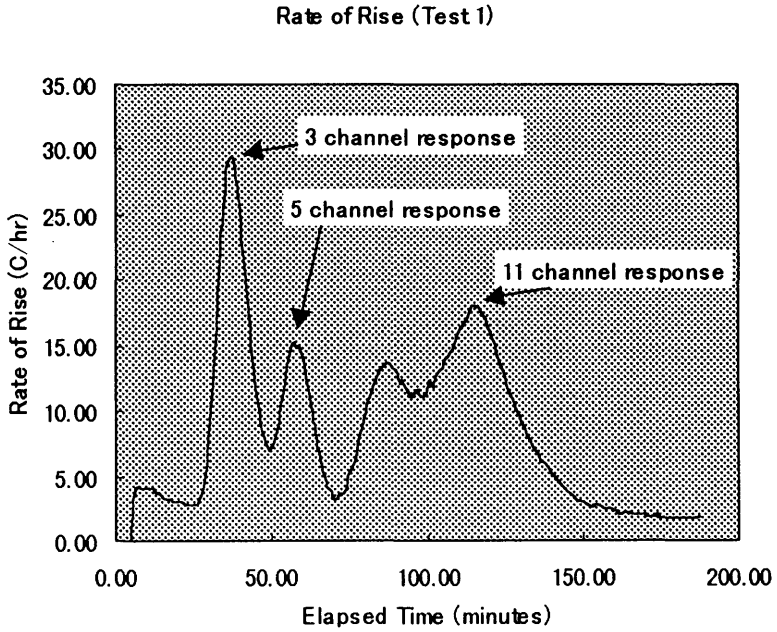


Fig. 3 Rate of Rise responses from strings having different number of channels

*Test 4*

This test was similar to test 3 with an inject + recirculate phase followed by an inject + purge phase. The reactor was hot and the recirculation flow was adjusted by throttling the compressor inlet and outlet valve to simulate very low flow AGS operation, which is 1.65 L/s. The first wave of moisture came through with a peak of about 6°C/hr at about 2.6 hours after starting injection. During the inject + purge period, the dew point dropped to around -30°C in about 2 hours.

*Test 5*

This test was done with two compressors and with an addition of 0.3% oxygen. In comparison with test 3 which has similar starting dew points and similar injection rates shows that the rate of rise was higher for a hot reactor than a cold reactor. The first wave appeared at one hour and the peak rate of rise of dew point was 23°C/hr.

*Test 5B*

This test was carried out under very similar conditions to test 5; very high flow rate with two compressors. The first signal appeared about one hour after the start of injection. The peak of the rate of rise of dew point was about 35°C/hr. As an example, the dew point trend obtained from test 5B is shown in figure 3.

*Test 6A*

This test was with a compressor and an injection into the 3 channels string. The first signal appeared about 25 minutes after the start of injection. Since a response corresponding to

normal operating conditions with 11 channel strings was not available, test 6A results were converted to 11 channel data using the conversion factor obtained from test 1.

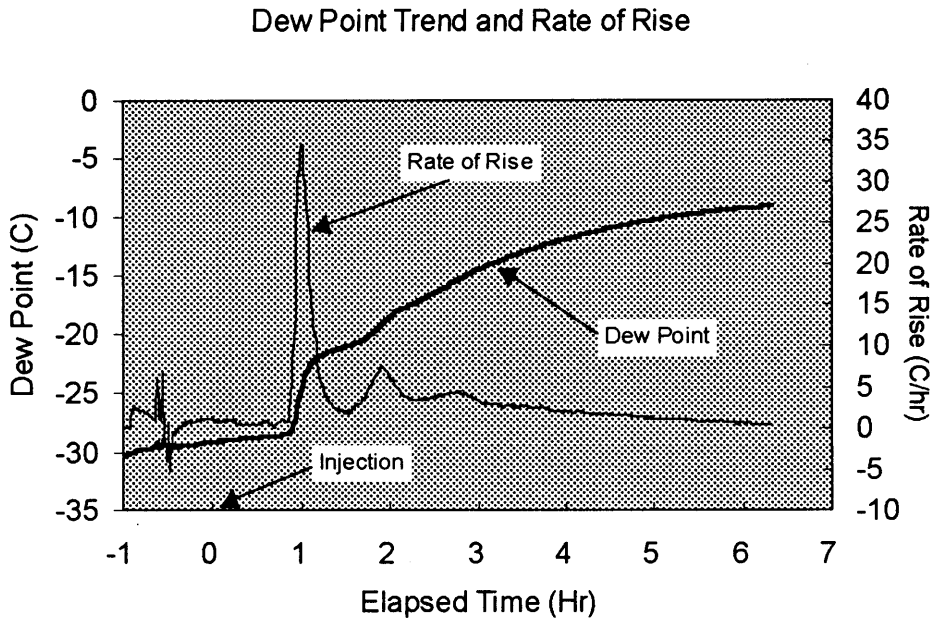


Fig. 4 Dew Point trend and Rate of Rise for Test 5B

The test results are summarized in table 2. When comparing the rates of rise for a cold reactor with those for a hot reactor, the responses at cold conditions are slower than those at hot conditions. Therefore, four data are used for determining the relationship between initiation time for rate of rise alarm and AGS flow rate, as shown in figure 4. It is valuable to note that, since the time for rate of rise alarm is the time required to pass through 11 channel plus connecting tubing length L, the relationship between time for rate of rise and flow rate should be a form of $y = C/x$, where y= time for Rate of Rise, C = constant, and x = Flow Rate. The curve fit, shown in figure 4, is very close to the expected form.

Table 2 : Test Summary for AGS Leak Detection

| Test No | Reactor Condition | No. of Channels | flow rate (L/s) | Rate of Rise (hr) | Peak of ROR (°C/hr) |
|---|---|---|---|---|---|
| 1 | Cold | 11 (3) | 3.26 | 1.88* (0.6) | 29 |
| 2 | Cold | 11 | 2.73 | 2 | 34 |
| 3 | Cold | 11 | 4.66 | 1.5 | 19 |
| 4 | Hot | 11 | 1.67 | 2.6 | 6 |
| 5 | Hot | 11 | 4.40 | 1 | 24 |
| 5B | Hot | 11 | 4.44 | 1 | 35 |
| 6A | Hot | 11 (3) | 3.08 | 1.31* (0.43) | 37 |

* data converted from 3 channels to 11 channels

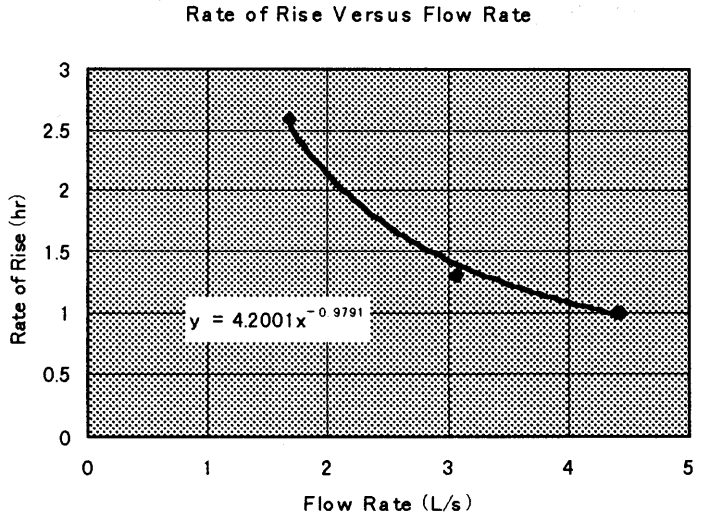


Fig. 5 Rate of Rise versus AGS flow rate for hot reactor condition

## Leak Location Test

*Current Leak Location Procedure*

A moisture level, showing a continuing tendency to increase, indicates a leak into the system from a calandria tube or pressure tube. To locate the leak source, the purge flow is passed through each of the four banks of 11 inlets in turn. The recirculation mode is changed to purge mode. Two out of the four headers valves are closed at one time based on the dichotomization and the moisture level is observed on a dew point analyzer. This will narrow the location down to one of the four banks.

In the bank giving the high moisture reading, the purge flow is passed through each of 11 inlets by closing the rotameter outlet needle valves in five of the lines. Based on the dichotomization process, lines with no channel leakage will be isolated and it will narrow the location down to one line which feeds three to eleven channels depending on the number of channels in series. Therefore, to locate the leaking string requires 6 dichotomization processes.

*Test Results (Test 3A, 5A, 6B)*

This test is similar to leak detection test 3, except that leaking and non-leaking bank and string valving operations were carried out after the first wave appeared. As shown in Fig. 4, the first wave appeared about 105 minutes after the injection.
When two non-leaking banks were valved out, a reduction in total flow was produced so that an increase in dew point was observed. Valving back in two non-leaking banks resulted in a reduction of dew point; but, the initial value before the valving out operation was not achieved because of continuing moisture injection. Valving out one non-leaking bank and one leaking bank resulted in drastically reducing the leaking string flow rate, thus a large reduction in dew point occurred. The opposite effect was seen on when valving in the concerned banks or strings. Valving out and in the leaking string showed a large change in dew point, whereas valving out and in six non-leaking strings produced only small effects.

In general, a significant reduction in the dew point was obtained when the leaking string or a bank containing the leaking string was valved out, and a significant increase in the dew point was obtained in the opposite case.

Two other tests, test 5A and test 6B, performed with a hot reactor, showed a similar trend. Three tests for leak location are summarized in table 3.

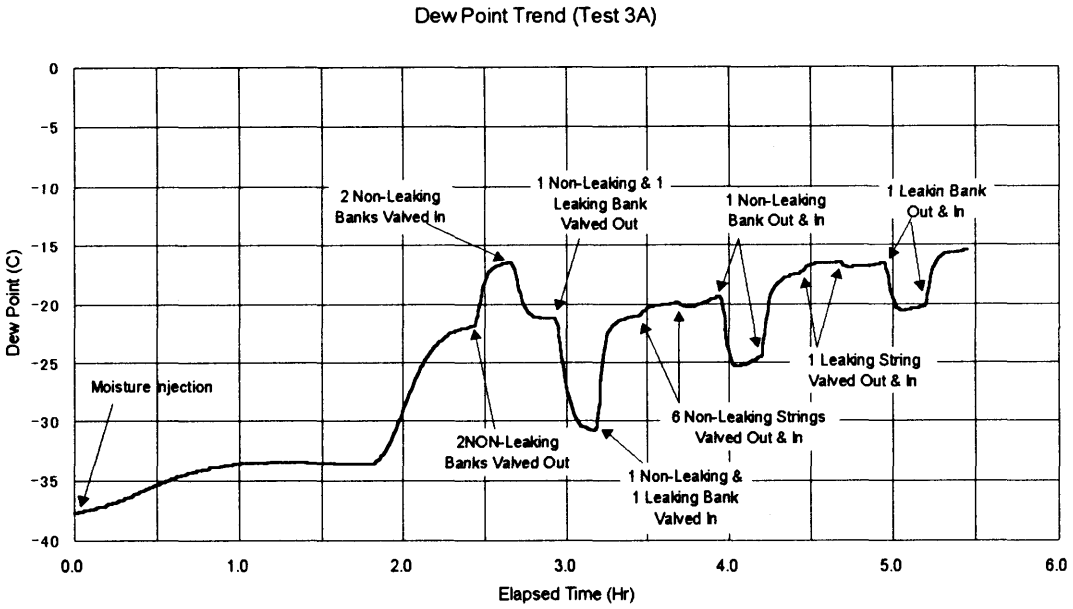


Fig. 6 Leak Location Test (Test 3A)

Table 3 Summary of Leak Location Test

| Operation | Test 3A | | | | Test 5A | | | | Test 6B | | | |
|---|---|---|---|---|---|---|---|---|---|---|---|---|
| | ΔP (kPa) | $T_{sat(1)}$ (Min.) | Out ROR (C/hr) | in ROR (C/hr) | ΔP (kPa) | $T_{sat(1)}$ (Min.) | Out ROR (C/hr) | in ROR (C/hr) | ΔP (kPa) | $T_{sat(1)}$ (Min.) | Out ROR (C/hr) | in ROR (C/hr) |
| 2NLB | 2.4 | 8 | 48 | -42 | 2.40 | 8 | 10 | -10 | 2.55 | 8 | 12 | -16 |
| 1LB+1NLB | 2.4 | 8 | -80 | 88 | 2.40 | 8 | -10 | 10 | 2.40 | 7 | -13 | 11 |
| 1NLB | 1.16 | 5 | 5 | -5 | | | | | | | | |
| 1LB | 1.16 | 7 | -40 | 40 | | | | | | | | |
| 6NLS | 0.73 | 4 | 5 | -5 | 0.51 | 7 | 2 | -2 | 0.58 | | | |
| 1LS | | 7 | -60 | 60 | | 7 | -5 | 5 | | 7 | -13 | 12 |

(1) time required for dew point trend to roll off

As shown in table 3, one operation of valving out or in takes only 7 to 8 minutes. When using the leak location procedure, the narrowing down from 4 banks to a leaking string, at least six dichotomization processes are needed and will therefore take less than 50 minutes. It is valuable to note two things: firstly, the dew point response was much faster than expected, and secondly, the rate of rise produced from a leaking string or a bank containing a leaking string is always higher than very high rate of rise alarm set point which is 4.5°C/hr. Before leak location test it was predicted that using the recirculation mode the second wave, affected by valving out or in operation, must appear at the time when the time as much as required for first wave elapses since the first wave appears. However, as shown in table 3 and Fig. 4, the

corresponding wave appeared immediately and the dew point trend rolled off in 7 to 8 minutes after valve operation. It means that the waves produced by valving out or in process were not made by moisture transportation. Therefore, even though the exact mechanism of such wave apparition is not yet clearly defined, it can be presumably drawn out, that the same trend can be obtained when the AGS is in a stagnant mode.

## 4. LBB Analysis and Its Application

Based on the current operating procedures a complete sequence of events are established from leak detection to the time of the reactor being placed in a cold depressurized state.

### Sequence of Events based on Current Operating Procedure[7]

The Sequence of Event (SOE) including the leak detection, confirmation, leak location and reactor shutdown should be developed based on station operating procedure. Leak detection can be made by a rate of rise alarm and/or beetle alarm. Normally the rate of rise alarm provides an earlier response to moisture so that in the SOE, leak detection is supposed to be made by rate of rise alarm. Based on the AGS test results (Fig. 3), a rate of rise alarm is to be initiated at 2.6 hours after the start of a leak, when the AGS is under very low flow operation.

Operators should reduce power from Full Power Hot (FPH) to Zero Power Hot (ZPH : 261°C and 8MPa). Reactor temperature drop with a maximum allowable cooldown rate, 2.8°C/min, is followed by a pressure drop with a maximum rate of 1bar/min. Since the beneficial effect of thermal maneuvering on DHC velocity is presented by Moan et al [7], the following thermal maneuvering is taken: reduce PHTS temperature from FPH to a temperature lower than ZPH by 40°C, hold this temperature for about 15 minutes and subsequently increase the temperature to ZPH again. After reaching ZPH, the AGS should be put into the stagnant mode and should be followed by the collection of leakage and the leak location process, according to the AGS abnormal operation procedure. As soon as the leaking source is located or total allowable duration time elapses, the reactor should be cooled down to below 100 °C with a maximum allowable cooldown rate and followed by pressure drop down to 3 Mpa. Under these conditions, the critical crack length of the pressure tube is very large, so that failure of the pressure tube is unlikely to occur. The cooldown should continue until the reactor is safely placed in a cold depressurized condition, using station procedure. To cool the reactor down from FPH to a condition below 90°C, maximum cooldown rates are assumed as follows: 2.8 °C /min for 310-260 °C, 2.4 °C /min for 260-150 °C, 1.2 °C /min for 150-90 °C, and 0.4 °C /min for below 90 °C as presented in FSAR of Wolsung unit 2[8]. The maximum pressure drop rate is assumed to be 1 bar/minute throughout the SOE.

### LBB Analysis

The crack length at each time step (every 0.1 hour), when time=ti, has been calculated using the following expression [1]:

$$L_i = L_{i-1} + (V_i + V_{i-1})(t_i - t_{i-1}) \qquad (4)$$

Where, Li = length of crack at time ti, Vi = DHC velocity at time ti.

The critical crack length at each time step was also generated from Equation (2). The LBB can be demonstrated by showing that the growing crack length is always below the critical crack length throughout the SOE. A cooldown path based on the foregoing SOE is shown in

Fig. 7 where temperatures and 10 times pressure at ROH are presented as a function of time elapsed after the initiation of leak. When using the SOE, LBB could not be assured because the crack length exceeds the CCL before leak detection as shown in Fig. 8.

Therefore, it was firstly required to reduce the time for leak detection. This could be achieved by increasing the AGS gas flow rate as shown in Fig. 5. The minimum gas flow rate of AGS was set to be 2.3 L/s so that the leak detection could be done within 1.9 hour after the start of leak. Secondly, pressure plateau at ZPH should be reduced from 8Mpa to 7Mpa to increase CCL at ZPH condition. Finally, cooldown process from ZPH to depressurized condition should be done in two steps: ZPH to 150°C and 150°C to cold state and pressure drop should be made in-between at 150°C. As a result, the LBB can be satisfied using this modified operating procedure as shown in Fig. 8.

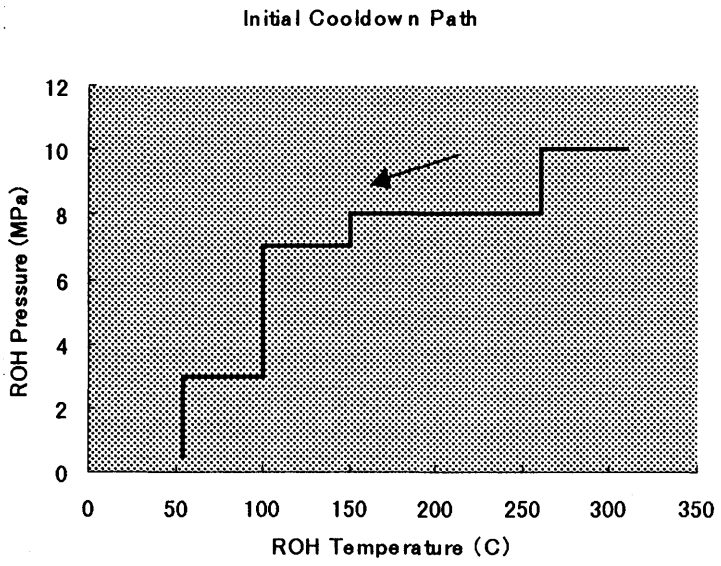


Fig. 7 Current cooldown path

## 5. Conclusion

A complete leak-before-break analysis was carried out for pressure tubes of a CANDU reactor considering leak detection and leak location capabilities. The detection and location capabilities for pressure tube leak were determined by a simulated moisture injection tests performed at Wolsung unit 2. A relationship of leak detection time versus AGS gas flow rate was derived and an appropriate minimum AGS gas flow rate meeting LBB was determined from this relationship. Leak location tests were carried out based on the current dichotomization process using valving out or in a leaking string or leaking bank containing a leaking string. The responses of dew point were very sensitive to valving out or in process such that very high rate of rise alarm could be initiated in 7 to 8 minutes following valving out or in whatever a leaking string was concerned. When using a dichotomization procedure, about 6 valving out or in operations are expected to locate a leaking string, which require less than 1 hour. These test results were used as inputs for LBB analysis.

The upper bound values of DHCV and pressure tube dimension expected after 15 years of operation were used and all the assumptions were made very conservatively. When using

current operation procedure with the foregoing AGS test results, LBB was not satisfied so that five main improvements were necessary to meet LBB: reducing leak detection time by increasing AGS gas flow rate, lowering pressure plateau at ZPH from 8Mpa to 7Mpa, inserting a pressure drop process during reactor cooldown from ZPH to cold depressurized condition, and providing a maximum allowable time for operator to take action for leak location procedure. From these LBB analyses results, reactor operating procedure and plant technical specifications were modified.

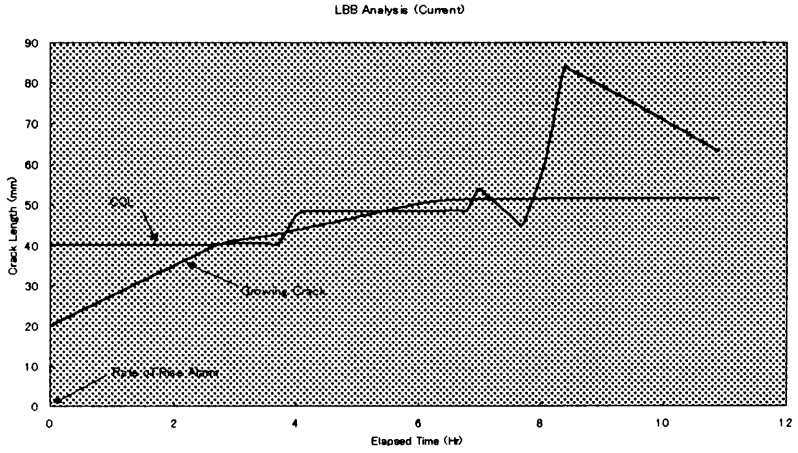


Fig. 8 LBB Analysis Results based on current operating procedure

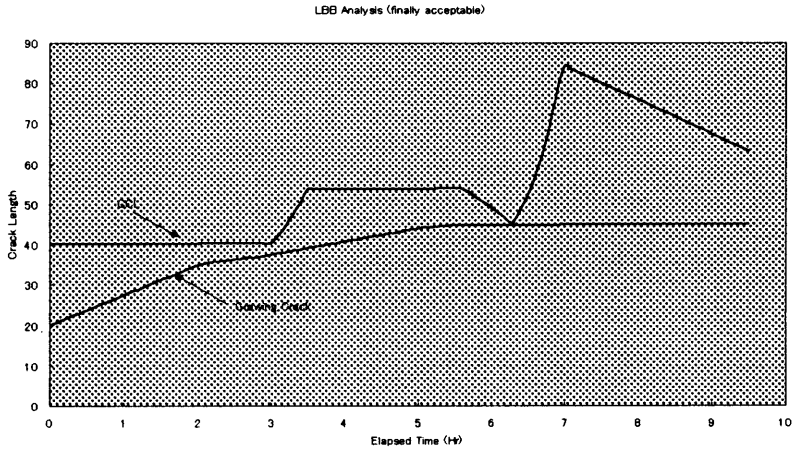


Fig. 9 LBB Analysis and corresponding cooldown procedure to meet LBB

**Reference**

[1] Fitness for Service Guidelines for Zr Alloy Pressure Tubes, COG-91-66, 1991 May.
[2] N. Azer, D.H. Barber, P.J Boucher, P.J. Ellis, J.K. Mistry, V.P. Singh and R. Zaidi, "Leak Detection Capability in CANDU Reactors", Specialist Meeting on LBB, Lyon, Oct. 1995
[3] G.D. Moan, C.E. Coleman, E.G. Price, D.K. Rogers and S. Sagat, "Leak-Before-Break in the Pressure Tubes of CANDU Reactors", Int. J. Pres. Ves. & Piping 43 (1990) 1-21.
[4] Design Report of Fuel Channel Stress Analysis for Wolsung NPP 2, 3, and 4, AECL, May 1995
[5] Preliminary Generic LBB Analysis for Wolsung Units 2, 3, & 4 by AECL, Oct. 1996
[6] Moisture Injection Tests at Wolsung Unit 2 prepared by V.P. Singh of Ontario Hydro, Aug. 1997
[7] PHTS Operating Procedure for Wolsung Units, Oct. 1997.

# IV-5 Approximate Evaluation Method for Ductile Fracture Analysis of Circumferentially Through-Wall-Cracked Pipe Subjected to Combined Bending and Tension

Naoki Miura (CRIEPI), Materials Science Department, Central Research Institute of Electric Power Industry, Japan

# Approximate evaluation method for ductile fracture analysis of circumferentially through-wall-cracked pipe subjected to combined bending and tension

N. Miura

Materials Science Department, Central Research Institute of Electric Power Industry
2-11-1, Iwado Kita, Komae-shi, Tokyo 201-8511 JAPAN

## Abstract

To estimate the structural integrity of the Light Water Reactor piping, combined loading consists of tensile load due to internal pressure and bending load under seismic condition should be considered as a basic loading mode. However, theoretical investigation on the methodology to evaluate ductile fracture behavior is not adequate to date. In this study, an approximate evaluation method for ductile fracture analysis of circumferentially through-wall-cracked pipe subjected to combined bending and tension was newly developed. This method can explicitly incorporate the contribution of both tension and bending. The effect of growing crack is also considered in the method. This method was then applied to the full-scale pipe fracture tests. Based on the comparison with experimental results as well as finite element calculations, it could be ascertained that the proposed method could well predict ductile fracture behavior under combined loading. The effect of combined loading on ductile fracture was sensitivity-studied using the proposed method. As a result, it was quantitatively found that the superposition of internal pressure reduced the maximum load of cracked pipe.

## 1. Introduction

To substantiate that pipe whip restraint and jet impingement shields can be eliminated, piping for nuclear power plant is required to satisfy Leak-Before-Break (LBB) analyses for postulated defects. One of the most important aspects in LBB analyses is to predict the ductile fracture behavior and the load-carrying capacity of a circumferentially through-wall-cracked pipe. Elastic-Plastic Fracture Mechanics (EPFM) methods can employ analytical approaches such as elaborate numerical simulations or some approximate evaluation methods. Numerical simulations are generally considered to give reliable predictions for a specific condition. However, approximate evaluation methods seem to be more useful to investigate the effect of various analytical situations systematically. Based on the $J$-Tearing theory, some methods have been proposed to evaluate the ductile fracture behavior of circumferentially through-wall-cracked pipe subjected to pure bending. When actual plant piping conditions are considered, however, the effect of the internal pressure acting as a tensile load also occurs. Theoretical investigation on the methodology to evaluate ductile fracture behavior under combined loading is not adequate to date. If combined loading effects are not properly considered, then the actual fracture resistance of the pipe could be in error.

In this study, an approximate evaluation method for ductile fracture analysis of circumferentially through-wall-cracked pipe subjected to combined bending and tension is newly developed. This method is intended to incorporate the contribution of both tension and bending. The method is then applied to the full-scale pipe fracture tests. The effect of combined loading on ductile fracture is sensitivity-studied using the proposed method.

## 2. Development of new evaluation method

### 2.1 Existing consideration on combined loading

Kumar and German (1988) have developed the GE/EPRI Estimation scheme for a circumferentially through-wall-cracked pipe subjected to combined bending and tension. Fully plastic solutions for power-law material were computed under proportional loading condition. Brust, et al. (1995) have presented more reliable solutions using elaborate three-dimensional finite element calculations under constant internal pressure condition. These solutions tabulated as functions of pipe dimension, crack dimension, strain hardening exponent, etc. are limited and discrete at this time. For example, the former solutions are given for only two radius/thickness ratios, two crack angles, and two or three hardening exponents. For the latter solutions, internal pressure is fixed to 15.5 MPa, which is equal to PWR operating condition, and cannot be a variable. Therefore, theses solutions are not always adequate to analyze ductile fracture behavior when analytical parameters such as crack angle or internal pressure significantly change during loading.

Paris/Tada method (Paris, 1983), LBB.NRC method (Klecker 1986), LBB.GE method (Brust, 1987), and LBB.ENG2 method (Brust, 1987 and Gilles, 1994) are other approximate evaluation methods which may have a potential to evaluate ductile fracture under combined loading. These methods were originally developed to apply to pure bending or pure tension. They are often applied to combined loading by substituting an internal pressure for an equivalent bending by some means. However, these approaches tend to give conservative prediction especially for the case with larger pressure (Brust, 1995). This might be because the interaction between tension and bending cannot be properly taken account in these cases. Attempts to evaluate $J$-integral under combined loading by adding $J$-integral due to pure tension and that due to pure bending were also seen in some instances, which have naturally no theoretical base since the principle of superposition cannot be available in nonlinear region.

### 2.2 Evaluation of moment-rotation relation

Consider a circumferentially through-wall-cracked pipe subjected to combined four-point bending and tension due to internal pressure shown in Fig. 1. Assume that the total load-point rotation, $\phi$ may be written as

$$\phi = \phi_C + \phi_{NC} \tag{1}$$

where $\phi_C$ and $\phi_{NC}$ are $\phi$ due to crack and $\phi$ without crack, respectively. $\phi_{NC}$ can be easily obtained as

$$\phi_{NC} = \frac{M L_{in}}{E I} \tag{2}$$

where $M$ is the applied moment, $L_{in}$ is the inner span, $E$ is the Young's modulus, and $I$ is the second moment of area for uncracked pipe. $\phi_C$ may be separated into its elastic and plastic components.

$$\phi_C = \phi_{EL} + \phi_{PL} \tag{3}$$

The $\phi_{EL}$ and $\phi_{PL}$ under combined loading are evaluated as the following procedures.

When a pipe is subjected to bending moment, $M$ and tensile load, $T$, bending stress, $\sigma_b$ and tensile stress, $\sigma_t$ are

$$\sigma_b \approx \frac{M}{\pi R^2 t}, \quad \sigma_t = \frac{T}{2 \pi R t} \tag{4}$$

where $R$ is the mean radius and $t$ is the pipe thickness. The stress intensity factor, $K_I$ is represented as the sum of its bending and tensile components, $K_b$ and $K_t$

$$K_I = K_b + K_t = \sigma_b \sqrt{\pi R \theta}\, F_b(\theta) + \sigma_t \sqrt{\pi R \theta}\, F_t(\theta) \tag{5}$$

where $\theta$ is the half crack angle, and the compliance functions, $F_b$ and $F_t$ are provided as functions of $\theta/\pi$ and $R/t$ based on Sanders' solutions (Klecker 1986).

$$F_b(\theta) = 1 + A_b \left(\frac{\theta}{\pi}\right)^{1.5} + B_b \left(\frac{\theta}{\pi}\right)^{2.5} + C_b \left(\frac{\theta}{\pi}\right)^{3.5} \tag{6}$$

$$\begin{bmatrix} A_b \\ B_b \\ C_b \end{bmatrix} = \begin{bmatrix} -3.26543 & 1.52784 & -0.072698 & 0.0016011 \\ 11.36322 & -3.91412 & 0.18619 & -0.004099 \\ -3.18609 & 3.84763 & -0.18304 & 0.00403 \end{bmatrix} \begin{bmatrix} 1 \\ R/t \\ (R/t)^2 \\ (R/t)^3 \end{bmatrix} \tag{7}$$

$$F_t(\theta) = 1 + A_t \left(\frac{\theta}{\pi}\right)^{1.5} + B_t \left(\frac{\theta}{\pi}\right)^{2.5} + C_t \left(\frac{\theta}{\pi}\right)^{3.5} \tag{8}$$

$$\begin{bmatrix} A_t \\ B_t \\ C_t \end{bmatrix} = \begin{bmatrix} -2.02917 & 1.67763 & -0.07987 & 0.00176 \\ 7.09987 & -4.42394 & 0.21036 & -0.00463 \\ 7.79661 & 5.16676 & -0.24577 & 0.00541 \end{bmatrix} \begin{bmatrix} 1 \\ R/t \\ (R/t)^2 \\ (R/t)^3 \end{bmatrix} \tag{9}$$

$\phi_{EL}$ are related with the strain energy due to crack, $U$ using the Castigliano's theorem.

$$\phi_{EL} = \partial U / \partial M \tag{10}$$

While the energy release rate, $G$ may be written as

$$G = K_I^2 / E = \partial U / \partial A \tag{11}$$

where $A$ is the crack area. From Eqs. (10) and (11),

$$\phi_{EL} = \frac{\partial}{\partial M} \int_0^A \frac{K_I^2}{E}\, dA \tag{12}$$

Since $M$ and $T$ are independent each other, substituting Eq. (5) into Eq. (12), then

$$\phi_{EL} = \frac{\sigma_b}{E} I_b(\theta) + \frac{\sigma_t}{E} I_t(\theta) \tag{13}$$

where

$$I_b(\theta) = 4 \int_0^\theta \theta\, F_b^2(\theta)\, d\theta \tag{14}$$

$$I_t(\theta) = 4 \int_0^{\theta} \theta\, F_b(\theta)\, F_t(\theta)\, d\theta \tag{15}$$

Thus the $\phi_{EL}$ can be explicitly calculated.

As for the evaluation of $\phi_{PL}$, the beam theory can be enforced to the pipe of nonlinear elastic material under the deformation theory of plasticity. This hypothesis is the same as the supposition used in the LBB.ENG2 method (Brust, 1987). Note that the LBB.ENG2 method considered the compatibility for pure bending or pure tension, while the new evaluation method attempts to take account of both bending and tension loading simultaneously.

The stress-strain relation is defined as the following power law.

$$\frac{\varepsilon}{\varepsilon_0} = \alpha \left(\frac{\sigma}{\sigma_0}\right)^n, \quad \varepsilon_0 = \frac{\sigma_0}{E} \tag{16}$$

Based on the beam theory with the assumptions that plane sections remain plane, the deflection of the beam and the related strain and stress distributions are illustrated in Fig. 2. The stress distribution has to be in equilibrium with the applied tensile load and the bending moment. This follows

$$R\,T = M_0\, \lambda\, \hat{K}_T\, g_T\, \beta \tag{17}$$

$$M = M_0\, \lambda \left\{ \hat{K}_M - \left[ \hat{K}_T\, g_T - \hat{K}_M\, g_M \right] \beta^2 \right\} \tag{18}$$

where $\beta$ identifies the location of the neutral axis shown in Fig. 2, $M_0$ is the yield moment for uncracked pipe given as

$$M_0 = 4\, \sigma_0\, R^2\, t \tag{19}$$

and the parameter, $\lambda$ is

$$\lambda = \left(\frac{R}{\alpha\, \varepsilon_0\, \rho}\right)^{\frac{1}{n}} \tag{20}$$

with $\rho$ as the radius of curvature. Functions $\hat{K}_M$, $\hat{K}_T$, $g_M$, and $g_T$ are introduced to approximate integral equations appeared in the process of the equilibrium calculations, which are given by

$$\hat{K}_M = \int_0^{\pi/2} (\sin\theta)^{\frac{1}{n}+1}\, d\theta = \frac{\sqrt{\pi}}{2} \frac{\Gamma\left(\frac{1}{2n}+1\right)}{\Gamma\left(\frac{1}{2n}+\frac{3}{2}\right)} \tag{21}$$

$$\hat{K}_T = \int_0^{\pi/2} (\sin\theta)^{\frac{1}{n}}\, d\theta = \frac{\sqrt{\pi}}{2} \frac{\Gamma\left(\frac{1}{2n}+\frac{1}{2}\right)}{\Gamma\left(\frac{1}{2n}+1\right)} \tag{22}$$

$$g_M = \frac{n+1}{n} \frac{2}{\pi} \tag{23}$$

$$g_T = \frac{1}{n} + \frac{2}{\pi} \tag{24}$$

The Gamma function, $\Gamma$ in Eqs. (21) and (22) can be approximated in the range of interest here by the Stirling's formula

$$\Gamma(z) = e^{-z} z^{z-0.5} \sqrt{2\pi} \times \left\{ 1 + \frac{1}{12z} + \frac{1}{288z^2} - \frac{139}{51840z^3} - \frac{571}{2488320z^4} \right\} \quad (25)$$

The process to lead the equilibrium equations with the above related functions are provided in Appendix A.

By solving Eqs. (17) and (18), the relation between moment (or load) and curvature can be written as follows. For the case of $M \neq 0$,

$$\frac{d^2y}{dx^2} = \frac{1}{\rho} = \frac{1}{R} \alpha \varepsilon_0 \left[ \frac{\kappa M}{\hat{K}_M M_0} \right]^n \quad (26)$$

where the parameter, $\kappa$ is given by

$$\kappa = \frac{1}{2} \left[ 1 + \sqrt{1 + \frac{16 \hat{K}_M (\hat{K}_T g_T - \hat{K}_M g_M) \left(\frac{\sigma_t}{\sigma_b}\right)^2}{\hat{K}_T^2 g_T^2}} \right] \quad (27)$$

Alternatively, for the case of $M = 0$,

$$\frac{d^2y}{dx^2} = \frac{1}{\rho} = \frac{1}{R} \alpha \varepsilon_0 \left[ \frac{\kappa R T}{\hat{K}_M M_0} \right]^n \quad (28)$$

$$\kappa = \frac{\sqrt{\hat{K}_M (\hat{K}_T g_T - \hat{K}_M g_M)}}{\hat{K}_T g_T} \quad (29)$$

where $x$ and $y$ are components of the coordinate shown in Fig. 3.

Again, after the manner of the LBB.ENG2 method for pure bending, considering that the existence of circumferential through-wall crack can be replaced by a pipe section with reduced thickness, $t_e$ extending for a distance $\hat{a}$ at the cracked section as shown in Fig. 3. The reduced thickness section is expected to simulate the reduction of the compliance due to the existence of the crack. Eqs. (26) and (28) can be analytically solved for all sections in Fig. 3 by applying appropriate boundary conditions. The detail calculations led from Eqs. (26) or (28) are omitted here, however, they can be accomplished in the similar way as the steps by Brust (1987). It is noted that $\kappa$ defined by Eq. (27) includes the stress components, so that Eq. (26) should be recursively computed as a function of $x$. Although, the beam of interest shows nonlinear elastic response and is independent of loading history. Therefore one may determine an arbitrary loading path up to a specific loading state. If the proportional loading is supposed, then $\kappa$ defined in Eq. (27) is not affected by the stress components, and is independent of $x$.

For the case of $M \neq 0$, the solution of Eq. (26) at the reduced thickness section is

$$\phi = \frac{1}{R} \left(\frac{t}{t_e}\right)^n \alpha \varepsilon_0 \left(\frac{\pi \kappa}{4 \hat{K}_M}\right)^n \left(\frac{\sigma_b}{\sigma_0}\right)^n x \quad (30)$$

$\phi_{PL}$ corresponds to $\phi$ at $x = \hat{a}/2$, then

$$\phi_{PL} = \frac{1}{R} \left(\frac{t}{t_e}\right)^n \alpha \varepsilon_0 \left(\frac{\pi \kappa}{4 \hat{K}_M}\right)^n \left(\frac{\sigma_b}{\sigma_0}\right)^n \frac{\hat{a}}{2} \quad (31)$$

$\phi_{EL}$ is obtained by taking $\alpha = 1$ and $n = 1$

$$\phi_{EL} = \frac{1}{R}\frac{t}{t_e}\varepsilon_0 \kappa_1 \frac{\sigma_b}{\sigma_0}\frac{\hat{a}}{2} \tag{32}$$

where

$$\kappa_1 = \kappa(n = 1) \tag{33}$$

From Eqs. (31) and (32), $\phi_{PL}$ can be evaluated as

$$\phi_{PL} = (\frac{t}{t_e})^{n-1} (\frac{\pi}{4\hat{K}_M})^n \alpha \frac{\kappa^n}{\kappa_1} (\frac{\sigma_b}{\sigma_0})^{n-1} \phi_{EL} \tag{34}$$

Similarly, for the case of $M = 0$, the solution of Eq. (28) at the reduced thickness section is

$$\phi_{PL} = \frac{1}{R} (\frac{t}{t_e})^n \alpha \varepsilon_0 (\frac{\pi\kappa}{2\hat{K}_M})^n (\frac{\sigma_t}{\sigma_0})^n x \tag{35}$$

$\phi_{PL}$ corresponds to $\phi$ at $x = \hat{a}/2$, then

$$\phi_{PL} = \frac{1}{R} (\frac{t}{t_e})^n \alpha \varepsilon_0 (\frac{\pi\kappa}{2\hat{K}_M})^n (\frac{\sigma_t}{\sigma_0})^n \frac{\hat{a}}{2} \tag{36}$$

$\phi_{EL}$ is obtained by taking $\alpha = 1$ and $n = 1$

$$\phi_{EL} = \frac{1}{R}\frac{t}{t_e}\varepsilon_0 2 \kappa_1 \frac{\sigma_t}{\sigma_0}\frac{\hat{a}}{2} \tag{37}$$

$$\kappa_1 = \kappa(n = 1) \tag{38}$$

From Eqs. (36) and (37), $\phi_{PL}$ can be evaluated as

$$\phi_{PL} = (\frac{t}{t_e})^{n-1} (\frac{\pi}{2\hat{K}_M})^n \alpha \frac{\kappa^n}{2\kappa_1} (\frac{\sigma_t}{\sigma_0})^{n-1} \phi_{EL} \tag{39}$$

The equivalent reduced thickness in Eqs. (34) and (39) may be taken so that the Net-Section collapse moment of the cracked pipe under bending condition is identical to that of the reduced thickness section.

$$4\sigma_f R^2 t\left[\cos\frac{\theta}{2} - \frac{1}{2}\sin\theta\right] = 4\sigma_f R^2 t_e\left[\cos\frac{\pi}{2}\frac{\sigma_t}{\sigma_f}\right] \tag{40}$$

where $\sigma_f$ is the flow stress. The term in the bracket in right side indicates the effect of superposing tensile stress, and is equal to the ratio of the plastic collapse moment of cracked pipe subjected to combined bending and tension, $4\sigma_f R^2 t_e\left[\cos(\frac{\theta}{2} + \frac{\pi}{2}\frac{\sigma_t}{\sigma_f}) - \frac{1}{2}\sin\theta\right]$ to that subjected to pure bending, $4\sigma_f R^2 t_e\left[\cos(\frac{\theta}{2}) - \frac{1}{2}\sin\theta\right]$ at $\theta = 0$. Since Eq. (40) is premised on the rigid perfectly plastic behavior, it gives better results for small cracks. While it tends to overpredict $\phi_{PL}$ for larger cracks (Gilles, 1991). In the present evaluation method, the correction factor of $\pi/4$ determined by Gilles (1991) is used. That is,

$$\frac{t}{t_e} = \begin{cases} \left[\cos\frac{\pi}{2}\frac{\sigma_t}{\sigma_f}\right] / \left[\cos\frac{\theta}{2} - \frac{1}{2}\sin\theta\right] & , \text{ for } \theta < \frac{\pi}{6} \\ \left[\frac{\pi}{4}\cos\frac{\pi}{2}\frac{\sigma_t}{\sigma_f}\right] / \left[\cos\frac{\theta}{2} - \frac{1}{2}\sin\theta\right] & , \text{ for } \theta > \frac{\pi}{4} \end{cases} \tag{41}$$

and are linearly interpolated between $\pi/6$ and $\pi/4$.

## 2.3 Evaluation of *J*-integral

When an experimental or an analytical relation between load and displacement is known, the $\eta$-factor approach can be applied to evaluate the *J*-integral, *J* for a circumferentially through-wall-cracked pipe subjected to four-point bending (Zahoor, 1981, Wilkowski, 1987). The existing evaluation methods mentioned above (i.e., Paris/Tada method, LBB.NRC method, LBB.GE method, and LBB.ENG2 method) that predict maximum load capability have the $\eta$-factor analyses embedded in them. The earlier $\eta$-factor solutions have been developed for cracked pipes under either pure bending or pure tension. *J* is defined as the release rate of potential energy of nonlinear elastic material, therefore, the $\eta$-factor solutions can be extended for combined loading if the energy release rate for cracked pipe subjected to multiple loads is generally described. Pan (1984) has investigated the energy release rate for stationary cracked body under multiple loads, and has derived a generalized *J* evaluation equation. Further, Miura and Wilkowski (1995) have developed the combined-load $\eta$-factor solution which was applicable to combined bending and tension taken account of growing crack. In this study, this combined-load $\eta$-factor solution is expected to be included in the present evaluation method.

When a circumferentially through-wall-cracked pipe shown in Fig. 1 is subjected to combined four-point bending and tension due to internal pressure, *J* can be given as follows in spite of loading paths.

$$J = \int_0^M \frac{\partial\phi}{\partial A}\Big|_{T,\,M}\,dM + \int_0^T \frac{\partial\delta}{\partial A}\Big|_{\phi=0,\,T}\,dT \tag{42}$$

where $\delta$ is the axial displacement shown in Figure 1. In the above equation, conditions that $\phi << 1$ and $\delta / 2 << L_Z$ (where $L_Z$ is the moment arm shown in Fig. 1) are also premised.

Here *J*, $\phi$, and $\delta$ are assumed to be divided into the elastic and plastic components,

$$J = J_{EL} + J_{PL} \tag{43}$$

where subscripts $_{EL}$ and $_{PL}$ denote elastic and plastic component, respectively. The elastic *J*, $J_{EL}$ is directly obtained from $K_I$ in Eq. (5).

$$J_{EL} = K_I^2 / E \tag{44}$$

And for the plastic *J*, $J_{PL}$,

$$J_{PL} = \int_0^M \frac{\partial\phi_{PL}}{\partial A}\Big|_{T,\,M}\,dM + \int_0^T \frac{\partial\delta_{PL}}{\partial A}\Big|_{\phi=0,\,T}\,dT \tag{45}$$

The $\delta_{PL}$ due to axial load is considered to be small, so that the second integration of the right side in Eq. (45) is negligible. By using the geometrical relations as,

$$A = 2\,R\,t\,\theta \tag{46}$$

$$\phi_{PL} / 2 = \Delta_{PL} / L_Z \tag{47}$$

$$M = L_Z / P \tag{48}$$

where $\Delta_{PL}$ is the plastic load-point displacement, and $P$ is the bending load shown in Fig. 1, then Eq. (45) can become

$$J_{PL} = \int_0^M \frac{\partial \phi_{PL}}{\partial A} \Big|_{T,\,M} dM = \frac{1}{R\,t} \int_0^P \frac{\partial \Delta_{PL}}{\partial \theta} \Big|_{s,\,P} dP \tag{49}$$

Note that the non-dimensional tensile stress, $s$ (defined as $\sigma_t/\sigma_f$) is used instead of $T$. Assuming that $\Delta_{PL}$ is a function only of the ratio of $P$ to the Net-Section collapse load, then $\Delta_{PL}$ can be expressed as

$$\Delta_{PL} = f\,(P / h_p\,(\theta, s)) \tag{50}$$

$$h_p\,(\theta, s) = \cos\left(\frac{\theta}{2} + \frac{\pi}{2}\,s\right) - \frac{1}{2}\sin\theta \tag{51}$$

where $h_p$ is equal to the ratio of the plastic collapse load of cracked pipe subjected to combined loading to that of uncracked pipe subjected to pure bending. Substituting Eq. (50) into Eq. (49), then gives

$$J_{PL} = 2 \int_0^{\Delta_{PL}} \eta_p\,P\,d\Delta_{PL} \tag{52}$$

$$\eta_p = -\frac{\partial h_p / \partial \theta}{2\,R\,t\,h_p} \tag{53}$$

This equation gives $J_{PL}$ for a stationary (non-growing) crack under bending and constant tension loading.

For a generalized case considered growing crack and tension changing, Eq. (50) is written in its inverse form,

$$P = h_p\,F\,(\Delta_{PL}) \tag{54}$$

In this equation, $\Delta_{PL}$, $\theta$, and $s$ are assumed to be independent of each other, and since $J_{PL}$ is a function of $\Delta_{PL}$, $\theta$, and $s$, the differential of $J_{PL}$ is

$$dJ_{PL} = \frac{\partial J_{PL}}{\partial \theta}\,d\theta + \frac{\partial J_{PL}}{\partial \Delta_{PL}}\,d\Delta_{PL} + \frac{\partial J_{PL}}{\partial s}\,ds \tag{55}$$

Substituting Eqs. (52) and (54) into Eq. (55), and are given by

$$J_{PL} = 2\int_0^{\Delta PL} \eta_p P \, d\Delta_{PL} + 2\int_{\theta_0}^{\theta} \gamma_p J_{PL} \, d\theta + 2\int_{s_0}^{s} \mu_p J_{PL} \, ds \tag{56}$$

where,

$$\gamma_p = -\frac{\partial^2 h_p / \partial \theta^2}{2\,\partial h_p / \partial \theta} \tag{57}$$

$$\mu_p = -\frac{\partial^2 h_p / \partial s\,\partial \theta}{2\,\partial h_p / \partial \theta} \tag{58}$$

The second term of the right side of Eq. (56) corresponds to the contribution of the crack growth. The functions $\eta$ and $\gamma$ in the original $\eta$-factor approach are replaced with functions $\eta_p$ and $\gamma_p$, respectively. The third term of the right side of Eq. (56) corresponds to the contribution of the tension changing. If an axial tension is constant, this term is equal to zero. For the case of $s = 0$ , Eq. (56) is naturally identical to the original $\eta$-factor solution. Figs. 4 to 6 show the values of $\eta_p$, $\gamma_p$, and $\mu_p$ as a function of $\theta$, respectively. It can be seen that these functions are affected by $s$ as well as $\theta$.

### 2.4 Evaluation method for ductile fracture analysis

By integrating the moment-rotation evaluation in Section 2.2 and the $J$-integral evaluation in Section 2.3 together with the criterion of crack extension, an evaluation method for ductile fracture analysis taken account of both combined loading and growing crack was newly established. The developed evaluation method has an ability to consider an arbitrary combined loading history by nature, however, constant tensile load due to internal pressure followed by external monotonic bending load is supposed in this paper.

Fig. 7 shows the schematic of the developed evaluation method. As shown in this figure, the unique relation between $J$ and $M$ is provided for a specific crack extension $\Delta a$. $J$ corresponding to the $\Delta a$ is determined by the $J$-$R$ curve, then $M$ can be fixed at the point on the $J$-$M$ curve. The relation between $M$ and $\phi$ is also unique for the specific $\Delta a$, so $\phi$ is given by the point on the $M$-$\phi$ curve. Repeating this process for a set of $\Delta a$, and taking an envelope of the points, then the prediction of the ductile fracture behavior with crack extension is accomplished. The flow of the evaluation procedure is summarized in Fig. 8.

## 3. Application to pipe fracture tests

### 3.1 Analytical object and condition

The developed evaluation method was applied to analyze full-scale pipe fracture tests under combined bending and internal pressure. The predicted ductile fracture behavior was compared with experimental results as well as finite element calculations to validate the propriety of the method.

Table 1 shows the matrix of six pipe fracture tests analyzed. These tests were performed as a part of the NRC's Degraded Piping Program - Phase II (Wilkowski, 1989) and the IPIRG-2 Program (Scott, 1997). The materials used for the tests were A106 Grade B and SA333 Grade 6 carbon steels, and Type 304 stainless steel. Tensile properties necessary to perform a fracture analysis are also listed in Table 1. All tests were performed at 288°C. Four tests were conducted under tension loading due to internal pressure followed by bending, and two tests were conducted under pure bending condition for comparison. Experiments 4131-7,

4131-3, and Experiments 4131-5, 4131-1 have almost the same dimensions and test conditions except for the loading condition. Using these cases, the effect of combined loading can be evaluated. Experiment 1.9 was performed under dynamic loading (time to crack initiation = 0.32 seconds). All the other experiments were conducted under quasi-static loading.

Two *J-R* curves were provided for the predictions for each material. One was the *J-R* curve obtained from compact tension (CT) specimen which had been cut from the test pipe. The other was the *J-R* curve obtained from the pipe fracture test using the combined-load $\eta$-factor approach (Miura, 1995). The use of the pipe *J-R* curve is desirable for the purpose of the validation of the proposed method, however, small specimen *J-R* data are typically applied because they are often the only data available, and because predicted results are generally considered to be lower bounds. The *J-R* curves used for the analysis are shown in Figs. 9(a) to (d). These *J-R* curves were extrapolated according to the equations shown in these figures.

A three-dimensional finite element analysis was carried out for Experiments 4131-7, 4131-3, 4131-5, and 4131-1 to confirm that the experimental results were appropriate. The analysis was conducted using the computer code "MARC" with twenty-noded solid elements. Fig. 10 shows an example of the finite element mesh for the analytical model. Tensile properties in Table 2 were used for the analysis. In the analysis, the internal pressure was applied first, then the bending moment was applied with the constant internal pressure. The experimental relation between $\Delta$ and $\Delta a$ was numerically followed for the crack growth condition.

### 3.2 Results of analysis

Figs. 11(a) to (f) show the predicted relations between bending load and load-point displacement compared with the experimental (and the analytical if available) relation(s).

Fig. 11(a) shows the load-displacement relations for Experiment 1.9 (carbon steel 6-inch diameter pipe under bending and pressure). The proposed method using the CT *J-R* curve significantly underestimates the load-displacement relation. The prediction using the pipe *J-R* curve is still lower than the experimental result. The CT *J-R* curve for this material was obtained using sidegrooved specimens which lowered the toughness by constraining plasticity, and resulted in large difference. One reason of the poor predictability might be due to the complex crack growth aspects such as angled, asymmetric, and fast crack growth for this specific experiment.

Fig. 11(b) shows the load-displacement relations for Experiment 1.8 (carbon steel 16-inch diameter pipe under bending and pressure). The drop of the displacement at about 275 mm in the experimental results just at maximum load is due to an unstable crack jump at this point. Although the proposed method using the both *J-R* curves gives slightly lower displacement than the experimental result, the predicted maximum moments are in good agreement with the experimental value.

Figs. 11(c) and (d) show the load-displacement predictions for Experiments 4131-7 (carbon steel 10-inch diameter pipe under pure bending) and Experiment 4131-3 (carbon steel 10-inch diameter pipe under bending and pressure), respectively. It can be seen that the proposed method realizes fine predictions independent of the presence of pressure by comparing with experimental and FEM results. The relations from the CT *J-R* curve are lower than that from the pipe *J-R* curve. However, the differences are small for both experiments.

Figs. 11(e) and (f) show the load-displacement predictions for Experiments 4131-5 (stainless steel 6-inch diameter pipe under pure bending) and Experiment 4131-1 (stainless steel 6-inch diameter pipe under bending and pressure), respectively. The similar trends as the case of Figs. (c) and (d) can be observed, and the good predictability is secured both for combined loading and for pure bending. There seems to be a slight difference between the experimental and the FEM load-displacement relation for Experiment 4131-5. The prediction based on the proposed method is closer to the FEM result rather than the experimental one.

Fig. 12 shows the predicted divided by the experimental maximum loads. The predictions by the proposed method using both the CT and pipe *J-R* curves and the prediction by FEM (if available) are provided for each experiment. The proposed method has an enough capability to predict maximum moment for various materials, pipe size and crack size. The use of the pipe *J-R* curves gives better predictions than the use of the CT *J-R* curves compared with

the experimental maximum loads. The predictions using the CT *J-R* curves are relatively conservative, however, the difference of the predicted maximum loads caused by the selection of the used *J-R* curve is not remarkable.

## 4. Sensitivity study on combined loading effect

### 4.1 Effect of internal pressure on ductile fracture

The effect of the superposing pressure on ductile fracture was investigated using the proposed method. An analytical object was SA333 Grade 6 carbon steel 4B × Schedule 80 cracked pipe at 288°C. Dimensions of the pipe were 52.85 mm in mean radius and 8.60 mm in thickness. A crack with the total angle of 30° was supposed. The constant internal pressure preceding bending moment was considered to be a parameter, so that the ratio of the tensile stress to the reference stress, $\sigma_t/\sigma_0$ was equal to 0.00, 0.05, 0.10, 0.15, 0.20, and 0.25. The tensile properties listed in Table 1 and the pipe *J-R* curve presented in Fig. 9(c) were used for the analysis.

Fig. 13 shows the relations between moment and rotation for various $\sigma_t/\sigma_0$. The relations have similar configuration, and the maximum moment decreases with increasing tensile stress. For the case of $\sigma_t/\sigma_0 = 0.25$ , the maximum moment is about 12% lower than that without tensile stress. It can be also seen that the rotation at the maximum moment decreases with increasing tensile stress.

Fig. 14 shows the relations between *J*-integral and moment for various $\sigma_t/\sigma_0$. Moment at the same *J*-integral decreases with increasing tensile stress, as is the case of Fig. 13. While the value of *J*-integral at the maximum moment is not affected by tensile stress.

### 4.2 Dependence of dimensional parameters on maximum moment

Next, a sensitivity analysis was performed to study how the effect of the superposing pressure was affected by typical dimensional parameters represented by crack angle and pipe diameter. Again, an analytical object was SA333 Grade 6 carbon steel Schedule 80 (pipe thickness in 8.60 mm) cracked pipe at 288°C. The same tensile properties as well as *J-R* curve as the above-mentioned analysis were applied. Table 2 shows the matrix of the analytical condition. For the case that the dependence of crack angle was to be seen, nominal diameter was fixed to 4B (mean radius in 52. 85 mm) and total crack angle was varied from 30° to 180°. On the other hand, for the case that the dependence of pipe diameter was to be analyzed, crack angle was fixed to 30° and nominal diameter was varied from 4B (mean radius in 52.85 mm) to 24B (mean radius in 289.3 mm). The constant internal pressure preceding bending moment was considered to be a parameter, so that the ratio of the tensile stress to the reference stress, $\sigma_t/\sigma_0$ was equal to 0.00, 0.05, 0.10, 0.15, 0.20, and 0.25 for both cases.

Fig. 15 shows the dependence of crack angle on maximum moment. The maximum moment gradually decreases with increasing tensile stress, and this trend becomes significant as the crack angle increases.

Fig. 16 shows the dependence of pipe diameter on maximum moment. The maximum moment again decreases with increasing tensile stress, and this tendency is clear for the larger diameter pipe. Thus, it is numerically found that the reduction of the maximum moment with increasing internal pressure becomes notable for larger crack angle and for larger pipe diameter.

## 5. Conclusions

In this study, an approximate evaluation method for ductile fracture analysis of circumferentially through-wall-cracked pipe subjected to combined bending and tension was newly developed. Existing evaluation methods are limited and are inadequate for practical use to analyze the effect of combined loading, while the proposed method can explicitly incorporate the contribution of both tension and bending. The effect of growing crack is also considered in the method. The method was then applied to the full-scale pipe fracture tests. It could be ascertained that the proposed method could well predict ductile fracture behavior under

combined loading. The effect of combined loading on ductile fracture was then sensitivity-studied using the proposed method. As a result, the effect of superposition of internal pressure as well as the dependency of crack angle and pipe diameter could be quantitatively evaluated.

## Appendix A Equilibrium equations and related functions

The equilibrium of the tensile load is expressed as

$$R\,T = \int_A \sigma\,\mathrm{d}A = 2\,R^2\,t \int_{-\pi/2}^{\pi/2} \sigma\,\mathrm{d}\theta = \frac{1}{2} M_0\,\lambda\,I_T \tag{A-1}$$

where $M_0$ and $\lambda$ are given in Eqs. (19) and (20), and $I_T$ is

$$I_T = -\int_{-\pi/2}^{-\beta} (-\sin\theta - \sin\beta)^{\frac{1}{n}}\,\mathrm{d}\theta + \int_{-\beta}^{\pi/2} (\sin\theta + \sin\beta)^{\frac{1}{n}}\,\mathrm{d}\theta \tag{A-2}$$

$I_T$ can be written using the areas $S_T^-$ and $S_T^+$ in Fig. A1.

$$I_T = -S_T^- + S_T^+ \tag{A-3}$$

Here, assuming that the curves surrounding $S_T^-$ and $S_T^+$ are similar to the function $f(\theta) = (\sin\theta)^{\frac{1}{n}}$ in the range of $[0, \pi/2]$, $S_T^-$ and $S_T^-$ are given by

$$S_T^- = \int_0^{\pi/2} (\sin\theta)^{\frac{1}{n}}\,\mathrm{d}\theta \times \frac{\frac{\pi}{2} - \beta}{\frac{\pi}{2}} \times (1 - \sin\beta)^{\frac{1}{n}} \tag{A-4}$$

$$S_T^+ = \int_0^{\pi/2} (\sin\theta)^{\frac{1}{n}}\,\mathrm{d}\theta \times \frac{\frac{\pi}{2} + \beta}{\frac{\pi}{2}} \times (1 + \sin\beta)^{\frac{1}{n}} \tag{A-5}$$

Substituting Eqs. (A-4) and (A-5) into Eq. (A-3) then gives

$$I_T = \hat{K}_T \left[ \left(1 + \frac{2\beta}{\pi}\right) (1 + \sin\beta)^{\frac{1}{n}} - \left(1 - \frac{2\beta}{\pi}\right) (1 - \sin\beta)^{\frac{1}{n}} \right] \tag{A-6}$$

where $\hat{K}_T$ is given in Eq. (22). If $\beta$ is enough small, $(1 \pm \sin\beta)^{\frac{1}{n}} \approx 1 \pm \frac{1}{n}\sin\beta$ is approximately satisfied, then

$$I_T = \hat{K}_T \left[ \frac{2}{n} \sin\beta + \frac{4\beta}{\pi} \right] \tag{A-7}$$

Further, supposing $\sin\beta \approx \beta$, and

$$I_T = 2\,\hat{K}_T \left[ \frac{1}{n} + \frac{2}{\pi} \right] \beta = 2\,\hat{K}_T\,g_T\,\beta \tag{A-8}$$

Substituting Eq. (A-8) into Eq. (A-1), one may write

$$R\,T = M_0\,\lambda\,\hat{K}_T\,g_T\,\beta \tag{A-9}$$

which is identical to Eq. (17).

Similar procedure is also employed for the equilibrium of the bending moment as follows

$$M = \int_A \sigma\,(R\sin\theta)\,dA = 2\,R^2\,t\int_{-\pi/2}^{\pi/2}\sigma\sin\theta\,d\theta = \frac{1}{2}M_0\,\lambda\,I_M \tag{A-10}$$

where $I_M$ is

$$\begin{aligned} I_M &= \int_{-\pi/2}^{-\beta}(-\sin\theta-\sin\beta)^{\frac{1}{n}}(-\sin\theta)\,d\theta + \int_{-\beta}^{\pi/2}(\sin\theta+\sin\beta)^{\frac{1}{n}}\sin\theta\,d\theta \\ &= \int_{-\pi/2}^{-\beta}(-\sin\theta-\sin\beta)^{\frac{1}{n}+1}\,d\theta + \int_{-\beta}^{\pi/2}(\sin\theta+\sin\beta)^{\frac{1}{n}+1}\,d\theta - I_T\sin\beta \end{aligned} \tag{A-11}$$

$I_M$ can be written using the areas $S_M^-$ and $S_M^+$ in Fig. A2.

$$I_M = S_M^- + S_M^+ - I_T\sin\beta \tag{A-12}$$

Assuming that the curves surrounding $S_M^-$ and $S_M^+$ are similar to the function $f(\theta) = (\sin\theta)^{\frac{1}{n}+1}$ in the range of $[0, \pi/2]$, $S_M^-$ and $S_M^+$ are given by

$$S_M^- = \int_0^{\pi/2}(\sin\theta)^{\frac{1}{n}+1}\,d\theta \times \frac{\frac{\pi}{2}-\beta}{\frac{\pi}{2}} \times (1-\sin\beta)^{\frac{1}{n}+1} \tag{A-13}$$

$$S_M^+ = \int_0^{\pi/2}(\sin\theta)^{\frac{1}{n}+1}\,d\theta \times \frac{\frac{\pi}{2}+\beta}{\frac{\pi}{2}} \times (1+\sin\beta)^{\frac{1}{n}+1} \tag{A-14}$$

Substituting Eqs. (A-13) and (A-14) into Eq. (A-12) then gives

$$I_M = \hat{K}_M\left[(1+\frac{2\beta}{\pi})(1+\sin\beta)^{\frac{1}{n}+1} + (1-\frac{2\beta}{\pi})(1-\sin\beta)^{\frac{1}{n}+1}\right] - I_T\sin\beta \tag{A-15}$$

where $\hat{K}_M$ is given in Eq. (21). Again, if $\beta$ is enough small, $(1\pm\sin\beta)^{\frac{1}{n}+1} \approx 1 \pm (\frac{1}{n}+1)\sin\beta$ is approximately satisfied, then

$$I_M = \hat{K}_M\left[2 + \frac{4}{\pi}(\frac{1}{n}+1)\,\beta\sin\beta\right] - I_T\sin\beta \tag{A-16}$$

Further, supposing $\sin\beta \approx \beta$, and

$$I_M = 2\,\hat{K}_M\left[1+\frac{n+1}{n}\frac{2}{\pi}\beta^2\right] - 2\,\hat{K}_T\left[\frac{1}{n}+\frac{2}{\pi}\right]\beta^2 = 2\left\{\hat{K}_M - \left[\hat{K}_T\,g_T - \hat{K}_M\,g_M\right]\beta^2\right\} \tag{A-17}$$

Substituting Eq. (A-17) into Eq. (A-10), one may write

$$M = M_0\,\lambda\left\{\hat{K}_M - \left[\hat{K}_T\,g_T - \hat{K}_M\,g_M\right]\beta^2\right\} \tag{A-18}$$

which is identical to Eq. (18).

The above derivation is based on the assumption that the $\beta$ is enough small. For example, when $\beta$ is less than $0.1\pi$, it was numerically ascertained that the difference of $I_T$ computed by Eqs. (A-2) and (A-8), and the difference of $I_M$ computed by Eqs. (A-11) and (A-17) are both less than 6%. $\beta$ is a function of strain hardening exponent, $n$ and the tensile to bending load ratio, $RT/M$. $n$ usually ranges between 1 to 10 for typical structural materials, and in that case, the condition of $\beta < 0.1\ \pi$ is satisfied when $RT/M$ is smaller than 0.4. Since a significant ductile fracture behavior occurs at much higher value of $RT/M$ than 0.4, the assumption on $\beta$ is considered to be appropriate for the loading mode of interest.

## References


Brust, F. W., Approximate Methods for Fracture Analysis of Through-Wall Cracked Pipes, NUREG/CR-4853, February 1987.

Brust, F. W., et al., Assessment of Short Through-Wall Circumferential Cracks in Pipes, NUREG/CR-6235, April 1995.

Gilles, P., Brust, F. W., 1994. Approximate Methods for Fracture Analysis of Tubular Members Subjected to Combined Tensile and Bending Loads, J. Offshore Mechanics and Arctic Engineering (OMAE), 116, 221-227.

Gilles, P., Brust, F. W., 1991. Approximate Fracture Methods for Pipes - Part I: Theory, Nucl. Eng. Des., 127, 1-17.

Klecker, R., et al., NRC Leak-Before-Break (LBB.NRC) Analysis Method for Circumferentially Through-Wall Cracked Pipes Under Axial Plus Bending Loads, NUREG/CR-4572, May 1986.

Kumar, V., German, M. D., Elastic-Plastic Fracture Analysis of Through-Wall and Surface Flaws in Cylinders, EPRI NP-5596, Final Report, January 1988.

Miura, N., Wilkowski, G., 1995. J-R Curves From Through-Wall-Cracked Pipe Tests - Combined Loading and Short Crack Considerations -, 1995 ASME Pressure Vessels and Piping Conf., 304, 171-179.

Pan, J., 1984. Some Considerations on Estimation of Energy Release Rates for Circumferentially Cracked Pipes, Trans. ASME J. Pressure Vessel Technol., 106, 391-398.

Paris, P. C., Tada, H., The Application of Fracture Proof Design Method Using Tearing Instability Theory to Nuclear Piping Postulating Circumferential Through Wall Cracks, NUREG/CR-3464, September 1983.

Scott, P., et al., IPIRG-2 Task 1 - Pipe System Experiments with Circumferential Cracks in Straight-Pipe Locations, NUREG/CR-6389, February 1997.

Wilkowski, G., et al., Analysis of Experiments on Stainless Steel Flux Welds, NUREG/CR-4878, April 1987.

Wilkowski, G. M., et al., Summary of Technical Results and Their Significance to Leak-Before-Break and In-Service Flaw Acceptance Criteria, NUREG/CR-4082, 8, March 1989.

Zahoor, A., Kanninen, M. F., 1981. A Plastic Fracture Mechanics Prediction of Fracture Instability in a Circumferentially Cracked Pipe in Bending - Part I: J-Integral Analysis, Trans. ASME J. Pressure Vessel Technol., 103, 352-358.

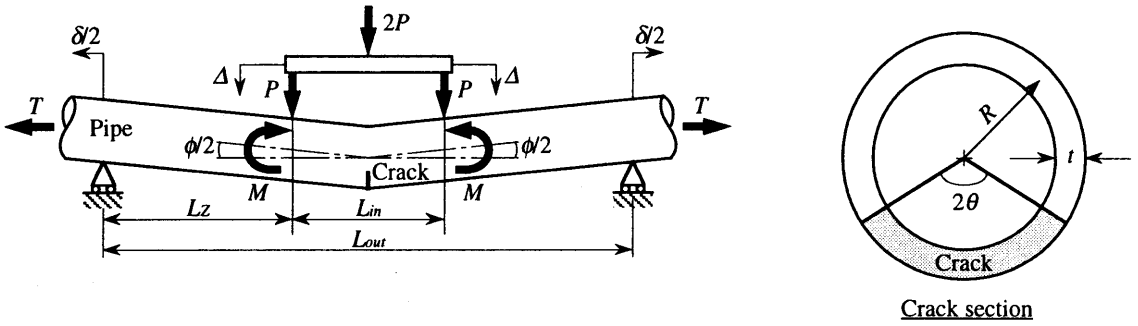


Fig. 1 Circumferentially through-wall-cracked pipe subjected to combind bending and tension load.

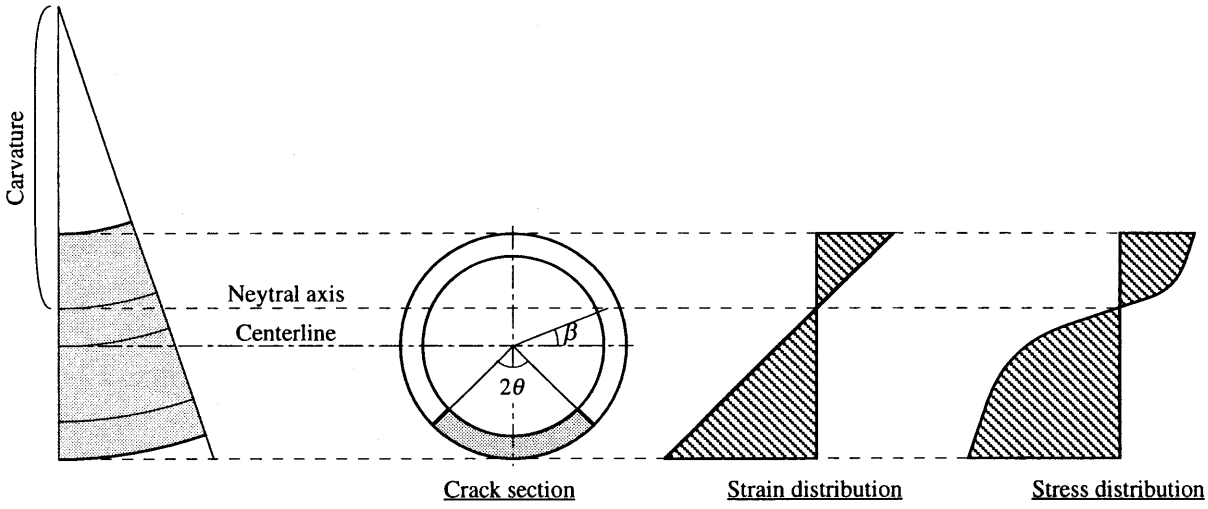


Fig. 2 Deflection of beam and related strain and stress distribution.

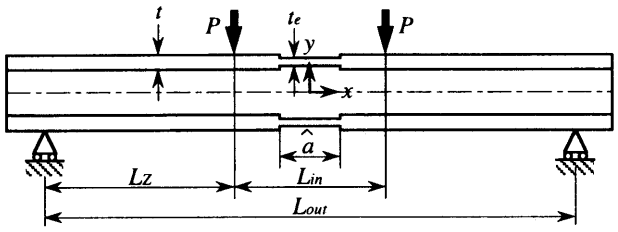


Fig. 3 Pipe geometry with equivalent reduced thickness.

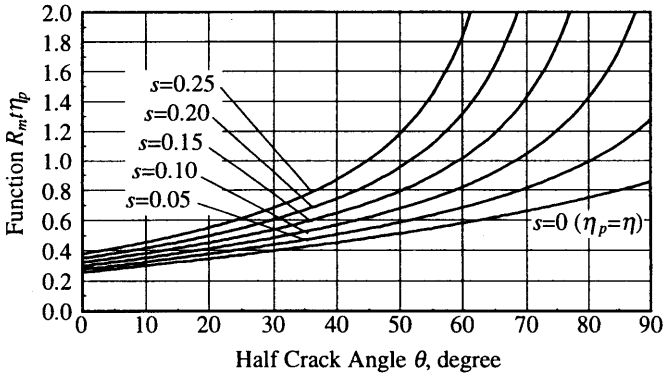


Fig. 4 Transition of $\eta p$ with $\theta$.

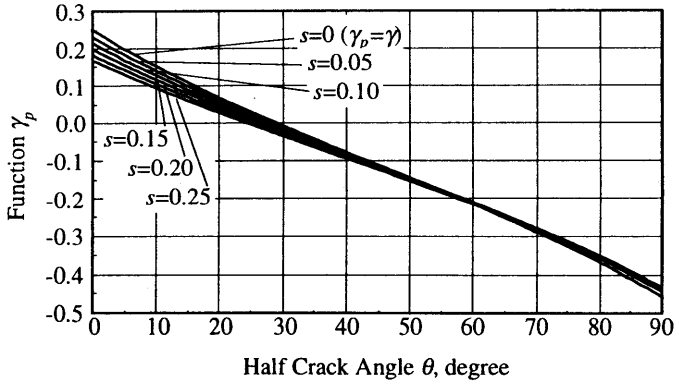


Fig. 5 Transition of $\gamma p$ with $\theta$.

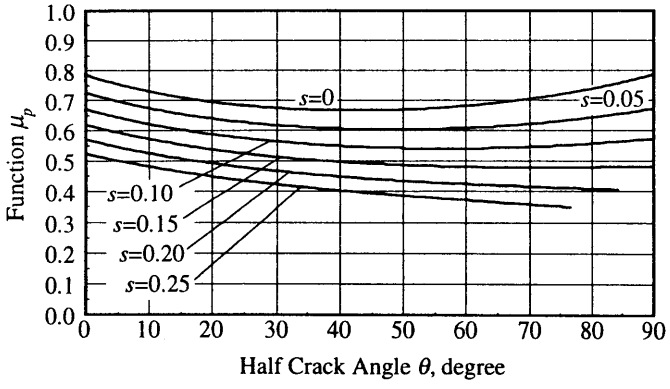


Fig. 6 Transition of $\mu p$ with $\theta$.

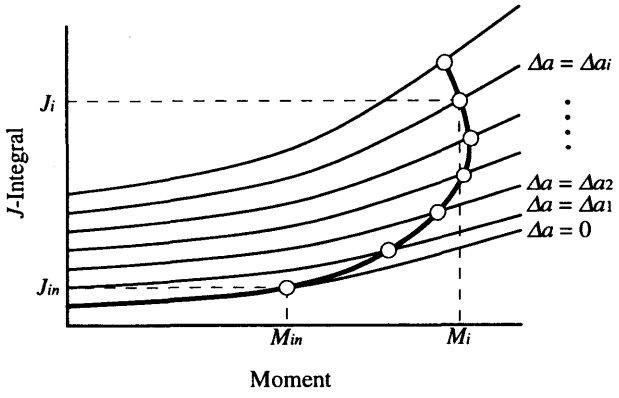


Fig. 7 Schematic of the approximate evaluation method for ductile fracture analysis.

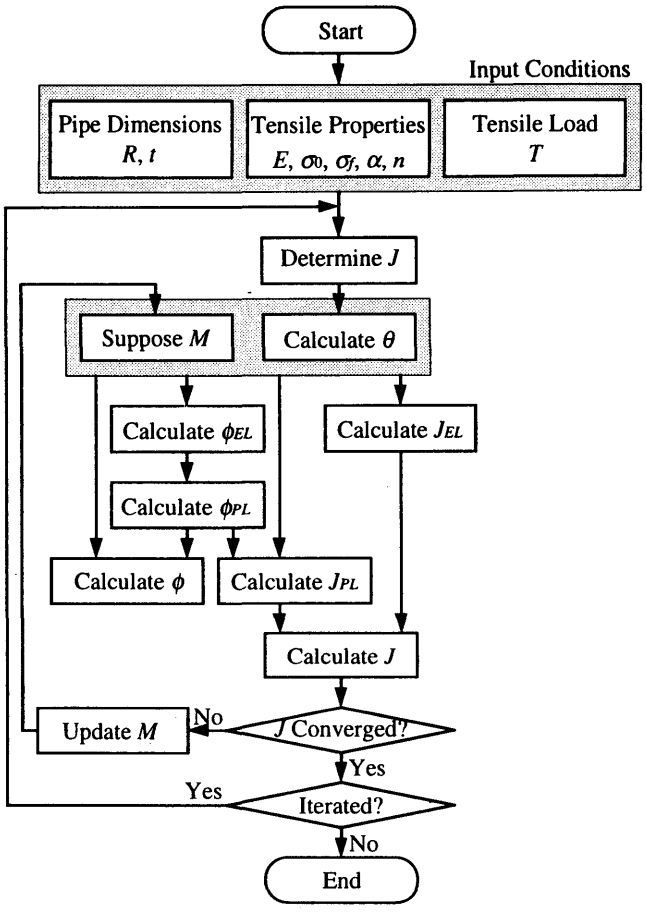


Fig. 8 Flow of approximate evaluation for ductile fracture analysis.

Table 3 Matrix of cracked pipe fracture tests and their tensile properties.

| Experiment No. | Material | Temper-ature | Loading Condition | Outer Diameter [mm] | Pipe Thickness [mm] | Initial Half Crack Angle | Outer /Inner Span [m] | Internal Pressure [MPa] | Young's Modulus [GPa] | Flow Stress [MPa] | Ref. Stress* σ0 [MPa] | Con-stant* α | Expo-nent* n |
|---|---|---|---|---|---|---|---|---|---|---|---|---|---|
| IPIRG-2 1.9 | A106 Gr. B C/S | 288 °C | Bending + Pressure | 168 | 8.8 | 45.0 ° | 6.10 0.91 | 15.5 | 193 | 419 | 249 | 2.78 | 3.43 |
| IPIRG-2 1.8 | A106 Gr. B C/S | 288 °C | Bending + Pressure | 399 | 26.2 | 21.9 ° | 11.58 3.35 | 15.5 | 193 | 361 | 216 | 1.38 | 5.05 |
| DP3-II 4131-7 | SA333 Gr. 6 Carbon Steel | 288 °C | Pure Bending | 273 | 18.3 | 62.3 ° | 5.94 1.63 | - | 193 | 383 | 239 | 5.21 | 3.23 |
| DP3-II 4131-3 | | | Bending + Pressure | 274 | 18.7 | 66.6 ° | 7.92 3.35 | 12.5 | | | | | |
| DP3-II 4131-5 | Type 304 Stainless Steel | 288 °C | Pure Bending | 159 | 13.9 | 69.8 ° | 3.25 1.22 | - | 183 | 295 | 131 | 9.58 | 3.21 |
| DP3-II 4131-1 | | | Bending + Pressure | 166 | 13.4 | 66.6 ° | 3.20 1.22 | 17.2 | | | | | |

* : Stress-strain relation described as $\frac{\varepsilon}{\varepsilon_0} = \frac{\sigma}{\sigma_0} + \alpha \left(\frac{\sigma}{\sigma_0}\right)^n$, $\varepsilon_0 = \frac{\sigma_0}{E}$

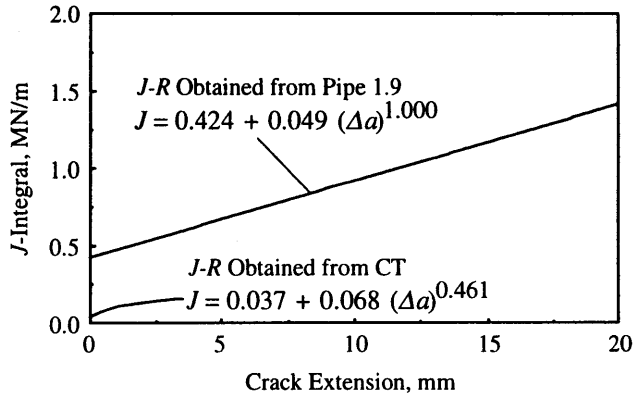


(a) A106 Gr. B C/S for Experiment 1.9

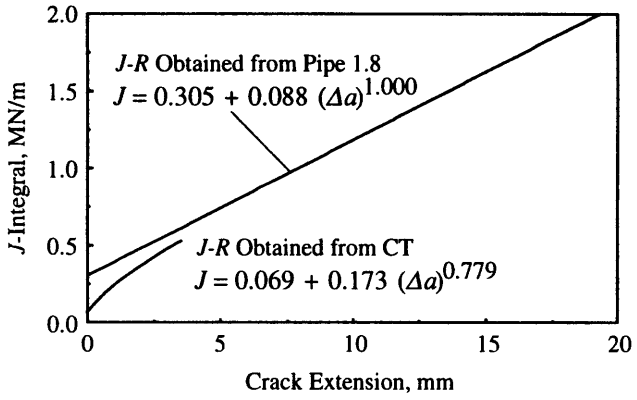


(b) A106 Gr. B C/S for Experiment 1.8

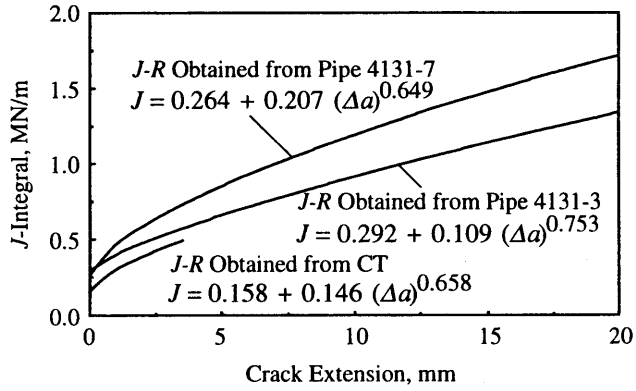


(c) SA333 Gr. 6 C/S for Experiments 4131-7 and 4131-3

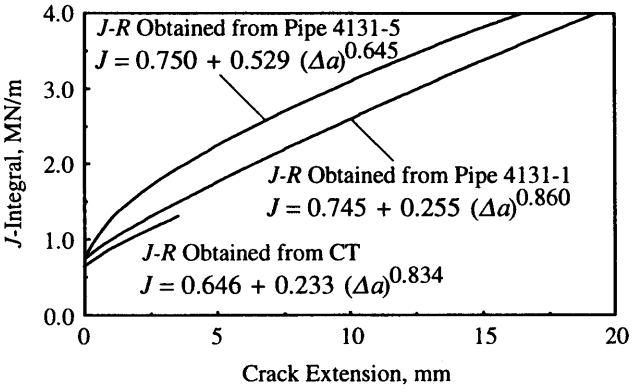


(d) Type 304 S/S for Experiments 4131-5 and 4131-1

Fig. 9 *J-R* curves used for ductile fracture analysis.

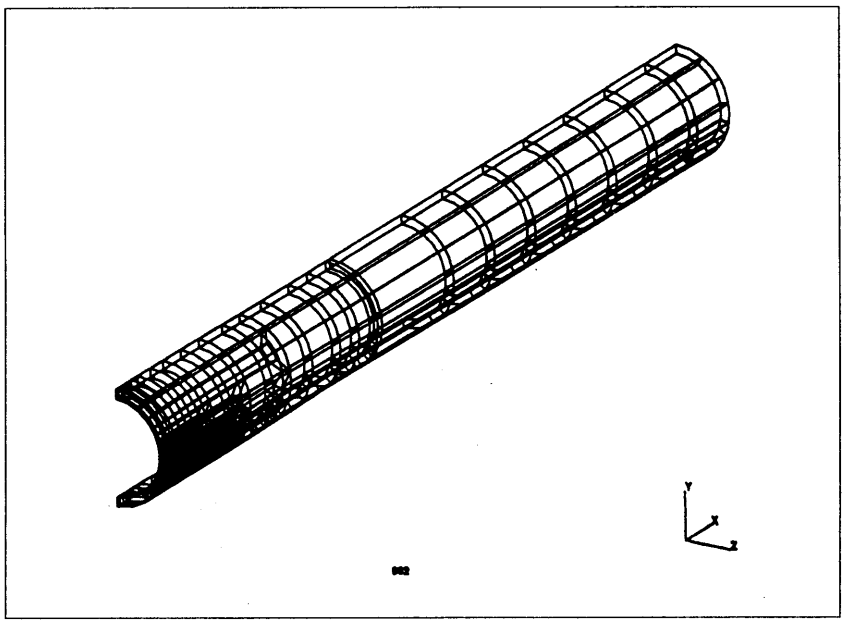

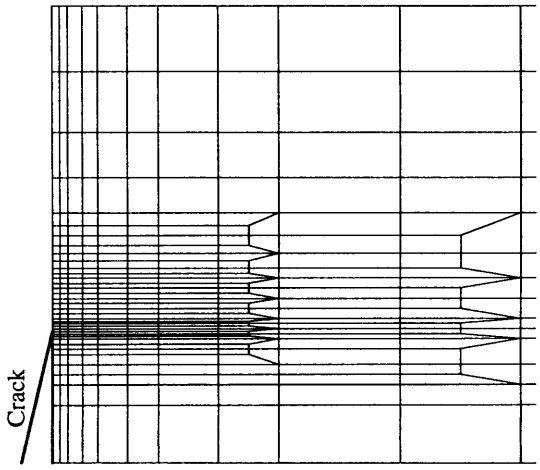


Extension around crack

Fig. 10 Example of finite element mesh.

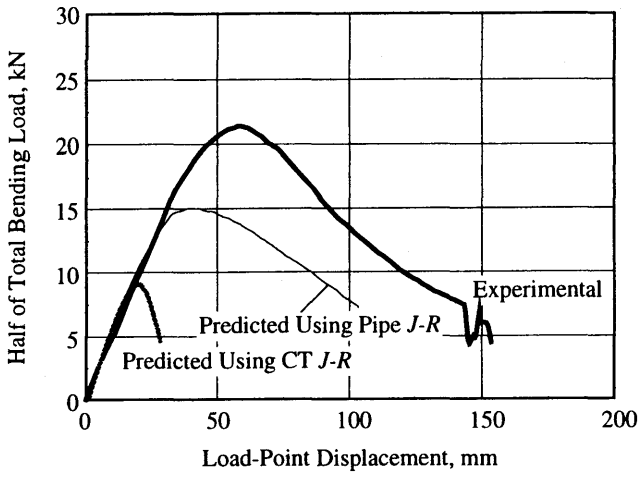


(a) Experiment 1.9
(A106 Gr. B C/S, pressure and dynamic bending)

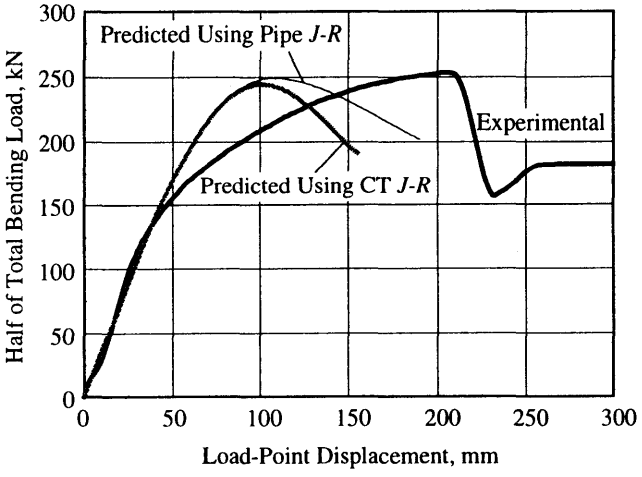


(b) Experiment 1.8
(A106 Gr. B C/S, pressure and bending)

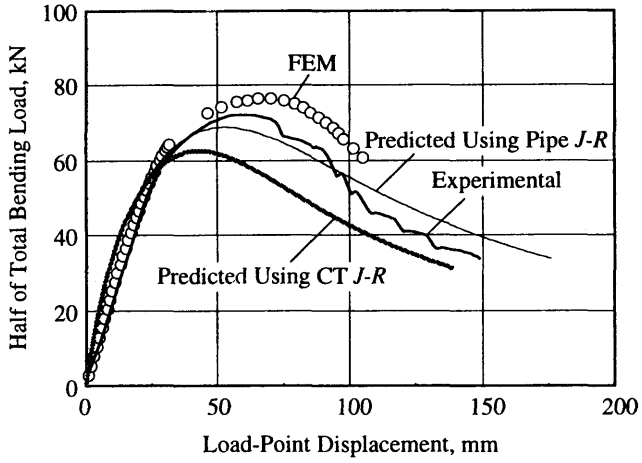


(c) Experiment 4131-7
(SA333 Gr. 6 C/S, pure bending)

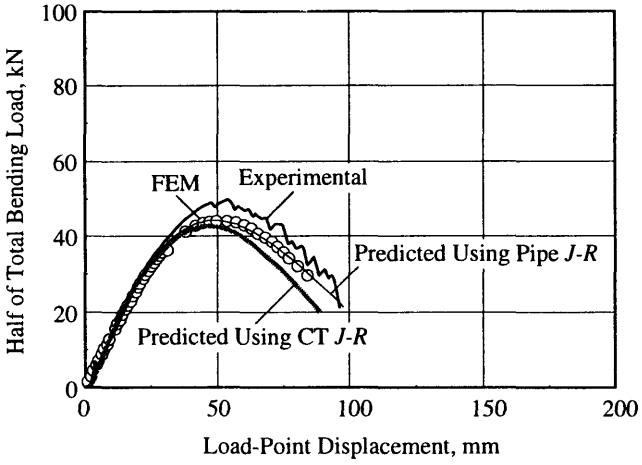


(d) Experiment 4131-3
(SA333 Gr. 6 C/S, pressure and bending)

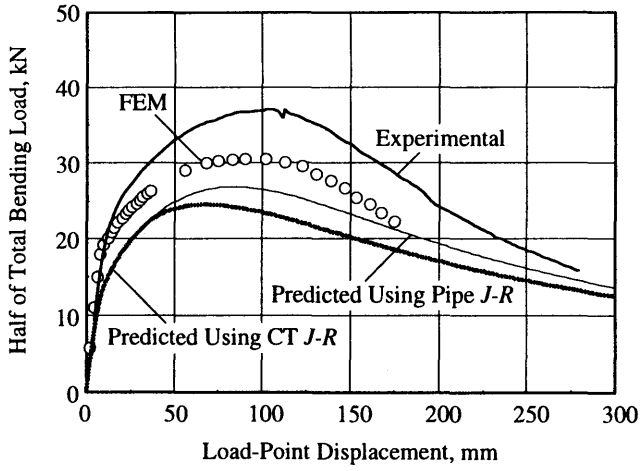


(e) Experiment 4131-5
(Type 304 S/S, pure bending)

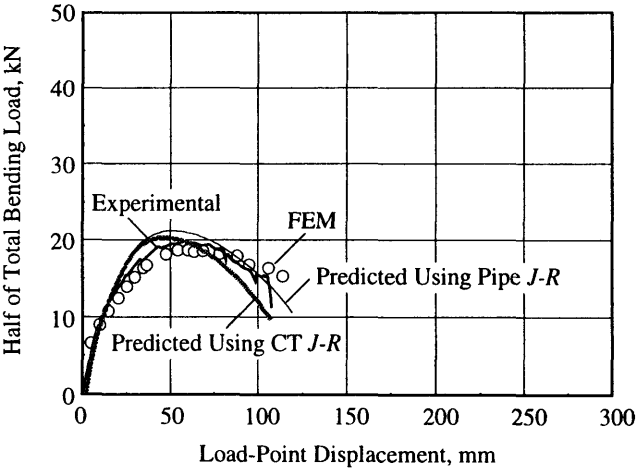


(f) Experiment 4131-1
(Type 304 S/S, pressure and bending)

Fig. 11 Comparison between experimental and predicted load versus load-point displacement relation.

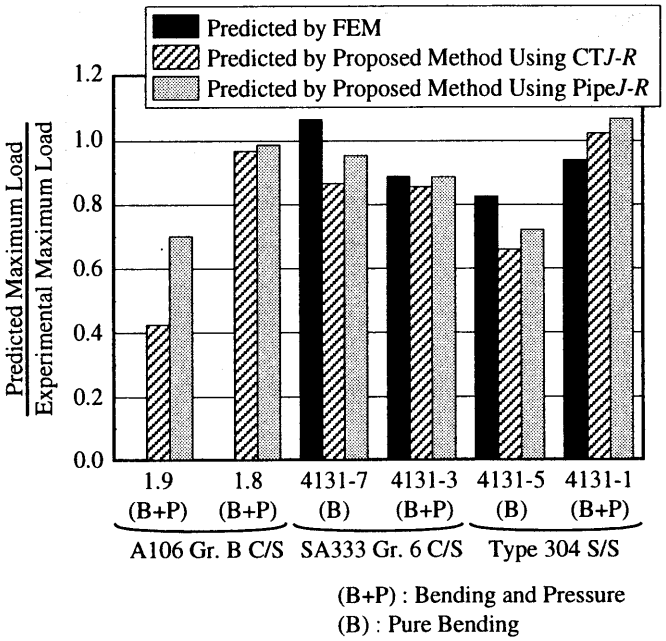


Fig. 12 Comparison between experimental and predicted maximum load.

Table 2 Matrix of sensitivity analysis.

| Material | Temp. | Diameter [Mean Radius] | Schedule [Thickness] | Total Crack Angle | $\sigma_f / \sigma_0$ |
|---|---|---|---|---|---|
| SA333 Gr. 6 Carbon Steel | 288°C | 4B [52.85 mm] | 80 [8.60 mm] | 30° | 0.00 |
| | | | | 60° | |
| | | | | 90° | |
| | | | | 120° | |
| | | | | 150° | |
| | | | | 180° | |
| | | 4B [52.85 mm] | | 30° | 0.05 |
| | | 8B [101.80 mm] | | | 0.10 |
| | | 12B [150.55 mm] | | | 0.15 |
| | | 16B [192.50 mm] | | | 0.20 |
| | | 20B [240.90 mm] | | | 0.25 |
| | | 24B [289.30 mm] | | | |

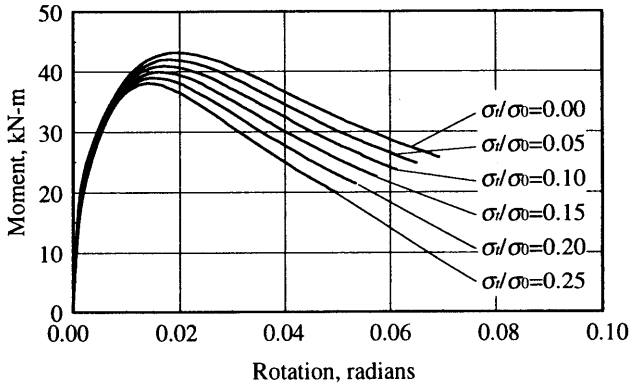


Fig. 13 Effect of internal pressure on moment-rotation relation (SA333 Gr. 6 C/S, 288°C, 4B×Sch. 80, $2\theta = 30°$).

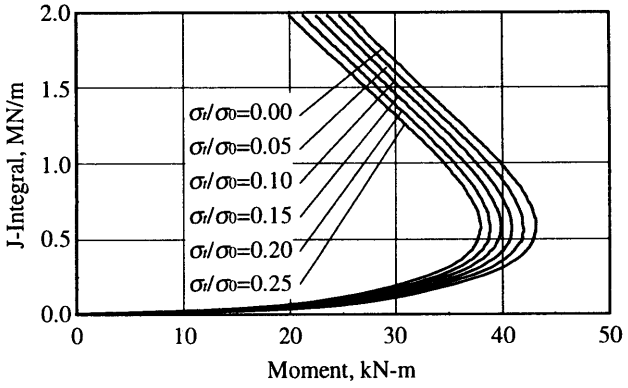


Fig. 14 Effect of internal pressure on J-integral-moment relation (SA333 Gr. 6 C/S, 288°C, 4B×Sch. 80, $2\theta = 30°$).

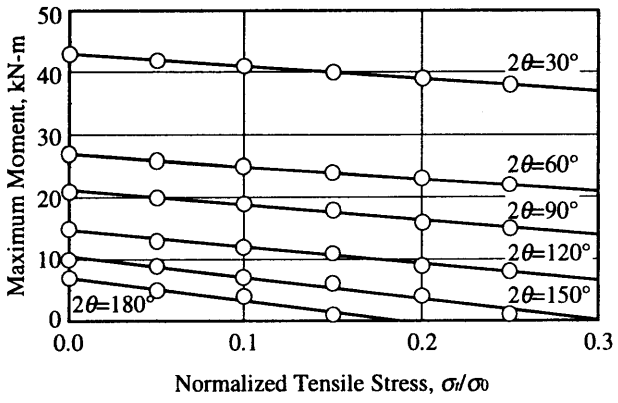


Fig. 16 Dependency of crack angle on maximum moment (SA333 Gr. 6 C/S, 288°C, 4B×Sch. 80, $2\theta$ = 30-180°).

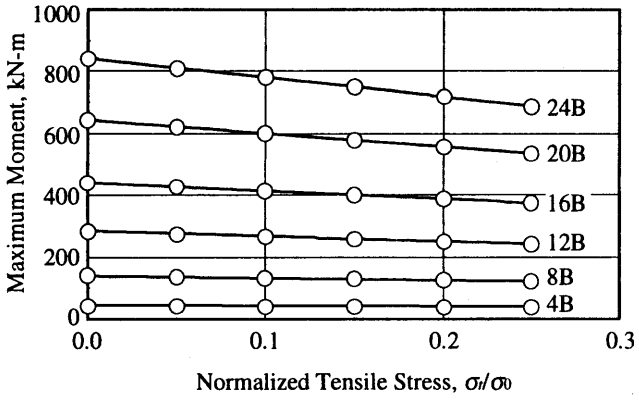


Fig. 17 Dependency of pipe diameter on maximum moment (SA333 Gr. 6 C/S, 288°C, 4-24B×Sch. 80, $2\theta$ = 30°).

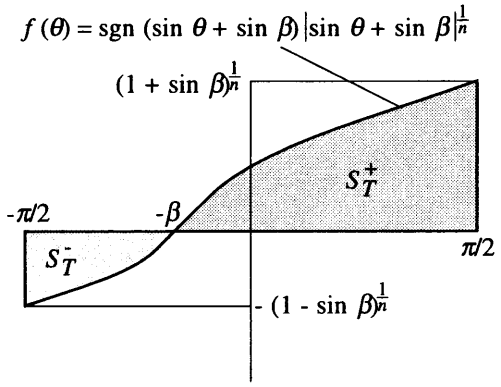


Fig. A.1 Schematic of parameters necessary to calculate equilibrium of tensile load

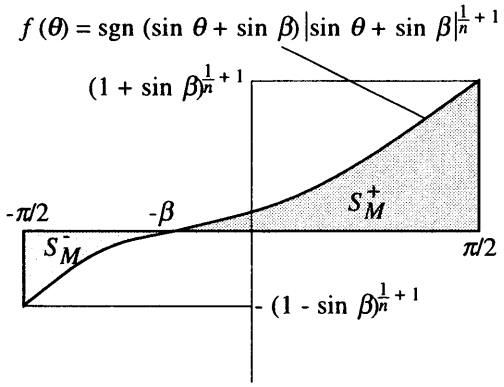


Fig. A.2 Schematic of parameters necessary to calculate equilibrium of bending moment

IV-6 Low Alloy Steel Piping Test for Fracture Criteria of LBB

Koji Koyama, Nuclear Plant Component Designing Section, Kobe Shipyard & Machinery Works, Mitsubishi Heavy Industries, Ltd., Japan

# LOW ALLOY STEEL PIPING TEST FOR FRACTURE CRITERIA OF LBB

Koji Koyama and Itaru Muroya
Mitsubishi Heavy Industries, Ltd.
Toshihiko Tanaka
The Japan Atomic Power Company
Takao Nakamura
The Kansai Electric Power Co., Inc.

## Abstract

Seven pipe fracture tests were performed to provide the data for establishing fracture criteria of Leak Before Break for the low alloy steel pipe.
Test pipes were 6-inch and 8-inch diameter pipes made of SFVQ1A or STPA24 low alloy steel. A circumferential through-wall crack was introduced at the center of a pipe, and four-point bending load was applied without internal pressure. Stable crack extensions were observed in all of the experiments.

To estimate the maximum applied load, the net-section criteria (NSC), R6 method Option 2 and Option 3 were used. The predicted values by three kinds of evaluation methods were compared with the experimental loads. Most of all the predicted maximum loads agreed well with the experimental maximum loads within 20% difference. The NSC gave the most accurate prediction but also gave unconservative results in some test cases. The predicted maximum loads by R6 Op.2 were conservative in all of the test cases. From the view point of conservativeness R6 method can be used for evaluation of the low alloy steel pipe fracture. Therefore, the LBB concept would be applied to the protective design standard against pipe break for the material.

## 1. INTRODUCTION

The concept of leak before break (LBB) has been applied to the protective design standard against pipe break since 1992 in Japan. The LBB applicability evaluation flow is shown in Fig.1-1. The current application of LBB concept is limited to the piping systems in the reactor cooling pressure boundary(RCPB) and of austenitic stainless steels. Nevertheless, this concept would also be applicable to other piping systems and other materials, provided that plant shutdown can be achieved before fatal pipe break, taking account of fracture behavior the pipe material and the reliability of the performance of leak detection systems.

The recent study of fracture mechanics confirmed the adequacy of application of the LBB concept to the piping system of carbon steel piping/1/, consequently, the LBB concept would be applicable to the piping systems, as well, of low alloy steel, which is the same ferritic material as carbon steel.

Moreover, the existing leak detection system will be also effective to the application of LBB concept for the PWR secondary piping systems inside the reactor containment vessel, such as main feedwater system.

This paper covers the experimental study performed on the fracture behavior of low alloy steel pipes, which is expected to be applied to the reactor coolant piping and feedwater piping in advanced PWRs in Japan.

# 2. TEST DESCRIPTION

## 2.1 Test Matrix

Seven pipe experiments were conducted to investigate the effects of the crack angle, material and pipe diameter on the fracture behavior. Table 2.1-1 shows the test matrix. In these tests, the 6-inch and 8- inch diameter pipes were used.

## 2.2 Test Pipes

The pipes were made of SFVQ1A and STPA24 low alloy steel (Japanese Industrial Standard Specification equivalent to ASME SA508 Cl.3 and SA335 Gr. P22 respectively). The test sections were of base metal pipes or shop fabricated metal active gas (MAG) welds joining two pieces of the pipe. The pipe geometry is shown in Fig. 2.2-1.

A initial circumferential through-wall flaw was introduced into the center of the test section by electric-discharge-machining(EDM) techniques, followed by cyclic loading until fatigue cracks extended to approximately 5 mm to sharpen the crack tip. Fig 2.2-2 shows the through-wall crack geometry.

## 2.3 Test Procedure

The test system is shown in Fig.2.3-1. This test system has a capacity of 100 tonf (980 kN) per ram and the maximum stroke is 500mm. The pipes was subjected four-point bending with the inner span of 800 mm and the moment arm length of 750mm. The experiments were conducted under displacement control with the displacement rate of 0.05 mm/sec.

The experiments of SFVQ1A pipes and the STPA24 pipes were conducted at 325℃ and 310℃, respectively. To achieve these temperature, the hot air was ventilated into the test section by the fan, and the heaters were used for the fine temperature adjustment of the center of the test section. The temperature was monitored by five thermocouples to be maintained at the designated test temperature. After reaching the temperature, the test pipes were allowed to stabilize at the test temperature at least 2 hours before applying bending moment load. No internal pressure was applied.

## 2.4 Instrumentation

The following data were collected using the personal computers. The grid lines with 2 mm intervals were drawn near the crack tip of the pipe surface to observe crack extension behavior. Crack extension behavior was also recorded by video camera.

- Applied load (at each ram)
- Load-line displacement (at each ram)
- Pipe ovalization
- Crack opening displacements at three locations
- Strain
- Temperature near the crack tip
- Crack extension in both crack tips

## 2.5 Material Characterization

The chemical compositions of the SFVQ1A and STPA24 steels are shown in Table 2.5-1.

The stress-strain curves and J-resistance curves were obtained using the test specimens taken from the pipes with the same sizes of the bending test pipes. For the fracture toughness test, the 1/2T CT specimens and 1T planform size CT specimens which had the thickness of 1/2-inch were taken from 6-inch diameter pipes and 8-inch diameter pipes, respectively. The true stress-strain curves of the base metals are shown in Fig. 2.5-1～Fig. 2.5-3. The J-resistance curves of the base metals and the weld metals are shown in Fig. 2.5-4～Fig. 2.5-9. Also shown in those figures the fitting curves by Ramberg-Osgood's law for the stress-strain curves and the power law for the J-resistance curves are drawn in the same figures.

Table 2.5-2 shows the tensile properties and the $J_{IC}$ values of the test materials. The flow stress is defined by the average of the 0.2% offset yield strength and the ultimate strength.

## 2.6 Pipe Fracture Experiment Results

The experimental results are summarized in Table 2.6-1. The total applied load versus load - line displacement curves are shown in Fig. 2.6-1 and Fig. 2.6-2. At first from a fatigue crack tip, two ductile cracks initiated and afterwards either of them propagated much longer than the other. All of the cracks propagated stably with the angle of about 45° to the pre-cracked cross sections.

According to the measured crack mouth opening displacement, the symmetrical opening behavior observed. The ovalization near the cracked section to the original diameter was within 2%.

# 3. EVALUATION OF PIPE EXPERIMENT

In this study the net-section collapse criterion (NSC) and R6 method (Option 2 and Option 3) were applied in order to estimate the maximum load. R6 Option 3 uses J-integral, which is calculated by the finite element analysis or the simplified equation as proposed by Zahoor /2/. In this study, the simplified J-integral calculation was chosen for R6 method, because J-integral analysis by the finite element method would be time consuming to evaluate the pipe fracture behavior for each of the seven pipe tests. Therefore by the following three steps the validity of the simplified J-integral is confirmed and the applicability of three evaluation method is investigated.

i. Validity of the modeling of the finite element analysis
ii. Evaluation of the accuracy and conservativeness of the simplified J-integral comparing with J-integral by the finite element analysis
iii. Evaluation of the accuracy of the predicted maximum applied load from each evaluation method

## 3.1 Numerical Analysis

(1) Description of the finite element(FE) models

The analyzed case was Experiment SFB1. The analyses were made with the FE code MARC (version K6-1). The FE model is shown in Fig.3.1-1. The model is one quarter of the test pipe was modeled due to symmetry. The element type was 20 node solid element. The total number of elements and nodes was 1056 and 5727, respectively. The load-line displacement was applied at the outer support points.

For the crack extension analysis, two models were prepared. One was Model 1 which had the crack length corresponding to the initial crack length of half angle 45° . The other was Model 2 which had the extended crack length at the maximum applied load in the experiment. As mentioned previously the cracks extended diagonally to the pre-cracked cross section, Model 2 had the projected crack extension to the pre-cracked cross section at the maximum load. The experimental load-line displacement was applied to Model 1 until just before the ductile crack initiation and the test load-line displacement at the maximum load was applied to Model 2.

(2) Global behavior of the test pipe

Fig. 3.1-2 shows the comparison of the calculated total applied load versus load-line displacement relation with the experimental result. Fig. 3.1-3 shows the similar comparison in the case of the crack mouth opening. In both comparisons, analytical results agree well with the experimental results. These results gives the validity of the FE modeling including consideration of the diagonal crack propagation.

## 3.2 Comparison of the Detailed and Simplified J-integral Calculation Methods

(1) Accuracy and conservativeness of the simplified J-integral

To calculate the simplified J-integral under the bending load, the stress-strain curve was fit by Ramberg-Osgood's law expressed by the following equation.

$$\varepsilon / \varepsilon_0 = (\sigma / \sigma_0) + \alpha \ (\sigma / \sigma_0)^n \qquad (3.2\text{-}1)$$

The fitting curve is already shown in Fig.2.5-1. The parameters of Ramberg-Osgood's law are as follows;

$\alpha$ =1.47, $\sigma_0$ = 413 MPa, $\varepsilon_0$ =2.19×$10^{-3}$, n = 7.91

Fig.3.2-1 shows the comparison of the simplified J-integral under the bending load with J-integral by the FE analysis. In these calculations the crack extension was ignored. At the bending stress of 392 MPa which is close to the maximum value in the experiment, the difference between both values is 10% and the simplified J gives conservative result.

(2) Comparison of Failure Assessment Curves (FAC)

Fig. 3.2-2 shows the comparison of FAC of R6 method Option 3 using the simplified J with that using J-integral by the FE analysis. Also from this figure the simplified J analysis method gives the accurate and conservative FAC.

## 3.3 Comparison of the Maximum Applied Load by Different Evaluation Method

(1) Analysis condition

Material properties, the stress-strain curves and J-resistance curves shown in Table 2.5-2 and Fig. 2.5-1～Fig. 2.5-9 has been used for the analysis. Because the accuracy was confirmed, the simplified J was used to obtain FAC in the case of R6 Option 3. To estimate the maximum load in the case of the pipes with the weld metal, the stress-strain curves of the base metal and J-resistance curves of the weld metal were used for the conservative assumption.

(2) Results

The maximum test loads normalized by the predicted maximum loads obtained from three different kinds of evaluation methods are shown in Fig. 3.3-1～Fig. 3.3-3.

The average values of the normalized maximum loads of seven tests are 1.05 from the NSC, 1.15 from R6 Op.2 and 1.09 from R6 Op.3. Most of all the predicted maximum loads agreed well with the experimental maximum loads within 20% difference. There are some cases that the normalized maximum load is below 1.0, two cases from the NSC, one case from R6 Op.3

and no case from R6 Op.2.

Therefore, from the viewpoint of the accuracy, the NSC gives the most accurate prediction, while from the viewpoint of the conservatism, the NSC may not always give conservative prediction and R6 Op.2 gives the most conservative results.

## 4. CONCLUSION

In order to provide the experimental data for establishing the leak before break criteria of the low alloy steel pipe, seven pipe fracture experiments were performed. Test pipes were 6-inch and 8-inch diameter pipes of SFVQ1A or STPA24 low alloy steel. A circumferential through-wall crack was introduced at the center of a pipe, and four-point bending load was applied without internal pressure. Stable crack extensions were observed in all of the experiments.

To estimate the maximum applied load, the net-section criteria, R6 method Option 2 and Option 3 were used. The predicted values by three kinds of evaluation methods were compared with the experimental loads. Most of all the predicted maximum loads agreed well with the experimental maximum loads within 20% difference. In detail, the NSC gave the most accurate prediction but also gave two unconservative results. The predicted maximum loads by R6 Op.2 were conservative in all of the experiment cases. From the view point of conservativeness R6 method can be used for evaluation of the low alloy steel pipe fracture.

The further analyses on the pipe with the actual geometry is continuously followed to establish the leak before break criteria of the low alloy steel pipe.

## 5. ACKNOWLEDGMENT

This test was funded by five Japanese PWR utilities, and the results on this study were discussed and reviewed in the committee under Thermal and Nuclear Power Engineering Society. The author acknowledges to the chairman Prof. Y. Asada, the committee members Prof. K. Miya, Dr. K. Shibata, Dr. K. Kashima and the other committee members including those from the utilities.

## 6. REFERENCES

/1/ Y. Asada, 'Development of Criteria for Protection Against Pipe Breaks in LWR Plants', pp.95-111, International Journal of Pressure Vessel & Piping, vol. 43, 1990.

/2/ A. Zahoor, Ductile Fracture Handbook Volume1, NP-6301-D N14-1 Research Project 1757-69, June 1989.

/3/ T. Tanaka, T. Nakamura, K. Koyama, I. Muroya, 'Four-Point Bending Tests of Low Alloy Steel Pipes in Japan', presented at the 7th German Japanese Joint Seminar, Sept. 1997.

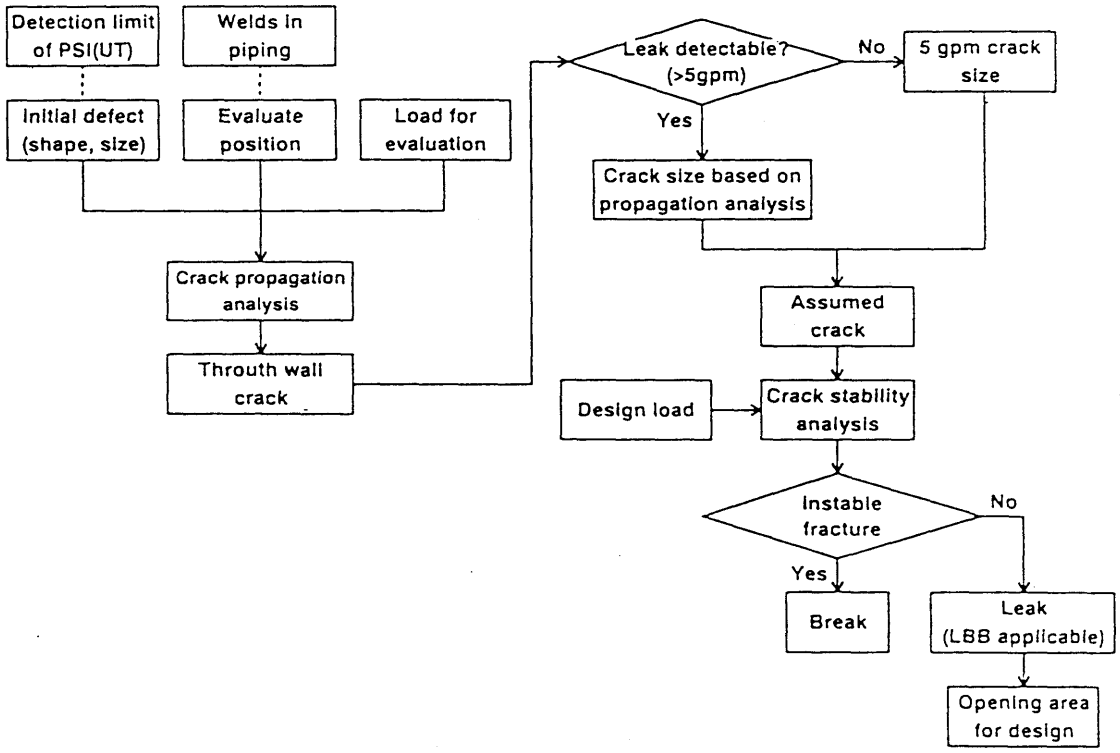


Figure 1-1 LBB applicability evaluation flow

Table 2.1-1 Test matrix of the pipe tests

| Experimental number | Material | Nominal diameter(inch) | Crack half angle(deg) | Crack geometry |
|---|---|---|---|---|
| SFB1 | SFVQ1A | 6 | 45 | TWC |
| SFW1 | SFVQ1A WELD | 6 | 45 | TWC |
| SFW2 | SFVQ1A WELD | 6 | 30 | TWC |
| SFB2 | SFVQ1A | 8 | 45 | TWC |
| SFW3 | SFVQ1A WELD | 8 | 45 | TWC |
| STB1 | STPA24 | 6 | 45 | TWC |
| STW1 | STPA24 WELD | 6 | 45 | TWC |

TWC: Through wall crack

Table 2.5-1 Chemical compositions of the test materials

(Weight %)

| Material | Nominal diameter(inch) | C | Si | Mn | P | S | Ni | Cr | Mo | V |
|---|---|---|---|---|---|---|---|---|---|---|
| SFVQ1A | 6 | 0.18 | 0.18 | 1.44 | 0.003 | 0.001 | 0.75 | 0.12 | 0.5 | <0.01 |
| SFVQ1A | 8 | 0.2 | 0.19 | 1.47 | 0.003 | 0.001 | 0.76 | 0.12 | 0.51 | <0.01 |
| STPA24 | 6 | 0.1 | 0.26 | 0.41 | 0.007 | 0.005 | - | 2.15 | 0.94 | - |

Table 2.5-2 Tensile properties and $J_{IC}$ values of the test materials

| Material (Base/Weld) | Diameter (inch) | Temperature (°C) | 0.2% offset yield strength (MPa) | Ultimate strength (MPa) | Flow stress (MPa) | $J_{IC}$ (kJ/m$^2$) |
|---|---|---|---|---|---|---|
| SFVQ1A (Base metal) | 6 | 325 | 413 | 577 | 495 | 696 |
| SFVQ1A (Weld metal) | 6 | 325 | 477 | 628 | 553 | 123 |
| SFVQ1A (Base metal) | 8 | 325 | 410 | 579 | 495 | 652 |
| SFVQ1A (Weld metal) | 8 | 325 | 457 | 630 | 544 | 270 |
| STPA24 (Base metal) | 6 | 310 | 245 | 482 | 364 | 623 |
| STPA24 (Weld metal) | 6 | 310 | 513 | 598 | 556 | 152 |

Table 2.6-1 Experimental results

| Experiment number | Pipe material | Outside pipe diameter mm (inch) | Wall thickness | Crack half angle (deg) | Total load at the crack initiation (kN) | Maximum total experiment load (kN) | Crack extension a1 (mm)(*) | Crack extension a2 (mm)(**) |
|---|---|---|---|---|---|---|---|---|
| SFB1 | SFVQ1A | 166.5 (6) | 15.7 | 45 | 196 | 282 | 14.8 | 9.0 |
| SFW1 | SFVQ1A MAG | 166.5 (6) | 15.7 | 45 | 216 | 254 | 6.4 | 3.1 |
| SFW2 | SFVQ1A MAG | 166.5 (6) | 15.7 | 30 | 226 | 339 | 13.3 | 9.0 |
| SFB2 | SFVQ1A | 217.6 (8) | 19.5 | 45 | 490 | 602 | 17.7 | 12.5 |
| SFW3 | SFVQ1A MAG | 217.6 (8) | 19.5 | 45 | 353 | 588 | 15.6 | 11.0 |
| STB1 | STPA24 | 165.4 (6) | 14.1 | 45 | 163 | 176 | 12.1 | 7.5 |
| STW1 | STPA24 MAG | 165.4 (6) | 14.1 | 45 | 123 | 199 | 18.1 | 13.0 |

(*) a1 : Absolute crack extension length

(**) a2 : Projected crack extension length to the pr-cracked cross section

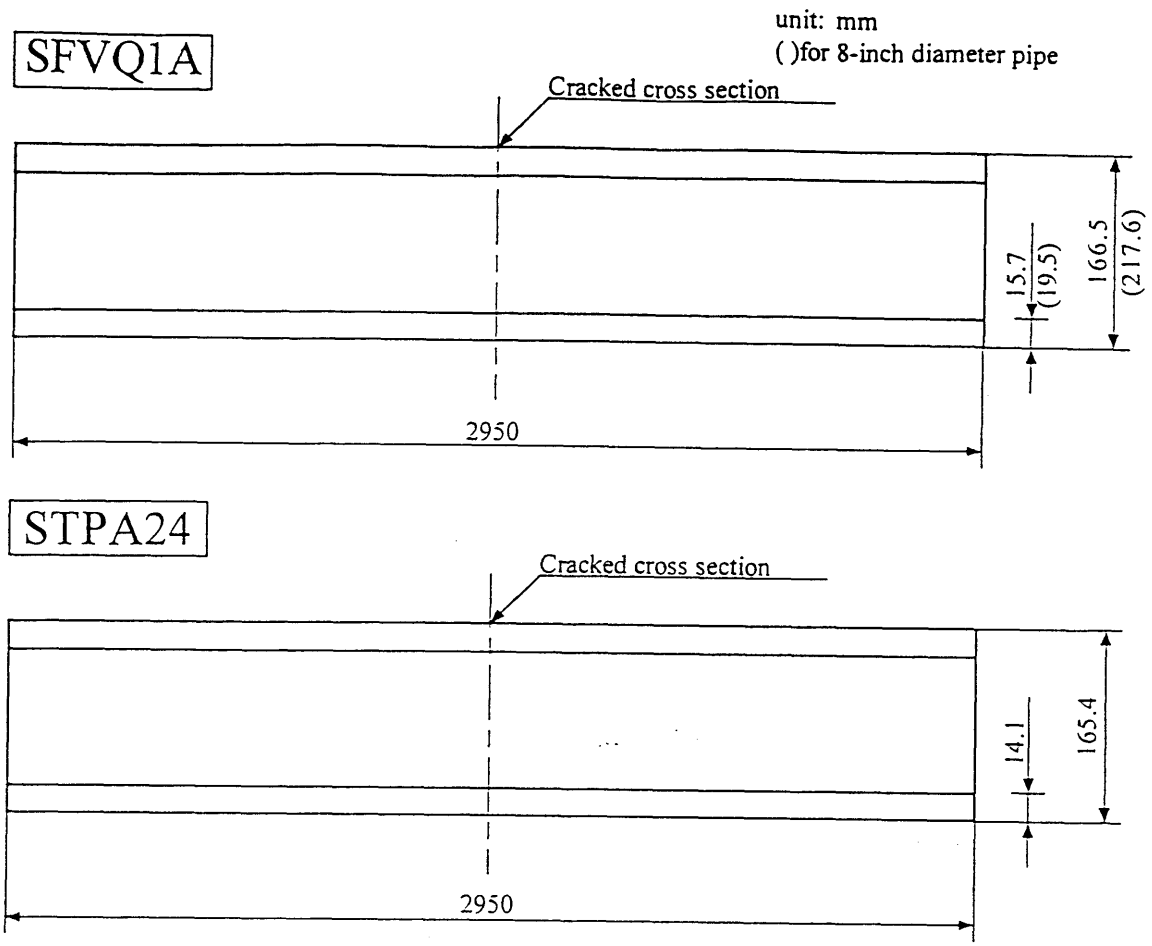


Fig.2.2-1 Geometries of the test pipes

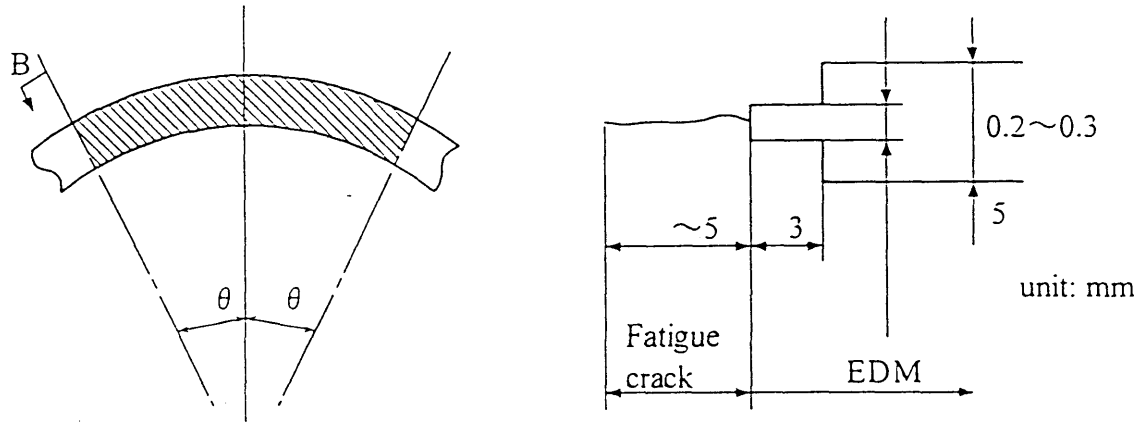


θ : Half crack angle

EDM:Electric-Discharge-Machining

Fig.2.2-2 Throngh-wall crack geometry

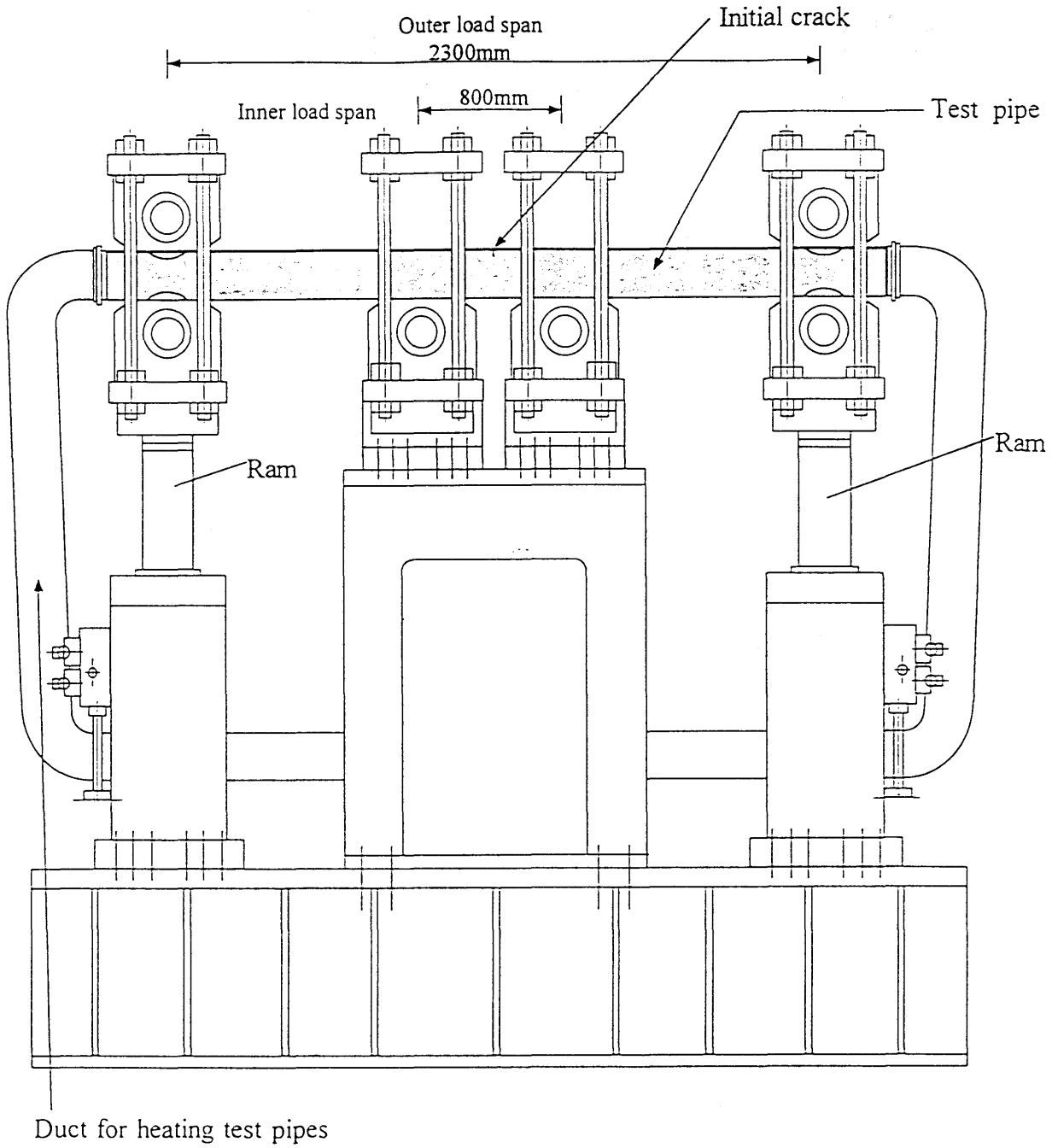


Fig.2.3-1 Test system

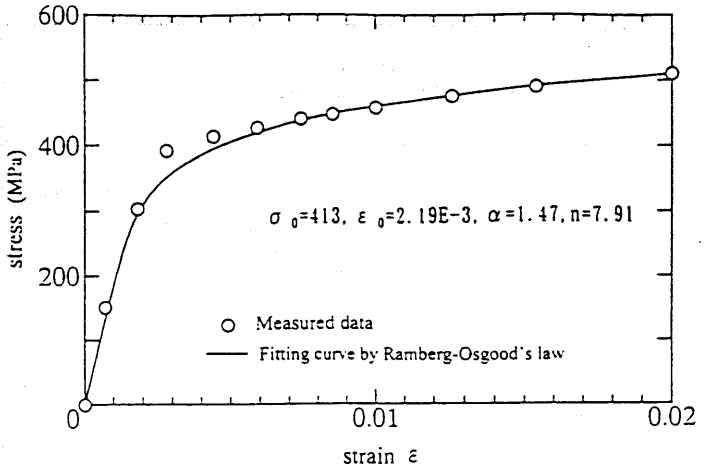


Fig.2.5-1 True stress-strain curve of the test material
(6-inch diameter SFVQ1A pipe(Base metal))

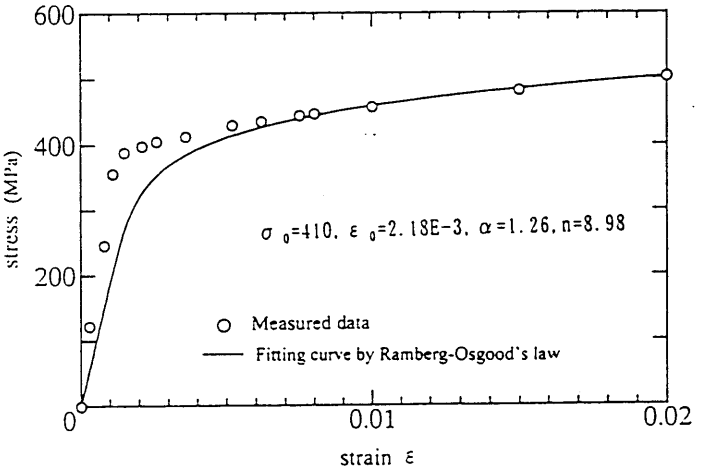


Fig.2.5-2 True stress-strain curve of the test material
(8-inch diameter SFVQ1A pipe(Base metal))

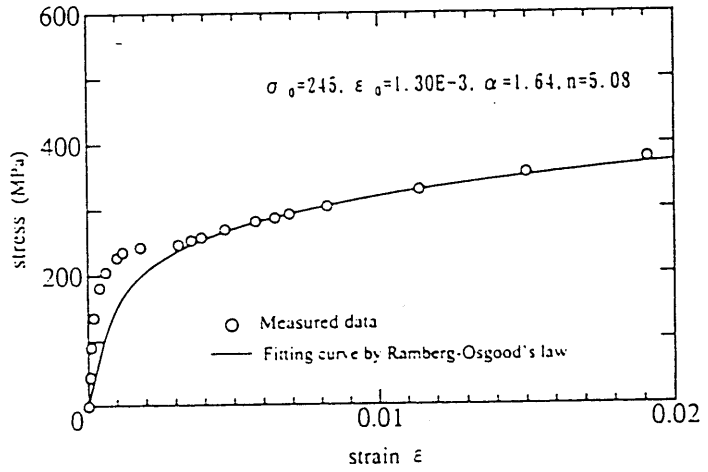


Fig.2.5-3 True stress-strain curve of the test material
(6-inch diameter STPA24 pipe(Base metal))

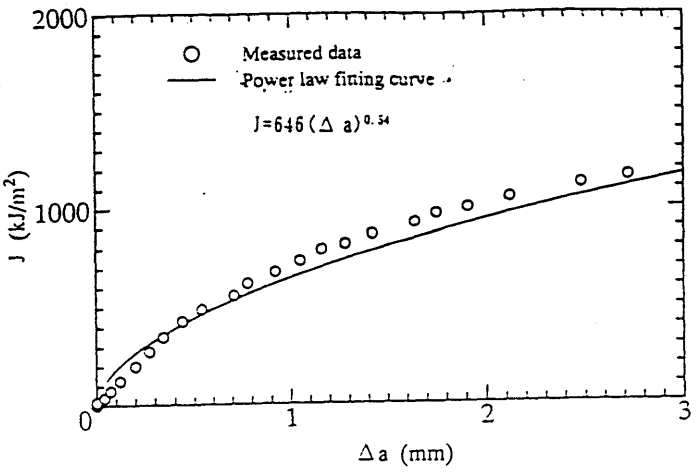


Fig.2.5-4 J-resistance curve of the test material
(6-inch diameter SFVQ1A pipe(Base metal))

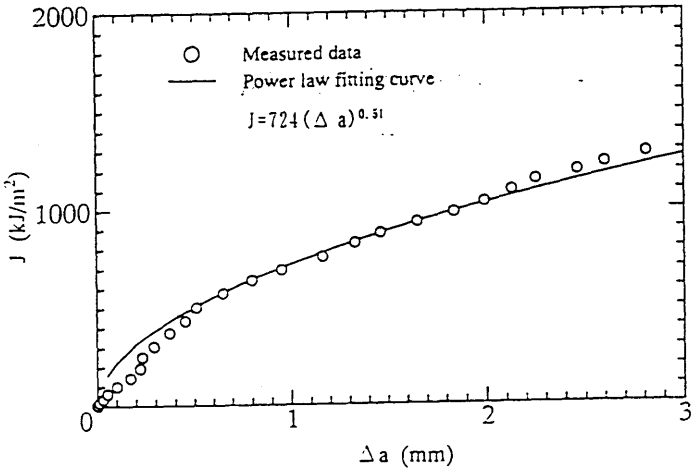


Fig.2.5-5 J-resistance curve of the test material
(8-inch diameter SFVQ1A pipe(Base metal))

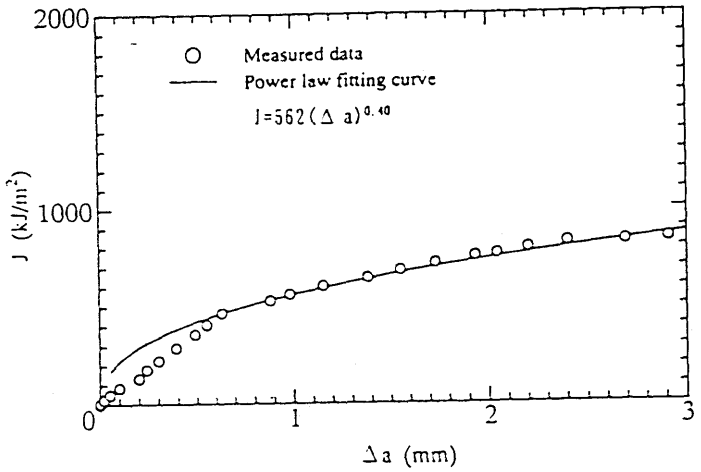


Fig.2.5-6 J-resistance curve of the test material
(6-inch diameter STPA24 pipe(Base metal))

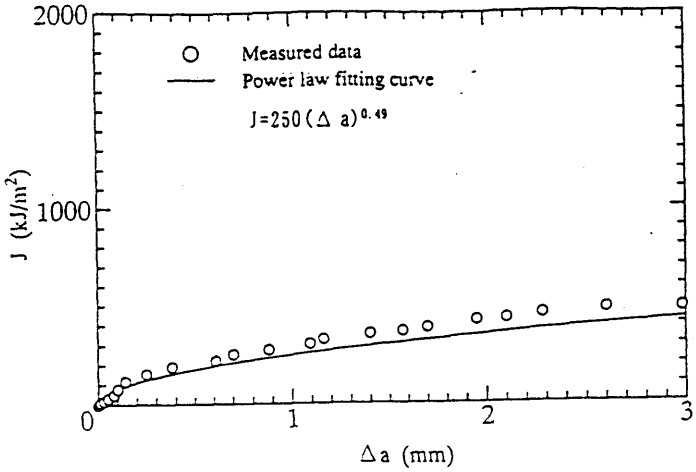


Fig.2.5-7 J-resistance curve of the test material
(6-inch diameter SFVQ1A pipe(Weld metal))

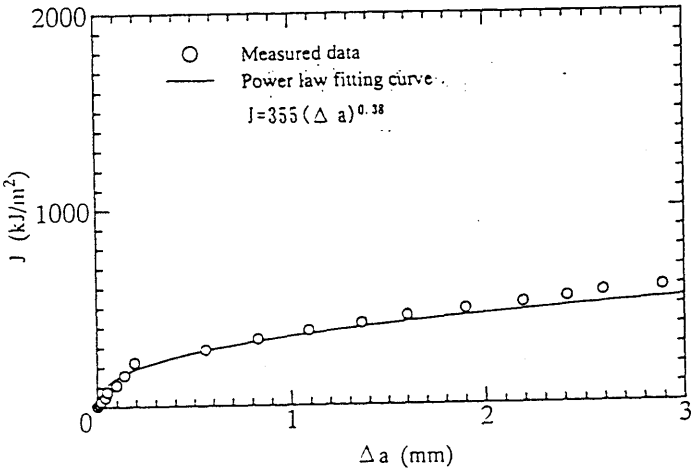


Fig.2.5-8 J-resistance curve of the test material
(8-inch diameter SFVQ1A pipe(Weld metal))

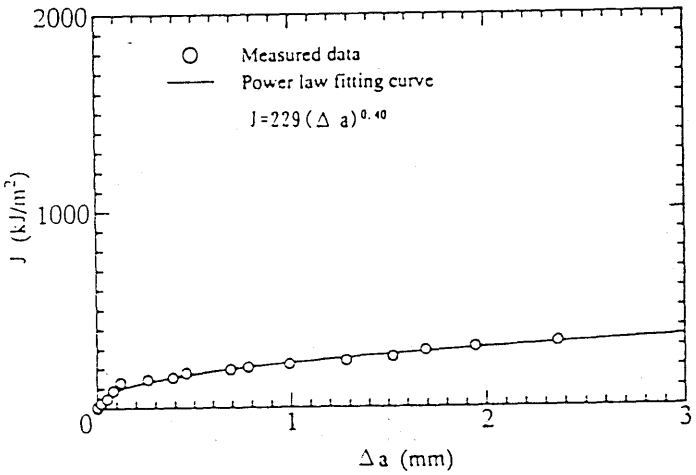


Fig.2.5-9 J-resistance curve of the test material
(6-inch diameter STPA24 pipe(Weld metal))

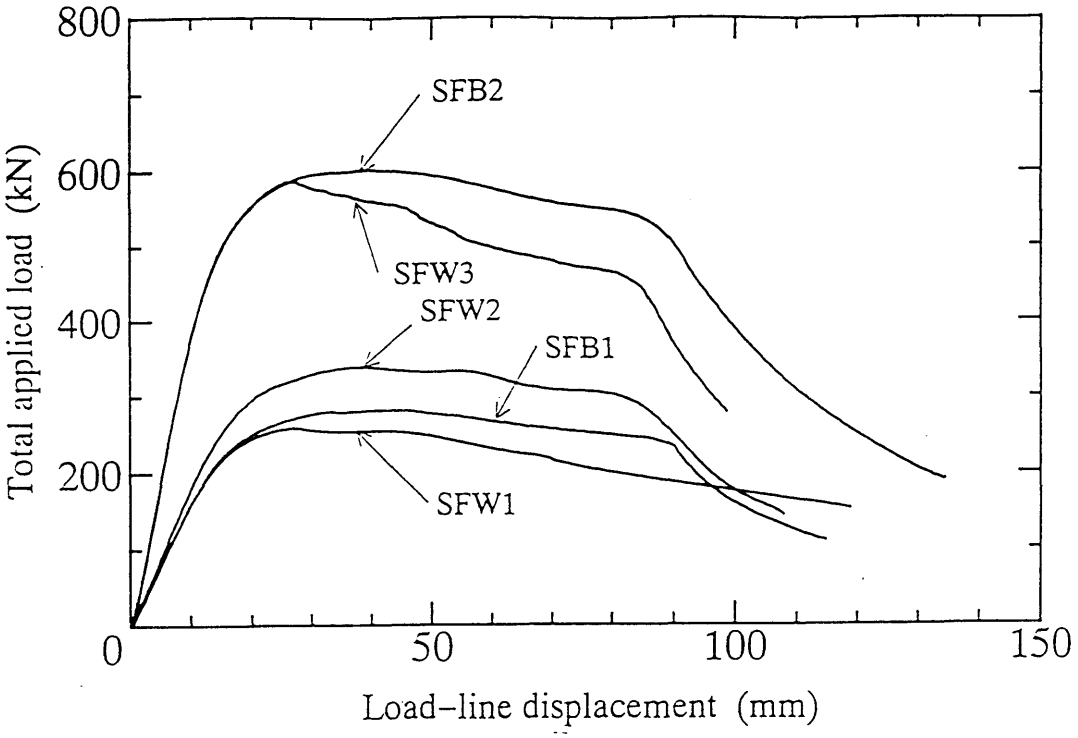


Fig.2.6-1 Load versus load-line displacement curve of SFVQ1A test pipes

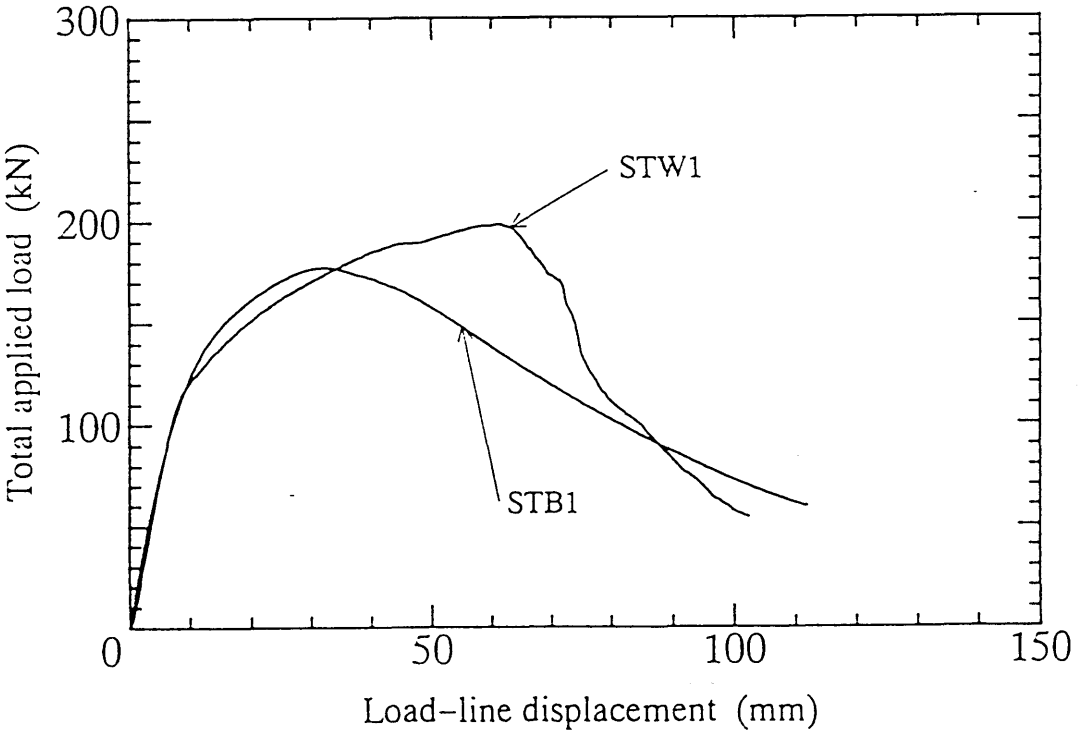


Fig.2.6-2 Load versus load-line displacement curve of STPA24 test pipes

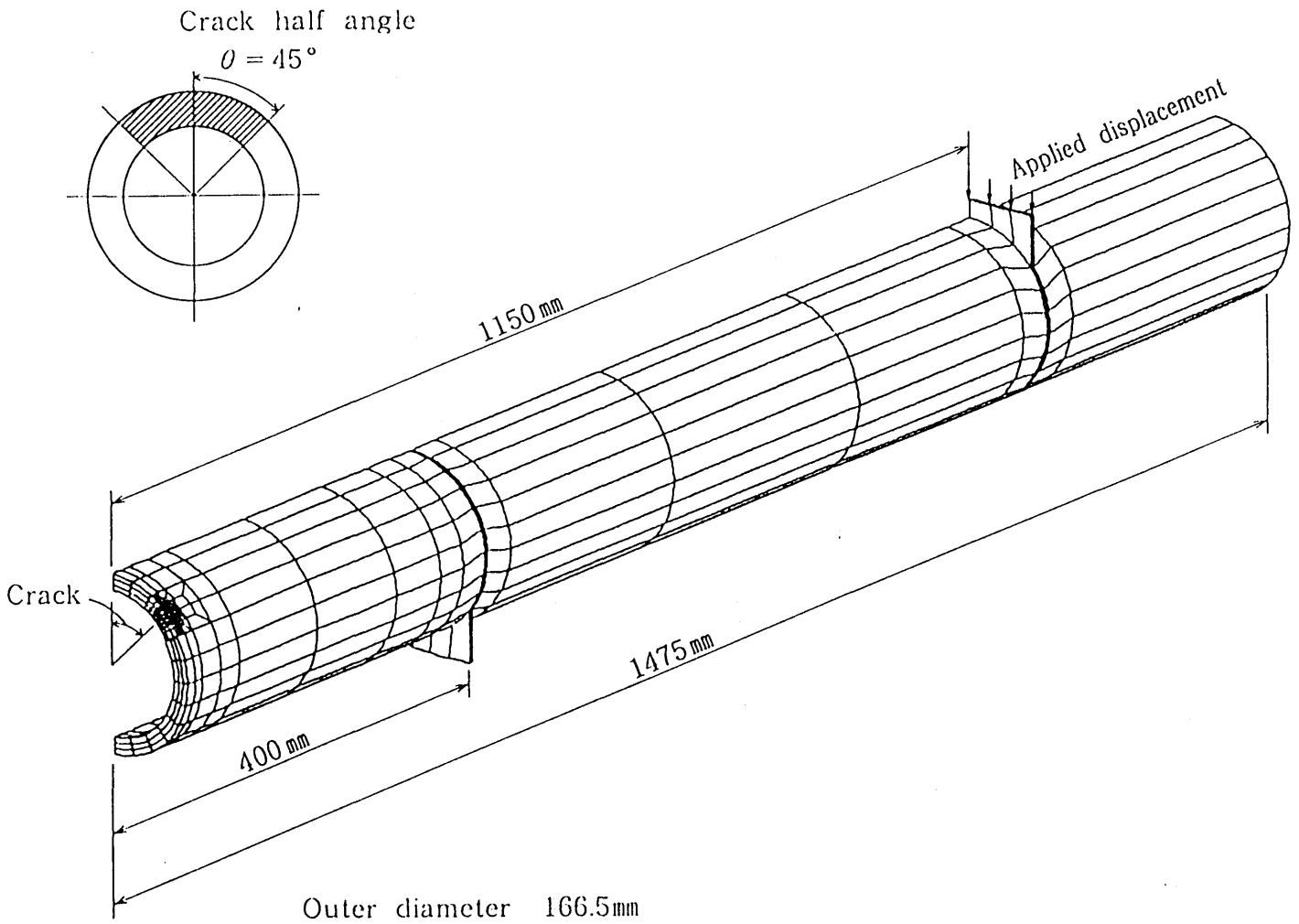


Fig.3.1 – 1 Finite element mesh of a test pipe

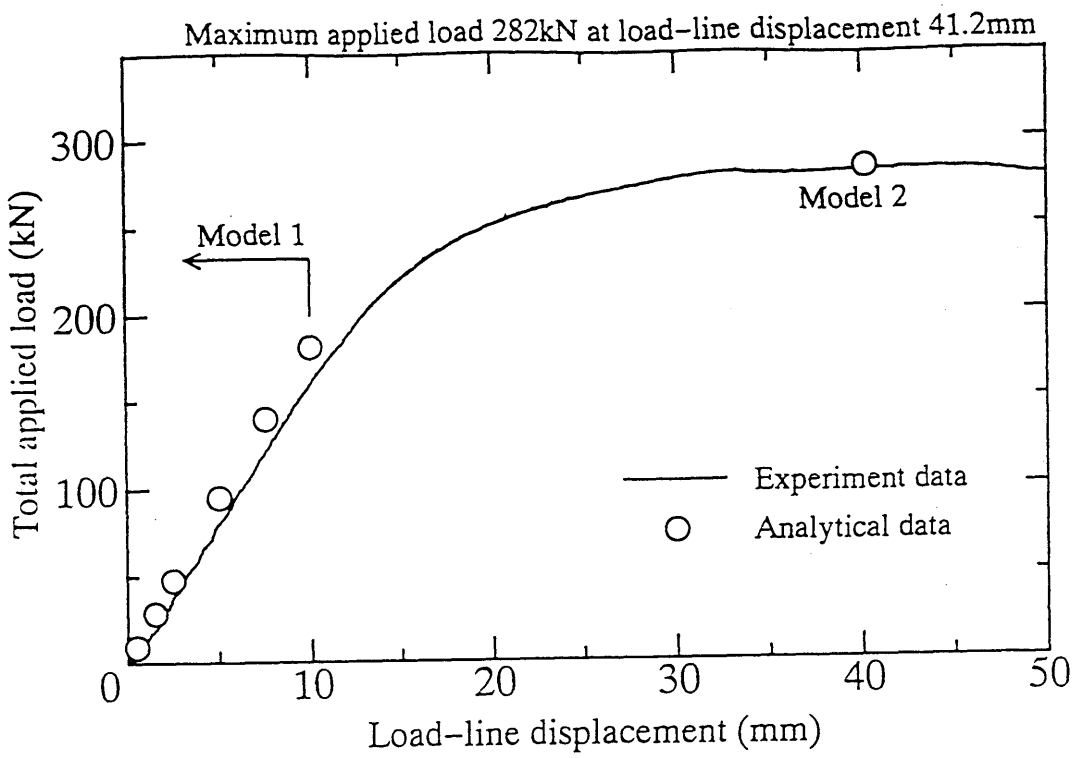


Fig.3.1-2 Comparison of the calculated total applied load versus load-line displacement curve with the experiment curve (6-inch diameter SFVQ1A pipe, Experiment SFB1)

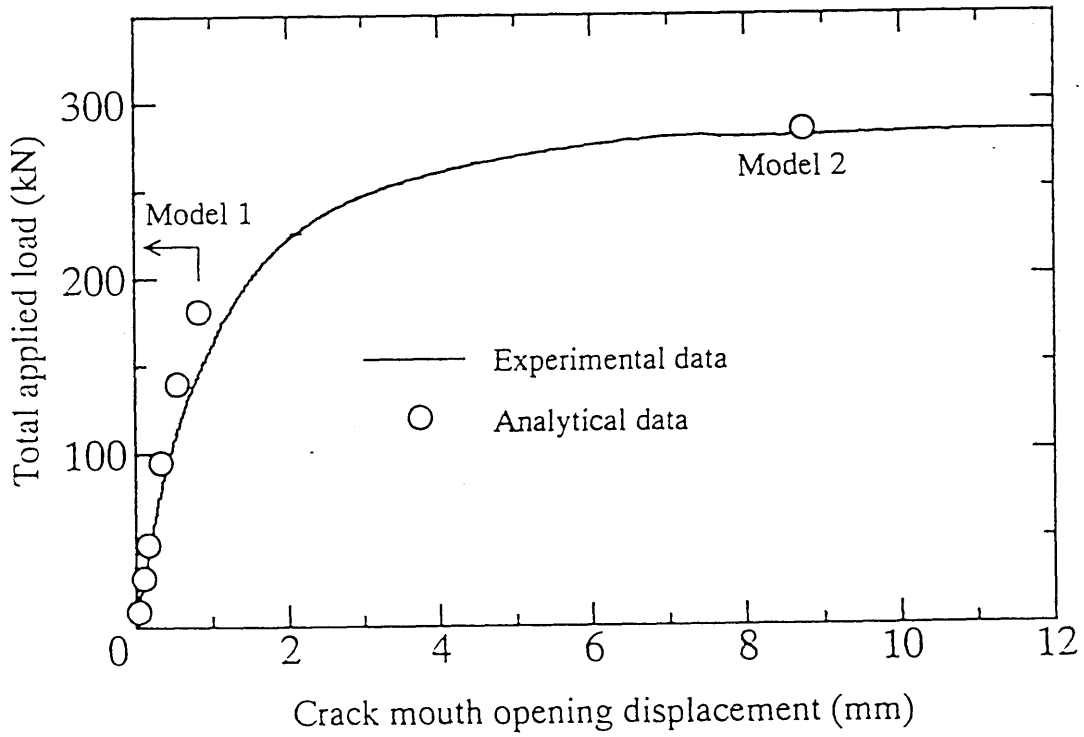


Fig.3.1-3 Comparison of the calculated total applied load versus crack mouth opening displacement curve with the experiment curve (6-inch diameter SFVQ1A pipe, Experiment SFB1)

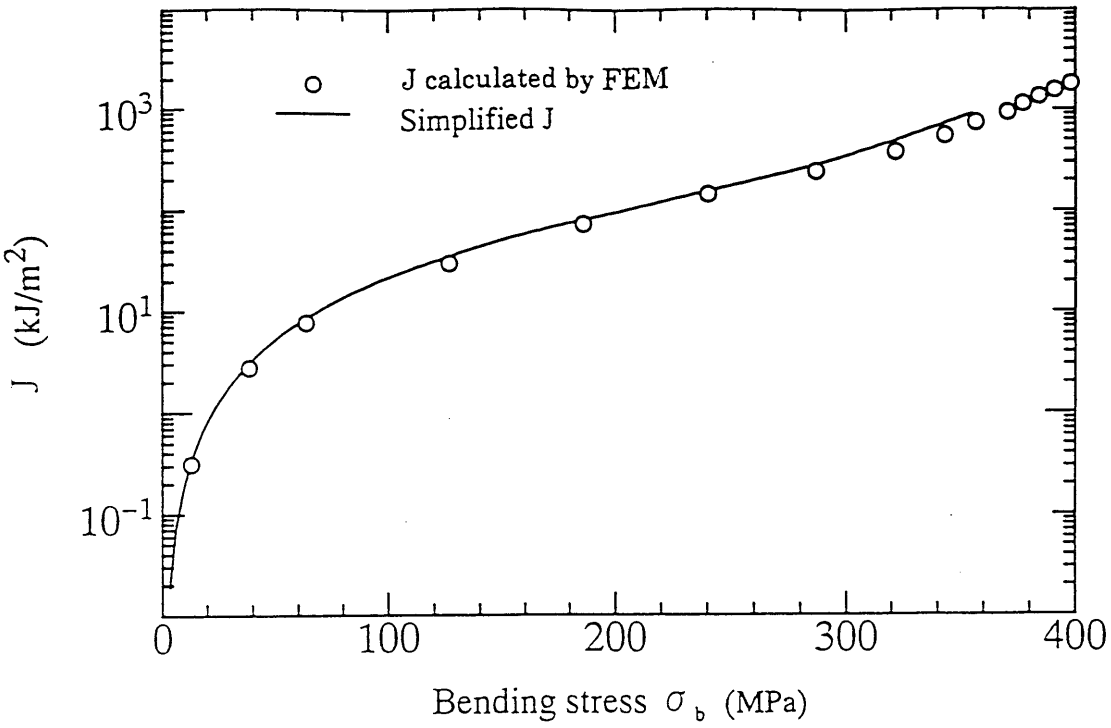


Fig.3.2-1 Comparison of the simplified J-integral with J-integral by FEM analysis
(6-inch diameter SFVQ1A pipe, Experiment SFB1)

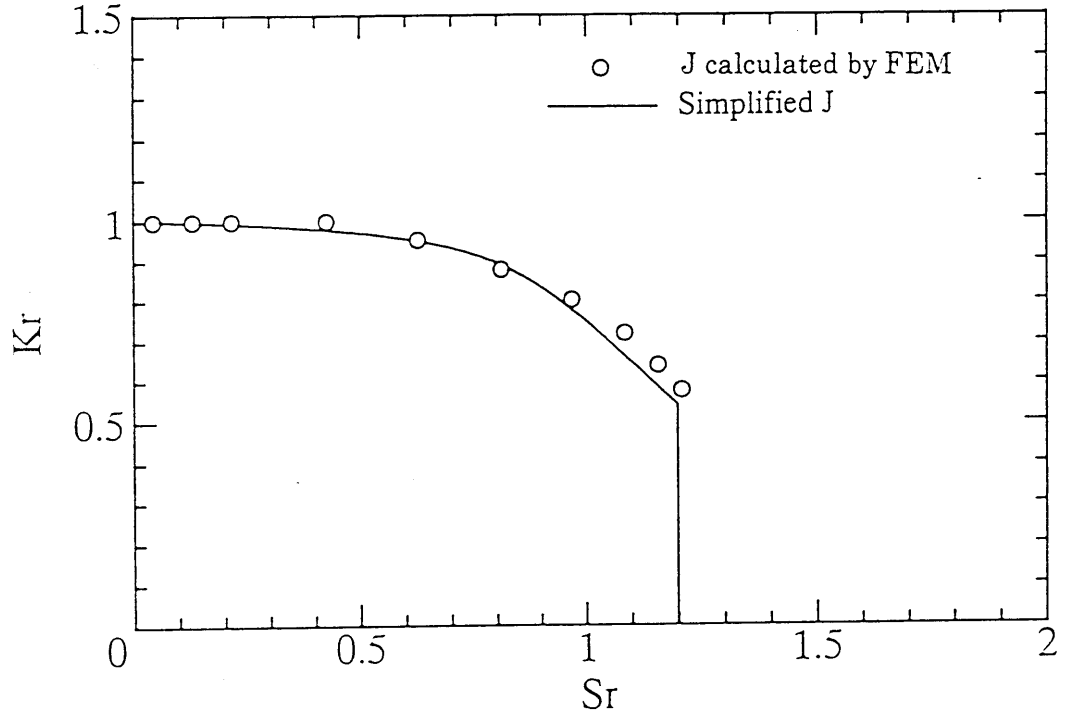


Fig.3.2-2 Comparison of FAC of R6 OP.3 using the simplified J-integral
with that using J-integral by FEM analysis
(6-inch diameter SFVQ1A pipe with crack half angle 45 °)

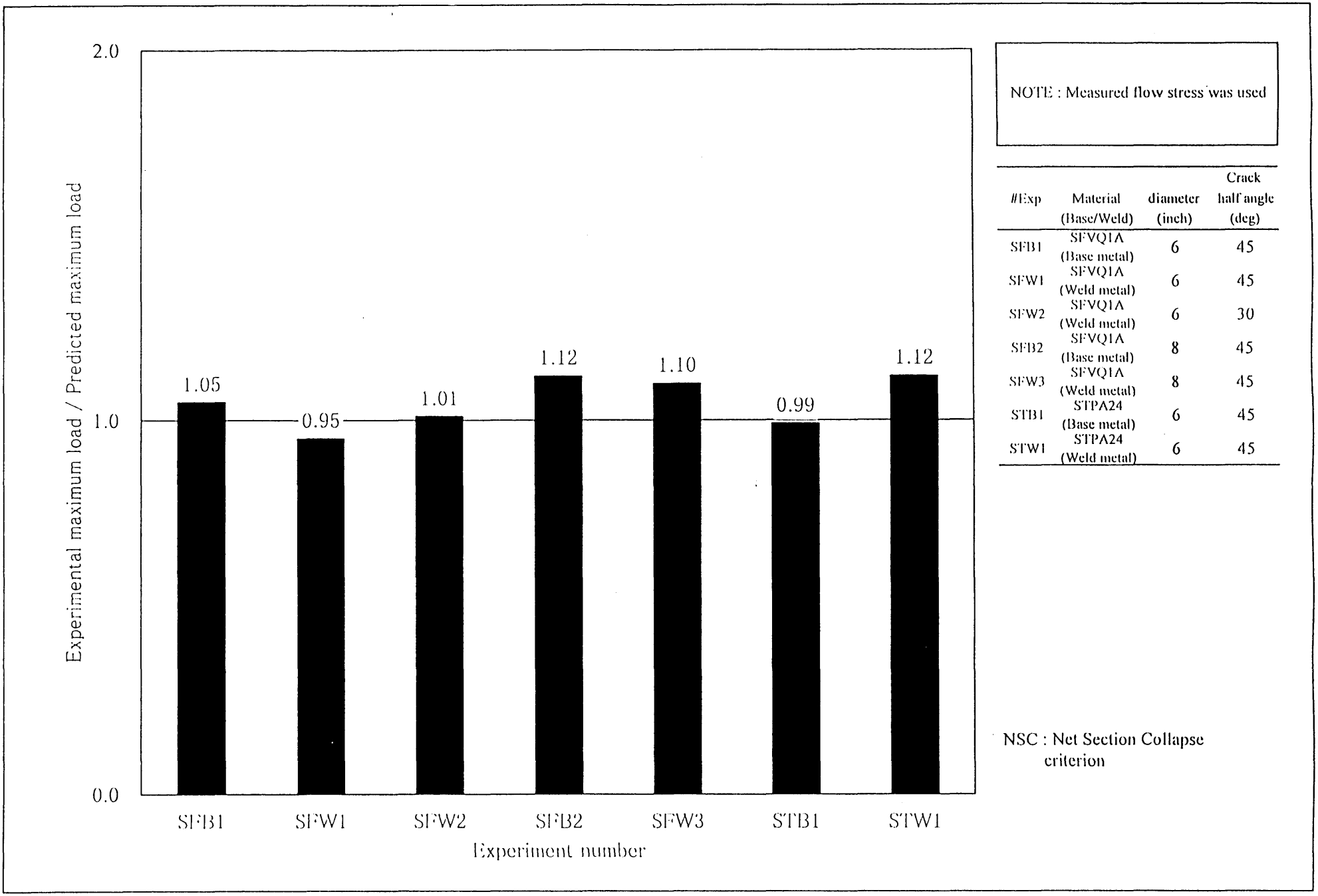


Fig.3.3-1 Normalized experimental maximum load by the predicted maximum load from NSC

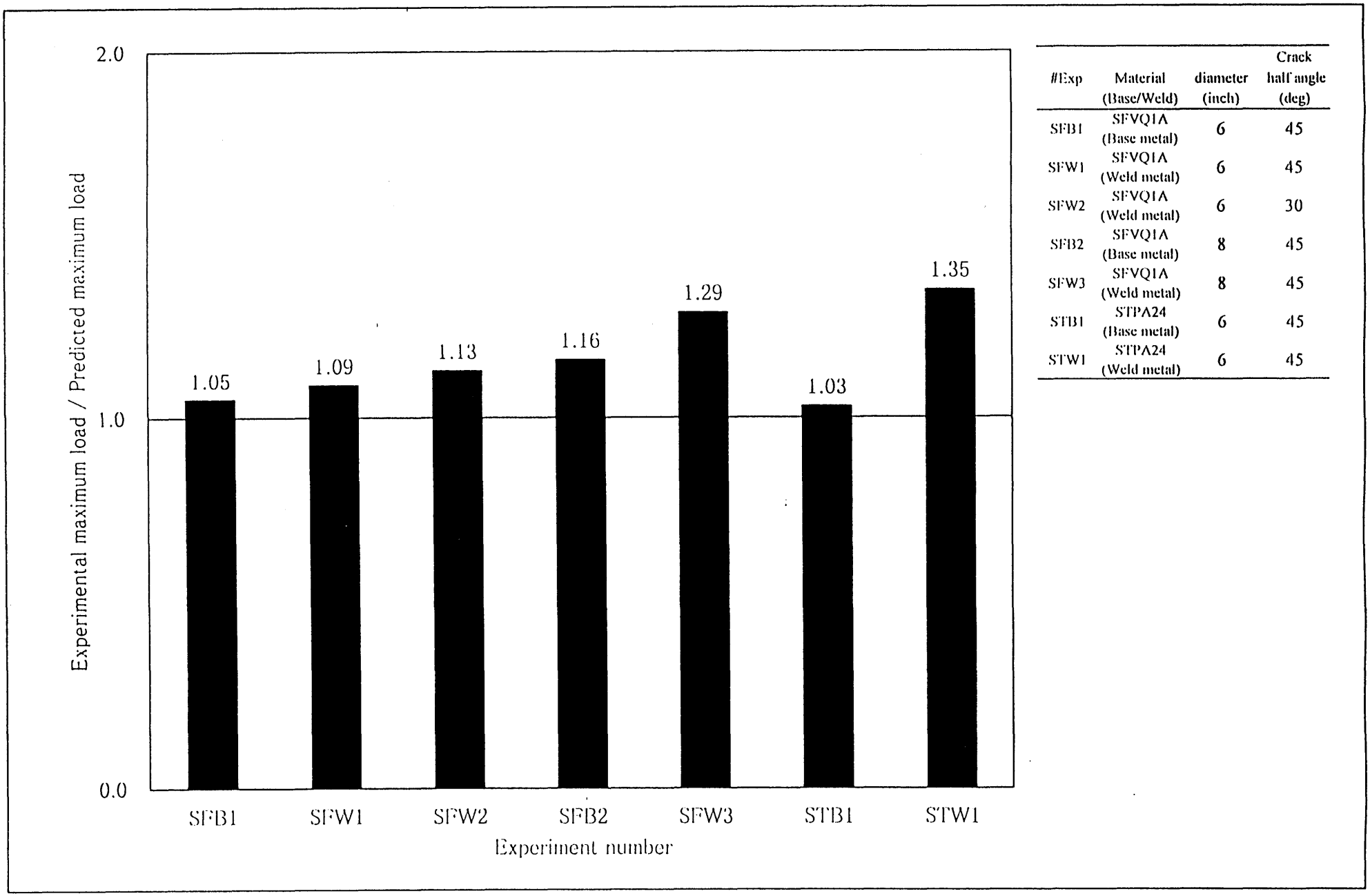


| #Exp | Material (Base/Weld) | diameter (inch) | Crack half angle (deg) |
|---|---|---|---|
| SFB1 | SFVQ1A (Base metal) | 6 | 45 |
| SFW1 | SFVQ1A (Weld metal) | 6 | 45 |
| SFW2 | SFVQ1A (Weld metal) | 6 | 30 |
| SFB2 | SFVQ1A (Base metal) | 8 | 45 |
| SFW3 | SFVQ1A (Weld metal) | 8 | 45 |
| STB1 | STPA24 (Base metal) | 6 | 45 |
| STW1 | STPA24 (Weld metal) | 6 | 45 |

Fig.3.3-2 Normalized experimental maximum load by the predicted maximum load from R6 Op.2

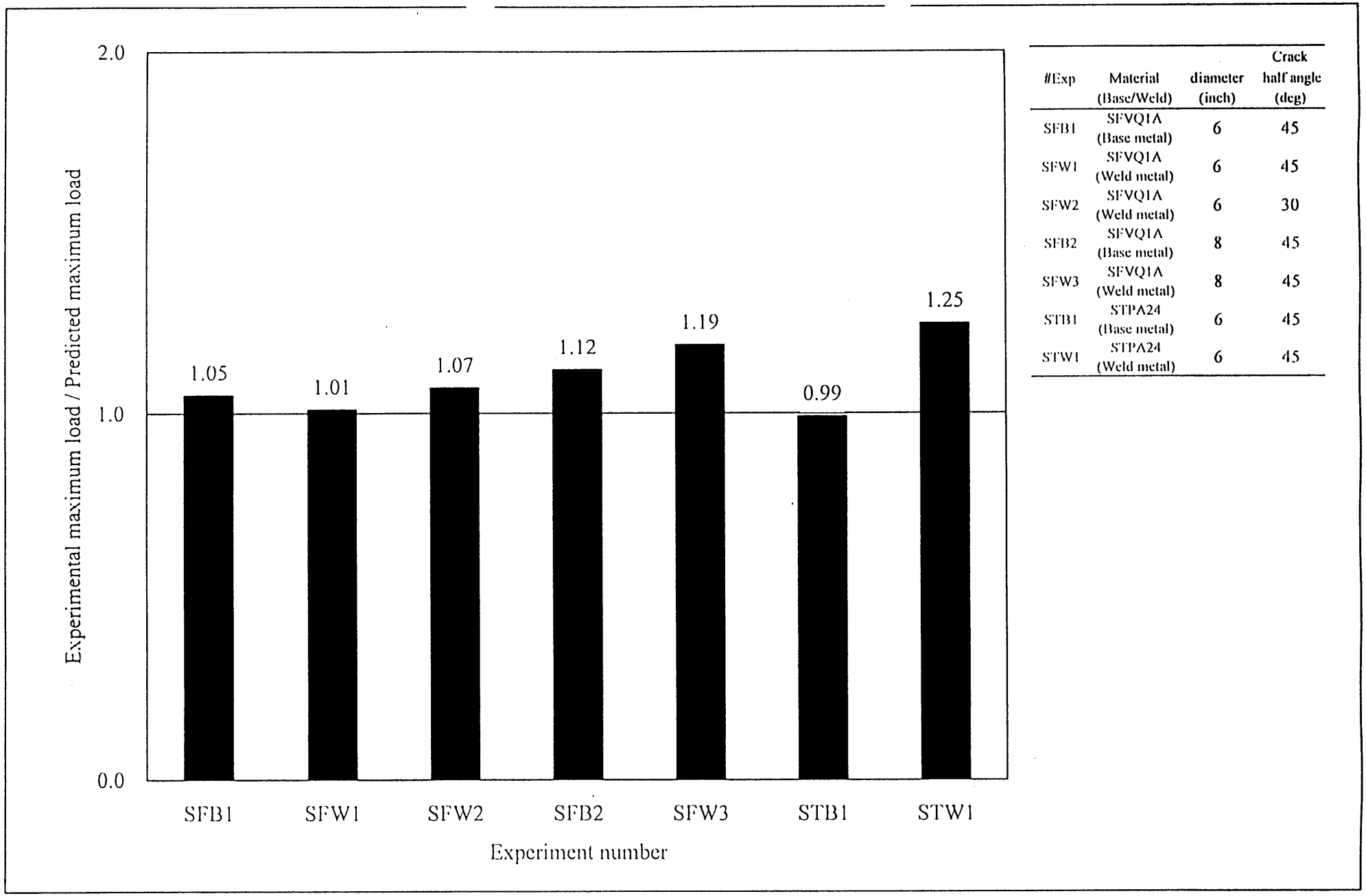


| #Exp | Material (Base/Weld) | diameter (inch) | Crack half angle (deg) |
|---|---|---|---|
| SFB1 | SFVQ1A (Base metal) | 6 | 45 |
| SFW1 | SFVQ1A (Weld metal) | 6 | 45 |
| SFW2 | SFVQ1A (Weld metal) | 6 | 30 |
| SFB2 | SFVQ1A (Base metal) | 8 | 45 |
| SFW3 | SFVQ1A (Weld metal) | 8 | 45 |
| STB1 | STPA24 (Base metal) | 6 | 45 |
| STW1 | STPA24 (Weld metal) | 6 | 45 |

Fig.3.3-3 Normalized experimental maximum load by the predicted maximum load from R6 Op.3

# Session V

# Material Characteristics

V-1 Effect of Reverse Cyclic Loading on Fracture Resistance Curves in CT Specimens

C. S. Seok, Sung Kyun Kwan University, Dept. of Mechanical Engineering, Korea

Y. J. Kim, Sung Kyun Kwan University, Dept. of Mechanical Design, Korea

J. I. Won, Sung Kyun Kwan University, Graduate School Dept. of Mechanical Design, Koera

# Effect of Reverse Cyclic Loading on the Fracture Resistance Curve in C(T) Specimen

**C.S.Seok[a], Y.J.Kim[a], J.I.Weon[a]**

**[a]School of Mechanical Engineering, Sung Kyun Kwan Univ., Suwon, Korea**

Fracture resistance (*J-R*) curves, which are used for elastic-plastic fracture mechanics analyses, are known to be dependent on the cyclic loading history. The objective of this paper is to investigate the effect of reverse cyclic loading on the *J-R* curves in C(T) specimens. Two parameters were observed to be effective on the *J-R* curves during the reverse cyclic loading. One was the minimum-to-maximum load ratio (*R*) and the other was the incremental plastic displacement ($\delta_{cycle}/\delta_i$), which is related to the amount of crack growth that occurs in a cycle. Fracture resistance test on C(T) specimens with varying the load ratio and the incremental plastic displacement were performed, and the test results showed that the *J-R* curves were decreased with decreasing the load ratio and decreasing the incremental plastic displacement.

Direct Current Potential Drop (DCPD) method was used for the detection of crack initiation and crack growth in typical laboratory *J-R* tests. The values of $J_i$ and $\delta_i$ were also obtained by using the DCPD method.

## 1. INTRODUCTION

This paper presents experimental results from cyclic displacement-controlled C(T) fracture tests. Seismic loading consists of dynamic loading and cyclic loading. According to a study by the International Piping Integrity Research Group (IPIRG) program[*1*], which pioneered the work on cyclic loading with C(T) and pipe specimens, the reverse cyclic loading was influenced by the parameters of load velocity, load ratio, and incremental plastic displacement. The reverse cyclic loading could contribute to the reduction of material's fracture toughness, i.e., *J-R* curve. This work is applicable to flawed-structure evaluations under seismic loading conditions, i.e. Leak-Before-Break (LBB) and in-service flaw evaluation criteria where seismic loading is addressed. In LBB and flaw evaluation criteria such as the ASME Section XI, the cyclic nature of the seismic loading is not implicitly accounted for on the potential effects on fracture toughness.

The objective of this paper is to study the effects of reverse cyclic loading on the nuclear piping integrity. In order to assess the effect of cyclic loading on fracture behavior, the experiments considering two different parameters were performed. One parameter is load ratio (*R*) and the other is incremental plastic displacement ($\delta_{cycle}/\delta_i$), which can be just as important as the load ratio parameter on the load-carrying capacity.

## 2. EXPERIMENTS

The test was performed at quasi-static loading rates. The detailed test procedure will be followed.

2.1 Material and specimen.

Material used in the test was SA 516 Gr. 70 carbon steel, which is used for nuclear piping. The chemical composition of the steel in weight percent is given by Table 1.

The specimens for tensile and fracture tests were cut from a rectangular plats. As specified in the ASTM E8[*2*] and E21[*3*], the tensile specimens were designed with 50.8-*mm* gauge length and 12.7-*mm* diameter. The specimens for the fracture toughness test were set to 1-in.-thick compact tension specimens in accordance with the ASTM E813. The crack plane of the compact tension specimens was set to the T-L orientation.

Table 1 Chemical composition of test material (Wt. %)

| C | Si | Mn | P | S | Cu | Ni | Cr | Sal | V | Nb |
|---|---|---|---|---|---|---|---|---|---|---|
| 0.21 | 0.33 | 1.06 | 0.019 | 0.003 | 0.02 | 0.01 | 0.02 | 0.031 | 0.016 | 0.004 |

2.2 Tensile and fracture test

A servo-hydraulic computer controlled material testing system was used. The test temperature was set to 288℃.

Table 2 summarizes tensile properties for SA 516 Gr. 70 carbon steel. Fig. 1 shows the schematic diagram of the fracture toughness test system. In order to measure load-line displacement, a high temperature capacitance type COD gauge was used. The DCPD method was used for measuring crack length and crack propagation. This system consists of a DC-power supply (30Amp.), pre-amplifier ($\times 10^4$), and filter (1*Hz* low pass filter).

The fracture toughness test procedure on cyclic loading is not clearly defined yet. Therefore, the fracture toughness test on cyclic loading was performed on the basis of the single specimen method specified in the ASTM E813[*4*] and E1152[*5*] for static fracture testing. The fatigue pre-cracking was preceded for a compact tension specimen in the same manner. According to the ASTM E813, the maximum load for pre-cracking was limited to prevent the influence of plastic deformation in case of the static fracture test. Under this load limit, the crack was extended to $a/w$=0.55. To produce the plane-strain condition, the pre-cracked C(T) specimens were 10% side grooved on each side with an edge angle of 45 °. The fracture resistance tests were performed by changing the load ratio of $R$ from 1 to -1. Fig. 2 shows the variation of load vs. load-line displacement for $R$=-1. To observe the variation of *J-R* curves with varying the incremental plastic displacement, $\delta_{cycle}/\delta_i$, the DCPD method was used. Fig. 3 shows the load vs. load-line displacement for $\delta_{cycle}/\delta_i$=1 and $R$=0. Firstly, the crack initiation displacement ($\delta_i$) was obtained from the load-line displacement vs. potential drop (voltage) curve as shown in Fig. 4. This crack initiation displacement was used for a criterion in determining the number of reverse cyclic loading for the fracture resistance tests.

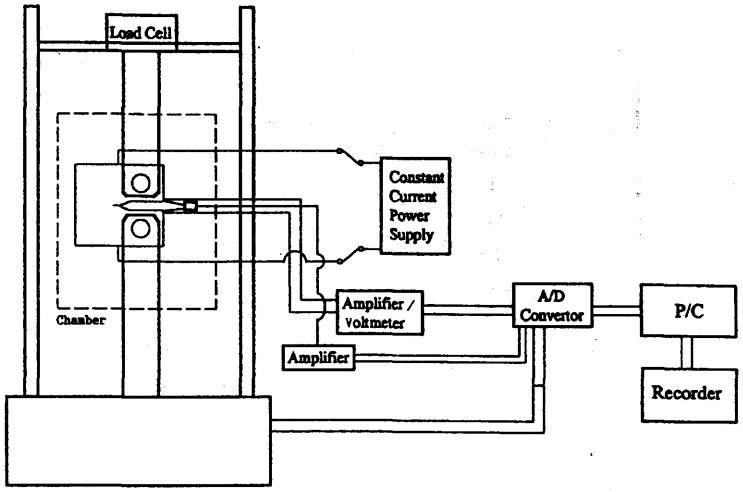


Fig. 1 Schematic diagram of the *J-R* test system

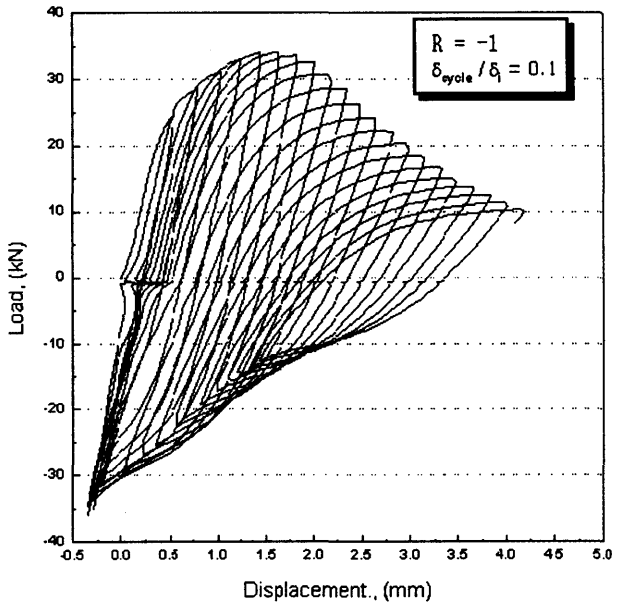


Fig. 2 Load vs. load-line displacement curve for cyclic load test ($R$=-1, $\delta_{cycle}/\delta_i = 0.1$)

## 2.3 Crack initiation[6 ~8]

DCPD method is one of the most accurate and sensitive techniques for detecting crack initiation. The Crack initiation during the tests was determined by plotting a linear line, so-called an E.P. blunting line, on the load-line displacement vs. potential drop curve, as illustrated in Fig. 4. In the beginning of the test, the crack tip area was controlled under

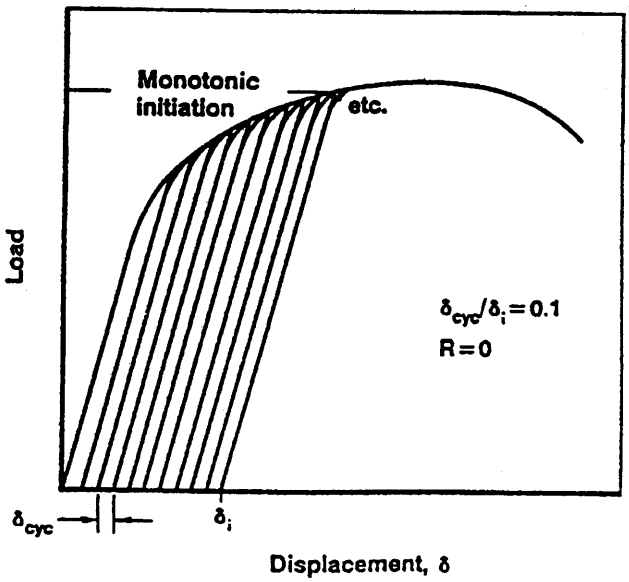


Fig. 3 Illustration of cyclic load test ($R$=0, $\delta_{cycle}/\delta_i$ = 0.1)

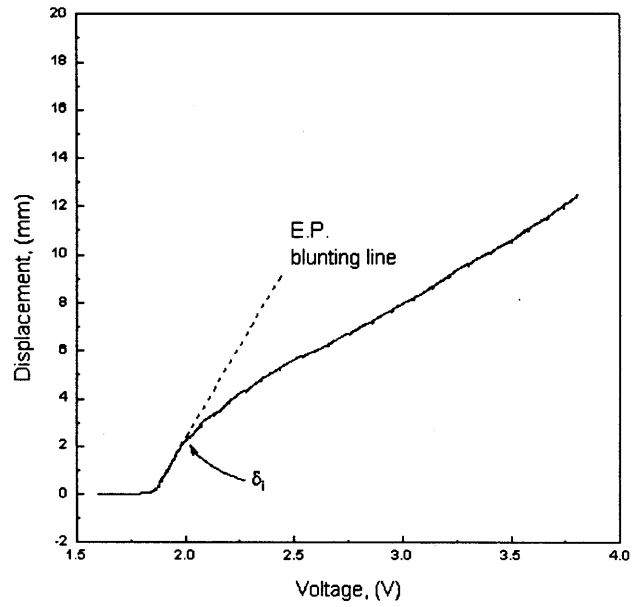


Fig. 4 Load-line displacement vs. EP data for SA 516 Gr. 70 steel

linear-elastic mode, and thus no change in the potential drop was observed. As the crack tip blunted with increasing load, a linear relation between the load-line displacement and the potential drop was observed up to the point of crack initiation. Therefore, the E.P. blunting line can be used to determine the crack initiation displacement ($\delta_i$). At the same time the value of $J$-integral corresponding to $\delta_i$ was proposed as $J_i$. In the present paper, the average value of crack initiation displacement determined with the monotonic loading was 0.92*mm*.

## 3. RESULTS

A summary of the fracture toughness test results performed at 288℃ was listed in Table 3. The *J-R* curves were fitted to a power-law equation, which is given by

$$J_R = C_1 (\Delta a)^{C_2}$$

The $C_1$ and $C_2$ values were obtained from the test and are also listed in Table 3.

In order to evaluate the effect of cyclic loading, the experiments were also conducted at quasi-static loading rates with a load ratio ($R$) ranging from -1 to 1. The effect of incremental plastic displacement was investigated by changing $\delta_{cycle}/\delta_i$ from 1/40 to 1/10 with a fixed load ratio of -1 considering the reverse cyclic loading condition.

Table 3 Summary of fracture toughness test results at 288℃

| Material | Strain Rate | Load Ratio ($R$) | Incremental Plastic Disp. ($\delta_{cycle}/\delta_i$) | $J_i$ ($kJ/m^2$) | $C_1$ | $C_2$ |
|---|---|---|---|---|---|---|
| SA 516 Gr. 70 | Quasi - Static | 1.0 | 1/10 | 313 | 345 | 0.35 |
| | | 0.5 | | 292 | 363 | 0.35 |
| | | 0.0 | | 262 | 323 | 0.33 |
| | | -0.3 | | 249 | 311 | 0.34 |
| | | -0.6 | | 182 | 239 | 0.31 |
| | | -0.8 | | 153 | 215 | 0.35 |
| | | -1.0 | | 134 | 180 | 0.28 |
| | | -1.0 | 1/5 | 134 | 191 | 0.35 |
| | | | 1/20 | 98 | 142 | 0.33 |
| | | | 1/30 | 85 | 121 | 0.30 |
| | | | 1/40 | 77 | 107 | 0.27 |

### 3.1 Effect of load ratio on C(T) specimens

The experimental results were presented in Fig. 5 in terms of *J*-integral with increasing crack extension. In these tests, only the load ratio was varied for 7 different values covering monotonic loading ($R$=1), $R$=0.5, $R$=0, $R$=-0.3, $R$=-0.6, $R$=-0.8, and $R$=-1 with a fixed incremental plastic displacement of $\delta_{cycle}/\delta_i$ = 0.1. The resulting *J-R* curves show that the *J* values are significantly reduced with decreasing the load ratio in the range of $\Delta a < 0.2(W-a_i)$. However, the decrease in the fracture resistance curve between $R$=1 and $R$=0.5 was not evident. This result proves the validity of ASTM E1152 requirement

which restricts the amount unloading up to 50% of the current load. Fig. 6 shows the $J_i$ values observed from the tests with 7 different load ratios. The corresponding $J_i$ value, the $J$-integral at crack initiation, was normalized by the $J_i$ value under monotonic loading condition. The normalized $J_i$ value was decreased with decreasing the load ratio. The $J_i$ value was about 60 percent of one for monotonic loading condition when the load ratio reached -0.6. When the load ratio reached -1, the *Ji* value was about 40 percent of one for monotonic loading condition.

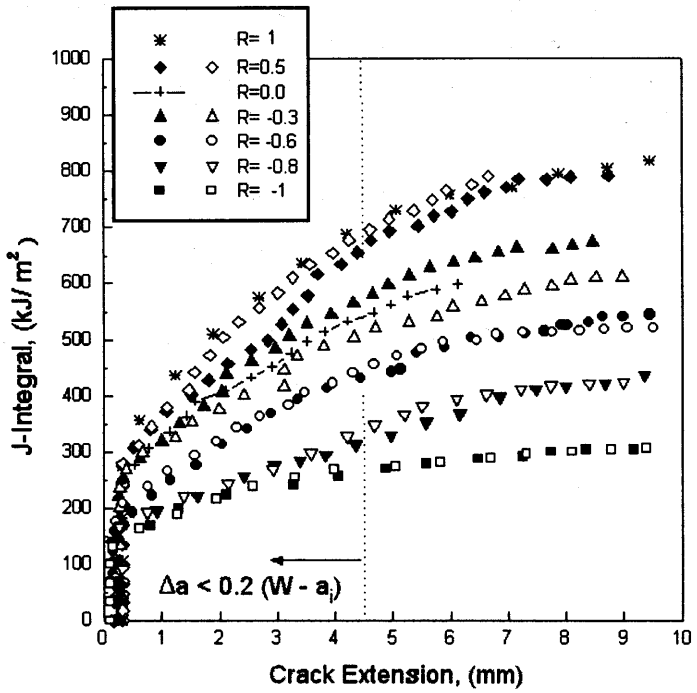


Fig. 5 Cyclic *J-R* curves for SA 516 Gr. 70 steel at 288℃ ($\delta_{cycle}/\delta_i$ =0.1)

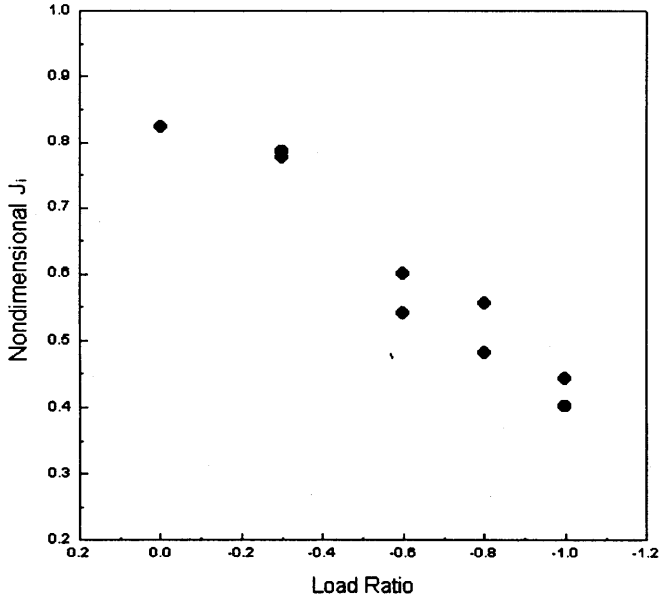


Fig. 6 Effect of load ratio for $J$ at crack initiation ($\delta_{cycle}/\delta_i$ =0.1)

3.2 Effect of incremental plastic displacement on C(T) specimens

The resulting *J*-integral vs. crack extension behavior was presented in Fig. 7. The experiments were also conducted at quasi-static loading rates, and the incremental plastic displacement, $\delta_{cycle}/\delta_i$, was set to 4 different values of 1/10, 1/20, 1/30, and 1/40 with a fixed load ratio of -1. The resulting *J-R* curves showed a decreasing tendency of *J*-integral values with decreasing the $\delta_{cycle}/\delta_i$ in the range of $\Delta a < 0.2(W-a_i)$. In particular, the *J-R* curves were considerably decreased when the $\delta_{cycle}/\delta_i$ value was changed from 1/10 to 1/20. Fig. 8 shows the variation of the $J_i$ value with decreasing the incremental plastic displacement. In this Fig., the corresponding $J_i$ value was normalized by the $J_i$ value for $\delta_{cycle}/\delta_i$=1/10. The normalized $J_i$ value was apparently decreased with a decrease in the incremental plastic displacement as shown in Fig. 8.

3.3 Discussion

It was observed from the tests that the *J-R* curves and the $J_i$ values were decreased with decreasing the load ratio and the incremental plastic displacement as shown in Figures 5 to 8. In general, the value of *J*-integral is measured from the load vs. load-line displacement curve. For the monotonic loading, the area defined as $A_{(BCD)}$ in Fig. 9 is used for the *J*-integral calculation. However, the phenomenon of crack opening and crack closure observed from the reverse cyclic loading test is quite different from the monotonic loading test as illustrated in Fig. 9. While the crack opening is occurred at point *B* for the monotonic loading, it occurred at point *A* for the reverse cyclic loading condition. Therefore, the value of *J*-integral which is the actual energy consumed with

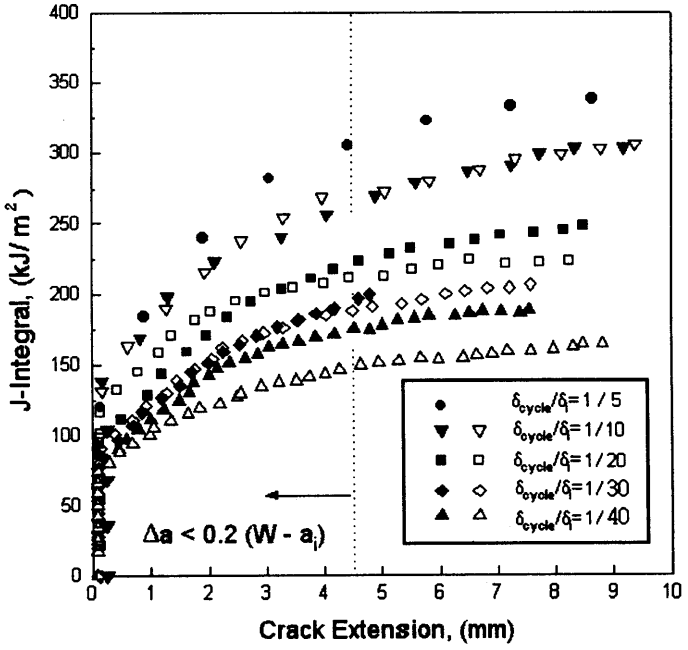


Fig. 7 Cyclic *J-R* curves for SA 516 Gr. 70 steel at 288℃ ($R$=-1)

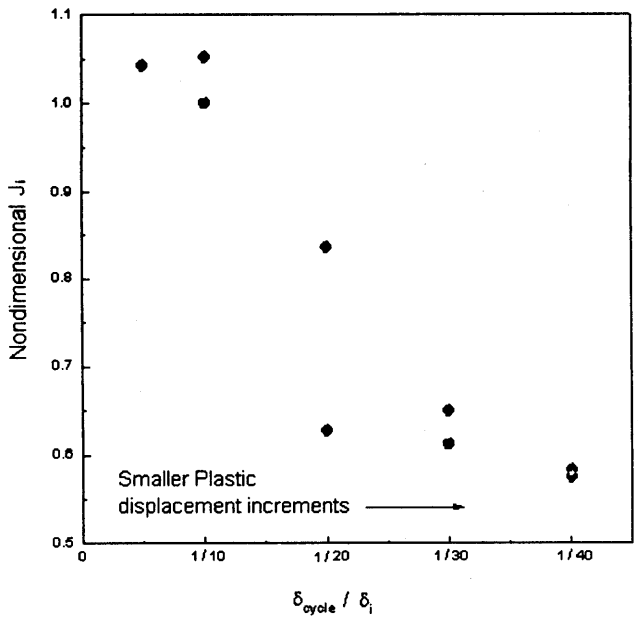


Fig. 8 Effect of incremental plastic displacement for $J$ at crack initiation ($R$=-1)

crack growth must be measured from the area specified as $A_{(ABCDE)}$ covering the point $P_{open}$ rather than $A_{(BCD)}$. In other words, calculating the $J$-integral for the reverse cyclic loading based on the area $A_{(BCD)}$ will underestimate the $J$-integral which should consider the area $A_{(ABDE)}$ to account for the effect of reverse cyclic loading. It will be one of reasons of decreasing the $J$-$R$ curves under the reverse cyclic loading. Therefore, the way of $J$-integral calculation for the reverse cyclic loading should be studied further regarding both tensile and compressive loading condition.

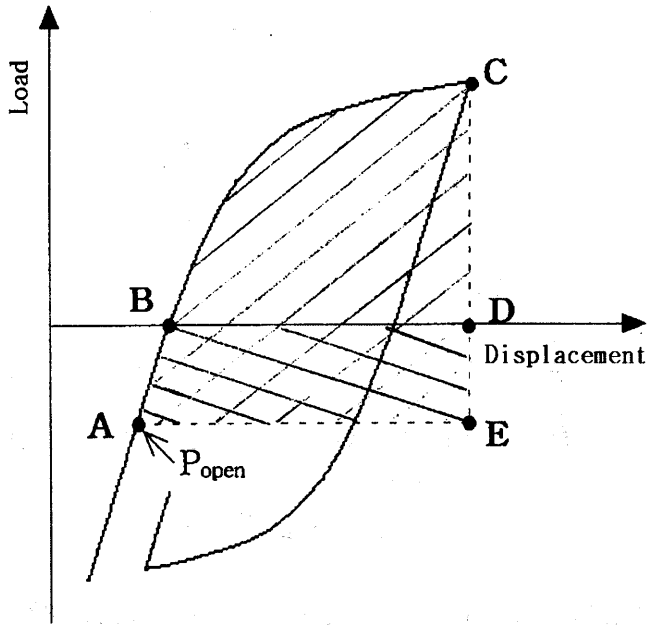


Fig. 9 Definition of area for the $J$ calculation under reverse cyclic loading

## 4. CONCLUSIONS

This paper presented the fracture resistance test results regarding the effect of reverse cyclic loading in C(T) specimens. The conclusions are summarized as follows:

(1) For the SA 516 Gr. 70 carbon steel, the *J-R* curves and the $J_i$ value were decreased with decreasing the load ratio and the incremental plastic displacement, respectively.

(2) When the load ratio was set to -1, the resulting *J-R* curves and the $J_i$ value were about 40～50 percent of those for the monotonic loading condition.

(3) In calculating *J*-integral under the reverse cyclic loading, both tensile and compressive loading should be considered. A further study on the test procedure regarding the reverse cyclic loading is recommended.

## 5. REFERENCE

[1] P. Scott, G. Kramer, P. Vieth, R. Francini, and Gery M. Wilkowski, The Effect of Dynamic and Cyclic Loading During Ductile Tearing on Circumferentially Cracked Pipe: Experimental Results, ASME PVP Vol. 280 (1994) 207～220.
[2] Standard Test Methods of Tension Testing of Metallic Materials, ASTM E8.
[3] Standard Test Methods for Elevated Temperature Tension Tests of Metallic Materials, ASTM E21.
[4] Standard Test Method for JIC, A Measure of Fracture Toughness, ASTM E813.
[5] Standard Test Method for Determining J-R Curves, ASTM E1152.
[6] G. M. Wilkoski, J. O. Wambaugh, and K. Prabhat, Single Specimen J Resistance Curve Evaluation Using the Direct-Current Potential Drop Method and Computerized Data Acquisition System, Fracture Mechanics : 15th Symposium, ASTM STP 833 (1984) 553～576.
[7] M. G. Vassilaros, and E. M. Hackett, J-Integral R-Curve Testing of High Strength Steels Utilizing the Direct-Current Potential Drop Method", Fracture Mechanics : 15th Symposium, ASTM STP 833 (1984) 535～552.
[8] Ad. Bakker, A DC Potential Drop Procedure for Crack Initiation and R-Curve Measurements During Ductile Fracture Tests, Elastic-Plastic Fracture Test Method, ASTM STP 856 (1985) 394～410.

V-2 The Frequency Effect on the Fatigue Crack Growth Rate of 304 Stainless Steel

Jien-Jong Chen & Yan-Shin Shih, Institute of Nuclear Energy Research Atomic Energy Council, Taiwan, Republic of China

# The frequency effect on the fatigue crack growth rate of 304 stainless steel

Jien-Jong Chen[a,b] and Yan-Shin Shih[b]

[a] Nuclear Division of Institute of Nuclear Energy Research, Box 3-3, Lung-Tan, Taoyuan Taiwan, Republic of China

[b] Mechanical Engineering , Chung-Yuan Christian University ,Chung-Li 32023,Taiwan,Republic of China

## ABSTRACT

Under cyclic loading condition, the fatigue crack growth (FCG) rate governed by stress intensity factor and stress ratio is well known. Walker's equation, Forman's equation and Elber's equation are the typical formulae of the FCG rate. However, the loading frequency effect on the FCG rate is still need to explore. The behavior of loading frequency effect has been studied on some of the visco-elastic material recently, and gives a more clear aspect of the frequency effect on the FCG rate. In physical sense, The knowledge is still lacking on for the loading frequency effect on the FCG rate for the 304 stainless steel. James had provided a lot of experiments, through the data analysis, he suggested an evaluation equation which is merely based upon the experimental illustration. In this study, the alternation of physical properties of the material under various loading frequency is used to illustrate the modification of FCG rate, and a new formula based upon modified Forman's equation has been provided.

## 1. Introduction

The modified Forman's equation(Forman et. al. ., 1992) which accounts the stress

intensity factor range, the mean stress level and other important parameters is one of the best formula for all the fatigue crack growth analysis. This equation is shown as following:

$$\frac{da}{dN} = \frac{C\Delta K^n[\Delta K - \Delta K_{th}]^p}{[(1-R)K_C - \Delta K]^q} \tag{1}$$

where $C$, $n$, $p$, $q$ are material constants, $R$ is stress ratio, $\Delta K_C$ is the critical stress intensity factor, and $\Delta K_{th}$ is threshold of stress intensity factor. Therefore, the modern codes of FCG analysis, such as NASA/FLAGRO(EMT,1995), NASCRACK(FAA, 1994), etc., have already incorporated this model to evaluate FCG rate of structural components. However, the FCG is a very complicated subject which can be affected by material properties, loading history, global structure with local crack geometry and environmental condition, *etc.* Hence, in the fatigue life analysis of machine components, there are still somewhat difference between predictions and experimental data. For experimental result, a great mount of these deviations may be caused by different testing conditions. Hence. considering as many as the important parameters into evaluation formula is still as a major topic for fatigue life assessment. Many of the modern structures may be operated for a wide range of loading frequency, and fatigue failure occurs during their service life. Therefore, the effect of cyclic loading frequency on the FCG rate is as an important research subject.

In the review by James(James, 1985), beside of the stress intensity factor, the FCG rates are precisely affected by some other parameters, and the cyclic loading frequency is a significant one of all the important parameters. However, due to the complicated interaction between material and loading, the behavior of the loading frequency effects on the FCG rate is still not clear.

In the analysis of FCG rate with loading frequency effect, there are two approaches have been published in the literature. One constructs the model of FCG rate with the frequency effect by analyzing experimental data, the other explains the underlying reason of cyclic loading frequency. From experimental data, the increasing the loading frequency generally decreases the FCG rate for various materials. In early 70's, a power law of loading frequency was added to the model by Mukherjee (Mukherjee, 1971)

$$\frac{da}{dN} = C_0 f^{-\lambda} (\Delta K)^n \tag{2}$$

where $f$ is loading frequency, $C_0, \lambda$ and $n$ are constants for a given combination of the material, temperature and environments. This model has also been adopted by Solomon and Coffin ( Solomon et. al., 1973), James (James 1979), Plumtree and Schafer (Plumtree et. al., 1984), and Yokobori and Sato (Yokobori et. al., 1976). Alternatively, James (James 1985) performs a curve fitting of experimental data, and suggested a formula as follow,

$$\frac{da}{dN} = C_0 F(\Delta K)^n \tag{3}$$

$$\log(F) = B_0 + B_1 X + B_2 X^2 + B_3 X^3 \tag{4}$$

where $F$ is frequency correction factor, $B_0, B_1, B_2$ and $B_3$ are fitting constants, and X is logarithm of the frequency in cycle/min. This approach gives a closely fitting with experimental data. Recently, some experimental datum show that a portion of FCG rate curve is independent of cyclic loading frequency. Hence, a new concept on critical frequency was presented by Makhlouf and Jones (Makhlouf, 1993) They accomplished a series of experiments on 18%-Cr. ferritic stainless steel with various

frequency at elevated temperature, a step function of relationship was presented as follows

$$\frac{da}{dN} = C\left(\frac{f}{f_c(T)}\right)(\Delta K)^n \quad \text{for} \quad f \le f_c \tag{5}$$

$$\frac{da}{dN} = C(\Delta K)^n \quad \text{for} \quad f > f_c \tag{6}$$

where $f_c(T)$ is a critical loading frequency on each temperature, such as $f_c(655\,^oC)$ is closed to 60 cpm and $f_c(500\,^oC)$ is near by 3 cpm.

For the underlying reason of loading frequency effect can be speculated by Yokobori and Kamei (Yokobori et. al., 1975) who use dislocation dynamic theory to analyze the behavior of strain rate sensitivity of material and derive the relationship as follow,

$$\frac{da}{dN} = C_0 f^{-\frac{m+1}{m+2}}(\Delta K)^{\frac{m+1}{m+2}} \tag{7}$$

where m is the exponent in the dislocation velocity equation $v = v_0(\tau_a / \tau_0^*)^m$, $\tau_a$ is applied shear stress, $\tau_0^*$ is a constant which represents the stress required to give $v = 1$ cm/sec. This equation reaches the same form as eq.(2), and can be regarded as physical basis of the power law equation, but the exponents of frequency and stress intensity factor in Yokobori's formula have the same value with negative sign is hard to confirm with experiments data.

The object of the present investigation is to study the effect of frequency on FCG rate of 304 stainless steel. A new FCG rate model is developed based on Modified Forman equation for better prescribing the loading frequency effect on FCG rate, it can not only offer closer prediction on FCG rate but also with physical in sense.

## 2. Data acquisition and analysis

The experimental FCG rate analysis of 304 stainless steel has been carried out by several authors (James et. al.,1971, Ohta et. al.1978, Hudson et. al. 1978,1982,1989,1991) for investigating the effect of the various parameters. All of the experimental data used in this analysis is obtained from the open literature. To avoid the loading hold time effect, most of the adopted data was generated by sawtooth loading waveform with a loading/unloading ratio of 7.78. The total FCG rate with different loading frequency versus stress intensity factor range is shown in Figure 1.

The datum appeared on various articles were shown with several typical forms and units. These basic raw datum are treated by using Forman's equation, firstly. For minimizing the effect of stress ratio, critical stress intensity factor and threshold of stress intensity factor, the crack growth rate can be expressed into the similar form with Paris equation and shown as following,

$$\frac{da}{dN}\frac{[(1-R)K_C-\Delta K]^q}{[\Delta K-\Delta K_{th}]^p}=C\Delta K^n \tag{8}$$

## 3. Loading Frequency Analysis

From the constructed raw data, the coefficients C and n in eq. (8) for different loading frequency can be calculated and shown in Table 1. The power coefficient, n, for different loading frequencies in Table 1 is very similar. Therefore, one may assume the power coefficient be not affected by loading frequency. A mean pwer coefficient has been determined using the following relation:

$$n_{MEAN}=\frac{\sum n\cdot M}{\sum M}=3.13546 \tag{9}$$

where n and M are the power coefficient and number of data with this power coefficient.

By the curve fitting of eq. (8) for all experimental datum, C and n are obtained, and the result shown in Fig. 2, One can find that the n value is the same as eq(9). To reduce the error of simulation, one considers that C depends on loading frequency, The new fitting material constant $C^*$ based on the power exponent of value 3.13546 can be obtained and shown in Table 2.

In the analysis of FCG rate with frequency effect, increasing the loading frequency increases dislocation density and decreases FCG rate. From mention above, the FCG rate can be expressed as a form of power exponent. Hence, a modified power law has been proposed as,

$$\frac{da}{dN} = \frac{C\Delta K^n [\Delta K - \Delta K_{th}]^p}{[(1-R)K_C - \Delta K]^q} \left(\frac{f}{f_{ref}}\right)^m \tag{10}$$

where $f_{ref}$ is a reference state loading frequency, and 2 cpm is used in this study.

**4. Result and Discussion**

The material constant ratio ($C^* / C^*_{ref}$) with respect to loading frequency ratio is shown as Figure 3, where $C^*_{ref}$ is the material constant of the reference state. One may fins that increasing the loading frequency ratio decreases the material constant ratio, and the material constant approaches to a low bound value 0.5 while f >3000 cpm. This feature reach the same conclusion with Makhlouf (Makhlouf, 1995). The curve fitting equation of the material constant ratio is shown as,

$$\frac{C^*}{C^*_{ref}} \propto \left(\frac{f}{f_{ref}}\right)^{-0.0802} \tag{11}$$

Substituting into equation (10), one obtains

$$\frac{da}{dN} = \frac{C^*_{ref}\Delta K^n[\Delta K - \Delta K_{th}]^p}{[(1-R)K_C - \Delta K]^q}\left(\frac{f}{f_{ref}}\right)^{-0.0802} \quad (12)$$

The fatigue crack growth rates for different loading frequency by James, eq. (12) and experimental data are shown in Figure 4-6. A closer fitting has achieved by the present model.

## 5. Conclusion

The wide-range loading frequency effect on 304 stainless steel at room temperature has been studied, and a new modification based on modified Forman's equation is also provided . Some conclusion are made as follows.

1. A new equation is proposed to replace the modified Forman's equation for counting the loading frequency effect on FCG rate. The deviation between James and new equation are very small.
2. Below the critical loading frequency, the FCG rate increased slightly with decreasing loading frequency at room temperature, this is caused by the higher strength feature of 304 stainless steel at room temperature.
3. The lower bound of FCG rate exists while $f > f_c$.

## Acknowledgment

This work was supported by National Science Council, Taiwan, Republic of China under grant number NSC-86-2212-E-033-004.

## Reference

Engineering Mechanics Technology, Inc., 1995. NASA/FLAGRO-Fatigue Crack Growth Computer Program Version 2.0, published by Engineering Mechanics Technology, Inc.

Failure Analysis Associates, Inc., 1994. NASCRAC-NASA Crack

Analysis Code. Version 3.0, published by Engineering Mechanics Technology, Inc.

Forman, R. G., Mettu,S. R., 1992. Behavior of surface and corner cracks subjected to tensile and bending loads in a Ti-6Al-4V alloy, Fracture Mechanics 22'th Symposium(Volume 1),ASTP STP 1131, Ernst, H. A., Saxena, A., McDowell, D.L., Eds., American Society for Testing and Materials, Philadalphia, pp. 519-646.

Hudson C. M., 1978. "Fracture Toughness and Fatigue Crack Growth for Metallic Alloys-Part I" International Journal of Fracture, Vol. 14, pp. R151-R184.

Hudson C. M., 1982. "Fracture Toughness and Fatigue Crack Growth for Metallic Alloys-Part II" International Journal of Fracture, Vol. 20, pp. R59-R117.

Hudson C. M., 1989. "Fracture Toughness and Fatigue Crack Growth for Metallic Alloys-Part III" International Journal of Fracture, Vol. 39, pp. R43-R63.

Hudson C. M., 1991. "Fracture Toughness and Fatigue Crack Growth for Metallic Alloys-Part IV" International Journal of Fracture, Vol. 48, pp. R19-R43.

James L.A., 1979. Frequency effects in the elevated temperature crack growth behavior of austenitic stainless steel -A design approach, Journal of Pressure Vessel Technology-Transactions of the ASME, Vol. 101, pp. 171-176.

James L. A., Jones D. P., 1985. "Fatigue Crack Growth Correlations for Austenitic Stainless Steels in Air", in Conference on "Predictive Capabilities in Environmentally Assisted Cracking. (Presented at the Winter Annual Meeting of the American Society of Mechanical Engineers.), ASME PVP Vol. 99, pp. 353-414.

James L.A., Schwenk E. B.,1971. Fatigue-crack propagation behavior

of Type 304 stainless steel at elevated temperature", Metallurgical Transactions of ASME, Vol. 2, pp. 491-496.

Makhlouf K. & Jones J.W., 1993. "Effect of Temperature and Frequency on Fatigue Crack Growth in 18% Cr. Ferritic Stainless Steel", International Journal of Fatigue, Vol. 15, No. 3, pp. 163-171.

Mukherjee B., & Burns D. J., 1971. Fatigue-crack growth in polymehylmethacrylate, Experimental Mechanics, Vol 11, pp. 433-439

Ohta A., Kosuge M. and Sasaki E., 1978. "Fatigue Crack Closure over The Range of Stress Ratios from -1 to 0.8 Down to The Stress Intensity Threshold Level in HT80 steel and SUS 304 Stainless Steel" International Journal of Fracture, Vol. 14, pp. 251-264

Plumtree A. & Schafer S., Waveform and frequency effects on the high temperature fatigue crack propagation rate of stainless steel" in Advances in Fracture Research (Fracture 84), VOL. 3. Published by Pergamon Press, Oxford, England New York, USA, pp. 2249-2256.

Solomon H.D. & Coffin L.F , 1973. Effect of frequency and environment on fatigue crack growth in A286 at 1100 F, in Fatigue at Elevated Temperature, Edited by Carden A.E. et. al., ASTM-STP 520 , Philadelphia, pp. 112-122.

Yokobori T. & Sato K., 1976. " The effect of frequency on fatigue crack propagation rate and striation spacing in 2024-T3 Aluminum alloy and SM-50 steel", Engineering Fracture Mechanics, Vol. 8, No. 1, pp. 81-88.

Yokobori T., Yokobori A. T., Jr. and Kamei A., 1975. "Dislocation Dynamics Theory for Fatigue Crack Growth", International Journal of Fracture, Vol. 11, No. 5, pp. 781-788

Table 1: The material constant of FCG of various loading frequency

| Loading frequency | C | n |
|---|---|---|
| 2 | 3.28537E-10 | 3.05656 |
| 4 | 1.55656E-10 | 3.14924 |
| 180 | 1.42886E-10 | 3.76247 |
| 400 | 1.95333E-10 | 3.07387 |
| 600 | 4.46146E-10 | 2.76236 |
| 3000 | 5.02579E-10 | 3.53131 |

Table 2 : The material constant $C^*$

| Loading Frequency (CPM) | Material Constant $C^*$ |
|---|---|
| 2 $(f_{ref})$ | 2.4561E-10 $(C^*_{ref})$ |
| 4 | 1.6619E-10 |
| 180 | 1.25698E-10 |
| 400 | 1.61628E-10 |
| 600 | 1.57514E-10 |
| 3000 | 1.4127E-10 |

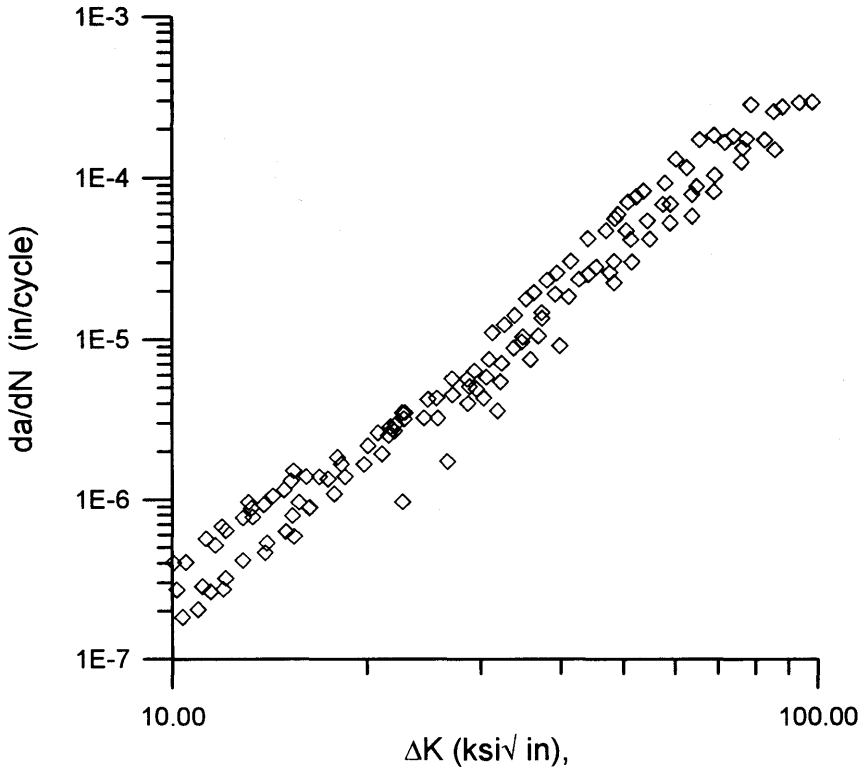


Figure 1 : The total FCG rate data for 304 stainless steel of various loading frequency and 75°

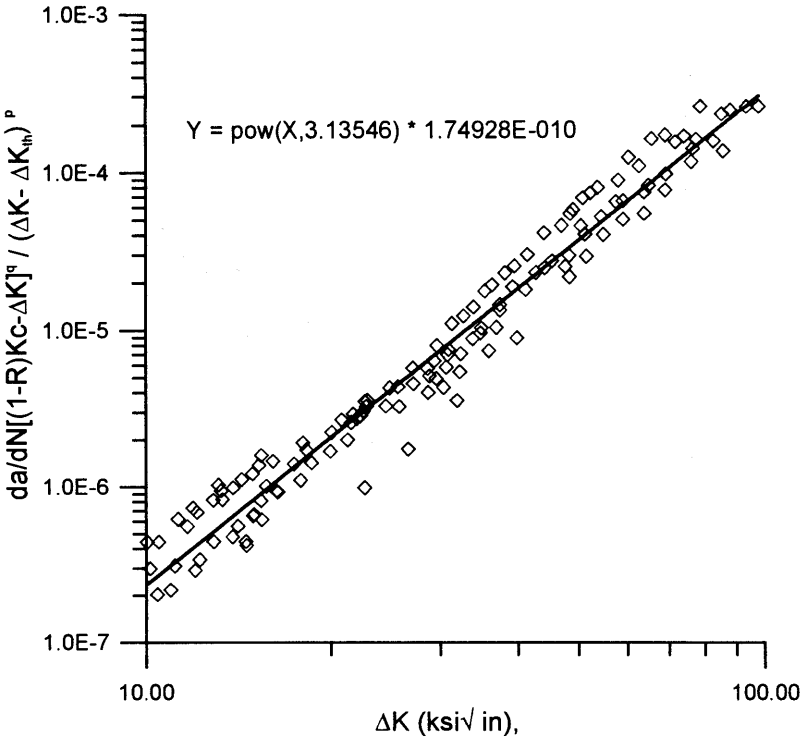


Figure 2 : The mean slope of the total FCG rate data for 304 stainless steel.

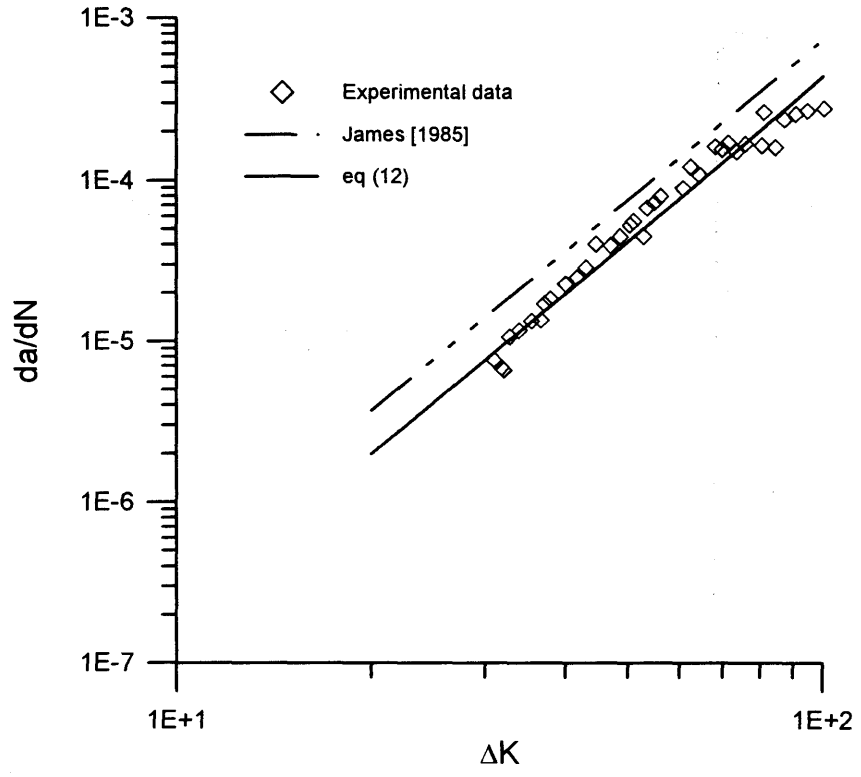


Figure 4 : The fatigue crack growth rate for SS 304 on 2 cpm of loading frequency and 75°F

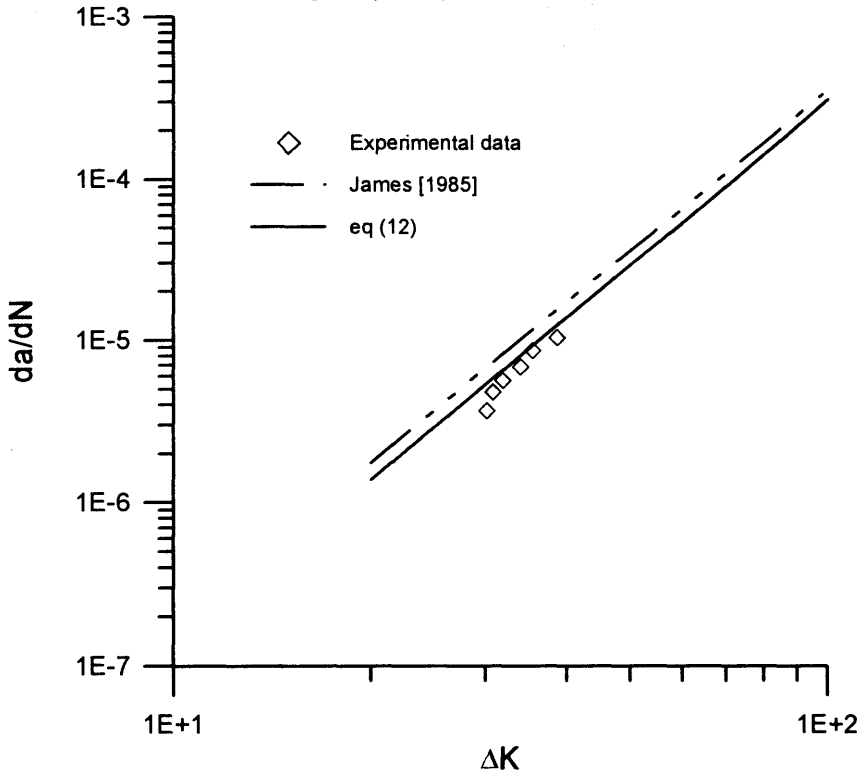


Figure 5 : The fatigue crack growth rate for SS 304 on 180 cpm of loading frequency and 75°F

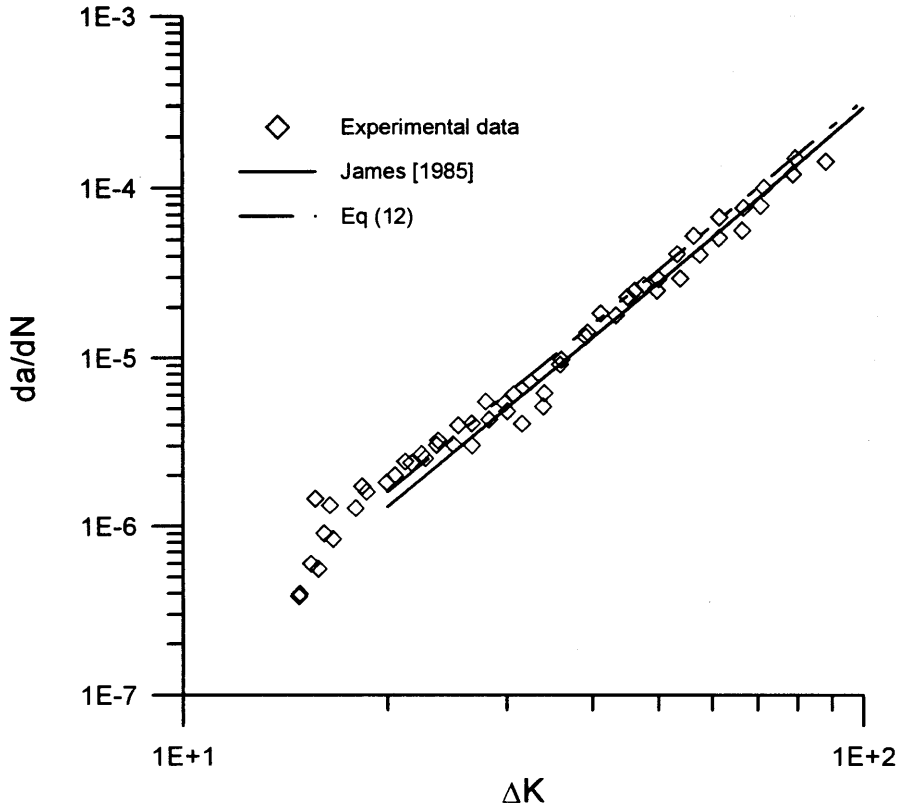


Figure 6 : The fatigue crack growth rate for SS 304 on 400 cpm of loading frequency and 75°F

V-3 Investigation on Fracture Toughness Evaluation Method for Reactor Pressure Vessel Surveillance

Kunio Onizawa, Tohru Tobitz & Masahide Suzuki,
Reactor Component Reliability Laboratory, Japan Atomic Energy Research Institute, Japan

# Investigation on Fracture Toughness Evaluation Method for Reactor Pressure Vessel Surveillance

Kunio ONIZAWA*, Tohru TOBITA and Masahide SUZUKI

*Reactor Component Reliability Laboratory, Japan Atomic Energy Research Institute, Tokai-mura, Naka-gun, Ibaraki-ken, 319-1195, Japan*

**Abstract**

To evaluate cleavage fracture toughness in the ductile-brittle transition range of RPV steels, the applicability of precracked Charpy-v (PCCv) specimens has been investigated. An approach based on the weakest link theory was applied to analyze the specimen size effect and the scatter of fracture toughness values. Four kinds of ASTM A533B class 1 steels made by Japanese steel makers were used.

The specimen size effect on cleavage fracture toughness was clearly seen among PCCv, 1T-CT and 4T-CT specimens. To obtain the equivalent data from PCCv specimens to 1T-CT specimens, the size correction scheme based on the weakest link theory was applied to the PCCv data. The scatter of fracture toughness values was considered to have a Weibull type distribution. Irradiation effect on the scatter was shown to be insignificant. The fracture toughness transition curves were determined by PCCv data according to the draft ASTM and the JEAC. The shift of the master curve by irradiation was somewhat greater than the Charpy 41J shift. The scheme for the estimation of lower bound fracture toughness was also studied.

## 1. INTRODUCTION

The brittle fracture of an RPV must be prevented, because it may lead to a catastrophic fracture of the vessel followed by severe accident. Therefore, the RPV is operated at higher temperature than the ductile-to-brittle transition temperature of the RPV steel. However, fast neutrons from the reactor core during operation can cause the increase of the transition temperature, i.e., the irradiation embrittlement. To assure the structural integrity of an RPV throughout the operational life, the fracture toughness after neutron irradiation are needed. To do this, the surveillance program for the RPV is performed according to a certain code and regulation. The results obtained from the Charpy impact tests according to the codes are used for the estimation of fracture toughness after irradiation[1, 2]. Most of the codes assume that the degree of irradiation embrittlement obtained from Charpy impact tests are equivalent to that of fracture toughness for the material concerned. Recent research, however, has indicated that the correlation is not always conservative in predicting the degree of irradiation embrittlement in terms of fracture toughness[3,4]. Fracture mechanics methodology is, therefore, necessary for the precise evaluation of irradiation embrittlement to assure the structural integrity of an RPV.

A methodology to evaluate fracture toughness of RPV steels has not been established

* Corresponding author. Tel: +81 29 282 5147; Fax: +81 29 282 5406;
e-mail: konizawa@popsvr.tokai.jaeri.go.jp

completely, particularly in the transition range. As the fracture toughness values from test specimens of the RPV steel show a large scatter in the ductile-to-brittle transition range, the fracture toughness should be evaluated with the statistical nature. This means that a certain statistical approach is necessary for the evaluation of the fracture toughness. Fracture toughness values from small size specimens, such as surveillance specimens, also show large effects on specimen size. Although intensive research[e.g. 5] has been conducted to establish the statistical treatment and the evaluation method of size effects in the past, the methods need a large number of specimens and/or relatively large size specimens[6]. The number and the size of surveillance specimens are limited by the small volume of a surveillance capsule. Therefore, further research is desired to resolve the limitation and to establish an improved surveillance test method that is applicable for the small number and the small sizes of specimens.

This paper describes the results of fracture toughness tests using four kinds of pressure vessel steels including an IAEA reference material JRQ. Based on the results of the fracture toughness tests by precracked Charpy specimens and standard size 1T-CT and 4T-CT specimens, a statistical analysis was performed to evaluate the scatter and the lower bound of fracture toughness in the transition temperature range. A part of this report was performed at JAERI in the framework of the IAEA Coordinated Research Program Phase-3[7].

## 2. EXPERIMENTS

### 2.1 Materials

Materials used in this study were four kinds of pressure vessel steels of ASTM A533B class 1. The one is designated JRQ, which was used as a correlation monitor material in the IAEA CRP-3[8]. The another material was chosen to have a large number of database for cleavage fracture toughness from small size specimens to large ones. The material is designated as JSPS A533B-1 which was used in the round robin study organized by The Japan Society for Promoting of Science (JSPS)[9]. The other materials were made as A533B-1 steels which were called as Steel A and Steel B that corresponded to the old age RPV steel and the modern steel, respectively. Chemical compositions of the materials are summarized in Table 1. Mechanical properties at room temperature for the materials are listed in Table 2.

### 2.2 Fracture Toughness Tests

Four types of specimens were used in this study, namely precracked Charpy (PCCv), 0.5T-DCT, 1T-CT and 4T-CT. In some cases the specimens were side-grooved by 10% on each side of the specimen after precracking. For JSPS A533B-1 steel, one of the authors performed fracture toughness tests using PCCv specimens machined from halves of broken 2T-CT specimens at SCK/CEN[10]. The notch orientation of the specimens is T-L direction for all specimens. All specimens were machined from the approximately quarter thickness position of the material. Fracture toughness tests were performed at mainly lower transition temperature range which a cleavage fracture was occurred before the limit load of the specimen. Some specimens were also tested at an upper shelf temperature range to obtain J-R curves.

Testing and evaluation for fracture toughness were performed according to ASTM standards[11,12] and JSME method[13]. A valid plane-strain fracture toughness, $K_{IC}$, could not be

obtained from the specimens except for 4T-CT specimens. The following method, therefore, was applied to obtain elastic-plastic fracture toughness. Fracture toughness values at cleavage fracture, Jc, were calculated based on the area under load-displacement curve up to the sudden load drop and the cleavage fracture load (see eq. 1). Fracture toughness $K_{JC}$ values were then converted from $J_C$ by the following equation (2). Elastic modulus E and Poisson's ratio $\nu$ were fixed to 206 GPa and 0.3 in this study, respectively.

$$J_C = J_{el} + J_{pl} = \frac{K_C{}^2}{E'} + \frac{\eta A_{pl}}{B_N b_0} \tag{1}$$

where Kc: Stress intensity factor at the cleavage fracture,

$\eta$ =2+0.522*($a_0$/W) for compact specimens,

$\eta$ =2 for PCCv specimens,

$A_{pl}$: Plastic part of the area under load-displacement curve,

$B_N$: Net thickness, $b_0$: Initial ligament (=W-$a_0$),

$a_0$: Initial crack length, W: Specimen width,

E'=E for ASTM, E'=E/(1- $\nu^2$) for JSME.

$$K_{JC} = \sqrt{E' J_C} \tag{2}$$

In the ASTM draft method[14], $\eta$ factor has been changed from 2.0 to 1.9 based on the 3-D detailed analysis for PCCv specimen[15]. This makes the fracture toughness value lower by maximum 5% in terms of J-integral. When some equations in the ASTM draft method are applied to the data, the new $\eta$ factor is used.

At upper shelf temperature range, $J_{IC}$ values and J-R curves for the materials except for the JSPS A533B-1 were obtained according to the JSME method. Ductile crack growth in a specimen during a test was measured by unloading elastic compliance method.

### 2.3 Irradiation

PCCv and 0.5T-DCT specimens of JRQ were irradiated in Japan Materials Testing Reactor (JMTR, thermal output 50MW). Fast neutron fluence for each specimen was calculated to be within the range from 1.9 to 2.5 x $10^{19}$ n/cm$^2$ (E>1 MeV). The displacement per atom (dpa) for iron by the irradiation to 2 x $10^{19}$ n/cm$^2$ (E>1 MeV) was about 3 x $10^{-2}$. Fast neutron flux was about 1.2 x $10^{13}$ n/cm$^2$s (E>1 MeV). Temperature for the specimens during irradiation was controlled in the range from 280 to 300 ℃. The shifts of Charpy transition temperatures and the hardening by neutron irradiation are summarized in Table 3[7].

Many specimens of Steel A and Steel B were also irradiated at JMTR. Sixteen PCCv specimens of the steels were encapsuled with ten Charpy-V specimens for the JMTR irradiation. Post irradiation tests for those specimens are now underway.

## 3. RESULTS AND DISCUSSION

### 3.1 Fracture Toughness Database

Figures 1 to 5 show cleavage fracture toughness data obtained in this study[16]. The

validity limit for the PCCv data based on equation (3) is indicated. This criterion has been stipulated in the JSPS method.

$$b_0, B > \frac{J_C \sigma_Y}{25} \tag{3}$$

The equation (3) used in the JSPS method is the same as the validity criterion on the determination of a $J_{IC}$ in the ASTM E813. For the PCCv specimen, the ligament size, $b_0$, is smaller than the specimen thickness, B. Therefore, $b_0$ is considered as a key parameter for the validity of PCCv data.

Figure 1 shows $K_{JC}$ values of unirradiated JRQ specimens tested in the transition range. At room temperature, cleavage fracture was not observed from any PCCv specimens, but from all 0.5TDCT and 1TCT specimens. When PCCv and 1T-CT data are compared at –80 ℃, it is seen that 1T-CT data are situated within the scatter range of PCCv data. The $J_{IC}$ value at 100 ℃ obtained from 1T-CT and 0.5T-DCT specimens by means of the JSME method is also indicated in the figure. Some data points of PCCv and compact specimens tested at upper transition temperature range exceeded the $J_{IC}$ value.

Figure 2 shows all cleavage fracture toughness data of irradiated JRQ specimens. Test temperatures for five PCCv and six 0.5TDCT specimens, performed in the frame work of IAEA CRP-3, were sparse from 0 to 100 ℃. We tested additional irradiated PCCv specimens; twelve specimens around 17 ℃ and ten at 35 ℃ so that a statistical analysis could be done.

Figure 3 shows fracture toughness values from PCCv specimens of JSPS A533B-1 steel with a large number of database by means of compact specimens from 0.5T to 4T[13]. The database includes –25, 0 and 25 ℃ data while PCCv were tested at 0 ℃. Obviously PCCv data show higher fracture toughness values than the other compact specimen data.

The cleavage fracture toughness data of Steel A are shown in Figure 4. The data include some valid $K_{IC}$ data from 4T-CT. The $K_{IC}$ data locates nearly the lowest bound of the other data. The PCCv data show higher $K_{JC}$ values than $K_{JC}$ of 1T-CT and $K_{IC}$ of 4T-CT data. The upper shelf fracture toughness, $J_{IC}$, obtained by 1T-CT at 20 ℃ is indicated in the figure. More than half of PCCv data at –50 ℃ exceeded the $J_{IC}$ value.

Figure 5 indicates the results of fracture toughness tests by specimens of Steel B. Valid $K_{IC}$ data points from 4T-CT are also shown in this figure. The $K_{IC}$ data lie nearly lowest bound of the other data. Similarly to Steel A, PCCv data indicate higher toughness values than the other CT data. The upper shelf fracture toughness, $J_{IC}$, obtained from 1T-CT at 20 ℃ is indicated in the figure. Several PCCv data at –80 ℃ exceeded the $J_{IC}$ value.

### 3.2 Specimen Size Effect on Cleavage Fracture Toughness

As is known well, a fracture toughness value from a small specimen can be higher than that from a large specimen. In addition to this, in the transition range, a statistical effect on cleavage fracture is apparent. This has been explained by the weakest link theory[17,18] that is based on the local inhomogeneity in the material. The theory treats the probability to find a particle that is located randomly in the material and that leads to the fracture of the specimen. Another reason is that the small specimen has insufficient length in thickness to keep small scale yielding and maintain a certain level of constraint at a crack tip, as compared with a large size specimen or a real heavy-section structure[19].

Figure 6 shows the effect of specimen thickness on fracture toughness value. Each value was normalized by $K_{IC}$ values for each testing condition. This figure clearly shows the size dependence on the mean value. The highest PCCv data was larger than four times of $K_{IC}$ value. The mean values of PCCv data except for invalid data were 1.5 to 2.2 compared to $K_{IC}$ value. On the other hand, the lowest value of PCCv data was approximately the same as the $K_{IC}$ value.

To obtain a reliable fracture toughness value from a small size specimen, several correction schemes have been proposed. Wallin[20] has proposed the following equation for correcting specimen size applicable to pressure vessel steels;

$$K_{JC\_y} = K_{\min} + (K_{JC\_x} - K_{\min})(B_x / B_y)^{1/m} \tag{4}$$

where $K_{JC\_x \text{ or } y}$: $K_{JC}$ for specimens of thickness, $B_{x \text{ or } y}$

$K_{\min} = 20\ MPa\sqrt{m}$

m = 4

Figure 6 includes the size effect correction curve based on the equation (4). The upper curve is corresponding to Steel B, the lower curve is for Steel A. The correction curve for Steel B overestimated 30% of $K_{IC}$ value by 4T-CT specimen. Unfortunately $K_{IC}$ value of JRQ was not available. However, the size correction was compared between PCCv and 1T-CT data. As a result, the correction provided the 1T-CT equivalent values from PCCv data. To verify the correction equation, we need more database including sufficient number of PCCv data.

### 3.3 Scatter of Fracture Toughness

The equation (4) is based on the weakest link theory. The theory assumes that the distribution of the fracture toughness values of a material can be described as a Weibull type statistics. Using three parameters, $K_{min}$, m and $K_0$, the fracture probability based on Weibull statistics can be expressed by the following equation[20].

$$P_f = 1 - \exp\left(-\left(\frac{K_{JC\_1T} - K_{\min}}{K_0 - K_{\min}}\right)^m\right) = 1 - \exp\left(-\left(\frac{K_{JC\_1T} - 20}{K_0 - 20}\right)^m\right) \tag{5}$$

where $P_f$: Median ranking($= (i - 0.3)/(N + 0.4)$)

m, $K_0$: Fitting parameters

All data obtained by the same-type specimens at a certain temperature can be analyzed by these equations (4) and (5). This equation (5) has also been incorporated into the ASTM draft method to describe the statistics of cleavage fracture toughness.

Figures 7 to 9 compare Weibull plots of PCCv data and 1T-CT data. PCCv data were corrected by equation (4) to 1T-CT thickness for comparison. These figures also include the fitting curve by equation (5). Figure 7 indicates that the corrected PCCv data and 1T-CT data of unirradiated JRQ are in good agreement. The parameter m in equation (5) were 2.3 and 2.5 for PCCv adjusted data and 1T-CT data, respectively. These values were much less than the theoretical value of four. Figure 8 shows the Weibull plots of PCCv data of irradiated JRQ. The m values were 2.8 and 3.1 for the data tested at 17 ℃ and 35 ℃, respectively. The slopes were again smaller than the theoretical values. However, it is noted that the m value became a bit large

after irradiation. In other words, neutron irradiation could make the data scatter smaller. This means that the scatter after irradiation may be estimated conservatively by applying the scatter before irradiation.

Figure 9 shows Weibull plot of steels A. In this case, 1T-CT data were well fitted by means of a theoretical m value. The mean value of corrected PCCv data was higher than that of 1T-CT data. For the data scatter, the corrected PCCv data showed the same tendency as PCCv of JRQ, that is, the m value was smaller than the theoretical value of four. For the lower bound data, however, approximately the same trend was seen between both data below 5% fracture probability. If the theoretical m value was used for data fitting, the lower tail of PCCv data is much higher than that of 1T-CT data.

Figure 10 summarizes the Weibull parameter m obtained from this study. Although a large scatter of m values was seen, the m value tends to decrease as specimen thickness decrease. To estimate the lower bound from a limited number of PCCv data, it may be helpful to use the experimental m value instead of the theoretical value.

### 3.4 Temperature Dependence of Fracture Toughness

The median value of the data can be obtained by $K_0$ from equation (5) and the following equation as a fracture probability $P_f$=0.5.

$$K_{JC\_1T(med)} = (K_0 - 20)[\ln(2)]^{1/4} + 20 \tag{6}$$

Using this median value, the temperature dependence of cleavage fracture toughness within the transition range is expressed by the following equation[14,20].

$$K_{JC\_1T(med)} = 30 + 70 \cdot \exp\{0.019 \cdot (T - T_0)\} \tag{7}$$

This equation has been established by statistical analyses using a huge database including unirradiated and irradiated RPV steels[20]. This equation, which is called a master curve, uniquely defines the cleavage fracture toughness transition curve. A reference temperature , $T_0$, can be calculated by

$$T_0 = T - \frac{1}{0.019} \cdot \ln\{(K_{JC\_1T(med)} - 30)/70\} \tag{7'}$$

Table 4 lists the $T_0$ values obtained from materials used in this study. Figure 11 shows the values of $T_0$ based on the method above as a function of specimen thickness. The values of $T_0$ from unirradiated JRQ and JSPS A533B-1 showed little effect on specimen thickness, while those of steels A and B showed a size effect to some extent. The $T_0$ values from PCCv data were about 20 ℃ lower than those values from 1T-CT data for both steels A and B. The deviation of 20 ℃ is larger than the deviation of 5~10 ℃ reported for some RPV steels in reference (21). The reason of the deviation is not clear for the moment. Additional tests might help to understand the reason because the number of valid data from PCCv specimen of Steels A and B were relatively small (<10).

Figure 12 shows all data as a function of the difference between test temperature and $T_0$ determined by PCCv data. The fracture toughness values were size-corrected to 1T thickness by equation (4). Below 30 ℃ of T-$T_0$, the master curve agrees well with the data. At the higher

transition range the master curve tends to overestimate the data. Of course, the use of the master curve to higher temperature should be restricted because the PCCv data is no longer valid above ~200 MPa$\sqrt{}$m.

Comparing the $T_0$ before and after irradiation, we obtain the shift of fracture toughness. Figure 13 shows the master curve for JRQ steel before and after irradiation. Before irradiation, the T0 value was determined by PCCv data tested at –80 ℃ and –50 ℃. The $T_0$ value after irradiation was the average of two $T_0$ values from two PCCv data sets tested at 17℃ and 35℃. The shift of $T_0$ by irradiation to JRQ was then calculated as 108 ℃. This shift is larger than the Charpy shift listed in Table 3 by about 20 ℃.

Based on Weibull statistics, tolerance bounds for the master curve can be drawn. Assuming the Weibull slope m=4, the third parameter $K_{min}$=20 and an infinite sampling size, a lower bound curve in the same form as equation (7) can be defined. Figures 12 and 13 indicate the lower tolerance bound curves. As mentioned before, the experimental data indicated larger scatter then the theory. The 5% lower bound curve is not enough to bound the experimental values. Instead of 5% bound curve, the 1% bound curve is in good agreement.

The Japanese code on the method for the fracture toughness test and evaluation, JEAC 4206[22], stipulates the method to obtain the lower bound toughness curve for the integrity assessment of RPV during a PTS transient. The curve can be defined as the lowest envelope of all the fracture toughness data points from the surveillance tests. The form of the curve is expressed by the following:

$$K_{IC} = 20.16 + 129.9 \cdot \exp\{0.0161 \cdot (T - T_{0J})\} \quad (8)$$

Figure 14 shows the JEAC $K_{IC}$ curve together with 1% tolerance bound curve based on the weakest link theory. To compare all data with those curves, the data points without size-correction were plotted as a function of T-$T_0$. The shape of JEAC $K_{IC}$ curve coincides well with the lowest data points. The 1% tolerance bound curve agrees with the JEAC $K_{IC}$ curve in the lower transition range but tends to become higher at higher temperature. Although this comparison is limited to only four material, the JEAC method could give the conservative estimation of the lower bound curve.

Applying equation (8) to the data of JRQ steel, we obtain the lower bound curves before and after irradiation, and hence the shift of the lower bound curves. Figure 15 indicates the JEAC $K_{IC}$ curves before and after irradiation together with all test data. The curve after irradiation was determined by shifting the $K_{IC}$ curve before irradiation by the amount of Charpy shift. The lower bound curves agreed well with the data up to upper transition range, leading to a conservative evaluation. When we compare the test data before and after irradiation, we obtain the shift of $T_{0J}$ value by irradiation of ~80 ℃. This values was slightly less than the Charpy shift. Therefore, the $K_{IC}$ curve after irradiation became conservative. This may depend on the statistical treatment of the data. If we had more data from irradiated specimens or less data from unirradiated specimens, we might have got less conservative $K_{IC}$ curve after irradiation.

The following equation (9) is the $K_{IC}$ curve in the ASME Sec. XI[1] to describe the lower bound fracture toughness of RPV steels.

$$K_{IC} = 36.5 + 22.8 \cdot \exp\{0.036 \cdot (T - RT_{NDT})\} \quad (9)$$

In this case, we need an $RT_{NDT}$ of the steel to define the $K_{IC}$ curve. The $RT_{NDT}$ is

determined by the combination of the results from drop weight test and Charpy impact test. The drop weight test can not be done after irradiation because the test requires relatively large size specimens. Therefore, Charpy impact results are used instead of the results of drop weight test to determine the irradiation effects. The adjusted $RT_{NDT}$ value after neutron irradiation is then calculated with the Charpy shift added to the initial $RT_{NDT}$. The $K_{IC}$ curve after irradiation is defined by an equation (9) using the adjusted value. This means that the irradiation effect on Charpy property and fracture toughness should be equivalent. Figure 16 shows the comparison of the experimental data and the ASME $K_{IC}$ curves. This figure clearly shows that all data are bounded by the ASME $K_{IC}$ curve based on $RT_{NDT}$. For the moment, the ASME method gives a good approximation for the lower bound curve. However, the shift of fracture toughness can be larger than Charpy shift as obtained from JRQ results. The lower bound curve for highly irradiated material should be carefully checked by fracture toughness tests.

## 4. SUMMARY AND CONCLUSIONS

To establish the method to evaluate fracture toughness values in the transition region, fracture toughness tests using PCCv to 4T-CT specimens were performed. Although post irradiation tests have finished only for JRQ, the following conclusion were drawn from the tests of four types of Japanese RPV steels and their analysis;

(1) The size effect correction based on the weakest link theory was not always enough to obtain an equivalent value from a PCCv specimen to a large specimen.
(2) For data scatter, experimantal value of the Weibull slope was not much affected and slightly decreased by neutron irradiation.
(3) According to the master curve, the shift of the curve by irradiation was evaluated to be somewhat greater than the Charpy 41J shift.
(4) JEAC $K_{IC}$ curves for JRQ data before and after irradiation could be conservative. However, large number of data before irradiation would be necessary.

## ACKNOWLEDGMENTS

A part of this work was carried out under the contract between JAERI and Science and Technology Agency of Japan under the auspices of the special account law for electric power development promotion. The authors would like to thank Dr. K. Shibata and Mr. Y. Nishiyama, Japan Atomic Energy Research Institute for their encouragement and helpful discussion, and many staffs at Hot Laboratory of JAERI for their careful testing of irradiated specimens. They are also grateful to Dr. T. Iwadate and Dr. Y. Tanaka of the Japan Steel Works, Ltd. for providing the JSPS A533B-1 material. The tests of PCCv specimens of JSPS A533B-1 were done at SCK/CEN during the period that one of the authors had stayed there.

## REFERENCES

(1) ASME Boiler and Pressure Vessel Code, Section XI, "Inservice Inspection of Nuclear Power Plant," American Society for Mechanical Engineers, 1995.

(2) Japanese Electric Association, "Methods of surveillance tests for structural materials of nuclear reactors," JEAC 4201-1991. (in Japanese)
(3) R. Nanstad et al., "Irradiation Effects on Fracture Toughness of Two High-Copper Submerged-arc Welds, HSSI Series 5," NUREG/CR-5913 Vol.1, October 1992, U.S.NRC.
(4) K. Wallin et al., "Beyond the Charpy - Improved toughness predictions and advanced surveillance," presented at Radiation Damage and Embrittlement in Pressure Vessel Steels - IGRDM Open Workshop, Santa Barbara, May 6, 1994.
(5) M.T. Miglin, et al., "Analysis of Results from the MPC/JSPS Round Robin Testing Program in the Ductile-to-Brittle Transition Region," Fracture Mechanics: Twenty-fourth Volume, ASTM STP 1207, J.D. Landes, D. E. McCabe and J. A. M. Boulet, Eds., Americal Society for Testing and Materials, Philadelphia, 1995, pp. 342-354.
(6) T. Iwadate et al., "An Analysis of Elastic-Plastic Fracture Toughness Behavior for JIC Measurement in the Transition Region," Elastic-Plastic Fracture: Second Symposium, Volume II-Fracture Resistance Curves and Engineering Applications, ASTM STP 803, American Society for Testing and Materials, 1983, pp. II-531-II-561.
(7) K. Onizawa et al., "JAERI contribution for the IAEA coordinated research program phase III on optimizing of reactor pressure vessel surveillance programmes and their analysis," JAERI-M 93-201, Japan Atomic Energy Research Institute (October 1993).
(8) CRP Sub-Committee, "Manufacturing History and Mechanical Properties of Japanese Materials Provided for The International Atomic Energy Agency," Japan Welding Engineering Society, Oct. 1986.
(9) JSPS 129 Committee, "Standard Test Method for Fracture Toughness within Ductile-Brittle Transition Range," Japan Society for Promoting Science, 1995.
(10) R. Chaouadi, "Fracture Toughness Measurements in the Transition Regime Using Small Size Samples," Small Specimen Test Techniques, ASTM STP 1329, W. R. Corwin, S. T. Rosinski, and E. van Walle, Eds., American Society for Testing and Materials, Philadelphia, 1998, to be published.
(11) ASTM E399-83, "Standard Test Method for Plane-Strain Fracture Toughness of Metallic Materials," Annual Book of ASTM Standards, Vol.03.01, American Standard for Testing and Materials, 1983.
(12) ASTM E813-89, "Standard Test Method for $J_{IC}$, A Measure of Fracture Toughness," Annual Book of ASTM Standards, Vol.03.01, American Standard for Testing and Materials, 1989.
(13) JSME S001-1992, "Standard Method of Test for Elastic-Plastic Fracture Toughness $J_{IC}$ (Supplement, 1st Edition)," The Japan Society of Mechanical Engineers, Feb., 1992.
(14) ASTM Draft 15, "Test Method for The Determination of Reference Temperature, T0, for Ferritic Steels in the Transition Range," Rev. 6-13-97, ASTM.
(15) M. Nevalainen and R. Dodds, "Numerical Investigation of 3-D Constraint Effects on Brittle Fracture in SE(B) and C(T) Specimens," NUREG/CR-6317, UILU-ENG-95-2001, July 1996.
(16) K. Onizawa, et al., "Investigation on the Evaluation of Cleavage Fracture Toughness Using PCCv Specimens in the Ductile-Brittle Transition Range of Reactor Pressure Vessel Steels," JAERI-Research 97-081, Nov. 1997.
(17) J.D. Landes and D.H. Shaffer, "Statistical Characterization of Fracture in the Transition

region," Fracture Mechanics: Twelfth Conference, ASTM STP 700, American Society for Testing and Materials, 1980, pp. 368-382.

(18) K. Wallin, "The Scatter in $K_{IC}$-Results," Engineering Fracture Mechanics, Vol. 19, No.6, pp.1085-1093, 1984.

(19) T. Anderson and R. Dodds, "Specimen Size requirements for Fracture Toughness Testing in the Ductile-Brittle Transition Region," Journal of Testing and Evaluation, Vol. 19, 1991, pp. 123-134.

(20) K. Wallin, "Irradiation Damage Effects on the Fracture Toughness Transition Curve Shape for Reactor Pressure Vessel Steels," International Journal of Pressure Vessel and Piping, 55(1993) pp.61-79.

(21) K. Wallin, "Validity of Small Specimen Fracture Toughness Estimates Neglecting Constraint Corrections," Constraint Effects in Fracture Theory and Applications: Second Volume, ASTM STP 1244, M. Kirk and Ad Bakker, Eds. American Society for Testing and Materials, Philadelphia, 1995.

(22) Japanese Electric Association, "Fracture Toughness Test Methods for Nuclear Power Plant Components," JEAC 4206-1991. (in Japanese)

Table 1 Chemical compositions of materials used in this study. (wt.%)

| Material | C | Si | Mn | P | S | Ni | Cr | Cu | Mo |
|---|---|---|---|---|---|---|---|---|---|
| JRQ | 0.18 | 0.24 | 1.42 | 0.017 | 0.004 | 0.84 | 0.12 | 0.14 | 0.51 |
| JSPS A533B-1 | 0.24 | 0.41 | 1.52 | 0.028 | 0.023 | 0.43 | 0.08 | - | 0.49 |
| Steel A | 0.19 | 0.30 | 1.30 | 0.015 | 0.010 | 0.68 | 0.17 | 0.16 | 0.53 |
| Steel B | 0.19 | 0.19 | 1.43 | 0.004 | 0.001 | 0.65 | 0.13 | 0.04 | 0.50 |

Table 2 Material properties at room temperature of materials used in this study.

| Material | $\sigma_{ys}$ (MPa) | $\sigma_{uts}$ (MPa) | Elongation (%) | Note |
|---|---|---|---|---|
| JRQ | 477 | 615 | 22.2 | |
| JSPS A533B-1 | 504 | 692 | 20.2 | Ref. (9) |
| Steel A | 469 | 612 | 26.4 | |
| Steel B | 462 | 597 | 24.9 | |

Table 3 Neutron irradiation effect on material properties of JRQ.

| Item | Fast Neutron Fluence | Irradiation Temperature | Index | Shift / Increase |
|---|---|---|---|---|
| Charpy shift | ~2.3x10$^{19}$ n/cm$^2$ | ~291 °C | $\Delta T_{41J}$ | 85 °C |
| | | | $\Delta T_{68J}$ | 89 °C |
| | | | $\Delta T_{50\%}$ | 86 °C |
| Hardening | ~1.6x10$^{19}$ n/cm$^2$ | ~288 °C | $\Delta \sigma_{ys}$ | 117 MPa |
| | | | $\Delta \sigma_{uts}$ | 107 MPa |
| | | | $\Delta$Elong. | -2.7 % |
| | ~2.2x10$^{19}$ n/cm$^2$ | ~286 °C | $\Delta$Hv(98N) | 41 VHN |

Table 4 Comparison of the values of $T_0$ determined according to the ASTM draft method.

| Material | JRQ unirradiated | | | | | |
|---|---|---|---|---|---|---|
| Specimen | B(mm) | $T_0$(°C) | N | r | Temp. (°C) | SG(%) |
| PCCv | 10.0 | −69.7 | 16 | 15 | −80 | 0 |
| PCCv | 10.0 | −66.0 | 8 | 8 | −80 | 20 |
| PCCv | 10.0 | −63.3 | 16 | 9 | −50 | 0 |
| 1TCT | 25.0 | −66.4 | 6 | 6 | −80 | 20 |

| Material | JRQ irradiated | | | | | |
|---|---|---|---|---|---|---|
| Specimen | B(mm) | $T_0$(°C) | N | r | Temp. (°C) | SG(%) |
| PCCv | 10.0 | 31.9 | 12 | 11 | 17 | 0 |
| PCCv | 10.0 | 47.8 | 10 | 10 | 35 | 0 |

| Material | JSPS A533B-1 | | | | | |
|---|---|---|---|---|---|---|
| Specimen | B(mm) | $T_0$(°C) | N | r | Temp. (°C) | SG(%) |
| PCCv | 10.0 | −1.1 | 10 | 7 | 0 | 0 |
| PCCv | 10.0 | − | 10 | 4 | 0 | 20 |
| 0.5TCT | 12.7 | 7.8 | 16 | 16 | −25 | 20 |
| 0.5TCT | 12.7 | 19.1 | 17 | 17 | 0 | 20 |
| 0.5TCT | 12.7 | 6.8 | 6 | 6 | 0 | 0 |
| 0.5TCT | 12.7 | 7.1 | 12 | 11 | 25 | 20 |
| 1TCT | 25.4 | 9.7 | 18 | 18 | −25 | 20 |
| 1TCT | 25.4 | 20.4 | 18 | 18 | 0 | 20 |
| 1TCT | 25.4 | 7.7 | 6 | 6 | 0 | 0 |
| 1TCT | 25.4 | 18.6 | 12 | 12 | 25 | 20 |
| 2TCT | 50.8 | 5.4 | 6 | 6 | 0 | 20 |

| Material | Steel A | | | | | |
|---|---|---|---|---|---|---|
| Specimen | B(mm) | $T_0$(°C) | N | r | Temp. (°C) | SG(%) |
| PCCv | 10.0 | −83.4 | 10 | 7 | −80 | 20 |
| 1TCT | 25.0 | −66.9 | 12 | 12 | −80 | 20 |
| 1TCT | 25.0 | −66.9 | 12 | 12 | −50 | 20 |

| Material | Steel B | | | | | |
|---|---|---|---|---|---|---|
| Specimen | B(mm) | $T_0$(°C) | N | r | Temp. (°C) | SG(%) |
| PCCv | 10.0 | −111.2 | 10 | 8 | −110 | 20 |
| 1TCT | 25.0 | −102.4 | 12 | 12 | −110 | 20 |
| 1TCT | 25.0 | −92.4 | 12 | 12 | −80 | 20 |

B: Specimen thickness
N: Total number of data used
r: Number of valid data
SG: Side grooving

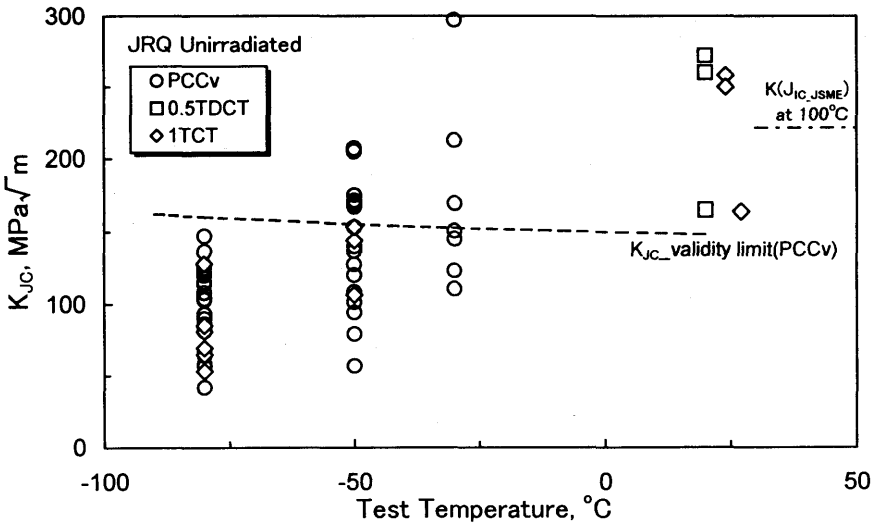


Figure 1--Fracture toughness test results of unirradiated JRQ steel.

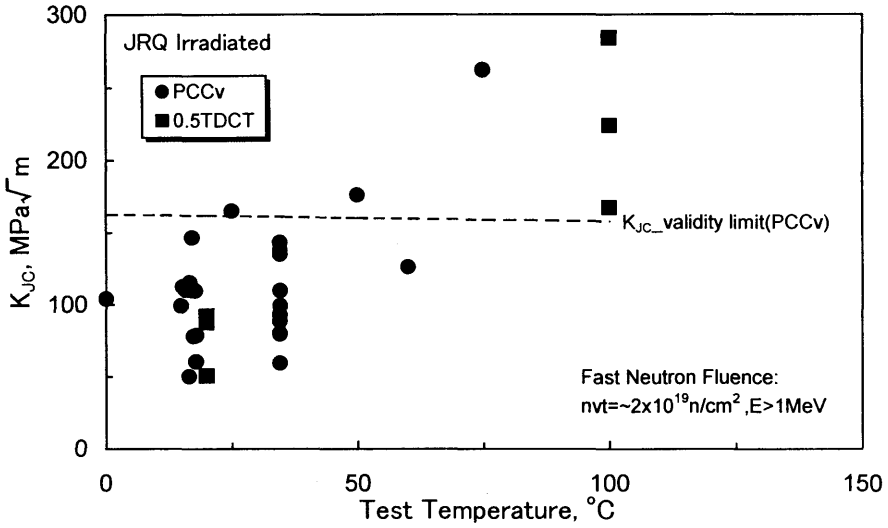


Figure 2--Fracture toughness test results of irradiated JRQ steel.

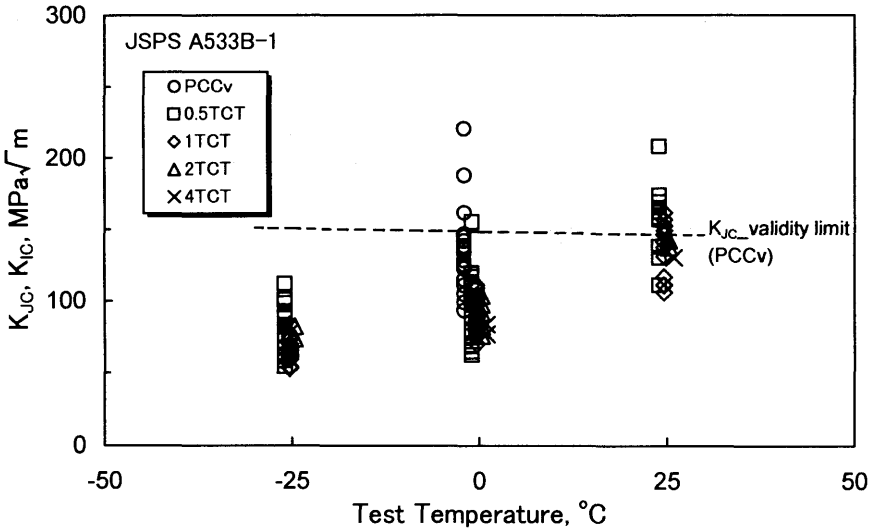


Figure 3--Fracture toughness test results of JSPS A533B-1 steel.

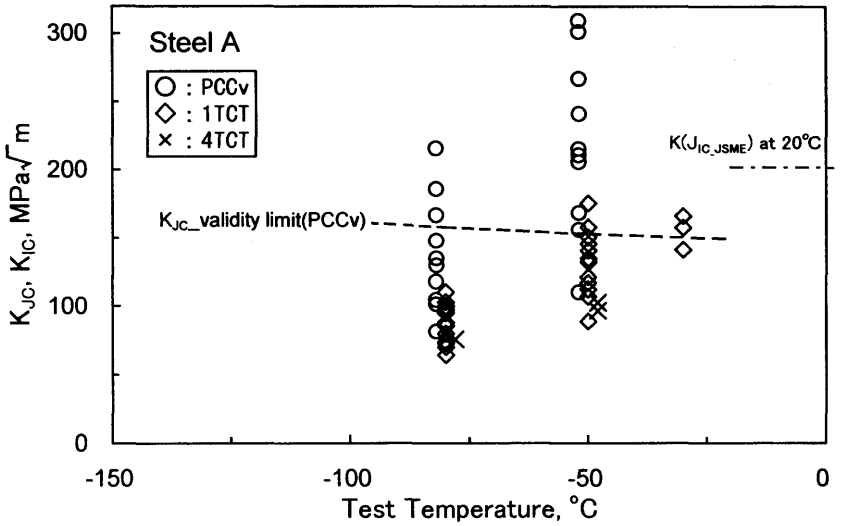


Figure 4--Fracture toughness test results of Steel A.

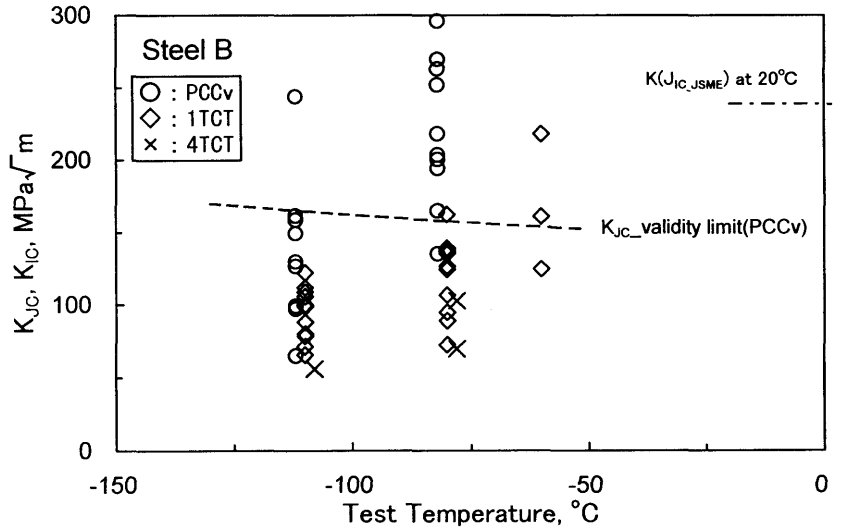


Figure 5--Fracture toughness test results of Steel B.

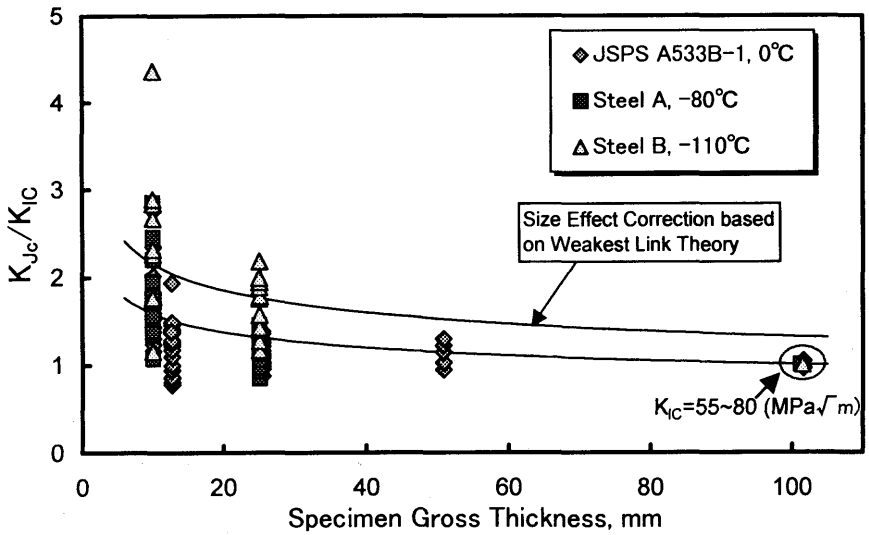


Figure 6--Normalized fracture toughness values as a function of specimen gross thickness.

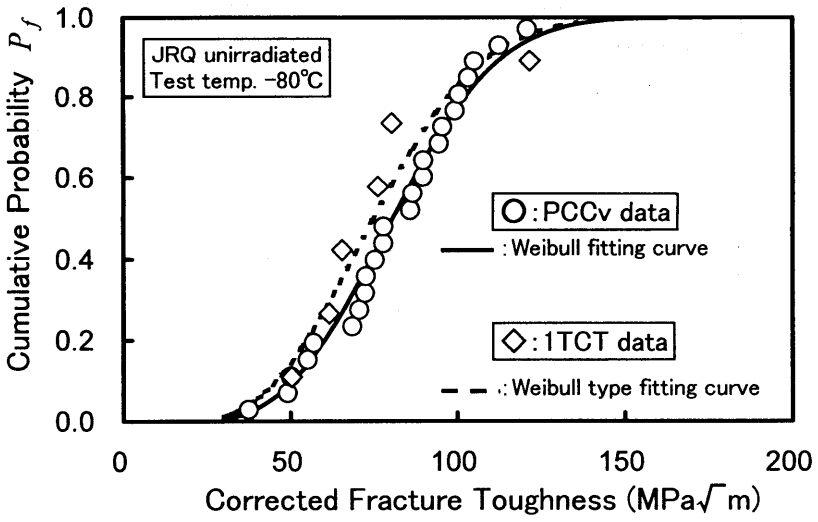


Figure 7--Weibull plots of unirradiated JRQ data at –80 ℃.

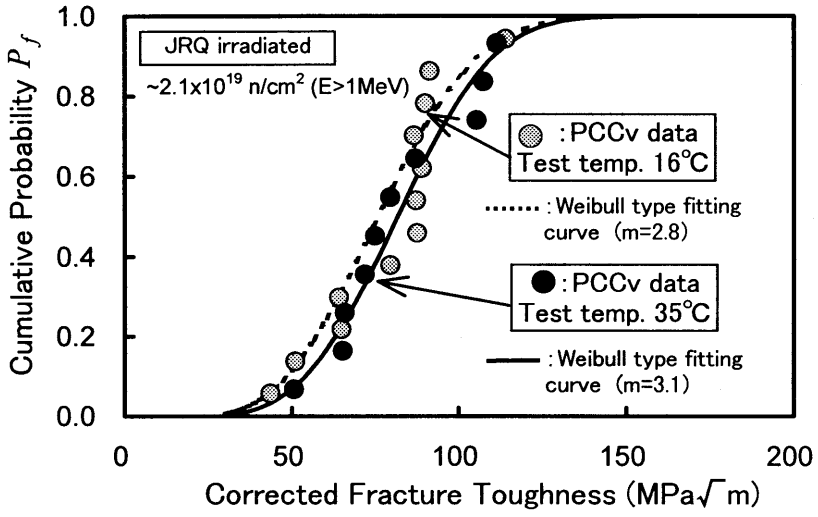


Figure 8--Weibull plots of irradiated JRQ data at 17 and 35 ℃.

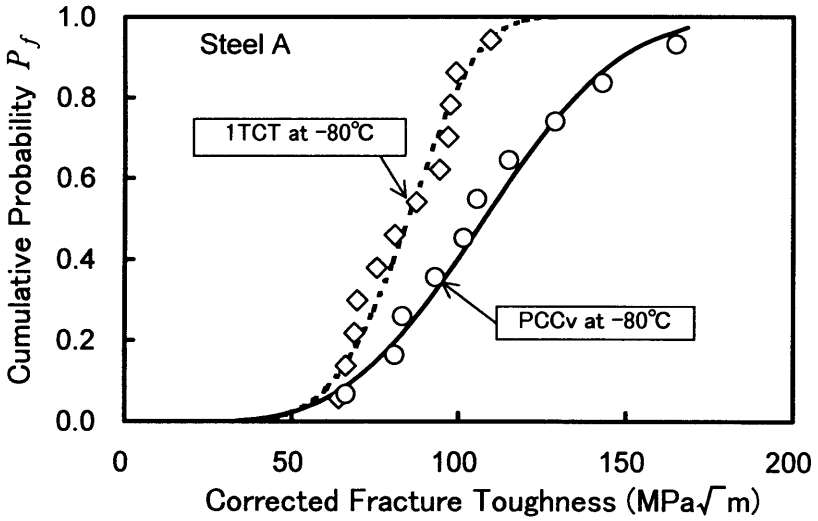


Figure 9--Weibull plots of Steel A data at –80 ℃.

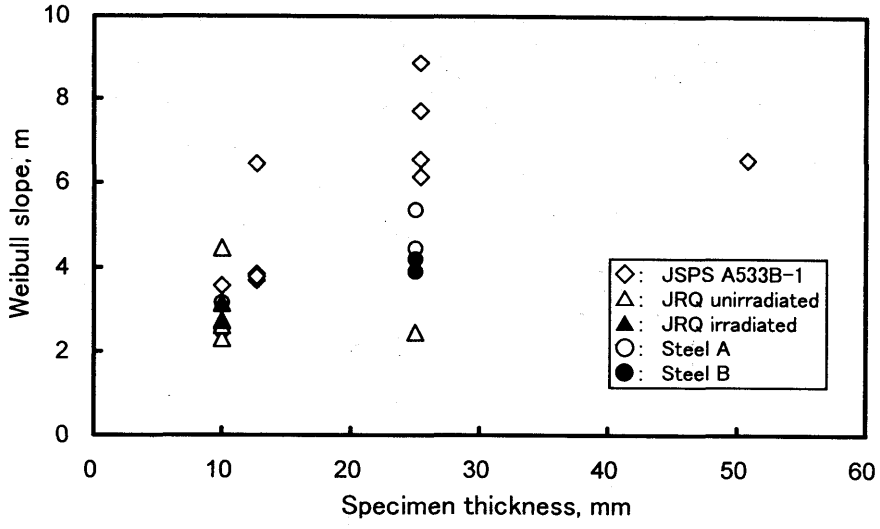


Figure 10—Comparison of Weibull slope m values as a function of specimen thickness.

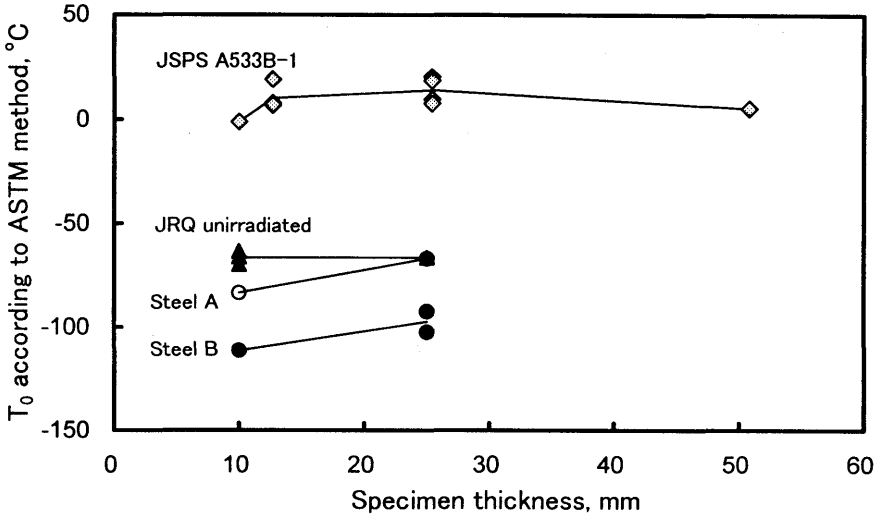


Figure 11--Comparison of reference temperature, $T_0$, according to the ASTM draft method as a function of specimen gross thickness.

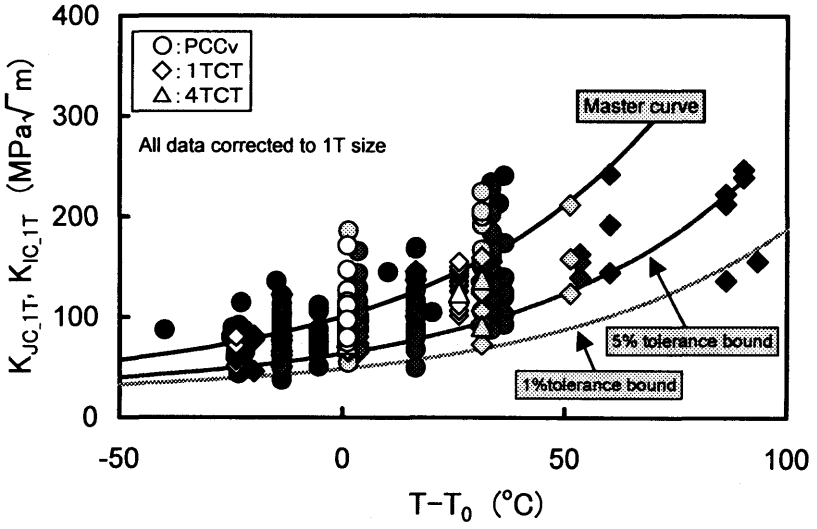


Figure 12--Size corrected data to 1T, the master curve and the 1% and 5% tolerance bound curves determined by PCCv data.

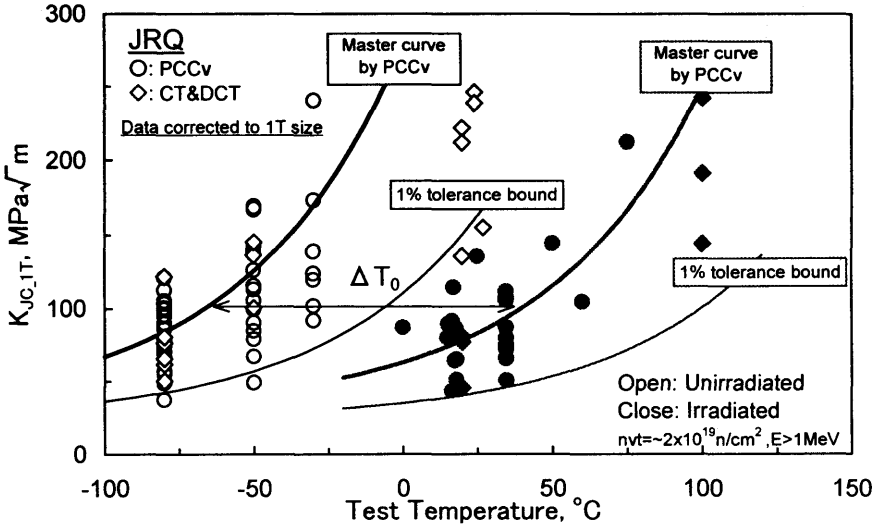


Figure 13—Master curves according to the ASTM draft method before and after irradiation.

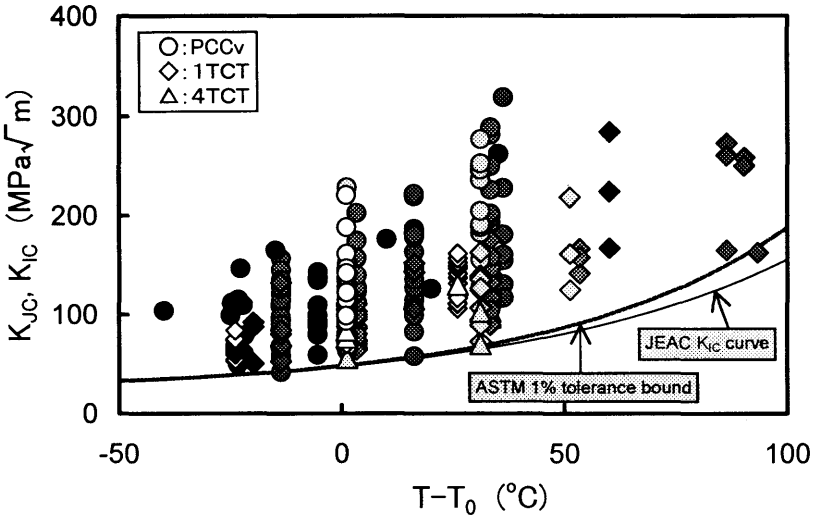


Figure 14--Comparison of the JEAC $K_{IC}$ curve and the ASTM 1% tolerance bound curve.

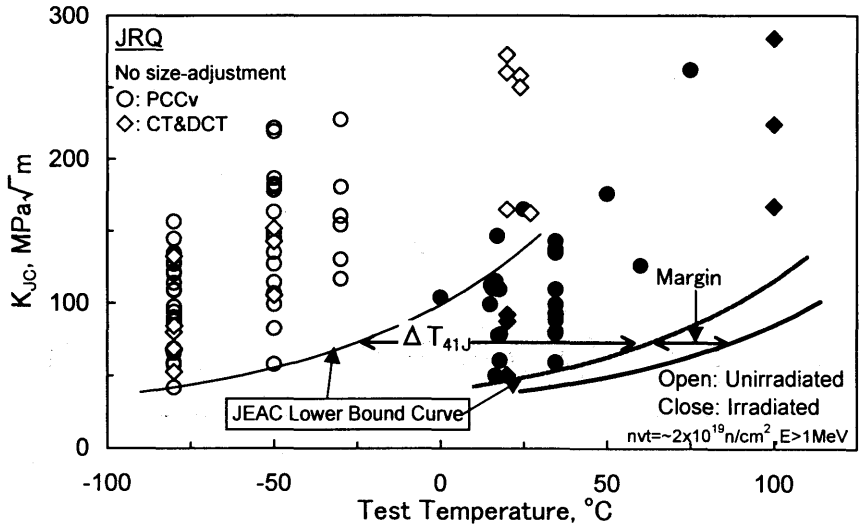


Figure 15--Lower bound curves according to the JEAC method steel before and after irradiation.

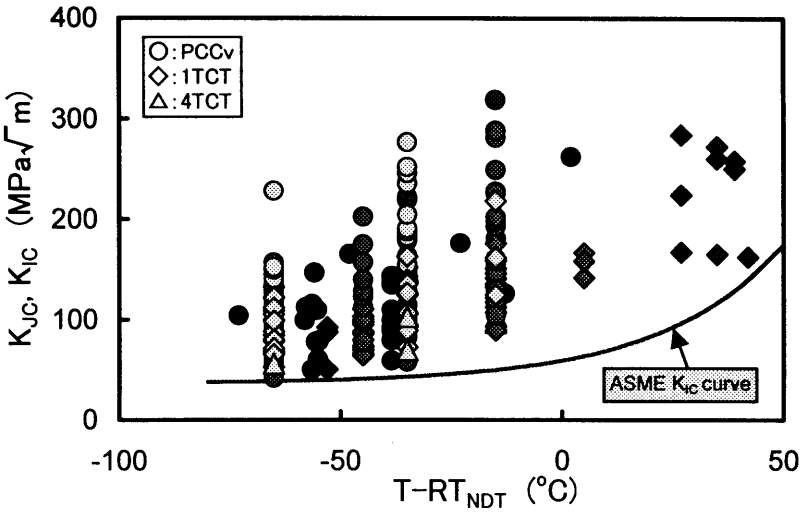


Figure 16—Comparison of all data and ASME $K_{IC}$ curve as a function of T-$RT_{NDT}$.